# The Thermoresponsive Behaviour of Selected Rare-earth Hafnate, Zirconate, and Titanate Compounds

Submitted by

Robert Peter Richardson BSc Hons (Wits)

University of the Witwatersrand

Supervised by

Professor David Gordon Billing

A dissertation submitted in fulfilment of the requirements of the degree of Master of Science

Department of Chemistry

University of the Witwatersrand

2016

# Declaration

I declare that this thesis is my own unaided work. It is being submitted for the Degree of Master of Science in Chemistry in the University of the Witwatersrand, Johannesburg. It has not been submitted

before for any degree or examination in any other University

_____

Signature of Candidate

on the ____day of _____ 2016

# Acknowledgments

I would like to thank the following people:

Prof Dave G Billing for being a great supervisor and for teaching me important aspects in chemistry as well as valuable lessons outside of the discipline.

Mashikoane Wilson Mogodi for all of the assistance in the lab and sharing a lot of good times together

Stuart Miller for his significant help in correcting my final write-up

My parents, Janine and Peter Richardson for their support during the completion of this dissertation. They helped me in my times of need and I am forever grateful to them.

My girlfriend, Leigshe Ballantyne, for always being by my side (and listening to my constant complaints).

The DST NRF Centre of Excellence in Strong Materials for funding and my bursary, without your aid this would not have been possible.

# Abstract

The lattice parameters and thermal expansion coefficients for $La_2Hf_2O_7$, $Eu_2Hf_2O_7$, $Gd_2Hf_2O_7$, $Y_2Hf_2O_7$, $Gd_2Zr_2O_7$, $Y_2Zr_2O_7$, $Eu_2Ti_2O_7$, $Gd_2Ti_2O_7$, and $Y_2Ti_2O_7$ were determined relative to temperature over the range of 30°C to 850°C. All materials were determined to be of the pyrochlore phase expect for $Y_2Hf_2O_7$, which crystallised in the defect fluorite phase. All materials were shown to have positive thermal expansion, which was not consistent over the experimental temperature range. The change in the thermal expansion coefficient was positive for $La_2Hf_2O_7$, $Y_2Zr_2O_7$, $Eu_2Ti_2O_7$ and $Y_2Ti_2O_7$, of which the largest change was experienced by $Y_2Zr_2O_7$. The remaining materials experienced a negative change in their thermal expansion coefficients. The largest negative change was experienced by $Gd_2Ti_2O_7$. It was shown that the x parameter of the 48f oxygen atom increased with increasing temperature. This had the effect of distorting the transition metal octahedral, and creating a more perfect rare-earth cube as the parameter increased.

# Table of contents

## Contents

# 1. Introduction

Functional materials can be considered as a driving force for technological advancement in modern society. Without their development and production, many modern necessities and conveniences would not exist, as functional materials provide the working mechanism for a number of technologies which include: electronics, energy, safe drinking water, catalysis, thermal-insulation, wear resistance, etc. Such properties can be seen in the range of materials in question, namely rare-earth hafnates, zirconates and titanates. The structures of interest here are the pyrochlore (*F* d-3m) and its related structure, defect fluorite (*F* m-3m).

The group of materials of the general formula $La_2M_2O_7$ (where La = lanthanides, M = a transition metal) fulfils many of the previously mentioned uses and properties. The pyrochlore and defect fluorite phase of a selection of these metals are the focus of this dissertation.

## 1.1. Powder X-Ray Diffraction

The principal technique used for analysis in this dissertation was variable temperature Powder X-Ray Diffraction (VT-PXRD). Powder X-Ray Diffraction (PXRD) is the diffraction of X-rays by a poly crystalline material. The random orientation of the crystallites within the powder causes a diffraction cone to be formed by the sample as the discrete diffraction peaks of each crystallite points in a different direction along the surface of the diffraction cone. The effect is that the three dimensions of information given by Single Crystal X-Ray diffraction is collapsed into one dimension of information in the powder diffraction pattern. In a PXRD experiment, the detector is scanned through a cross section of all the diffraction cones (a summation of discrete crystallite diffraction peaks oriented at different angle to form a diffraction cone), measuring each as an intensity peak at a particular angle (measured as $^{\circ}2\theta$). Each peak corresponds to a unique set of Miller planes within the crystal structure of the sample material. These Miller planes are then used to determine crystallographic information via standard crystallographic methods.

In VT-PXRD, the crystallographic information (in particular the unit cell parameters) is determined for a sample over a range of discrete temperatures. This analysis highlights changes in the material with respect to temperature.

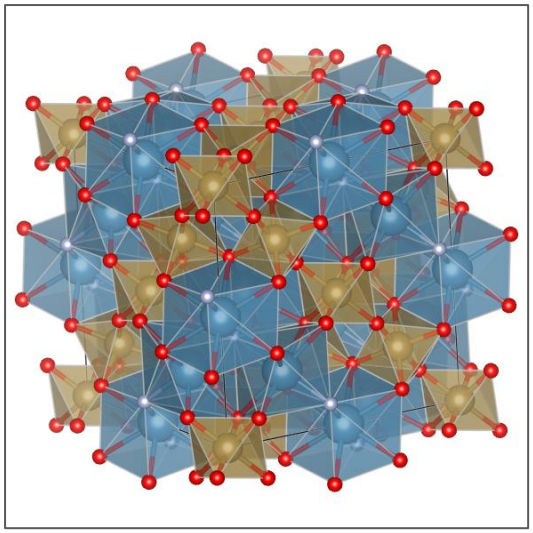

*Figure 1-1: Natural pyrochlore Calcium Tantalate ($Ca_2Ta_2O_6F$)*

## 1.2. Structural Characteristics

The materials in question (when stoichiometric in chemical formulae) crystallise in one of two structures, namely the pyrochlore or the defect fluorite structure types. These structure types are based on the minerals of the same name. The pyrochlore mineral has a chemical formula of $(Na,Ca)_2Nb_2O_6(OH,F)$. Figure 1.1 illustrates a tantalite variation on natural pyrochlore. The general formula of the range of structures of this type is $A_2B_2O_6O'$, where O' can be O, OH or F (Chakoumakos, 1984). In the case presented here, O' can be considered as O. One of the principal requirements for the structure is that the radius of cation A has to be larger than that of cation B. This can be expressed as a ratio, forming the pyrochlore within a certain range of that ratio. At ambient temperatures the stability range for the existence of a pyrochlore structure is given by: $r_A/r_b$ = 1.46 to 1.78 (see section 3 for the plot), where the lower limit is characteristic of $Gd_2Zr_2O_7$ and the upper limit characterised by $Sm_2Ti_2O_7$ (Ewing, Weber, & Lian, 2004). Under high pressures, this stability range is extended from 1.29 to 2.30 (this includes germinate and silicate pyrochlores) (Ewing, Weber, & Lian, 2004). As a result of these criteria, many pyrochlore analogues of hafnates, zirconates, stannates and titanates are formed due to the large number of potential acceptable co-cations. As the radii of the A and B cations become more similar, the likelihood of random distribution increases, and hence promotes the formation of the defect-fluorite phase (Ewing, Weber, & Lian, 2004). Pyrochlore structures have a face centred cubic unit cell of the *F*d-3m space group (No.227) (figure 1.2) and is a 2x2x2 supercell of the defect fluorite lattice, with ordering of cation and oxygen vacancies (Ewing, Weber, & Lian, 2004). This ordering may be best understood with the use of Wyckoff position notation. Cations A and B lie on the 16d and 16c positions respectively, each with -3m point symmetry (i.e. a threefold roto-inversion along the [111] direction and a mirror plane along the [110] direction). Oxygen one (O1) lies on the 8b position characterised by -43m point symmetry (i.e. A four-fold roto-inversion along the [100]

directions, a threefold rotation along the [111] direction and a mirror plane along the [110] direction). Oxygen two (O2) lies on the 48f position with a point symmetry of 2mm. This particular point symmetry allows the x coordinate of the anion to vary depending on the particular crystal in question. It is this ability to vary position that gives rise to a number of properties of the pyrochlore structure type. The last noteworthy position is position 8a, which in the unit cell belongs to oxygen three (O3), which is absent in a perfect pyrochlore. Position 8a is characterised by the same point symmetry as position 8b (I.e.-43m) (Bilbao crystallographic server 20/06/2014) (Ewing, Weber, & Lian, 2004) (Chakoumakos, 1984). It is the existence of this position that allows for a disordered state to exist, and allows for greater conductivity of oxygen ions through the lattice. Since all atoms except for $O_{48f}$ lie on special positions, only two parameters are required to describe the unit cell, namely the lattice parameter, a, and the x-coordinate for $O_{48f}$ (Ewing, Weber, & Lian, 2004).

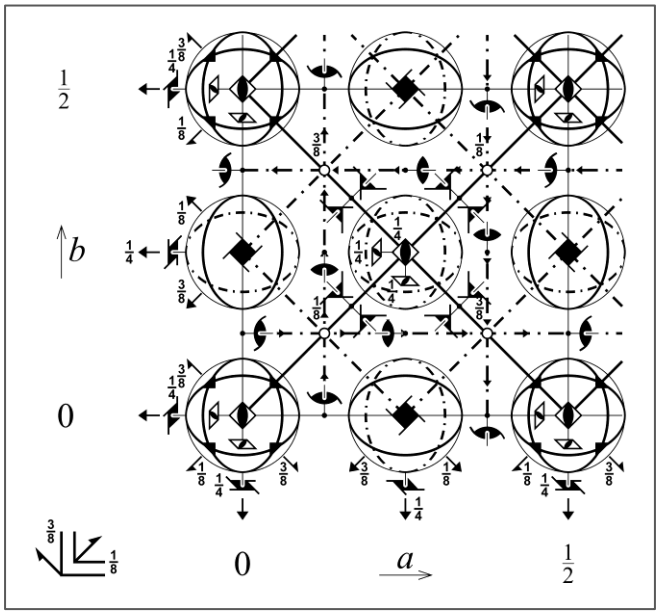


*Figure 1-2: A space group diagram for F d-3m (origin at -3) (Cockcraft, 1997-1999) (permission for use from Dr. J.K. Cockcroft)*

It is important to note that the Space Group *F* d-3m has two possible origin choices. This arises from the geometric equivalence of positions 16c and 8a, and 16d and 8b respectively. One setting places position 8a on the origin occupied by an oxygen atom. This places the lanthanide on position 16d at (5/8, 5/8, 5/8), the transition metal at position 16c at (1/8, 1/8, 1/8) and O3 (the oxygen vacancy) in 8b at (1/2, 1/ 2, 1/ 2). The second origin choice, the one used in this study and by many other studies, places the transition metal in the 16c site on the origin. This causes the 16d lanthanide site to occur at (1/2, 1/ 2, 1/ 2), and the 8b O2 site at (3/8, 3/8, 3/8). In both cases, the 48f O1 position remains unchanged at (x, 1/8, 1/8) (Shlyakhtina & G., New solid Electrolytes of the Pyrochlore Family, 2012).

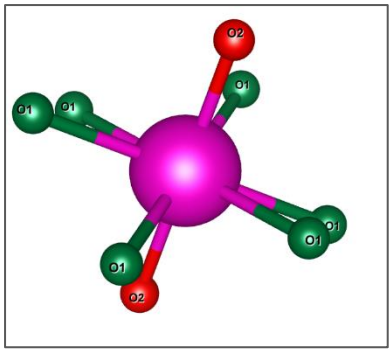


*Figure 1-3: Coordination of oxygen about the lanthanide ion in the pyrochlore phase (the equatorial oxygen ions (represented as dark green balls I.e. O1) are the 48f positions, and the axial oxygen ions are the 8b positions)*

Each atomic site has a particular coordination associated with it. Site A is coordinated by six $O_{48f}$ and two $O_{8b}$ anions; Site B is coordinated by six $O_{48f}$ anions; the $O_{48f}$ anions are coordinated by two A and two B cations; $O_{8b}$ is coordinated by four A cations; and the vacant position 8a is coordinated by four B cations (Ewing, Weber, & Lian, 2004) (Chakoumakos, 1984). The 16a site, that being the site of the rare earth element, has been described as having a coordination of equatorial oxygen atoms in a puckered ring formation, analogous to cyclohexane in its chair form (Greedan, 2006) (figure 1.3)

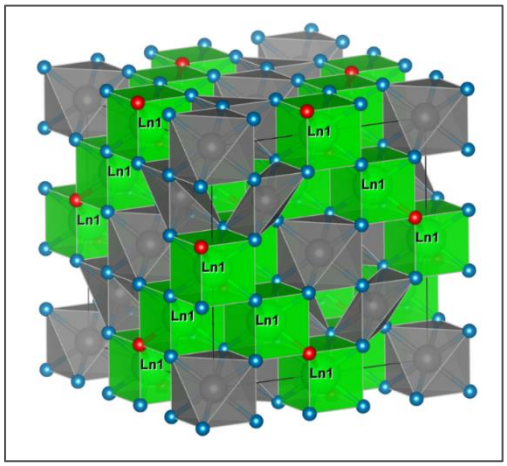


*Figure 1.4: Cubic lanthanide polyhedra when O48f has x = 0.375 (adapted from* (Chtoun, Hanebali, Garnier, & Kiat, X-rays and neutrons rietveld analysis of the solid solutions (1-x)(A2 Ti2 O7) - x(Mg Ti O3) (A = Y or Eu), 1997)

A useful method for describing the pyrochlore structure is through the description of connectivity of polyhedra. There are two types of polyhedra that exist within the pyrochlore lattice, 8-fold and 6-fold. The exact type of polyhedron formed is determined by the x coordinate of the 48f oxygen anion. At x = 0.375, the six-fold polyhedron is at its most distorted, whilst the 8-fold polyhedron is a cube (see figure 1.4), which forms the defect-fluorite structure. At x = 0.3125, the 6-fold polyhedron forms a

perfect octahedron (see figure 1.5), whilst the 8-fold polyhedron forms a distorted scalenohedron, a polyhedron where each face forms a scalene triangle, and can be viewed as a distortion of a cube (Ewing, Weber, & Lian, 2004) (Chakoumakos, 1984). Due to the supercell formation of the pyrochlore structure, visualisation can be considered as difficult. For this reason, several interpretations of the structure shall be given here to act as a comprehensive description of the structure for visualisation.

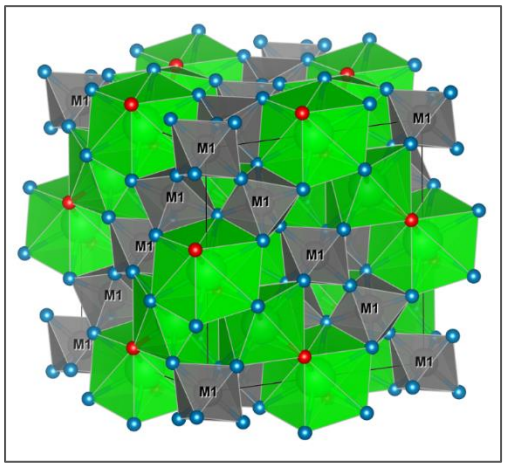


*Figure 1-5: Perfect octahedral coordination of cation M when $O_{48f}$ has x = 0.3125 (adapted from (Chtoun, Hanebali, Garnier, & Kiat, X-rays and neutrons rietveld analysis of the solid solutions (1-x)(A2 Ti2 O7) - x(Mg Ti O3) (A = Y or Eu), 1997))*

Harvey et al describe the pyrochlore lattice as a face centred cubic 2x2x2 supercell of the fluorite phase, missing one eighth of the anions in an ordered fashion (Harvey, Ashbrook, Lumpkin, & Redfern, 2006). The general formula for the pyrochlore structure type given previously does not indicate the groupings of pyrochlore compounds (based on the valency of the A and B cations), as described by Subramanian *et al*. In the review by Subramanian et al, the groupings of various pyrochlore oxides were made according to the valency of the A and B cations. The two major groups are the II-V and the III-IV pyrochlores. These groups can be further divided into perfect, defect and substitutional pyrochlores (Subramanian, Aravamudan, & Subba Rao, 1983).

An important description of the pyrochlore structure which aids in descriptions of spin ice (and visualisation of the structure in general) is the use of the Kagome lattice, or tri-hexagonal lattice. The lattice, illustrated in figure 1.6a, is an array of regularly repeating hexagons and triangles. In the pyrochlore structure, this arrangement can be seen in the planes formed by the lanthanide ions in the 16c position. In three-dimensional space, the lanthanides form alternating stacked planes, as can be seen in figure 1.6b. The importance of this arrangement is that it causes the geometric frustration that leads to the formation of a magnetic frustration with unpaired electrons. This is seen in the pyrochlores gadolinium, dysprosium, terbium and holmium titanates. (Greedan, 2006).

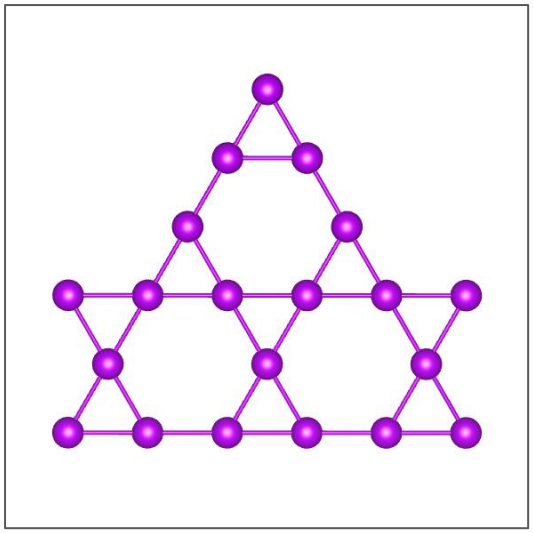

*Figure 1-6a: A kagome lattice in a pyrochlore unit cell*

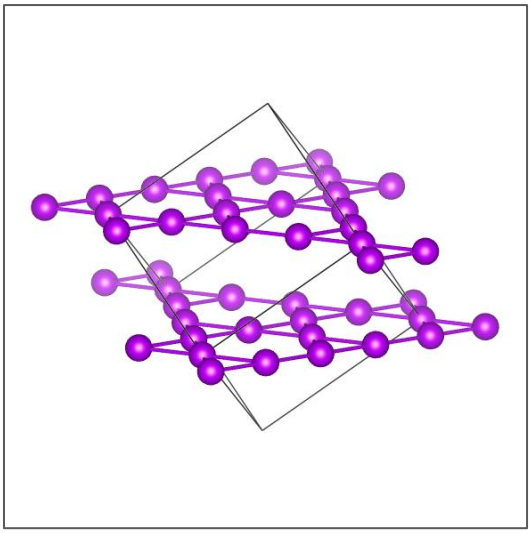

*Figure 1-6b: A kagome lattice in a pyrochlore unit cell*

Variants on the pyrochlore structure have been reported. These include structures with stoichiometrically missing cations and anions of chemical formulae $AB_2O_7$ and $A_2B_2O_6$ respectively, and an inverse pyrochlore where the A and B cations occupy each other's positions (Ewing, Weber, & Lian, 2004) (Moriga, Yoshiasa, Kanamaru, & Koto, 1989) (Chakoumakos, 1984). It has been observed that pyrochlores can support vacancies of cations without phase changes, hence allowing for the aforementioned variant structures (Zhang, Yu, Cheng, & Hou, 2012).

When pyrochlores lie close to the pyrochlore/defect-fluorite phase boundary, they have a tendency to be unstable, and undergo phase changes at high temperature, often to disordered phases (Ewing, Weber, & Lian, 2004) (Fuentes, Boulahya, Maczka, Hanazu, & Amador, 2005)

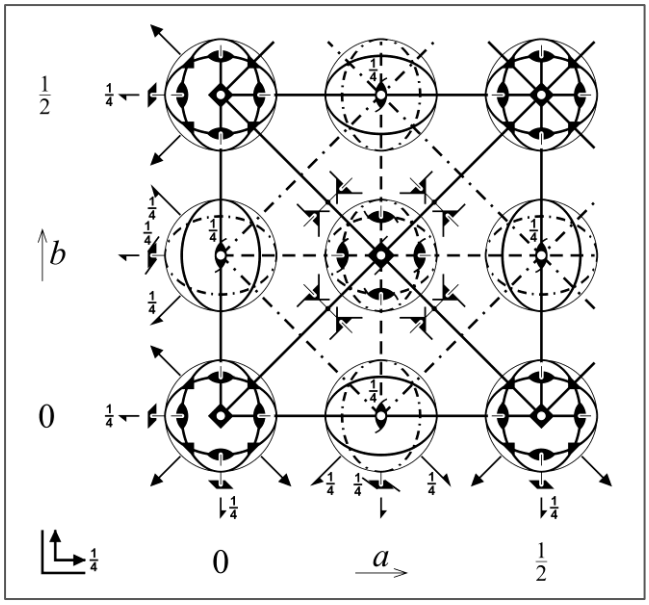


*Figure 1-7: A space group diagram of F m-3m (Cockcraft, 1997-1999)* (Permission obtained from Dr. J.K. Cockcroft)

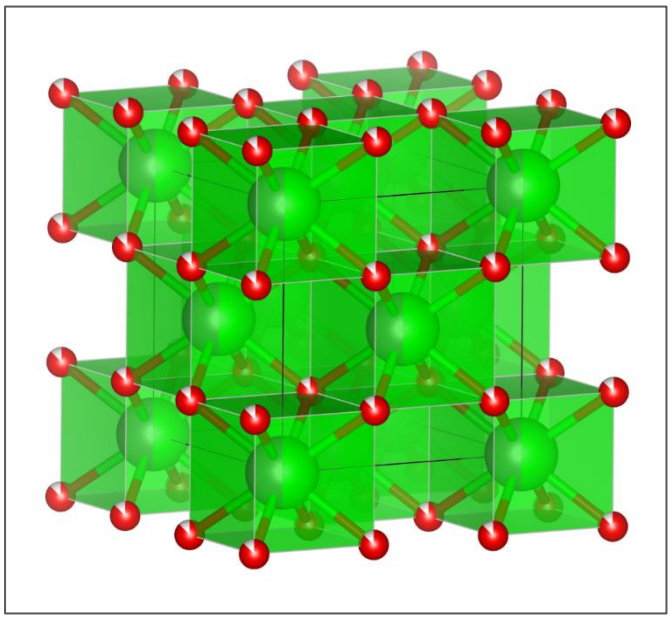

*Figure 1-8: The unit cell of defect Fluorite material. Note that both cations A and B occupy the same site, and that oxygen (the red spheres) are only 7/8 complete, implying randomized vacancies (Lee Y. , Sheu, Deng, & Kao, 2009)*

The defect-fluorite phase is based on the mineral fluorite with chemical formula of $CaF_2$, which crystallizes in the *F* m-3m space group (figure 1.7). The term defect fluorite arises from the valency of the cations in the structure being 3+ and 4+, hence charge neutrality with 4 oxygen anions become impossible. This forces disordered oxygen vacancies distributed throughout the lattice. In the defect fluorite cell, both the A and B cations lie on the same position, namely the 4a position. This position has a point symmetry of m-3m (i.e. mirror planes along the {100} and the {110} families of planes, and a three-fold roto-inversion along the (111) direction). The only unique oxygen position lies on the 8c site, with a point symmetry of -43m. This site has an occupancy of 0.75 due to the valency of the

cations as discussed previously. The effect of this position is the formation of perfectly cubic polyhedra made up of cations surrounded by eight oxygen atoms (figure 1.9). All of the atoms within the defect fluorite unit cell lie on special positions (Zhurova, Maximov, Simonov, & Sobolev, 1996). It is possible to synthesise a defect-fluorite phase from cations of the correct radii to form the pyrochlore phase. This was demonstrated by Lee *et al* where they synthesised gadolinium zirconate in the defect-fluorite phase by the polymeric citrate precursor method, and calcining the product between 700 and 1200 °C. The material converted to a disordered pyrochlore when sintered at 1300 or 1400 °C (Lee Y. , Sheu, Deng, & Kao, 2009).

Rare-earth hafnate, zirconate, and titanate pyrochlores and defect-fluorite materials are all oxide-based ceramics, and can therefore be produced by standard ceramic manufacturing techniques. The most common methodology for synthesis is via solid state reactions. This method suffers from poor homogeneity and high synthesis temperatures, where temperatures reaching 1500 °C are sometimes inadequate at achieving homogeneity of the cations (Ewing, Weber, & Lian, 2004). Other methodologies include mechanochemical synthesis, co-precipitation (both basic and acidic) (Zhang, Yu, Cheng, & Hou, 2012), Citrate methods, the Pechini method and (the focus method of this study) sol gel, with sole emphasis on alkoxide condensation.

As discussed by Yanagida et al in the book “The chemistry of ceramics, pure zirconia can exist in three possible phases depending on temperature. These phases include monoclinic (M), tetragonal (T) and defect-fluorite (F). The M-T and T-F transitions occur at 1173°C and 2370°C respectively (Yanagida, 1996). These transition temperatures can be lowered by the addition of a stabiliser (i.e. large ions that prevent the reverse phase change from occurring). Yttrium, along with the other rare-earths in this dissertation and several other ions can be used for such an effect. Altering the mole percentage of stabiliser in the solid solution will allow for different phases to be stable at room temperature. The point where the cubic defect fluorite phase becomes stable denotes when the material can be referred to as “fully stabilised”. In the case of yttrium zirconate, this point occurs just below 20 Mol % at room temperature. This implies that the materials in this dissertation are not at risk of cross contamination with other phases typical of pure zirconia (Birkby, 1994).

## 1.3. Rietveld Refinement

Rietveld refinement is a least squares minimisation of a whole powder pattern. The refinement uses physical parameters in order to minimise a residual function, given by:

1.3.1) $S_y = \sum_i w_i (y_i - y_{ci})^2$

where $S_y$ is the residual, the quantity being minimised, $W_i = 1/y_i$, $y_i$ is the observed intensity for the $i^{th}$ step, and $y_{ci}$ is the calculated intensity for the $i^{th}$ step and contains the refinable, physically relevant, parameters.

In order to produce meaningful Rietveld refinements, the powder pattern must be observed as a collection of individual reflection profiles. Each of these profiles have particular characteristics describing them, including their peak height, peak breadth, and the shape of their peak tails as well as an area associated with the peak itself. The objective of the Rietveld refinement is to calculate the intensity caused by a model of a system, and match it to an observed pattern. Adjusting parameters allows for the calculated pattern to be incrementally altered to match the observed pattern. In general, unit cell parameter, instrumental parameters, atom positions and Beq's can be refined, in this study, the atom positions remained fixed except for the 48f parameter on O1. These parameters lie within the function $y_{ci}$, mentioned previously in the description of the residual function and given by:

1.3.2) $$y_{ci} = s \sum_K L_K |F_K|^2 \phi(2\theta_i - 2\theta_K) P_K A + y_{bi}$$

where $y_{ci}$ is the calculated intensity at the $i^{th}$ step, s is the scale factor and should not be confused with the residual, S, $L_K$ includes the Lorentz polarisation and multiplicity factors, $F_k$ is the structure factor for the $K^{th}$ Bragg reflection, φ is the reflection profile function, $P_K$ is the preferred orientation function, A is the absorption factor and $y_{bi}$ is the background intensity at the $i^{th}$ step.

As can be seen from equation 2.1 and 2.2, a calculated intensity for each data point along the powder pattern is subtracted from the observed. When the observed and calculated intensities match adequately, their final value should be near zero. It is at this point that the calculated parameters should be physically correct, and hence used in structural descriptions of the system under study (caution must be taken to ensure the model is representative of the actual structure, it is possible to fit a polynomial accurately whilst determining incorrect parameters. Use chemical knowledge to ensure such errors are minimized). Arriving at the point where the two values adequately match requires the evaluation of a set of normal equations of the derivatives of all the calculated intensities, $y_{ci}$, with respect to each parameter. The solution for the equations is then achieved by solving the inversion of the normal matrix. Its elements $M_{jk}$ are given as:

$$1.3.3)\ M_{jk} = -\sum_i 2\, w_i \left[ (y_i - y_{ci}) \frac{\partial^2 y_{ci}}{\partial x_j \partial x_k} - \left( \frac{\partial y_{ci}}{\partial x_j} \right) \left( \frac{\partial y_{ci}}{\partial x_k} \right) \right]$$

Here, $x_j$ and $x_k$ are the same set of adjustable parameters. The procedure becomes an iterative one since the residual is non-linear. These shifts are defined as follows:

$$1.3.4)\ \Delta x_k = \sum M_{jk}^{-1} \frac{\partial S_y}{\partial x_k}$$

Each calculated shift should produce a more accurate model when compared to the previous. In practise, the starting model needs to be close to the global minimum of the system. If not, the refinement may converge within a local minimum, giving the false pretence of a final, correct, solution. This is a problem of all non-linear least squares refinements. Different strategies can be employed to avoid false minima. To give some examples, multiple data sets (of different kinds, such as X-ray and neutron) can be employed and refined simultaneously, or the use of constraints can prevent the refinement from diverging from the suspected global minimum.

Chemical knowledge is often a useful tool to ensure that the refinement has been calculated satisfactorily. Visualisation software can be used to inspect the output structure to ensure atoms are not moving from symmetrically specific positions. Bond lengths can also be used as a safeguard from an incorrect refinement, along with unrealistic values for refined parameters.

Table 1 below gives a list of simultaneously refinable parameters divided into two sections, namely *per phase* and *Global*.

*Table 1.1: Parameters involved in Rietveld refinment*

| ***Per phase* Parameters** |
|---|
| $X_j$ $Y_j$ $Z_j$ $B_j$ $N_j$<br><br>Where $X_j$, $Y_j$, and $Z_j$ are position coordinates, $B_j$ is an isotropic thermal parameter, and $N_j$ is the site occupancy multiplier. All off which apply to the $j^{th}$ atom of the unit cell.<br><br>Scale factor<br>Specimen profile breadth parameters<br>Lattice Parameters<br>Overall Temperature Factor<br>Individual Anisotropic Thermal Parameters<br>Preferred Orientation<br>Crystallite Size and Microstrain<br>Extinction |
| ***Global* Parameters** |
| 2θ-Zero<br>Instrumental Profile<br>Profile Asymmetry<br>Background<br>Wavelength<br>Specimen Displacement<br>Specimen Transparency<br>Absorption |

Listed here are some important definitions of select parameters which are of significant importance outside of the switch on sequence described later in this chapter.

There are several analytical peak profiles used to fit the calculated pattern the observed. Common functions include Gaussian, Lorentzian, Voigt, Pseudo-Voigt, Pearson VII, Split Pseudo-Voigt and Split Pearson VII. The Gaussian and Lorentzian functions used, on their own in each case, do not satisfactorily describe peak shape, often miscalculating the tails of the peak. The Voigt function, a convolution of the Gaussian and Lorentzian, solves the inadequacies of both functions but finds very limited use in profile fitting in powder diffraction. According to Will (Will, 2006), this is because the Voigt function requires highly resolved peaks, as observed in structures of high symmetry, which do not require a functions such as the Voigt to correctly fit their shape. The most commonly used functions are the Pseudo Voigt and the Pearson VII. The analytic function used in this study to fit peak shapes was the Pearson VII function (Will, 2006). The Pearson VII function is given by:

$$1.3.5)\ PVII = \frac{C_0}{H_K}\left[1 + 4^*\left(2^{1/m} - 1\right)\frac{(2\theta_2 - 2\theta_K)^2}{H_K^2}\right]^{-m}$$

Where m is refined as a function of 2θ,$m = NA + \frac{NB}{2\theta} + \frac{NC}{(2\theta)^2}$, NA, NB and NC all refineable parameters, $H_K$ is the full width at half maximum (FWHM) for the $K^{th}$ diffraction peak. $C_0 = \frac{2\sqrt{m}\left(2^{1/m}-1\right)^{1/2}}{\sqrt{(m-0.5)}\pi^{1/2}}$ (Young, 1993). The Pearson VII function was chosen for this study as it provided a better fit to the observed peaks in comparison to the other available functions in TOPAS (AXS, 2008).

In the event of a sample not having a suitable cif file from which a starting model can be established, a Le Bail refinement can be used to determine the starting parameters for the variable temperature Rietveld refinement. A Le Bail refinement involves fitting the peaks of an experimental powder pattern in order to extract their intensities (Le Bail, 2005). Here the method was not used to extract intensities, but to determine the positions of diffraction peaks accurately and hence determine the size of the unit cell. Fortunately, the unit cell of defect fluorite is cubic which simplifies this procedure significantly.

The switch on sequence, as discussed by Young, is intended to reduce errors in the refinement due to correlated parameters (Young, 1993). Such correlations can be seen in background functions of unnecessarily high order. This can cause unwanted shifts, and may contribute falsely to peak intensities. The suggested switch on sequence according to Young is as follows:

1. Scale: The scale parameter is both linear and stable, but if incorrect can cause severe errors within the refinement. An example of this can be seen when a poor scale factor or a poor structural model causes the refinement of the scale factor to become much smaller as the difference between a pattern and nothing is less than two poorly matched patterns.
2. Specimen displacement: Although non-linear in nature, the function describing specimen displacement is very stable. In the Bruker software package TOPAS (used in this study), the sample displacement correction is defined as a 2θ offset and is refined as the following equation: $2\theta = -2Rad(c)\cos(\theta)/Rs$ (AXS, 2008). This parameter is refined prior to the zero-error as it can be assumed that the zero error on a correctly aligned diffractometer will not change significantly, and errors from misalignment can hence only be due to specimen displacement. An incorrect height of a specimen has the effect shifting observed peaks, indicating incorrect lattice parameters. The shift in the diffraction peaks is more pronounced at lower angles as differences in height have a more dramatic effect on the diffraction geometry than what is observed at high angles. This can be refined simultaneously with the scale parameter (AXS, 2008) (Young, 1993). In figure 2.5, an illustration of the sample displacement error is given. Sample holder A has a lower sample height than Sample holder B. As can be seen by the reflected radiation (given as red lines) sample holder B reflects the same hkl to a higher point. The detector, due to its circular goniometer movement, will detect the hkl peak later on the 2θ scale with respect to Bragg Brentano geometry. This causes a 2θ displacement of that particular peak, erroneously indicating a smaller d-spacing.

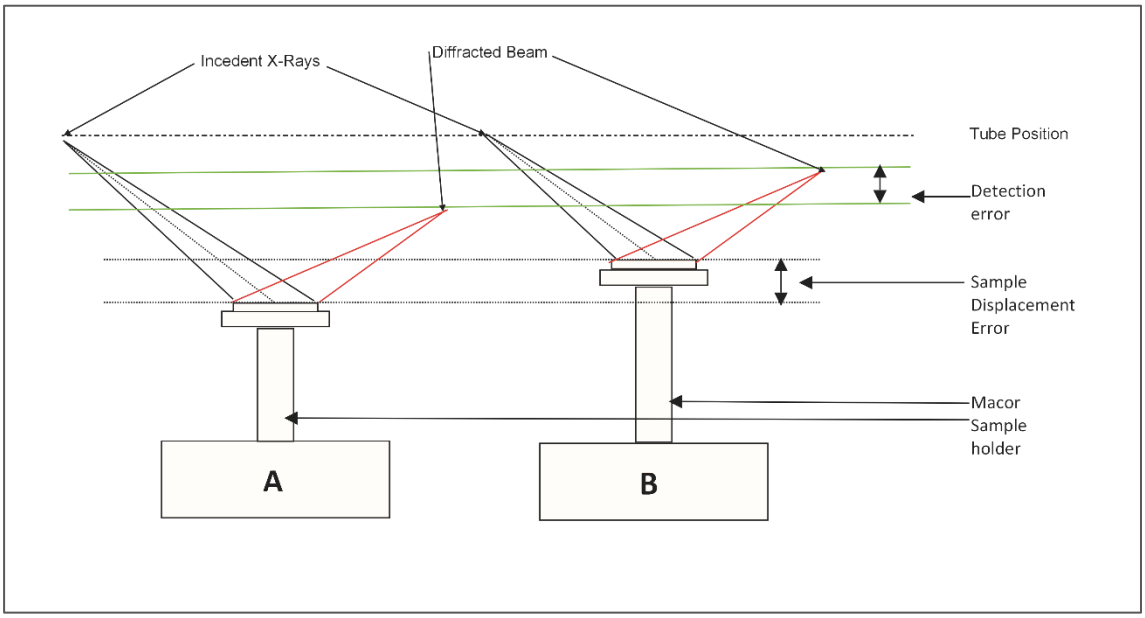


*Figure 1-9 Sample Displacement error.*

3. Flat background function (i.e. zero order background function): the background function provides a means for which non-Bragg diffracted data can be accounted. It is suggested to perform a flat background refinement initially as higher order background functions can contribute to peak intensities, hence causing errors in the observed intensities. A flat background function can reduce the Rwp value quite significantly. Refining a flat background does require that the background is reasonably flat by inspection. This should be refined second, after the scale and specimen displacement parameters.
4. Lattice parameters: refinement of lattice parameters occurs by non-linear functions, but remains stable. The refinement of lattice parameters can be seen graphically as the position of diffraction peaks. A significant error in the lattice parameter can cause an incorrect hkl value to "lock on" to an incorrect peak. This will undoubtedly indicate the presence of an incorrect phase and can be avoided through the use of a good estimation of the lattice parameters prior to refinement. This estimation will improve the refinement results of all previously discussed parameters. These parameters should be refined either second (simultaneously with a flat background function), or third.
5. More Background (i.e. higher order background function): after the lattice parameters have been refined, most of the peak intensity would have been ascribed, and hence the remaining background can be accounted for without risk of contributing to such peak intensities. The higher order background functions are polynomial fits to the background which can fit to the shape of a varying background (such as amorphous content). The refinement should be stable provided that the lowest order background function is used to describe the shape of the background. This is required as redundant parameters become correlated to other parameters and hence cause errors.
6. W (i.e. a peak width parameter): W is a peak width parameter used in equation 1.3.6, given as $1.3.6)\ H^2 = Utan^2\theta + Vtan\theta + W$, (where H, U and V are refinable peak shape parameters) described by Caglioti *et al* to describe peak width (Caglioti, 1958). It is refined prior to the other two values, U and V, because it is not dependent on angle. It should be noted that these parameters are highly correlated. The refinement of this parameter should only occur if a peak shape function involving the parameter is used. This parameter should be refined on its own, either third or fourth depending on previous refinement decisions.
7. Atomic coordinates: At this point in the refinement, most of the intensity should be ascribed to previously refined parameters. This allows for the atomic coordinates to be refined correctly, without significant changes that would result in unrealistic bond lengths. In the scope of this study, there is only one such parameter that can actually be refined, that being

the x position of the 48f oxygen site. This is advantageous as it reduces the number of required parameters, and hence improves the accuracy of the refinement and limits the possibility of additional correlated parameters. Young suggests that at this point in the refinement, graphics of the calculated pattern, the observed pattern and the difference plot should be scrutinised to determine whether or not preferred orientation is apparent.

8. Occupancies and thermal parameters: these parameters describe the chance of finding an atom on a site and the volume in which the atom vibrates respectively. It should be noted that these values are highly correlated and should be refined with caution. They are refined at this point as there is little available intensity/area which they may account for. If these values were refined earlier, they could account for a large portion of the observable intensity and an unrealistic answer may occur, such as thermal parameters which are significantly large or negative (implying that they occupy negative space), and occupancy factors which are above unity.
9. The remaining peak shape parameters: in the case presented by Young, this would include U and V of equation 1. These parameters are refined at this point as they are dependent on diffraction angle, and an earlier refinement would make them subject to significant correlation effects.
10. Anisotropic thermal parameters: it is perhaps inadequate to describe the motion of an atom in a crystal as perfectly spherical. Atomic bonds, potential barriers, etc., all contribute to misshaping this spherical motion. The anisotropic thermal parameters account for these conditions.
11. Zero-error: At this point, all required parameters have been refined (with respect to the desired output). A zero-point error refinement, although not needed, may improve the refinement to a certain degree, particularly if there is suspicion to misalignment in the diffractometer itself. This is most often unlikely.

## 1.4. Uses of pyrochlores and defect-fluorites

Hafnate, zirconate and titanates of the pyrochlore and defect fluorite structure types have been observed to have the following uses and properties: catalytic supports; ferromagnetic materials; ionic conduction of oxygen; luminescence properties; magneto resistance; photocatalytic splitting of water; properties of quantum liquids and spin ices; a host material for radioactive waste; superconductivity; and thermal barrier coatings.

These materials are of great importance for their uses as solid electrolytes in solid oxide fuel cells. The aim is for these materials to replace the current favoured material, yttria stabilised zirconia (YSZ), in order to allow for varying thermal expansions. The objective was to produce a material with the same

oxygen conductivity, but with greater thermal stability and a closer match of thermal expansion coefficients to the anode and cathode materials in use. This matching of thermal expansion coefficients will assist in preventing thermal cycling from damaging the fuel cell. Both the pyrochlore and defect-fluorite phases have promise as ionic conductors since their structures allow for ionic conductivity. This is apparent through the existence of vacancies in the defect fluorite, and an unoccupied site in the pyrochlore (Tuller, 1994). Although these vacancies do allow for ionic conduction, often improvements are required. This is exemplified in the literature (Kramer & Tuller, 1995) with modifications on gadolinium titanate pyrochlore. Additions of up to 15 mol% of Ca on the A site or Al on the B site lead to significant increases in ionic conductivity. A computational study by Catlow *et al* indicated that in the system $Gd_2O_3$ – $ZrO_2$ – $TiO_2$ the oxygen anionic conduction mechanism was greatly influenced by the location of the ordered oxygen vacancy site 8b, the disorder in the cationic lattice which caused the environments of the 48f and 8b oxygen sites to become closer to a defect fluorite environment instead of a pyrochlore environment. This too enhanced the ability for oxygen migration. It was noted in their calculations that a higher percentage of zirconia improved conductivity as opposed to a high titania percentage, even though the zirconia rich pyrochlore exhibited a higher migration energy barrier (Wilde & Catlow, 1998). A study by Fagg *et al* discussed the conductivity of yttria stabilized zirconia doped with niobium. The system they studied was limited to the cubic defect fluorite phase. What was uncovered in the study was that yttria concentrations of 35% and above caused increased activation energy for conduction and that additions of niobia improved conductivity in low amounts (note: the phase of the material was of the defect-fluorite structure). They specifically indicated that a higher concentration of transition metal elements lead to an increased electronic conduction in reducing conditions and that the optimal composition for mixed conduction occurred at the lower yttria edge of the defect fluorite solid solution (Fagg & Irvine, 1998).

The pyrochlore $Cd_2Re_2O_7$ was shown to exhibit superconductivity at a temperature of 1.0K, although the material did not have the same space group as the perfect pyrochlore structure. As described by Hanawa *et al*, the material underwent a phase change from the pyrochlore space group of *F* d-3m (figure 1.1) to *F* 4-3m, another cubic space group, at a temperature of 200 K. They also discussed a significant change in the resistivity and the magnetic susceptibility as a result of the phase change. This was most likely due to a change in electronic structure (Hanawa, Yamaura, Muraoka, Sakai, & Hiroi, 2002). However, no references to superconducting pyrochlores or defect fluorite materials of lanthanide hafnates, zirconates and titanates could be found.

The defect pyrochlore $Pb_2Pb_xRu_{2-x}O_{6+\delta}$ was shown to be a suitable catalytic support of Pt particles. This was illustrated successfully by Goodenough and Castellano where they achieved 100 % CO conversion for a particular sample synthesised in a platinum crucible. In addition to this, the support material was

shown to convert NO to $N_2$ without the aid of Pt particles (Goodenough & Castellano, 1982). However, there are no references to the use of hafnate, zirconate and titanate pyrochlores being used as catalyst supports.

Several pyrochlore materials have shown promise as thermal barrier coating materials. Notably, $La_2Zr_2O_7$, when applied to a surface via plasma spraying, displayed significant resilience to a flame at a temperature of 1200 °C. This exceeded the performance of the other materials in the study, namely $SrZrO_3$ and $BaZrO_3$. $La_2Zr_2O_7$ also displayed a lower thermal expansion coefficient and thermal conductivity, again indicating its superior performance as a thermal barrier material (Vassen, Cao, Tietz, Basu, & Stöver, 2000).

A large number of pyrochlore and defect fluorite materials have been investigated for their ability to incorporate actinide waste chemicals into their crystal lattice. Several of these materials have also been shown to be resistant to amorphization from radiation damage, which will enhance the lifetime in which they can be used to store such waste materials. A particularly effective pyrochlore in this regard is $Gd_2Zr_2O_7$, whereas $Gd_2Sn_2O_7$ was shown to become amorphous after much less exposure to radiation. This was attributed to the covalency of the Sn-O bond (Ewing, Weber, & Lian, 2004).

Certain pyrochlore materials have been shown as potential photocatalysts for hydrogen production by splitting of water. This was successfully illustrated by Uno *et al* for a series of lanthanide zirconates Including lanthanum, cerium, neodymium, and samarium zirconates. The materials exhibited hydrogen production when exposed to a 500 W xenon lamp. *Ab initio* calculations were performed on the structures to determine their band gaps. Uno *et al* obtained values of 3.52, 2.86, 2.67, and 2.53 eV for the band gaps of the lanthanum, samarium, cerium and neodymium zirconates respectively. These results indicated that these materials have a narrower band gap than what is seen in pure zirconia. As a result of this, the neodymium and samarium zirconates exhibit catalytic activity when exposed to visible light (Uno, et al., 2006).

This dissertation seeks to determine the thermal expansion coefficients of several pyrochlore/defect fluorite materials and in doing so will answer several related questions, such as: the phase of the target materials, what is the effect of the synthesis technique on the materials, and how tolerant the materials are to temperature change. In the next section, these questions shall be discussed in depth with their proposed answers.

# 2. Experimental and Diffractometer Calibration

## 2.1. Synthesis

The synthesis of the materials was carried out in house by Tshifhiwa Sidogi as a part of her Honours project.

Stoichiometric amounts of the required rare earth nitrates (i.e. $Y(NO_3)_3.4H_2O$, $La(NO_3)_3.6H_2O$, $Eu(NO_3)_3.5H_2O$, $Gd(NO_3)_3.6H_2O$) were dissolved in dry ethanol. This was mixed with a stoichiometric amount of the required transition metal alkoxide (i.e. hafnium butoxide, zirconium isopropoxide and titanium isopropoxide). The resulting mixture formed a gel which was allowed to dry overnight. The gel formed a puck which was heated in a furnace to burn off the organic components resulting in an amorphous white powder in each case. The powders were calcined at temperatures increasing in 50°C steps until a crystalline sample was obtained. The crystalline samples were used in the experiments outlined in this dissertation.

## 2.2. D2 calibration

The calibration procedure for the D2 phaser was performed in order to provide an accurate crystallographic description of the prepared materials.

Calibration of the Bruker D2 Phaser in this case requires a means for determining the sample displacement accurately. This was achieved by using lanthanum hexaboride standard 660a as its fine peak shape allows for accurate measurement of d-spacing.

Two standard samples were scanned, NIST_$LaB_6$_1(660A) (a sample obtained from a sealed bottle), and NIST_$LaB_6$_2(660A) (the same standard which had been exposed to atmospheric conditions for a significant amount of time).

The scan parameters for the calibration are listed below:

- Scan Range: 10 to 90° 2θ
- No spin
- Increment: 0.02641. . .°2θ per measurement
- Scan time: 50 min
- Sample 1 file name: d2_13_1757
- Sample 2 file name: d2_13_1758

The D2 phaser had the following instrumental parameters in place at the time of calibration:

- Goniometer
    - Primary radius: 70.7 mm

    - Secondary radius: 70.7 mm
- Detector 2θ angular range: 5°
- Slits
    - Primary Soller slits: 2.5°
    - Secondary Soller slits: 2.5°
- X-Ray source
    - Cu cathode
    - Voltage: 30 kV
    - Current: 10mA

The sample displacement was determined using the listed lattice parameter for lanthanum hexaboride and fixing it as a parameter in TOPAS. The refinement proceeded follows:

The zero order background function was fitted without any other parameters open for refinement. This lowered the Rwp value of the refinement to approximately 30. The next refinement step included the structure model obtained from an $LaB_6$ cif file from the ICSD (reference code: 152466), with the scale and sample displacement allowed to refine (Guangrong & Flemming, 2005). The lattice parameter was fixed at 4.1549, according to the cif file. The scale was refined to account for the counting stats of the measurement. Next to be refined was the Pearson VII function parameters to account for peak shape. This was followed by a refinement on a $6^{th}$ order background function. The crystallite size was also refined. Finally, a zero error was refined. The sample displacement was determined to be -0.09mm.

## 2.3. Experimental

### 2.3.1. D2 pattern

The output data from the Bruker D2 were used to create an initial structural model which was then used with the D8 VT analysis. The data was also used in determining the sample height required for the Anton Paar XRK900, which has a variable height and requires calibration, particularly after exchanging sample holders. Additionally, significant height differences can occur even if the sample holder is not removed from the mount as the mount is screwed in place inside the furnace. The description of finding the sample height for the XRK 900 is described in detail in the appendix section, along with the procedure of operating the D2.

After the patterns have been collected, the phase purity of the samples are determined. This was done using Bruker software EVA (Evaluation Plus), a program for peak matching and data manipulation. The

background noise level of the patterns were removed in order to allow for easier matching of database peak sets of previously refined structures. Once matches were found according to the particular elemental composition, the structure files for the phases were obtained from the Inorganic crystallographic structural database (ICSD). These crystallographic information files (cif) were used as the starting models for the D2 pattern structure refinements. The cif files were chosen according to their quality, which involved choosing files with less missing data and lower R values.

Once adequate cif files were found, they were loaded into a second piece of Bruker software, TOPAS. TOPAS is used for Rietveld refinement procedures and contains calculation capabilities for various peak shapes intended for: data fitting of background functions, errors and fundamental parameters for modelling the effect an instrument has on the final data. The cif files corresponding to the particular pattern to be refined were loaded into the software, which uses information from the cif file such as lattice and thermal parameters. The cif derived values were used as the starting values for the refinement procedure (AXS, 2008).

To avoid unnecessary errors in the refinement, a "switch on sequence" was employed to reduce parameter correlation. The rationale behind a switch on sequence arises from parameters such as background and peak shape functions competing to account for the same intensity, regardless of whether or not one of the parameters is actually involved in producing that intensity during the X-ray experiment.

The refinement should be specific to the experimental set-up. In this case, the X-ray source was a Cobalt tube fitted with an iron filter on the Bruker D2 phaser Diffractometer. There was an air scatter slit to remove signal contribution from this effect.

The refinements were performed iteratively according to the described switch on sequence. Once completed, the results were saved and used for the starting parameters of the Bruker D8 refinements and as a means to determine the sample height for the Anton Paar XRK 900, as discussed in section 7.1.2 of the appendix.

## 2.4. Data analysis

The data obtained from a diffraction experiment performed on a Bruker diffractometer is recorded in the RAW file format, which allows for phase identification through Evaluation Plus software (EVA) and Rietveld refinement through TOPAS (AXS, 2008).

### 2.4.1. Phase Identification

Phase identification, within the confines of this project, involved the use of Bruker software Evaluation plus. This software was used to match the peaks observed within the diffraction pattern to peak

positions determined previously, stored within a database. The software, in its most basic use, searches for database patterns that match the experimental pattern within particular search parameters, which include: elemental composition, mineral name, or particular database entries. The database used to match powder patterns was the PDF2 2004. In the event of a database entry not being available for a particular diffraction pattern, a calculated pattern was matched to the experimental pattern. The calculated patterns were created in MERCURY (Macrae, 2008) from cif files obtained from the ICSD.

### 2.4.2. Rietveld refinement

As discussed in the introduction, a specific switch-on sequence was employed during the refinement of each material to determine suitable starting parameters for the VT-PXRD Rietveld refinements. The specific sequences are listed below detailing any variations from the previously described method (Young, 1993).

### 2.4.3. Europium hafnate

After setting up the refinement in the standard way, the following switch on sequence was used to ensure an accurate refinement:

1. First order Background function (Chebychev)
2. Sample displacement, Scale and lattice parameter
3. Pearson VII parameters (peak shape)
4. A sixth order background function (Chebychev)
5. Crystallite size
6. Fractional coordinates
7. Surface roughness (Pitschke, 1993)
8. Thermal Parameters (Beq)

The first order background function was employed first to account for a larger portion of intensity in the diffraction pattern without influencing the intensity caused by Bragg reflections. This lowered the chance of the Pearson VII function from fitting background as part of a Bragg peak. After this, the parameters regarding the structure were freed and allowed to refine, beginning with sample displacement, scale and then lattice parameter. The sample displacement accounted for any errors found in setting the height of the sample holder in the XRK 900, the scale allowed for the intensity of the peaks to be scaled correctly since the time per step and the step length alters the heights of all observable peaks and the lattice parameter was refined to compare to a literature value (loaded into Topas via a cif file).

The Pearson VII parameters were allowed to refine next. These account for the width of the peak caused by both the instrument and the sample. After this refinement, it was noted that there was an overestimated peak at low 2θ values. This was accounted for using a surface roughness correction in step 6.

A sixth order background function was then employed to account from the remaining non-linear background. The contributions to this background could be disorder in the unit cell, air scattering, and/or fluorescence (which not likely as none of the elements in the material fluoresce under CuKα radiation).

The x coordinate of the 48f oxygen atom was refined after the sixth order background function.

This was followed by a surface roughness correction. Surface roughness occurs when a sample is not adequately smooth for diffraction. The effect can be observed in a diffraction pattern as peaks in the experimental pattern being less intense than those in the calculated pattern. This only occurs at low angles. The reason for this is at low angles, the X-ray beam illuminates the sample at an oblique angle. If the surface is rough, the illuminated area has peaks and valleys instead of being a continuous mass. The lack of material off which to diffract reduces the intensity.

The final parameters to be refined were the thermal parameters, labelled Beq. These were refined last as they are the least stable and tend to account for all remaining peak width as they model thermal motions of atoms in the lattice. Refinement before the end can result in these parameters either becoming erroneously large, or having a negative value, implying that they vibrate in negative space which has no physical meaning.

### 2.4.4. Yttrium hafnate

1. First order Background function (Chebychev)
2. Sample displacement, Scale and lattice parameter
3. Pearson VII parameters (peak shape)
4. A sixth order background function (Chebychev)
5. Crystallite size
6. Surface roughness (Pitschke, 1993)
7. Thermal Parameters (Beq)

Similar to the situation involving the europium hafnate defect fluorite phase, possible surface roughness was observed and corrected.

### 2.4.5. Gadolinium hafnate

1. First order Background function (Chebychev).

2. Lattice parameter and scale
3. Sample displacement
4. Pearson VII parameters (after fixing sample displacement)
5. A sixth order background function
6. Fractional coordinates
7. Crystallite size (Pitschke *et al*)
8. Thermal parameters (Beq)

The switch on sequence was different for the gadolinium hafnate ambient temperature refinement because no losses of intensity were observed for the low angle peaks, implying that no surface roughness was observed. To ensure lower competition between the lattice parameters and sample displacement, the sample displacement was fixed before the Pearson VII parameters were refined.

### 2.4.6. Lanthanum hafnate

1. First order Background function (Chebychev)
2. Sample displacement, Scale and lattice parameter
3. Pearson VII parameters (peak shape)
4. A sixth order background function (Chebychev)
5. Crystallite size
6. Surface roughness (Pitschke, 1993)
7. Thermal Parameters (Beq)

### 2.4.7. Yttrium zirconate

1. First order background function (Chebychev)
2. Lattice Parameter and scale
3. Sample displacement
4. Fixed sample displacement and PVII parameters
5. Sixth order background function (Chebychev)
6. Crystallite size

### 2.4.8. Gadolinium zirconate

1. First order background function (Chebychev)

2. Lattice Parameter and scale
3. Sample displacement
4. Fixed sample displacement and PVII parameters
5. Sixth order background function (Chebychev)
6. Fractional coordinates
7. Crystallite size
8. Thermal Parameters

### 2.4.9. Europium titanate

1. First order Background function (Chebychev)
2. Lattice Parameter and scale
3. Sample Displacement
4. Fixed sample displacement and refined PVII parameters
5. Sixth order background function
6. Crystallite size
7. Surface roughness (Pitschke, 1993)
8. Fractional coordinates
9. Thermal parameters

### 2.4.10. Yttrium titanate

1. First order background function (Chebychev)
2. Sample displacement and scale
3. Lattice parameters
4. Pearson VII parameters
5. Simple axial model
6. Sixth order background function (Chebychev)
7. Crystallite size
8. Fractional coordinates (rutile not refined)
9. Thermal parameters (Beq)
10. Adsorption correction

### 2.4.11. Gadolinium titanate

1. First order Background function (Chebychev)
2. Lattice Parameter and scale
3. Sample displacement

4. Pearson VII parameters (refined after fixing sample displacement
5. Surface roughness A1 only
6. Sixth order background function (Chebychev)
7. Fractional coordinates
8. Thermal parameters (Beq)

It was noted that after step four (the refinement of the Pearson VII parameters) that there was an overestimated peak height for low angle peaks. As discussed previously, this error was corrected for by a surface roughness function.

### 2.4.12. Lanthanum titanate

The diffraction data for this compound were not refined as they did not form the target compound required for this study. A further study involving the analysis of each phase formed from this particular sol gel reaction would fully elucidate structural and thermal expansion data for this observation.

## 2.5. References


Aroyo, M., Kirov, A., Capillas, C., Perez-Mato, J., & Wondratshek, H. (2006). Bilbao Crystallographic Server II: Representations of crystallographic point groups and space groups. *Acta Crystallographica, A62*, 115-128.

Aroyo, M., Perez-Mato, J., Capillas, C., Kroumova, E., Ivanchev, S., Madariaga, G., . . . Wondratschek, H. (2006). Bilbao Crystallographic Server I: Databases and Crystallographic computing programs. *Z.Krist, 221*(1), 12-27.

Aroyo, M., Perez-Mato, J., Orobengoa, D., Tasci, E., de la flor, G., & Kirov, A. (2011). Crystallography online: Bilbao Crystallographic server. *Bulgarian Chemistry community, 43*(2), 183-197.

Askeland, D., & Phulé, P. (2006). *The Science and Engineering of Materials.* Toronto, Canada: Thomson Canada Limited.

AXS, B. (2008). *TOPAS V4: General profile and structure analysis software for powder diffraction data - User's Manual.* Karlsruhe, Germany: Bruker AXS.

Caglioti, G. P. (1958). Choice of Collimators for a Crystal Spectrometer for Neutron Diffraction. *Nuclear Instruments, 3*, 223-228.

Chakoumakos, B. (1984). Systematics of the Pyrochlore Structure Type, Ideal A2B2X6Y. *Journal of Solid State Chemistry*(53), 120-129.

Chen, H., Gao, Y., Liu, Y., & Luo, H. (2009). Coprecipitation synthesis and thermal conductivity of La2Zr2O7. *Journal of Alloys and Compounds*(480), 843-848.

Chien, C. S. (1978). Mossbauer effect studies of europium pyrochlores. *Physical review, 18*(5), 2031-2038.

Chtoun, E., Hanebali, L., & Garnier, P. (2001). Analyse par diffraction des rayons X, methode de Rietveld, de la structure des. *Annales de Chimie (Paris)*, 32.

Chtoun, E., Hanebali, L., Garnier, P., & Kiat, J. (1997). X-rays and neutrons rietveld analysis of the solid solutions (1-x)(A2 Ti2 O7) - x(Mg Ti O3) (A = Y or Eu). *European Journal of Solid State Inorganic Chemistry*(34), 553-561.

Cockcraft, J. (1997-1999, March 12). *High-Resolution Space Group Diagrams and Tables*. Retrieved March 12, 2014, from A Hypertext Book of Crystallographic Space Group Diagrams and Tables: http://img.chem.ucl.ac.uk/sgp/LARGE/227bz1.htm

Ewing, R. C., Weber, W. J., & Lian, J. (2004). Nuclear waste disposal-pyrochlore (A2B2O7): Nuclear waste form for immobilization of plutonium and "minor"actinides. *journal of Applied Physics, 95*(11), 5949-5969.

Fagg, D., & Irvine, J. (1998). The Optimisation of Mixed Conduction in potential S.O.F.C. Anode Materials. *Ionics, 4*, 61-71.

Farmer, J., Boatner, L., Chakoumakos, B., Du, M., Lance, M., Rawn, C., & Bryan, J. (2014). Structural and crystal chemical properties of rare-earth titanate pyrochlores. *Journal of Alloys and Compounds*(605), 63-70.

Fuentes, A., Boulahya, K., Maczka, M., Hanazu, J., & Amador, U. (2005). Synthesis of disordered pyrochlores, A2Ti2O7 (A=Y, Gd and Dy), by mechanical milling of constituent oxides. *Solid State Sciences, 7*, 343-353.

Fujihara, S., & Tokumo, K. (2005). Multiband Orange-Red Luminescence Of Eu3+ Ions Based on the Pyrochlore-Structured Host Crystal. *Chemistry of Materials*(17), 5587-5593.

Goodenough, J., & Castellano, R. (1982). Defect Pyrochlore as Catalyst Supports. *Journal of Solid State Chemistry, 44*, 108-112.

Greedan, J. (2006). Frustrated rare earth magnitism: Spin glasses, spin liquid and spin ices in pyrochlore oxides. *Journal of Alloys and Compounds*, 444-455.

Guangrong, N., & Flemming, R. (2005). Rietveld refinement of LaB6:data from micro-XRD. *Journal of Applied Crystallography, 38*, 757-759.

Hail, S., Wuensch, B., & Prince, E. (1990). Neutron Rietveld analysis of anion and cation disorder in the fast-ion conducting pyrochlore system Y2 (Zr(x) Ti(1-x))2 O7. *Materials Research Society Symposia Proceedings*, 81-86.

Hanawa, M., Yamaura, J., Muraoka, Y., Sakai, F., & Hiroi, Z. (2002). Structural phase transition in the superconducting pyrocchlore oxide Cd2Re2O7. *Journal of Physics and Chemistry of Solids, 63*, 1027-1030.

Harvey, E. J., Ashbrook, S. E., Lumpkin, G. R., & Redfern, S. A. (2006). Characterisation of the (Y1-xLax)Ti2O7 system by powder diffraction and nuclear magnetic resonance methods. *Journal of Materials Chemistry, 16*, 4665-4674.

Harvey, E., Whittle, K., Lumpkin, G., Smith, R., & Redfern, S. (2005). Solid solubilities of (la Nd)2(Zr, Ti)2O7 phases deduced by neutron diffraction. *Journal of Solid State Chemistry, 178*, 800-810.

Heredia, A., Quintana Garcia, M., Perez Mazariego, J., & Escamilla, R. (2010). X-ray diffraction and Raman spectroscopy on Gd2(Ti2-yTey)O7 prepared at high pressure and temperature. *Journal of Alloys and Compounds, 504*, 446-451.

Knop, O., Brisse, F., & Castelliz, L. (1969). Pyrochlores. V. Thermoanalytic, X-ray, neutron, infrared, and dielectric studies of A2Ti2O7. *Canadian Journal of Chemistry, 47*, 971-990.

Kramer, S., & Tuller, H. (1995). A novel titanate-based oxygen ion conductor: Gd2Ti2O7. *Solid state ionics, 82*, 15-23.

Krishnan, R., Srinivasan, R., & Devanarayanan, S. (1979). *Thermal Expansion of Crystals.* Oxford: Pergamon Press Ltd.

Kutty, K., Rajagopalan, S., & Mathews, C. (1994). Thermal Expansion Behaviour of Some Rare Earth Oxide Pyrochlores. *Materials Research Bulletin, 29*(7), 759-766.

Le Bail, A. (2005). Whole powder pattern decomposition methods and applications: A retrospection. *Powder Diffraction, 20*(4), 316-326.

Lee, Y., Sheu, H., Deng, J., & Kao, H.-C. (2009). Preparation and fluorite-pyrochlore phase transformation in Gd2Zr2O7. *Journal of Alloys and Compounds, 487*, 595-598.

Loong, C.-K., Richardson, J. J., Ozawa, M., & Kimura, M. (1994). Crystla structure and short range oxygen defects in La- and Nd-modified ZrO2. *Journal of Alloys and Compounds, 207/208*, 174-177.

Macrae, C. B.-M. (2008). Mercury CSD 2.0 - new features for the visualization and investigation of crystal structures. *Journal of Applied Crystallography, 41*, 466-470.

Mandal B.P., B. A. (2007). Order-disorder transition in Nd(2-y)-Gd(y)Zr(2)O(7) pyrochlore solid solution: An X-ray diffraction and Raman spectroscopy study. *Journal of Solid State Chemistry, 180*, 2643-2648.

Mandal, B., Pandey, M., & Tyagi, A. (2010). Gd2Zr2O7 pyrochlore: potential host matric for some constituents of thoria based reactor's waste. *Journal of Nuclear Materials, 406*, 238-243.

Miller, W., Smith, C., Mackenzie, D., & Evans, K. (2009). Negative thermal expansion: a review. *Journal of material science, 44*, 5441-5451.

Momma, K. I. (2011). VESTA 3 for three-dimensional visualization of crystal, volumetric and morphology data. *Journal of Applied Crystallography, 44*, 1272-1276.

Mori, M., Tompsett, G., Sammes, N., Suda, E., & Takeda, Y. (2003). Compatibility of GdxTi2O7 pyrochlores (1.72<x<2.0) as electrolytes in high-temperature solid oxide fuel cells. *Solid State Ionics, 158*, 79-90.

Moriga, T., Yoshiasa, A., Kanamaru, F., & Koto, K. (1989). Crystal structrue analyses of the pyrochlore and fluorite-type Zr2Gd2O7 and anti-phase domain structure. *Solid State Ionics, 31*, 319-328.

Pitschke, W. M. (1993). Incorperation of microadsopriton corrections in Rietveld analysis. *Powder Diffraction, 8*(4), 223-228.

Pruneda, J., & Artacho, E. (2005). First-principles study of structural, elastic, and bonding properties of pyrochlores. *Physical Review B*, 085107.

Rabenau, A. (1950). Perowskit- und Fluoritphasen in den Systemen Zr O2 - La O1.5 - Mg O und Zr O2 - La O1.5 - Ca O. *Zeitschrift fuer Anorganische und Allgemeine Chemie*(288), 221-234.

Roy, R., Agrawal, D., & H.A., M. (1989). Very Low Thermal Expansion Coefficient Materials. *Annual Review of Materials Research*, 59-81.

Shannon, R. (1976). Revised Effective Ionic Radii and Systematic Studies of Interatomic Distances in Halides and Chalcogenides. *Acta Crystallographica, A*(32), 751-767.

Shlyakhtina, A., & G., S. L. (2012). New solid Electrolytes of the Pyrochlore Family. *Russian Journal of Electrochemistry, 48*, 1-25.

Shlyakhtina, A., Knotko, A., Boguslavskii, M., Stefanovich, S., Kolbanev, I., Larina, . . . Shcherbakova, L. (2007). Effect of non-stoichiometry and sythesis temperature on the structure and conductivity of Ln2+xM2-xO7-x/2 (Ln = Sm-Gd; M=Zr, Hf; x=0-0.286). *Solid State Ionics, 178*, 59-66.

Shlykhtina, A. B. (2006). Structure and electrical conductivity of Ln2+x Hf2-x O7-x/2 (Ln= Sm - Tb; x=0, 0.096. *Neorganicheskie Materialy*, 579-586.

Subramanian, M., Aravamudan, G., & Subba Rao, G. (1983). Oxide Pyrochlores - a review. *Progress in Solid State Chemistry, 15*, 55-143.

Tabira, Y., Withers, R., Minervini, L., & Grimes, R. (2000). Systematic structural change in selected rare earth oxide pyrochlores as determined by wide-angle CBED and a comparison with the results of atomistic computer simulation. *Journal of Solid State Chemistry*, 25.

Tuller, H. L. (1994). Oxygen ion conduction and structural disorder in conductive oxides. *Journal of Physics and Chemistry of Solids, 55*(12), 1393-1404.

Uno, M., Kosuga, A., Okui, M., Horisaka, K., Muta, H., Kurosaki, K., & Yamanaka, S. (2006). Photoelectrochemical study of lanthanide zirconium oxides, Ln2Zr2O7 (Ln = La, Ce, Nd, Sm). *Journal of Alloys and Compounds, 420*, 291-297.

Vassen, R., Cao, X., Tietz, F., Basu, D., & Stöver, D. (2000). Zirconates as New Materials for Thermal Barrier Coatings. *Journal of the American Ceramic Society, 83*(8), 2023-2028.

Whittle, K., Cranswick, L., Redfern, S., Swainson, I., & Lumpkin, G. (2009). Lanthanum pyrochlores and the effect of yttrium addition in the systems La(2-x) Y(x) Zr2 O7 and La(2-x) Y(x) Hf2 O7. *Journal of Solid State Chemistry, 182*(3), 442-450.

Wilde, P., & Catlow, C. (1998). Defects and diffusion in pyrochlore structured oxides. *Solid state Ionics, 112*, 173-183.

Will, G. (2006). *Powder Diffraction: The Rietveld Method andthe Two-Stage Method.* Berlin, Heidelburg: Springer.

Young, R. (1993). Introduction to the Rietveld Method. In R. Young, *The Rietveld Method* (pp. 1-39). Oxford: Oxford University Press.

Zhang, J., Yu, J., Cheng, X., & Hou, S. (2012). Thermal expansion an solubility limits of cerium-doped lanthanum zirconates. *Journal of Alloys and Compounds, 525*, 78-81.

Zhang, Z., Xiao, H., Zu, X., Fei, G., & Weber, W. (2009). First-principles calculation of structural and energetic properties for A2 Ti2 O7 (A= Lu, Er, Y, Gd, Sm, Nd, La). *Journal of Materials Research, 24*(4), 1335-1341.

Zhurova, E., Maximov, B., Simonov, V., & Sobolev, B. (1996). Structural studies of Ca F2 (at 296 K) and Ca1-x Prx F2+x , x= 0.1 (at 296 and 170 K) crystals. The changes in the fluorite anionic motif in the partial substitution of Ca(2+) by Pr(3+) cations. *Kristallografiya, 41*, 438-443.

Zub, Y. (2007). Design of Functionalized Polysiloxane adsorbents and Their Environmental Applications. In P. Innocenzi, Y. Zub, & V. Kessler, *Sol Gel Methods for Materials Processing* (pp. 1-8). Kyiv, Ukraine: Springer; NATO Public Diplomacy Division.

# 3. Hypothesis and questions

The following questions and hypotheses discuss the expected behaviour of the materials in question, under variable temperature conditions and forms the basis for the discussion in section 5. In the scope of this project, these hypotheses are related to: the link between defect-fluorite and pyrochlore structure types, how changes in temperature cause changes (if any) within these structure types and the effect of atomic displacements on polyhedral networks.

As discussed previously, an aim of the project is to corroborate the lattice parameters of previously elucidated structures found in literature and to determine the same constants for those structures that are missing information in the literature. Table 1.3.1 in the appendix (section 7) includes specific crystallographic information unique to the pyrochlore and defect fluorite structures and includes both stoichiometric and non-stoichiometric variants of these compounds. The vast majority of the compounds listed are non-stoichiometric.

Focussing on the hafnate series, $Y_2Hf_2O_7$ (in *F* d-3m and *F* m-3m), $La_2Hf_2O_7$ (*F* m-3m), $Eu_2Hf_2O_7$ (*F* m-3m), and $Gd_2Hf_2O_7$ (*F* m-3m) are missing from the literature. This may be indicative of the stability region of pyrochlore formation, as discussed in the introduction of this text. The region lies between $r_A/r_B$ = 1.46 to 1.78 (Ewing, Weber, & Lian, 2004) which is illustrated in figure 3.1 as the area between the red and blue lines. Plotted over this are the radius ratios calculated from literature ionic radius values (Shannon, 1976). From figure 3.1, it is clear that yttrium hafnate does not fall in the region, yet europium, lanthanum and gadolinium hafnates do. This may explain why a structure for yttrium hafnate in either the pyrochlore or the defect fluorite phase is not available.

Table 3.1 lists the Ionic radii for all relevant ionic radii obtained from Shannon *et al*. The table has been included for completion and for quick reference. The coordination numbers for each ion were determined by inspection of a europium titanate pyrochlore (illustrated from the structure submitted by Chtoun *et al*, illustrated in VESTA (a crystallographic visualization software package) (Chtoun, Hanebali, Garnie, & Kiat, 1997), and similarly for the defect fluorite phases using gadolinium zirconate (Lee Y. , Sheu, Deng, & Kao, 2009).

*Table 3.1: Select ionic radii (Shannon, 1976)*

| Ion | Coordination | Ionic radius (Å) |
|---|---|---|
| $La^{3+}$ | 8 | 1.160 |
| $Eu^{3+}$ | 8 | 1.066 |
| $Gd^{3+}$ | 8 | 1.053 |
| $Y^{3+}$ | 8 | 1.019 |
| $Ti^{4+}$ | 6 | 0.605 |
| $Zr^{4+}$ | 6 | 0.72 |
| $Hf^{4+}$ | 6 | 0.71 |
| $Ti^{4+}$ | 8 | 0.74 |
| $Zr^{4+}$ | 8 | 0.84 |
| $Hf^{4+}$ | 8 | 0.83 |

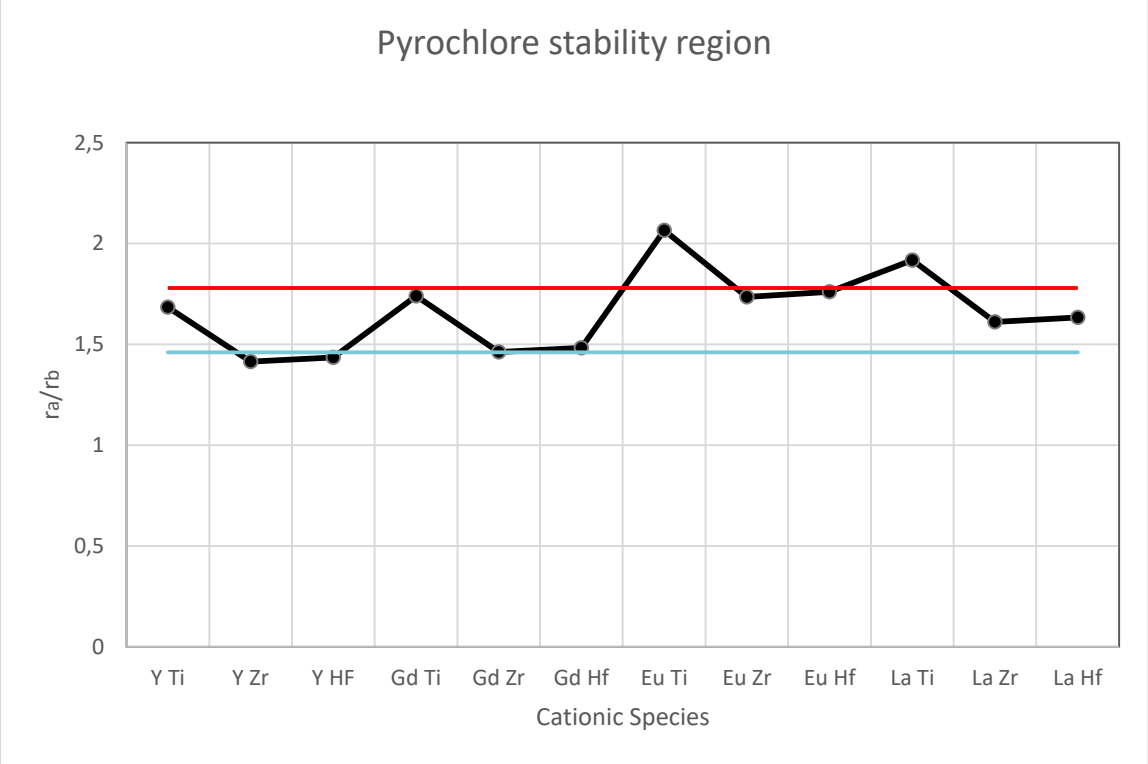


*Figure 3.1: a plot of pyrochlore stability relative to cationic radii ratios. The range exists between $r_A/r_b$ = 1.46 to 1.78 (Ewing, Weber, & Lian, 2004)*

There is only one reported structure of yttrium zirconate which crystallises in the pyrochlore structure type. This is of interest as the $r_A/r_B$ value of ytrrium to zirconium lies below the pyrochlore stability range. The particular structural entry was obtained from first principles calculations (Pruneda & Artacho, 2005). Can this result be confirmed experimentally? The first approach would be to

synthesise the material and obtain a PXRD pattern of the material, this would highlight if the material is defect fluorite or pyrochlore. Secondly, a comparison of bond lengths of the pyrochlore phase (Pruneda & Artacho, 2005) to those observed in the experimentally obtained defect fluorite structures would indicate if a pyrochlore of those particular dimensions is feasible. Of gadolinium zirconate's 20 entries in the ICSD, eight crystallize in the defect fluorite structure type. Gadolinium zirconate lies on the boundary of pyrochlore stability. Could this explain its ease in forming both phases? Of lanthanum zirconate's 26 entries, only three crystallise in the defect-fluorite phase. Entry 28991 in the ICSD can be considered as a problematic reference as no R values were given in its paper and one of its temperature factors is missing (Rabenau, 1950). As an attempt to modify $ZrO_2$ with lanthanum and neodymium respectively, Loong *et al* found a minor phase of lanthanum zirconate defect-fluorite. Although this was a non-stoichiometric compound (with respect to cationic composition), the existence of a defect fluorite phase for lanthanum zirconate was confirmed, and the non-stoichiometry hints at a compositional stability range for the phase (Loong, Richardson, Ozawa, & Kimura, 1994).

All entries for europium, yttrium, gadolinium and lanthanum titanates crystallise in the pyrochlore structure type. This contradicts the pyrochlore stability range described by Ewing *et al*, particularly for europium titanate. As can be seen in figure 3.1, the radius ratio for europium titanate and lanthanum titanate lie well above the upper limit of the stability range at values of 2.06 and 1.92 respectively (Shannon, 1976). New questions arise from this: what is the pyrochlore stability range including compounds such as europium titanate? Does the synthetic procedure affect the stability range, or is it the stability range submissive to other physical parameters, such as particle size? Lanthanum titanate has only two entries available, both are missing R values for their refinements. (Pruneda & Artacho, 2005) (Zhang, Xiao, Zu, Fei, & Weber, 2009).

## 3.1. Questions

### 3.1.1. What are the coefficients of thermal expansion for these materials?

As discussed in the introduction, there are conflicting values listed for these materials. It is one of the aims to confirm which of these sources has the correct account of the thermal expansion coefficients. The description provided by Kutty *et al*, described the thermal expansion coefficient as a parameter dependant on temperature (Kutty, Rajagopalan, & Mathews, 1994). This description ascribes more meaning to the thermal expansion characteristics than what was described by Zhang *et al* (Zhang, Yu, Cheng, & Hou, 2012). Kutty reported a linear positive change in thermal expansion coefficients with increasing temperature. Do all the pyrochlore materials in the series related to this study exhibit this trend of a linear increase in thermal expansion coefficients?

### 3.1.2. How does the alkoxide condensation sol-gel synthetic procedure affect the products?

There are several methodologies for synthesising pyrochlore and defect-fluorite materials. These include co-precipitation, solid state synthesis, mechanochemical synthesis and sol-gel synthesis, the latter being the focus of the study. The sol-gel synthetic method does suffer from the drawback of the availability of metal alkoxides.

Each methodology has pros and cons. The solid state synthetic method involves heating the mixed reagents to high temperatures which causes ion migration through particle boundaries. This has the added advantage in that no additional precursors or solvents are required. A disadvantage to the method is that it requires high temperatures for extended periods of time, often requiring specific heating steps. This can prove to be a costly manufacturing technique. Another disadvantage comes in a lack of homogeneity of the product. This is caused by the mixing of powders, which is not as intimate as wet chemical approaches.

The co-precipitation method involves dissolving the precursors in a solvent, and then adjusting the pH level such that the precursors precipitate out of solution as described by Chen *et al*. The obtained product is then heat treated to ensure complete reaction and to form the final oxide. The advantage of this methodology is that very intimate mixing of the reagents can occur, ensuring good homogeneity throughout the product. The improved mixing also implies lower heat treatment temperatures. The disadvantages of this approach include the requirement of soluble reagents, and that the reagents may precipitate at differing pH values, as can be seen in a study by Chen *et al*, where they demonstrated how lanthanum and zirconium species were precipitated from an aqueous solution. The precipitation of both species occurred simultaneously for pH values between 10 and 13, and zirconium species precipitated first when pH values were between 4.5 and 8.35 (Chen, Gao, Liu, & Luo, 2009).

The mechanochemical methodology involves grinding the precursor materials together for an extended period of time in a planetary mill. This method is particularly advantageous as there are no additional reagents (such as solvents) and the reaction occurs at ambient temperatures. This was highlighted in the work by Fuentes *et al*, where they successfully demonstrated that mechanochemical synthesis of yttrium, gadolinium and dysprosium titanates is possible, but does yield disordered materials (Fuentes, Boulahya, Maczka, Hanazu, & Amador, 2005).

The sol gel methodology, discussed in the Section 3.2.1., was selected due its minimal requirements, and its lower required temperatures for heat treatment.

### 3.1.3. What are the possible structural changes that can be observed within both structure types?

The defect-fluorite phase, as discussed previously, has no general positions within its unit cell. It is also a cubic phase, implying only one available lattice constant. These constraints limit the possible atomic movement throughout the unit cell. Given that the A cationic site (4a) is occupied in a 1:1 ratio of lanthanides to transition metals, a possible phase change can occur where the randomly dispersed cations order at high temperatures, thus forming the pyrochlore phase. Other than this possible phase change, a lattice expansion or contraction could take place. However, the presence of vacancies could allow for transverse vibrations to take place (Miller, Smith, Mackenzie, & Evans, 2009), and would allow for rigid unit modes[1] to gain mobility. This is unlikely as the vacancies are not ordered and the orchestrated movement associated with rigid unit modes and negative thermal expansion would not occur (Miller, Smith, Mackenzie, & Evans, 2009).

The pyrochlore lattice type also has no available general positions, but the x-parameter on $O_{48f}$ is variable. It is therefore possible to see the following structural changes with respect to temperature changes: Bond lengths associated with $O_{48f}$, polyhedral geometry, and lattice expansion or contraction. The bond associated with $O_{48f}$ include all the M-O bonds to the transition metal, such as titanium(IV) depicted in figure 3.2, and all the equatorial Ln-O bonds (Chtoun, Hanebali, Garnier, & Kiat, X-rays and neutrons rietveld analysis of the solid solutions (1-x)(A2 Ti2 O7) - x(Mg Ti O3) (A = Y or Eu), 1997). A shift in the x-parameter of $O_{48f}$ would cause significant distortions in the polyhedral geometry of both M and Ln species within the same lattice. A question to answer would then be: What effect does a change in temperature have on polyhedral geometry in pyrochlore phases?

[1] A rigid unit mode is an approximation used to describe polyhedra. The assumption is that the change in M-O bonds is negligible, and hence the polyhedron can be viewed as a single rigid unit.

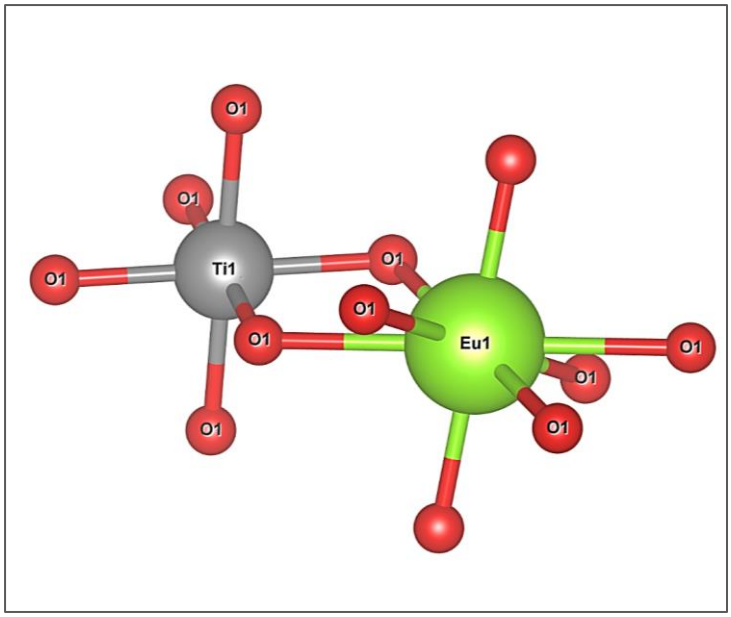


*Figure 3.2: Bonding of O1 in the 48f position in europium titanate pyrochlore (Chtoun, Hanebali, Garnier, & Kiat, X-rays and neutrons rietveld analysis of the solid solutions (1-x)(A2 Ti2 O7) - x(Mg Ti O3) (A = Y or Eu), 1997)*

### 3.1.4. How does this link to the coefficients of thermal expansion?

In the pyrochlore structure type, all atoms lie on special positions with the exception of the x-position of the $O_{48f}$. The extent to which this value varies determines the geometry of the metal polyhedra. Determining how $O_{48f}$ changes with temperature can allow one to determine how the polyhedra change shape with temperature. This has implications on the environment of the metal ions within the structure. The changes in geometry may also give insight into a possible mechanism of thermal expansion within these materials.

## 3.2. Proposed answers to the aims of this project

### 3.2.1. Synthesis via sol-gel

The synthesis of pyrochlore and defect-fluorite phases via an alkoxide condensation sol-gel process will yield the desired product. Similar results have been observed previously with tin based pyrochlores (Fujihara & Tokumo, 2005). Titanium, zirconium and hafnium are all capable of a valency of 4+, hence allowing for the method to be effective as the metal species in the starting reagents have the correct valency.

An expected result will be the formation of the fluorite phase prior to the formation of the pyrochlore phase. The reasoning for this is that the significant mixing of the two cationic species in the sol will encourage a random distribution of cations throughout the oxide matrix. Upon excessive heat treatment, the cations should order, hence forming the pyrochlore super-lattice. The evidence to suggest this is the case was outlined by Chen *et al*, where different co-precipitation methods caused

species to precipitate at different pH values (the natural dropping method). When a reverse dropping method was employed, both species precipitated simultaneously. The natural dropping method yielded a pyrochlore structure upon calcination, while the reverse dropping method first produced a defect fluorite phase which converted to a pyrochlore phase upon heat treatment (Chen, Gao, Liu, & Luo, 2009).

### 3.2.2. Confirmation of lattice parameters

The lattice parameters of this study will corroborate those in literature provided the structure exists in literature (the defect-fluorite phase of lanthanum hafnate and the pyrochlore of yttrium zirconate are examples of structures which don't have a literature reference). The reason for this assumption is the choice of synthetic procedure. Sol-gel synthesis can very accurately control the molar amount of a species, and the low temperature at which synthesis takes place ensures that the sublimation of a particular species does not occur.

### 3.2.3. Coefficients of thermal expansion

The coefficients of thermal expansion for the materials of this study are most likely to have a positive thermal expansion. This prediction can be made in that none of the structural features required for zero or negative thermal expansion are present in the literature structures of each material. The features required are transverse vibrations, libration mechanisms, movements of rigid unit modes, and phase transitions as described by Miller *et al* (Miller, Smith, Mackenzie, & Evans, 2009). The first three mechanisms cannot occur due to both the pyrochlore and defect fluorite structure types being devoid of corner sharing polyhedra. The presence of only face and edge sharing polyhedra prevents these mechanisms form occurring.

However, the rigidity of face and edge sharing polyhedra will limit the thermal expansion capabilities of the materials, and will most likely prevent the occurrence of high thermal expansion, as discussed by Roy et al. (Roy, Agrawal, & Mckinstry, Very Low Thermal Expansion Coefficient Materials, 1989)

## 3.3. References

Aroyo, M., Kirov, A., Capillas, C., Perez-Mato, J., & Wondratshek, H. (2006). Bilbao Crystallographic Server II: Representations of crystallographic point groups and space groups. *Acta Crystallographica, A62*, 115-128.

Aroyo, M., Perez-Mato, J., Capillas, C., Kroumova, E., Ivanchev, S., Madariaga, G., . . . Wondratschek, H. (2006). Bilbao Crystallographic Server I: Databases and Crystallographic computing programs. *Z.Krist, 221*(1), 12-27.

Aroyo, M., Perez-Mato, J., Orobengoa, D., Tasci, E., de la flor, G., & Kirov, A. (2011). Crystallography online: Bilbao Crystallographic server. *Bulgarian Chemistry community, 43*(2), 183-197.

Askeland, D., & Phulé, P. (2006). *The Science and Engineering of Materials.* Toronto, Canada: Thomson Canada Limited.

AXS, B. (2008). *TOPAS V4: General profile and structure analysis software for powder diffraction data - User's Manual.* Karlsruhe, Germany: Bruker AXS.

Caglioti, G. P. (1958). Choice of Collimators for a Crystal Spectrometer for Neutron Diffraction. *Nuclear Instruments, 3*, 223-228.

Chakoumakos, B. (1984). Systematics of the Pyrochlore Structure Type, Ideal A2B2X6Y. *Journal of Solid State Chemistry*(53), 120-129.

Chen, H., Gao, Y., Liu, Y., & Luo, H. (2009). Coprecipitation synthesis and thermal conductivity of La2Zr2O7. *Journal of Alloys and Compounds*(480), 843-848.

Chien, C. S. (1978). Mossbauer effect studies of europium pyrochlores. *Physical review, 18*(5), 2031-2038.

Chtoun, E., Hanebali, L., & Garnier, P. (2001). Analyse par diffraction des rayons X, methode de Rietveld, de la structure des. *Annales de Chimie (Paris)*, 32.

Chtoun, E., Hanebali, L., Garnie, P., & Kiat, J. (1997). X-rays and neutrons rietveld analysis of the solid solutions (1-x)(A2 Ti2 O7) - x(Mg Ti O3) (A = Y or Eu). *European Journal of Solid State Inorganic Chemistry*(34), 553-561.

Cockcraft, J. (1997-1999, March 12). *High-Resolution Space Group Diagrams and Tables*. Retrieved March 12, 2014, from A Hypertext Book of Crystallographic Space Group Diagrams and Tables: http://img.chem.ucl.ac.uk/sgp/LARGE/227bz1.htm

Ewing, R. C., Weber, W. J., & Lian, J. (2004). Nuclear waste disposal-pyrochlore (A2B2O7): Nuclear waste form for immobilization of plutonium and "minor"actinides. *journal of Applied Physics, 95*(11), 5949-5969.

Fagg, D., & Irvine, J. (1998). The Optimisation of Mixed Conduction in potential S.O.F.C. Anode Materials. *Ionics, 4*, 61-71.

Farmer, J., Boatner, L., Chakoumakos, B., Du, M., Lance, M., Rawn, C., & Bryan, J. (2014). Structural and crystal chemical properties of rare-earth titanate pyrochlores. *Journal of Alloys and Compounds*(605), 63-70.

Fuentes, A., Boulahya, K., Maczka, M., Hanazu, J., & Amador, U. (2005). Synthesis of disordered pyrochlores, A2Ti2O7 (A=Y, Gd and Dy), by mechanical milling of constituent oxides. *Solid State Sciences, 7*, 343-353.

Fujihara, S., & Tokumo, K. (2005). Multiband Orange-Red Luminescence Of Eu3+ Ions Based on the Pyrochlore-Structured Host Crystal. *Chemistry of Materials*(17), 5587-5593.

Goodenough, J., & Castellano, R. (1982). Defect Pyrochlore as Catalyst Supports. *Journal of Solid State Chemistry, 44*, 108-112.

Greedan, J. (2006). Frustrated rare earth magnitism: Spin glasses, spin liquid and spin ices in pyrochlore oxides. *Journal of Alloys and Compounds*, 444-455.

Guangrong, N., & Flemming, R. (2005). Rietveld refinement of LaB6:data from micro-XRD. *Journal of Applied Crystallography, 38*, 757-759.

Hail, S., Wuensch, B., & Prince, E. (1990). Neutron Rietveld analysis of anion and cation disorder in the fast-ion conducting pyrochlore system Y2 (Zr(x) Ti(1-x))2 O7. *Materials Research Society Symposia Proceedings*, 81-86.

Hanawa, M., Yamaura, J., Muraoka, Y., Sakai, F., & Hiroi, Z. (2002). Structural phase transition in the superconducting pyrocchlore oxide Cd2Re2O7. *Journal of Physics and Chemistry of Solids, 63*, 1027-1030.

Harvey, E. J., Ashbrook, S. E., Lumpkin, G. R., & Redfern, S. A. (2006). Characterisation of the (Y1-xLax)Ti2O7 system by powder diffraction and nuclear magnetic resonance methods. *Journal of Materials Chemistry, 16*, 4665-4674.

Harvey, E., Whittle, K., Lumpkin, G., Smith, R., & Redfern, S. (2005). Solid solubilities of (la Nd)2(Zr, Ti)2O7 phases deduced by neutron diffraction. *Journal of Solid State Chemistry, 178*, 800-810.

Heredia, A., Quintana Garcia, M., Perez Mazariego, J., & Escamilla, R. (2010). X-ray diffraction and Raman spectroscopy on Gd2(Ti2-yTey)O7 prepared at high pressure and temperature. *Journal of Alloys and Compounds, 504*, 446-451.

Knop, O., Brisse, F., & Castelliz, L. (1969). Pyrochlores. V. Thermoanalytic, X-ray, neutron, infrared, and dielectric studies of A2Ti2O7. *Canadian Journal of Chemistry, 47*, 971-990.

Kramer, S., & Tuller, H. (1995). A novel titanate-based oxygen ion conductor: Gd2Ti2O7. *Solid state ionics, 82*, 15-23.

Krishnan, R., Srinivasan, R., & Devanarayanan, S. (1979). *Thermal Expansion of Crystals.* Oxford: Pergamon Press Ltd.

Kutty, K., Rajagopalan, S., & Mathews, C. (1994). Thermal Expansion Behaviour of Some Rare Earth Oxide Pyrochlores. *Materials Research Bulletin, 29*(7), 759-766.

Le Bail, A. (2005). Whole powder pattern decomposition methods and applications: A retrospection. *Powder Diffraction, 20*(4), 316-326.

Lee, Y., Sheu, H., Deng, J., & Kao, H.-C. (2009). Preparation and fluorite-pyrochlore phase transformation in Gd2Zr2O7. *Journal of Alloys and Compounds, 487*, 595-598.

Loong, C.-K., Richardson, J. J., Ozawa, M., & Kimura, M. (1994). Crystla structure and short range oxygen defects in La- and Nd-modified ZrO2. *Journal of Alloys and Compounds, 207/208*, 174-177.

Macrae, C. B.-M. (2008). Mercury CSD 2.0 - new features for the visualization and investigation of crystal structures. *Journal of Applied Crystallography, 41*, 466-470.

Mandal B.P., B. A. (2007). Order-disorder transition in Nd(2-y)-Gd(y)Zr(2)O(7) pyrochlore solid solution: An X-ray diffraction and Raman spectroscopy study. *Journal of Solid State Chemistry, 180*, 2643-2648.

Mandal, B., Pandey, M., & Tyagi, A. (2010). Gd2Zr2O7 pyrochlore: potential host matric for some constituents of thoria based reactor's waste. *Journal of Nuclear Materials, 406*, 238-243.

Miller, W., Smith, C., Mackenzie, D., & Evans, K. (2009). Negative thermal expansion: a review. *Journal of material science, 44*, 5441-5451.

Momma, K. I. (2011). VESTA 3 for three-dimensional visualization of crystal, volumetric and morphology data. *Journal of Applied Crystallography, 44*, 1272-1276.

Mori, M., Tompsett, G., Sammes, N., Suda, E., & Takeda, Y. (2003). Compatibility of GdxTi2O7 pyrochlores (1.72<x<2.0) as electrolytes in high-temperature solid oxide fuel cells. *Solid State Ionics, 158*, 79-90.

Moriga, T., Yoshiasa, A., Kanamaru, F., & Koto, K. (1989). Crystal structrue analyses of the pyrochlore and fluorite-type Zr2Gd2O7 and anti-phase domain structure. *Solid State Ionics, 31*, 319-328.

Pitschke, W. M. (1993). Incorperation of microadsopriton corrections in Rietveld analysis. *Powder Diffraction, 8*(4), 223-228.

Pruneda, J., & Artacho, E. (2005). First-principles study of structural, elastic, and bonding properties of pyrochlores. *Physical Review B*, 085107.

Rabenau, A. (1950). Perowskit- und Fluoritphasen in den Systemen Zr O2 - La O1.5 - Mg O und Zr O2 - La O1.5 - Ca O. *Zeitschrift fuer Anorganische und Allgemeine Chemie*(288), 221-234.

Roy, R., Agrawal, D., & H.A., M. (1989). Very Low Thermal Expansion Coefficient Materials. *Annual Review of Materials Research*, 59-81.

Shannon, R. (1976). Revised Effective Ionic Radii and Systematic Studies of Interatomic Distances in Halides and Chalcogenides. *Acta Crystallographica, A*(32), 751-767.

Shlyakhtina, A., & G., S. L. (2012). New solid Electrolytes of the Pyrochlore Family. *Russian Journal of Electrochemistry, 48*, 1-25.

Shlyakhtina, A., Knotko, A., Boguslavskii, M., Stefanovich, S., Kolbanev, I., Larina, . . . Shcherbakova, L. (2007). Effect of non-stoichiometry and sythesis temperature on the structure and conductivity of Ln2+xM2-xO7-x/2 (Ln = Sm-Gd; M=Zr, Hf; x=0-0.286). *Solid State Ionics, 178*, 59-66.

Shlykhtina, A. B. (2006). Structure and electrical conductivity of Ln2+x Hf2-x O7-x/2 (Ln= Sm - Tb; x=0, 0.096. *Neorganicheskie Materialy*, 579-586.

Subramanian, M., Aravamudan, G., & Subba Rao, G. (1983). Oxide Pyrochlores - a review. *Progress in Solid State Chemistry, 15*, 55-143.

Tabira, Y., Withers, R., Minervini, L., & Grimes, R. (2000). Systematic structural change in selected rare earth oxide pyrochlores as determined by wide-angle CBED and a comparison with the results of atomistic computer simulation. *Journal of Solid State Chemistry*, 25.

Tuller, H. L. (1994). Oxygen ion conduction and structural disorder in conductive oxides. *Journal of Physics and Chemistry of Solids, 55*(12), 1393-1404.

Uno, M., Kosuga, A., Okui, M., Horisaka, K., Muta, H., Kurosaki, K., & Yamanaka, S. (2006). Photoelectrochemical study of lanthanide zirconium oxides, Ln2Zr2O7 (Ln = La, Ce, Nd, Sm). *Journal of Alloys and Compounds, 420*, 291-297.

Vassen, R., Cao, X., Tietz, F., Basu, D., & Stöver, D. (2000). Zirconates as New Materials for Thermal Barrier Coatings. *Journal of the American Ceramic Society, 83*(8), 2023-2028.

Whittle, K., Cranswick, L., Redfern, S., Swainson, I., & Lumpkin, G. (2009). Lanthanum pyrochlores and the effect of yttrium addition in the systems La(2-x) Y(x) Zr2 O7 and La(2-x) Y(x) Hf2 O7. *Journal of Solid State Chemistry, 182*(3), 442-450.

Wilde, P., & Catlow, C. (1998). Defects and diffusion in pyrochlore structured oxides. *Solid state Ionics, 112*, 173-183.

Will, G. (2006). *Powder Diffraction: The Rietveld Method andthe Two-Stage Method.* Berlin, Heidelburg: Springer.

Young, R. (1993). Introduction to the Rietveld Method. In R. Young, *The Rietveld Method* (pp. 1-39). Oxford: Oxford University Press.

Zhang, J., Yu, J., Cheng, X., & Hou, S. (2012). Thermal expansion an solubility limits of cerium-doped lanthanum zirconates. *Journal of Alloys and Compounds, 525*, 78-81.

Zhang, Z., Xiao, H., Zu, X., Fei, G., & Weber, W. (2009). First-principles calculation of structural and energetic properties for A2 Ti2 O7 (A= Lu, Er, Y, Gd, Sm, Nd, La). *Journal of Materials Research, 24*(4), 1335-1341.

Zhurova, E., Maximov, B., Simonov, V., & Sobolev, B. (1996). Structural studies of Ca F2 (at 296 K) and Ca1-x Prx F2+x , x= 0.1 (at 296 and 170 K) crystals. The changes in the fluorite anionic motif in the partial substitution of Ca(2+) by Pr(3+) cations. *Kristallografiya, 41*, 438-443.

Zub, Y. (2007). Design of Functionalized Polysiloxane adsorbents and Their Environmental Applications. In P. Innocenzi, Y. Zub, & V. Kessler, *Sol Gel Methods for Materials Processing* (pp. 1-8). Kyiv, Ukraine: Springer; NATO Public Diplomacy Division.

# 4. Results

An important observation regarding the appearance of several materials' diffraction patterns must be made. Several of the materials (namely Europium hafnate, Gadolinium hafnate and gadolinium zirconate) yielded diffraction patterns which were difficult to discriminate between the defect fluorite and pyrochlore phases. The more accurate phase description of these materials were determined by Raman spectroscopy (where the vibration (phonon) modes of the oxygen metal bond more easily discriminate between the defect fluorite and pyrochlore phases, depending on the number of apparent phonon modes) in a separate independent study.[*] The reason for the difficulty in discriminating between the two phases via XRD resides in the signal to noise ratio of the diffraction patterns. The (111) peak lies below the noise threshold due to the poor crystallinity of the samples, evident from the width of their diffraction peaks. The only material to form the defect fluorite phase was yttrium hafnate[*].

## 4.1. Lanthanide hafnates

### 4.1.1. Lanthanum hafnate

#### Phase analysis

The D2 (ambient co-PXRD) pattern of the material $La_2Hf_2O_7$ indicates the presence of the pyrochlore phase due to the existence of the pyrochlore superstructure peaks, particularly the (111) peak located at lower angles, as can be seen in figure 4.1. This was also confirmed via Raman spectroscopy in a separate study*. These super cell peaks are significantly lower in intensity than what is observed for the peaks that would normally be shared with those of the defect fluorite phase. This indicates that the 48f position (i.e. an oxygen position) has been extended near the limits of stability of the pyrochlore phase. This statement, however, can only be confirmed by Rietveld refinement, which shall be discussed in section 5. In a peak matching analysis, the phase determined to be present was found to be a defect fluorite phase. This was found to be incorrect as the remaining peaks were not due to impurity phases such as oxides of the starting materials. Overlaying a calculated pattern derived from the cif file of the structure obtained from the ICSD, indicates that the sole presence of the pyrochlore

[*] Miller and Billing, unpublished results

Supporting information may be obtained from Dr Stuart F. Miller; stuart.miller@wits.ac.za

phase is correct. Figure 4.2 reveals the presence of the pyrochlore phase, as seen by the (111) peak at approximately 13 °2θ

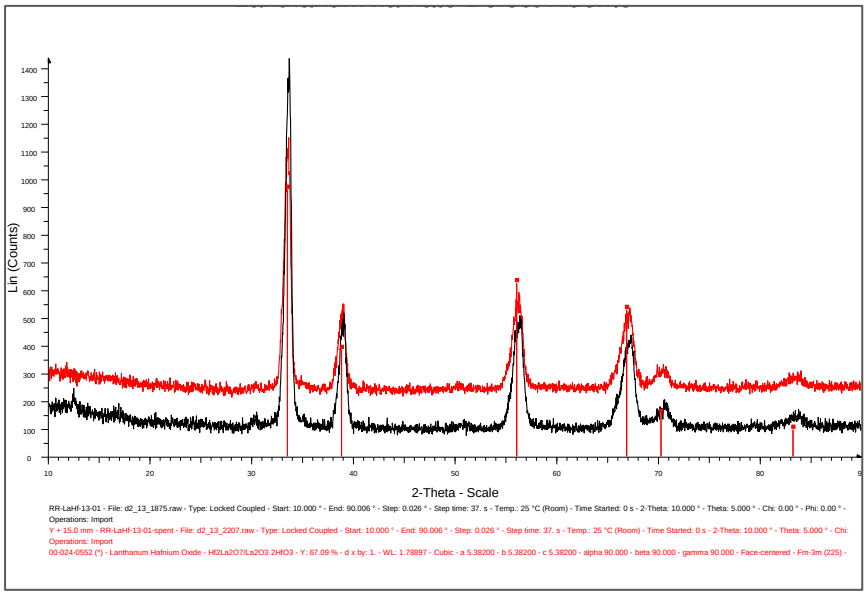


*Figure 4-1: A D2 Pattern of lanthanum hafnate oxide before (black) and after (red) the VT-PXRD experiment.*

The intensity of this second D2 pattern is lower than the first due to the measurement using less sample on a zero background holder. This loss of intensity is the reason for the super-cell peaks (seen in the black pattern in figure 4.1) to disappear in the red pattern.

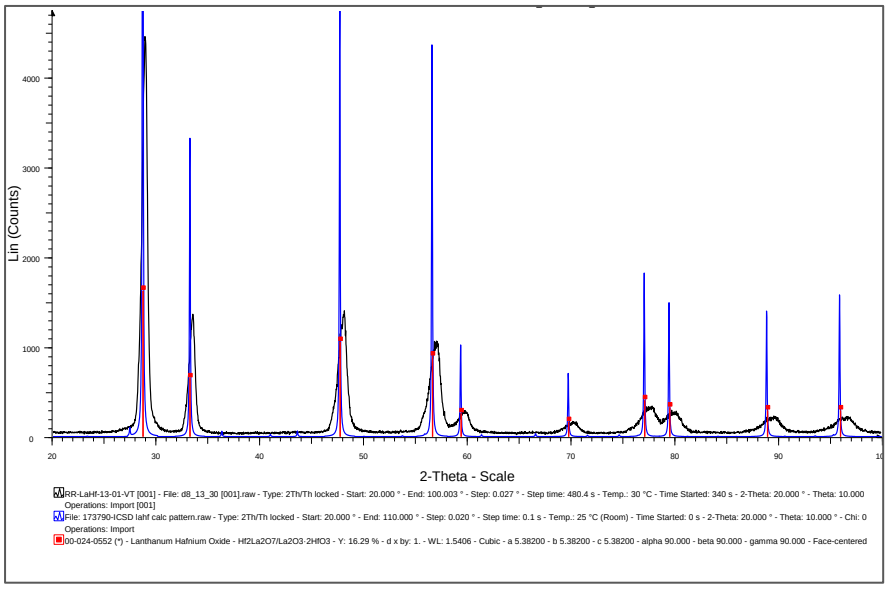


*Figure 4-2: A calculated pattern overlaid on the 30° C pattern of CuK$_{\alpha 2}$ measurement*

It is important to note that the above mentioned peaks were not apparent in the CuK$_{\alpha 2}$ pattern, which had significantly higher counting statistics. Overlaying the CoK$_{\alpha 2}$ pattern with that of the CuK$_{\alpha 2}$ pattern

indicates that the potential pyrochlore peaks are only observed cobalt radiation data, which may be related to the performance difference between the two different detectors in use. The loss of the super-cell peaks in the $CuK_{\alpha 2}$ pattern may also be described by the width of the major diffraction peaks and the reduced range of angles in which diffraction peaks are observed due to the shorter wavelength of X-Rays used. The width of the major peaks added with the background hides the smaller supercell peaks from observation.

Careful observation of each of the patterns in the variable temperature analysis indicated that no phase change occurred on heating, only a slight shift of the peaks towards lower angles was seen, indicating the presence of positive thermal expansion. Additional peaks formed upon cooling, which can be seen in the cascading pattern (grey pattern in figure 4.3). Overlaying the previously mentioned calculated pattern of the pyrochlore phase confirms that two of the newly formed peaks do correspond to the formation of the pyrochlore phase.

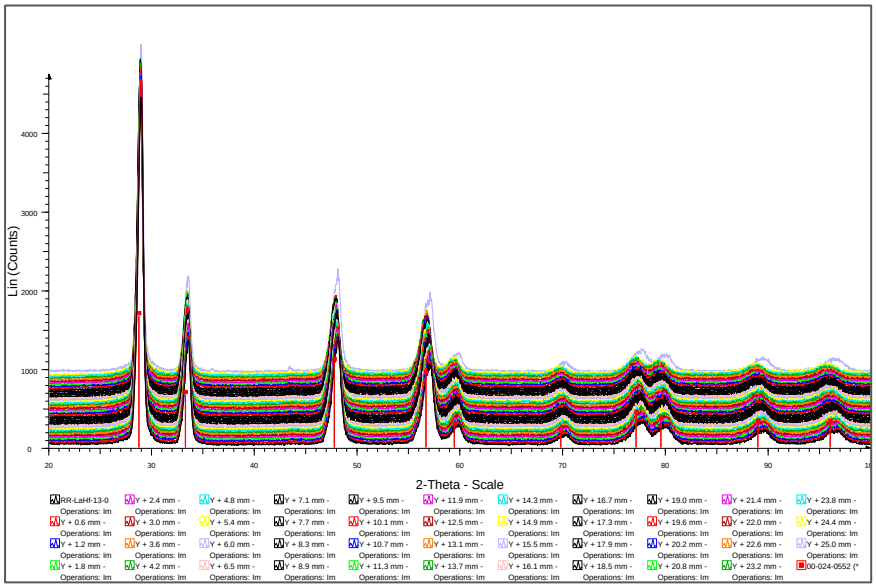


*Figure 4-3: Cascading diffraction patterns of $La_2Hf_2O_7$*

From this information, the decision was taken to refine the lanthanum hafnate data as a pyrochlore structure. This can also be seen in the calculated pattern, where the peaks unique to the pyrochlore super-cell cannot be adequately seen, yet the presence of certain additional peaks as discussed previously indicate the pyrochlore lattice.

An important observation to note was that of the particularly strange peak shapes observed for all of the variable temperature patterns, which can be seen in figures 4.2 and 4.3. They are perhaps best

described as two, slightly overlapping peaks. The overlaid calculated pattern appears to correspond with the preceding peak in each case of this overlap, where it occurs.

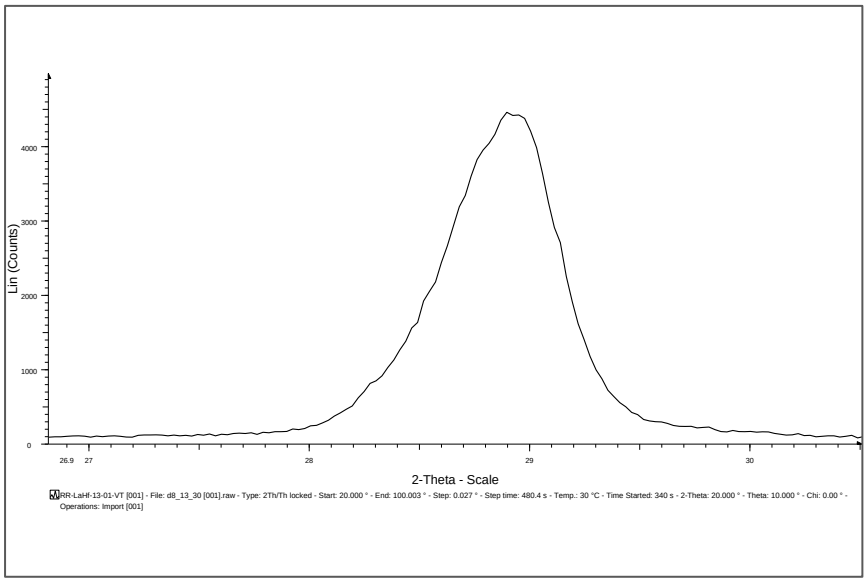


*Figure 4-4-4: A single peak from the diffraction pattern of $La_2Hf_2O_7$*

Another important note is that the appearance of the additional peaks may have come from contamination in the XRK 900 in the form of corrosion of the inner steel lining becoming loosened from the high temperatures and thermal expansion of the steel inside the furnace chamber. The loss of these peaks in the D2 pattern of the spent material can be attributed to the mixing of the contaminant with the rest of the material resulting in the diffracting contribution lying below the background of the measurement. Also, less material was used in the post variable temperature ambient diffraction scan.

Structural observations

The difference plot from the $CoK_{\alpha 2}$ (ambient) pattern refinement illustrated in figure 4.5 indicates a precise fit, showing only some distortion below the principle peak and some scattered spots of additional noise.

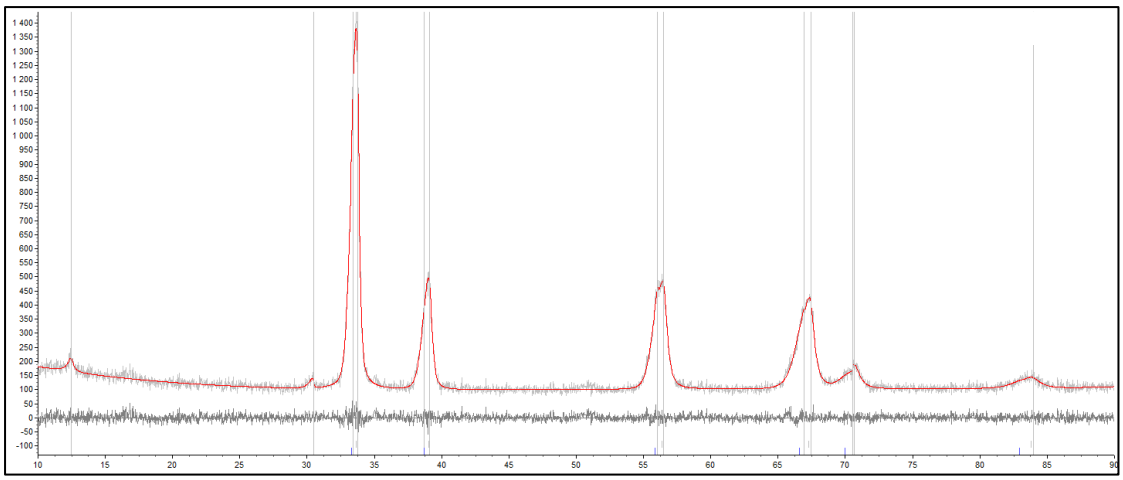

*Figure 4-5: The CoK$_{\alpha 2}$ difference plot of La$_2$Hf$_2$O$_7$ obtained after completion of the Rietveld refinement procedure discussed in section 2.4.6.*

The difference plot for the CuK$_{\alpha 2}$ radiation (Bruker D8) 30°C pattern of lanthanum hafnate is not as precise as the CoK$_{\alpha 2}$ as there is a discrepancy in describing the tip of the major peaks.

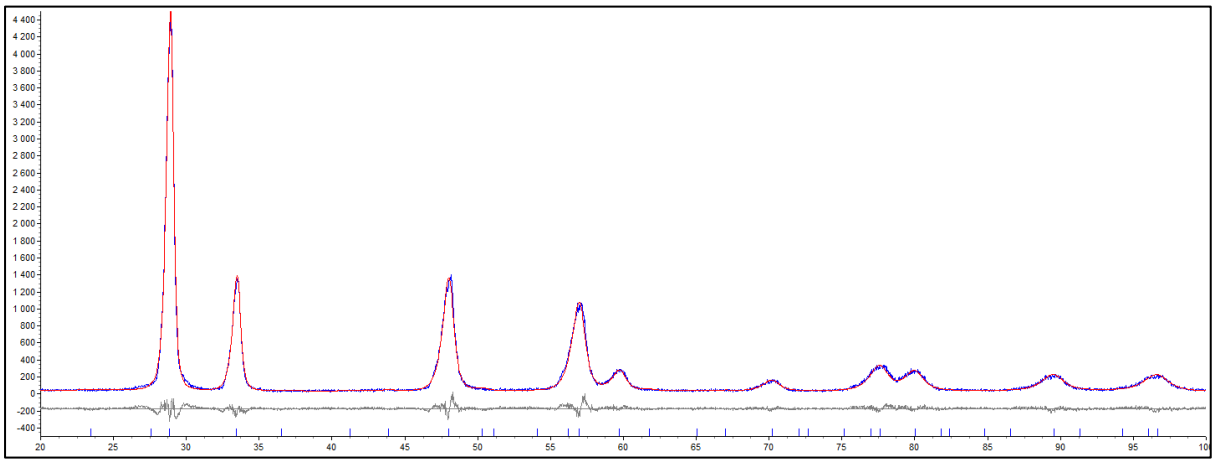

*Figure 4-6: The CuKα2 difference plot of La2Hf2O7 obtained after completion of the Rietveld refinement procedure discussed in section 2.4.6.*

In the range of 30 to 850 °C, lanthanum hafnate exhibited a lattice parameter increase from 10.717(1) Å to 10.796(1) Å. The goodness of fit for the variable temperature regime decreases as temperature increases, as can be seen in figure 4.7. The goodness of fit did fluctuate around this decreasing trend, and exhibited an unfortunately high value over the temperature range.

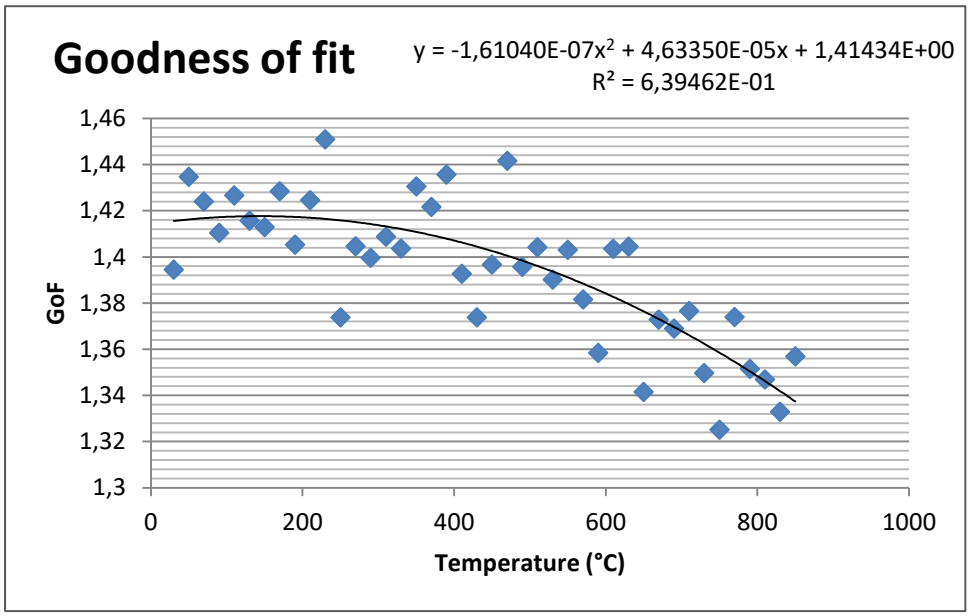


*Figure 4-7: the Goodness of fit for $La_2Hf_2O_7$ relative to temperature for the VT-PXRD sequential refinement.*

Similarly, the Rwp values were high, ranging from 10.762 at 250 °C to 11.555 at 850 °C with much fluctuation in-between. This can be seen in figure 4.8.

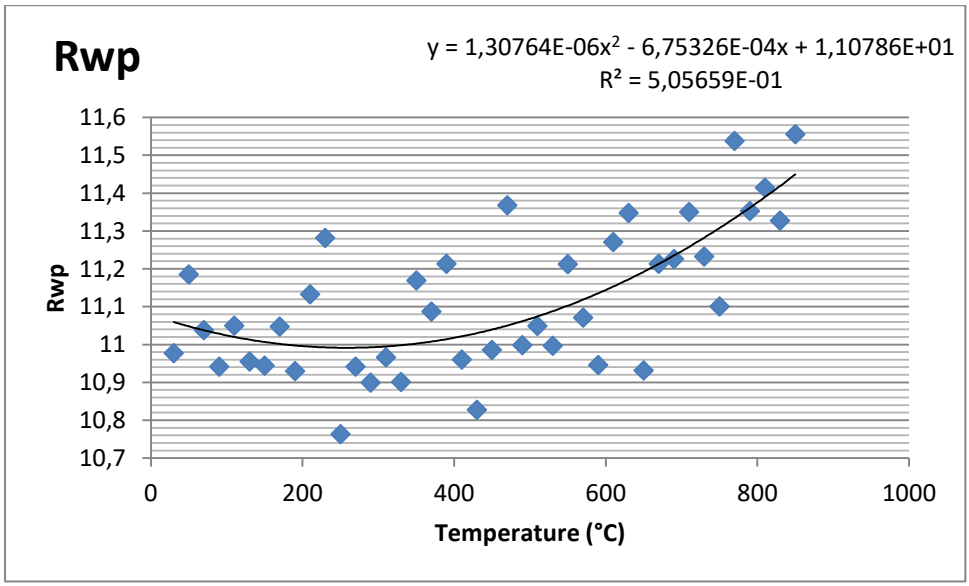


*Figure 4-8: The Rwp Values for the sequential Rietveld refinement of $La_2Hf_2O_7$.*

The thermal parameter of the hafnium ion placed on position 16c followed an increasing trend which fluctuated around a polynomial line fitted to the data, as can be seen in figure 4.9. The minimum Beq value was 0.498 at 30 °C, and the maximum was 1.249 at 550 °C.

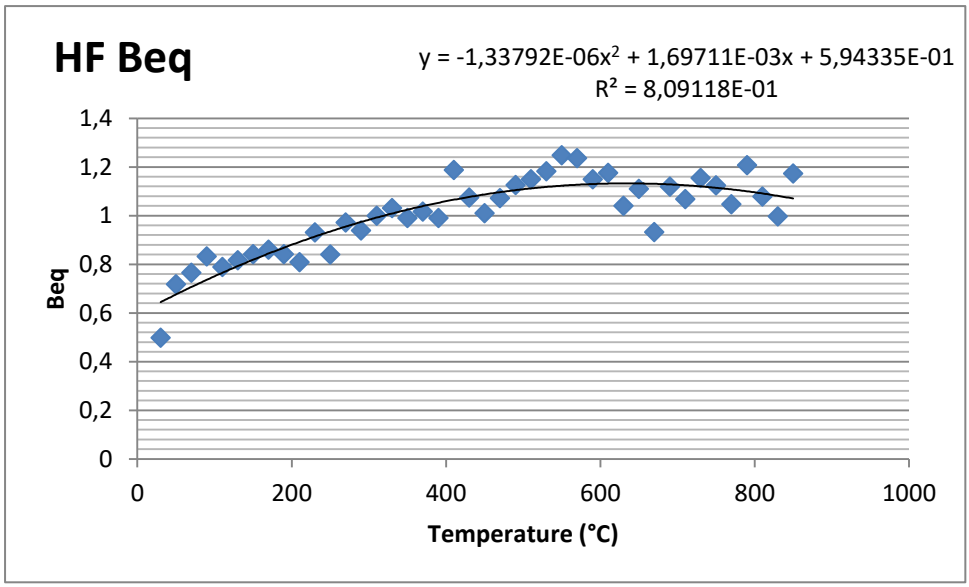


*Figure 4-9: The hafnium Beq thermal parameter relative to temperature for $La_2Hf_2O_7$.*

Both oxygen ions and the lanthanum ion returned highly fluctuating thermal parameters as can be seen in Figures 4.10, 4.11 and 4.12. This may explain the poor figures of merit obtained for the refinements.

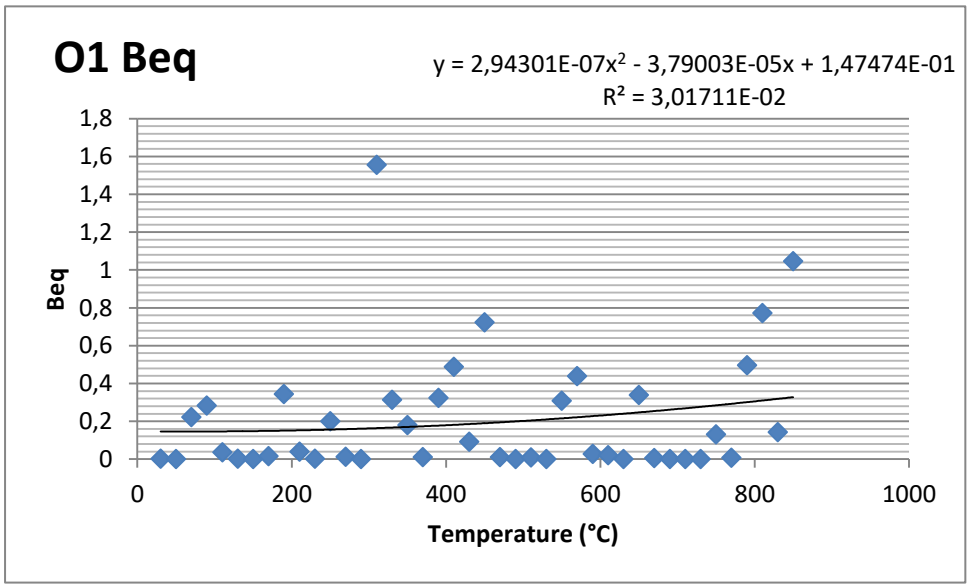


*Figure 4-10: The Beq thermal parameter for the 48f oxygen relative to temperature for the sequential Rietveld refinement of $La_2Hf_2O_7$.*

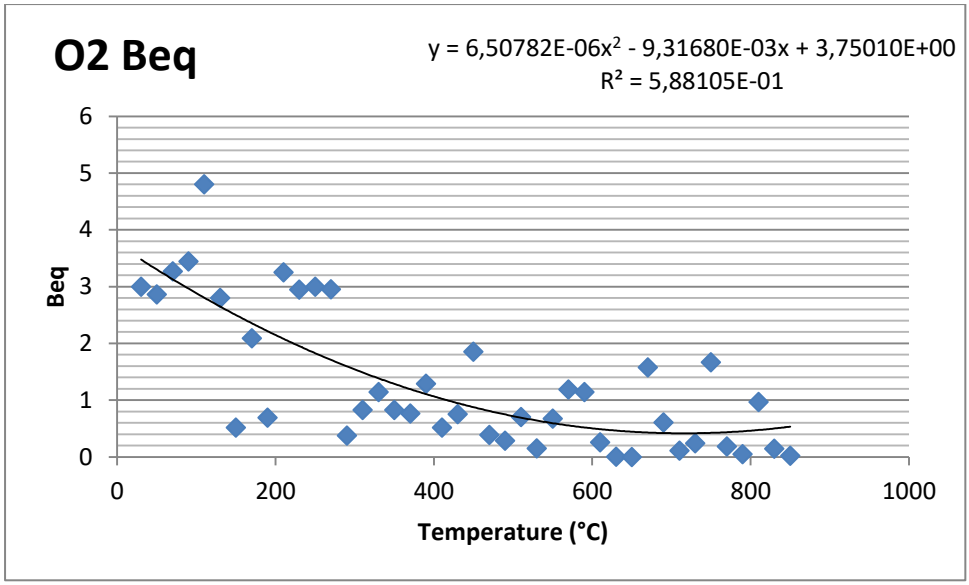


*Figure 4-11The Beq thermal parameters for the 8a oxygen of $La_2Hf_2O_7$*

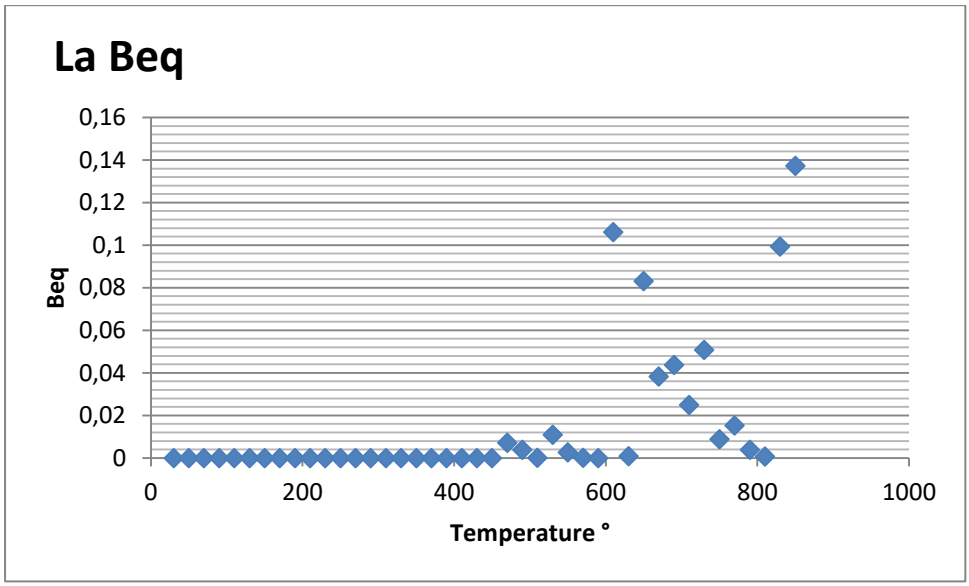


*Figure 4-12: The Beq thermal parameter for La in $La_2Hf_2O_7$ relative to temperature.*

Figure 4.13 appears linear, but fitting with a polynomial function returned a $R^2$ value closer to unity. Using this function, the coefficient of thermal expansion was calculated relative to temperature, and indicated a linear increase in the coefficient, following the equation $\alpha = 2.222 \times 10^{-9}x + 8.251 \times 10^{-6}$, receiving a minimum of 8.31 ppm.°$C^{-1}$ at 30 °C and a maximum of 10.13ppm. °$C^{-1}$ at 850 °C. The average coefficient of thermal expansion was 9.23 ppm. °$C^{-1}$.

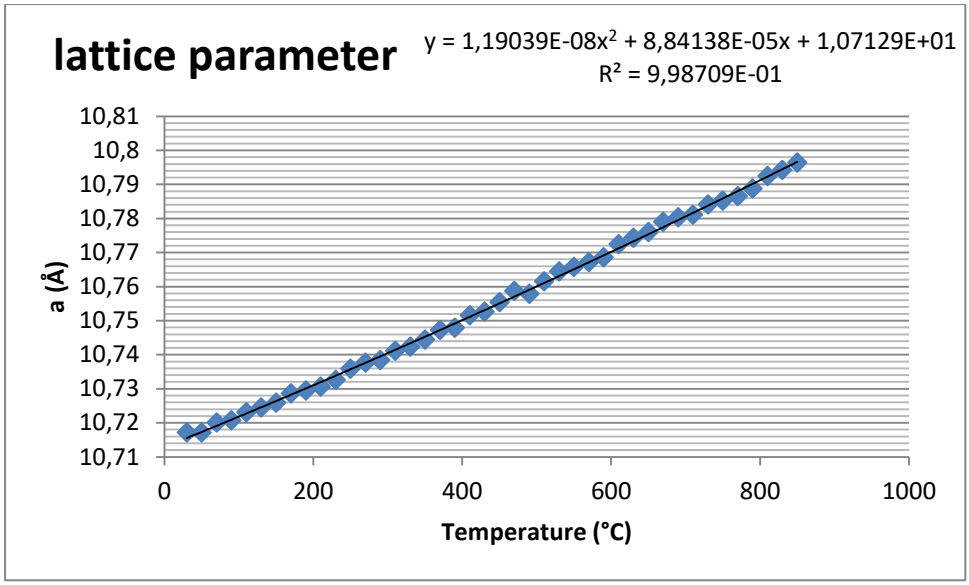


*Figure 4-13: The lattice parameter expansion against temperature for $La_2Hf_2O_7$.*

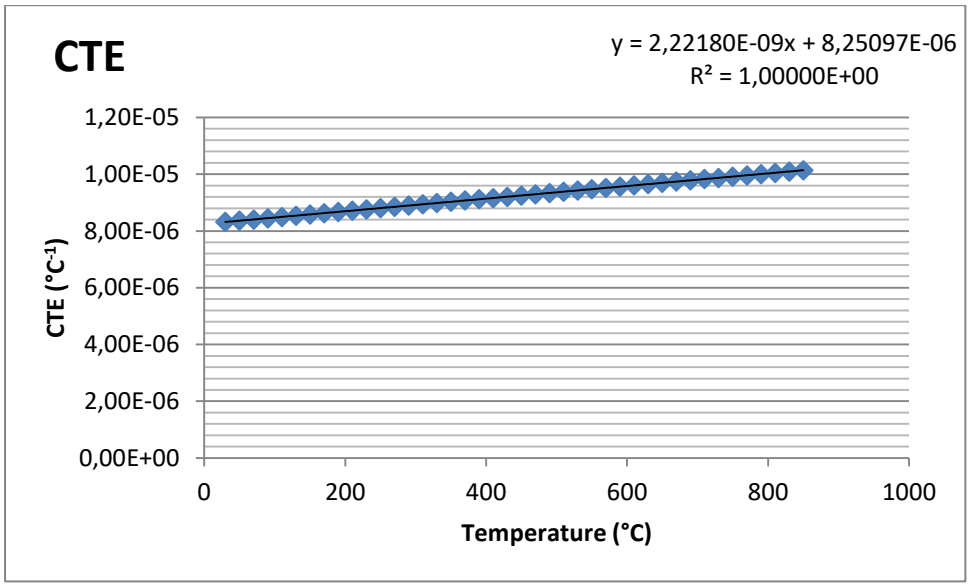


*Figure 4-14: The Coefficient of thermal expansion for $La_2Hf_2O_7$ relative to temperature.*

### 4.1.2. Europium hafnate refinement results

#### Phase analysis

The distinction between a pyrochlore phase and a defect fluorite phase in the measured diffraction patterns was not immediately discernible, but from careful inspection of the pattern taken by the D2 diffractometer (with CoKα2 radiation, as seen in figure 4.15), a slight indication of a pyrochlore is implied by the presence of a very low angle peak located at 12.319° 2θ. The peak is very diffuse, but most likely relates to the (111) plane of the pyrochlore structure. In a peak matching analysis using Diffrac Plus EVA, no matched phase could be found for the pattern taken using CoKα2 radiation.

Similarly, the variable temperature patterns of the same compound under CuKα2 radiation did not yield a match from the available database (see figure 4.16). The pyrochlore phase, as discussed earlier, was determined by Raman spectroscopy in a separate study*.

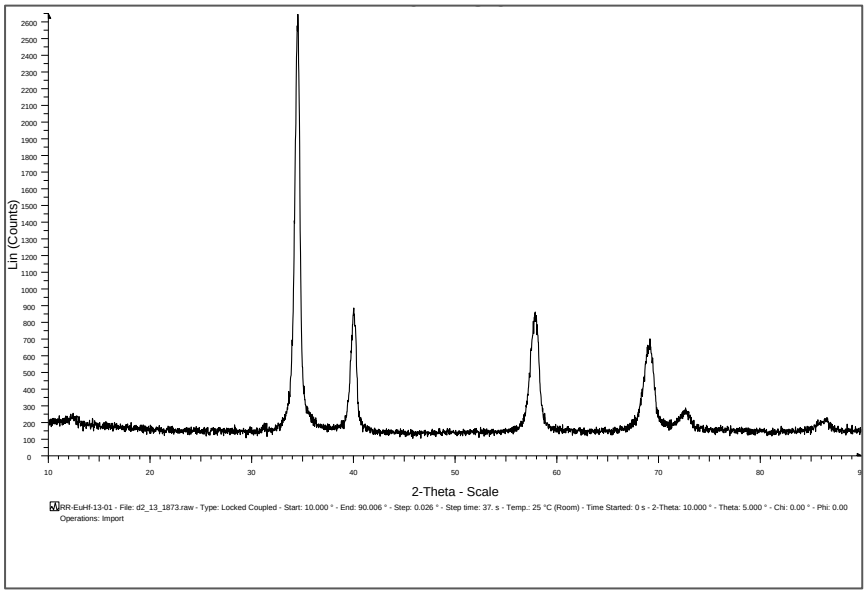


*Figure 4-15: A CoKα2 Pattern for $Eu_2Hf_2O_7$*

Careful observation of each pattern in the variable temperature measurement, coupled with comparison of each pattern to the previously measure pattern, indicated that there was no observable phase transition as the temperature was increased. However, there was a slight shift in the peaks towards lower angles, implying a positive thermal expansion. Most importantly, several peaks did emerge upon cooling back down to 30°C. These peaks may have been caused by contamination from corrosion within the XRK 900's furnace chamber. The peaks can be seen as the last pattern in grey in figure 4.16.

* Miller and Billing, unpublished results

Supporting information may be obtained from Dr Stuart F. Miller; stuart.miller@wits.ac.za

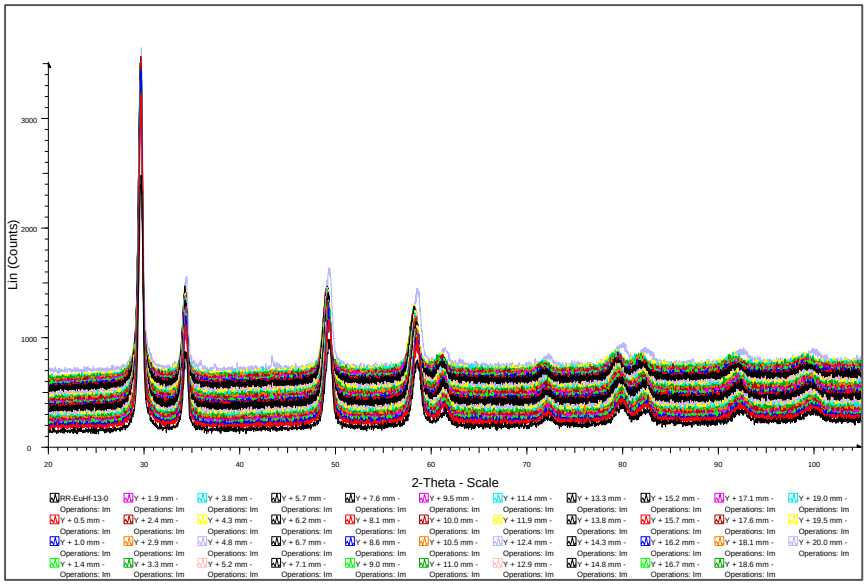


*Figure 4-16: A cascading plot of diffraction patterns obtained from a VT-PXRRD experiment for $Eu_2Hf_2O_7$.*

In a separate pattern of the remaining material (after the variable temperature measurement was taken using $CoK_{\alpha 2}$ radiation) as indicated in figure 4.17, one can see that the peaks observed in the 30°C pattern of the variable temperature measurement are not apparent. This arose from the smaller amount of sample used in the post variable temperature experiment, hence lowering the intensity of the supercell reflections. The only difference between the D2 patterns of the initial sample and after the heat treatment is a slight intensity difference, which can be ascribed to the amount of sample available for measurement. The second measurement used far less sample on a zero-background holder, hence providing less material for scattering, describing the lower intensity. There was also a loss of the slight, broad peak at 12.317°2θ.

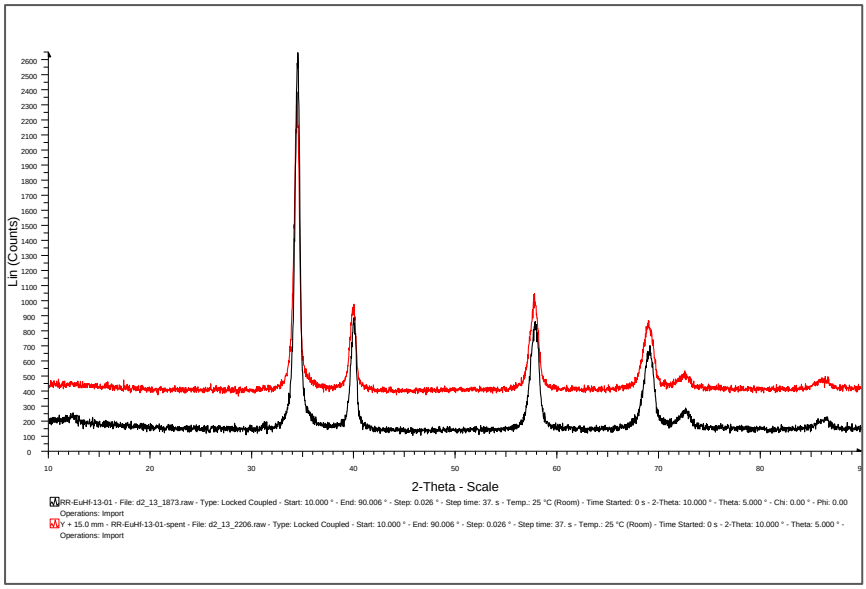


*Figure 4-17: A comparison of diffraction patterns taken before and after the VT-PXRD experiment for $Eu_2Hf_2O_7$. Note that the black and red patterns are before and after the experiment respectively. The red pattern has been offset vertically for clarity.*

## Structural observations

The difference plot for Europium hafnate obtained from the Rietveld refinement of CoKα2 (ambient) data indicates a good fit, with some mismatch describing the tip of each peak, with the largest discrepancy occurring for the principle peak

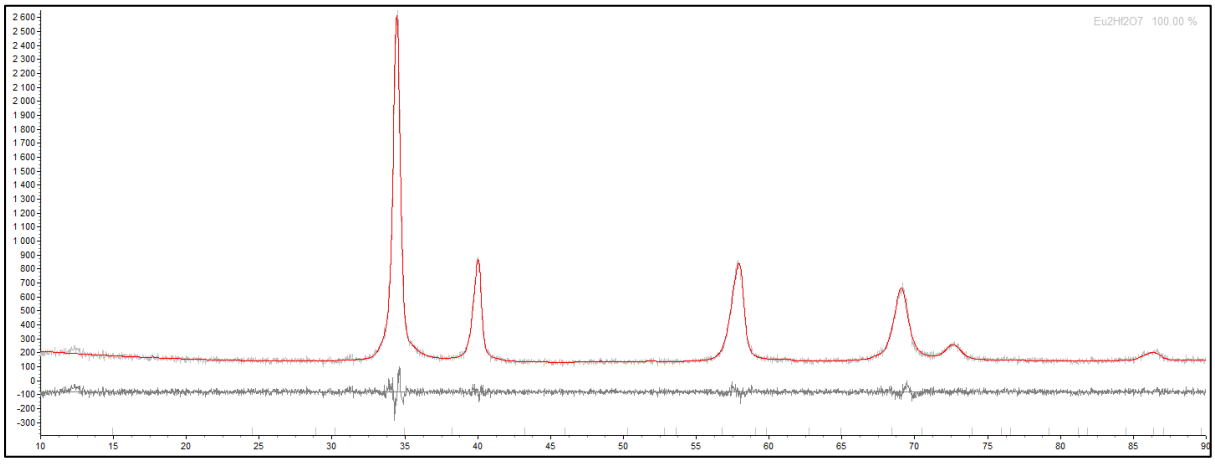


*Figure 4-18: The $CoK_{\alpha 2}$ difference plot of $Eu_2Hf_2O_7$ obtained after completion of the Rietveld refinement procedure discussed in section 2.4.3.*

The model chosen for the 30°C $CuK_{\alpha 2}$ pattern, obtained from the VT-PXRD experiment for europium hafnate was not capable of describing the super lattice peaks of the pyrochlore. This is evident in figure 4.19, where the software has calculated intensity for the super lattice peaks when they were not intense enough to be measured. However, the positions of the major peaks remain precise, and hence the lattice parameter information remains precise

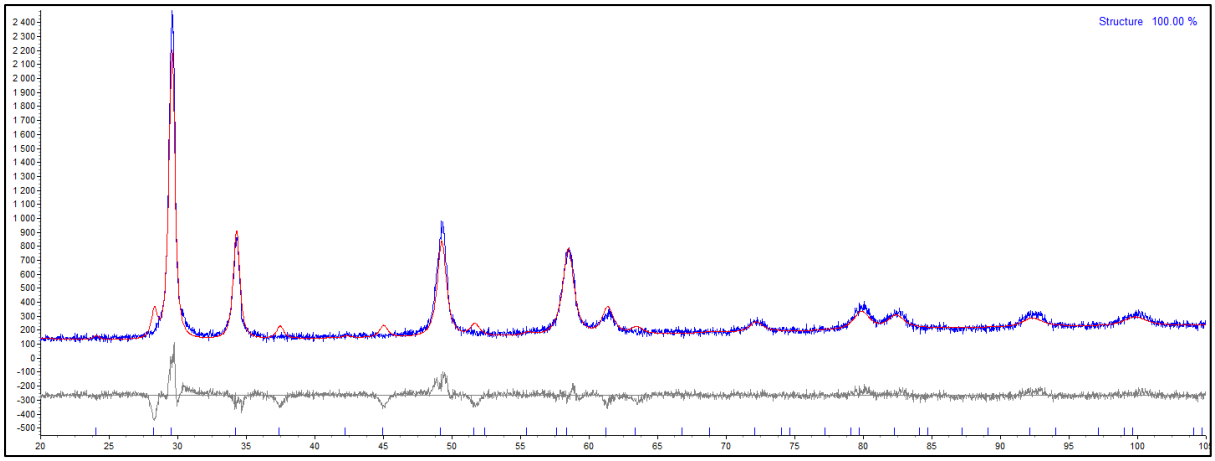


*Figure 4-19: The $CuK_{\alpha 2}$ difference plot of $Eu_2Hf_2O_7$ obtained after completion of the Rietveld refinement procedure discussed in section 2.4.3.*

The choice of starting model for the Rietveld refinement included the use of the pyrochlore phase in accordance to the observations in the phase analysis described previously, despite the missing pyrochlore peaks (hidden by the background signal). The pyrochlore phase of europium hafnate displayed a positive thermal expansion as can be seen by figure 4.20. The lattice expansion followed a polynomial based trend over the temperature range from 30 °C to 850 °C. The lattice parameter varies from 10.477(1) Å to 10.515(1) Å over the entire temperature range investigated.

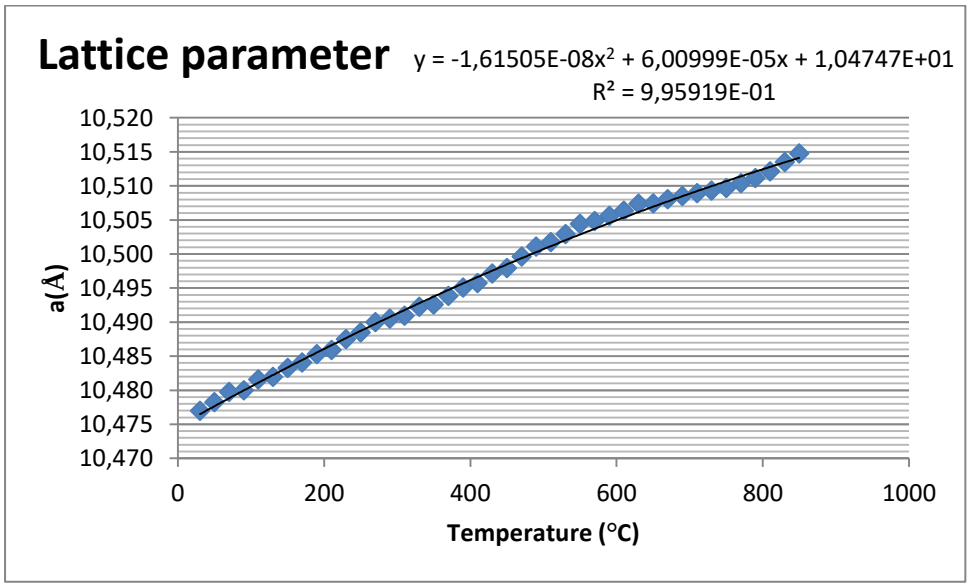


*Figure 4-20: lattice parameter change relative to temperature for $Eu_2Hf_2O_7$.*

The goodness of fit has been plotted against temperature in figure 4.21, which appears to fluctuate about a value of 1.950. It is incorrect to attempt to fit a function to this data due to the fluctuation. The goodness of fit varied from a maximum of 2.06 at 70 °C and a minimum of 1.79 at 30 °C. Although a fluctuation of the goodness of fit can be seen, all the values lie within an acceptable range for this value implying that there is little discrepancy between the calculated mode and the observed data.

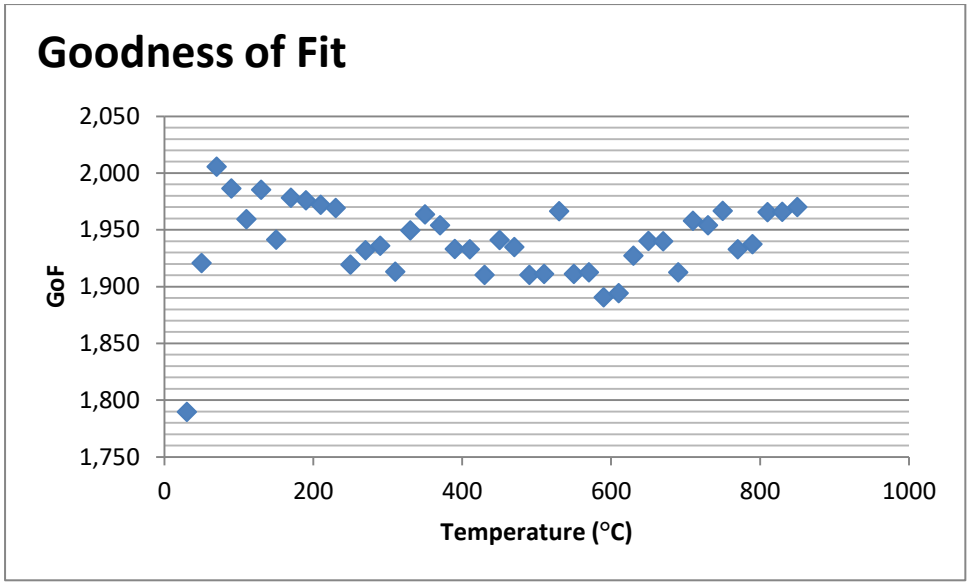


*Figure 4-21: The Goodness of fit relative to temperature for the VT-PXRD sequential Rietveld refinement of $Eu_2Hf_2O_7$ diffraction data.*

The Rwp values relative to temperature can be seen in figure 4.22. From this figure, the Rwp values increased with increasing temperature. However, the values fluctuate significantly with a maximum value of 12.366 at 850 °C and a minimum value of 11.288 at 250 °C. The Rwp trend increases in value from the minimum Rwp until the highest temperature is obtained. This may be indicative of a change in peak shape with temperature, causing more mismatch between the calculated and observed patterns

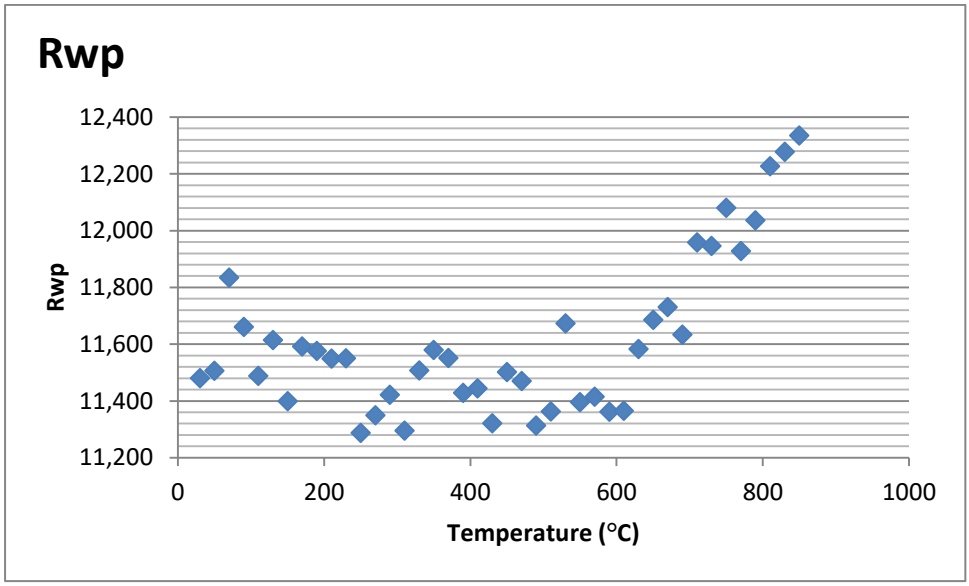


*Figure 4-22: The Rwp values relative to temperature for the VT-PXRD sequential Rietveld refinement of $Eu_2Hf_2O_7$ diffraction data.*

The thermal parameter (Beq) for europium on site 16d (*F* d-3mZ) has increased to the imposed limit in Topas, as can be seen in figure 4.23. The limit was set to ensure refinement stability. As a result, the trend line has been omitted.

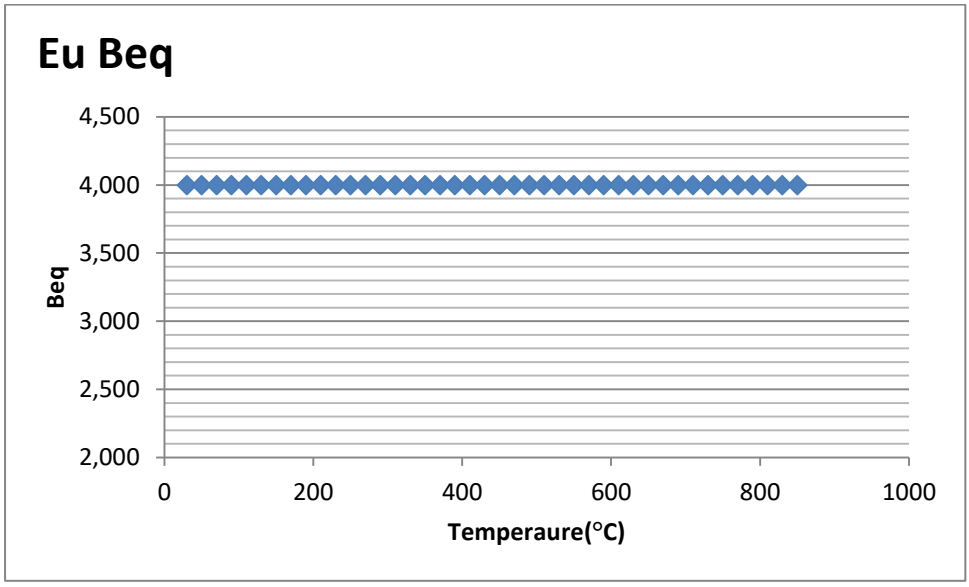


*Figure 4-23: The Europium Beq values relative to temperature for the VT-PXRD sequential Rietveld refinement of $Eu_2Hf_2O_7$ diffraction data.*

The thermal parameter for the hafnium atom at site 16c (*F* d-3mZ), plotted against temperature in figure 4.24, follows a similar trend to that of europium, where the Beq values have lowered to the lower limit imposed in Topas for refinement stability.

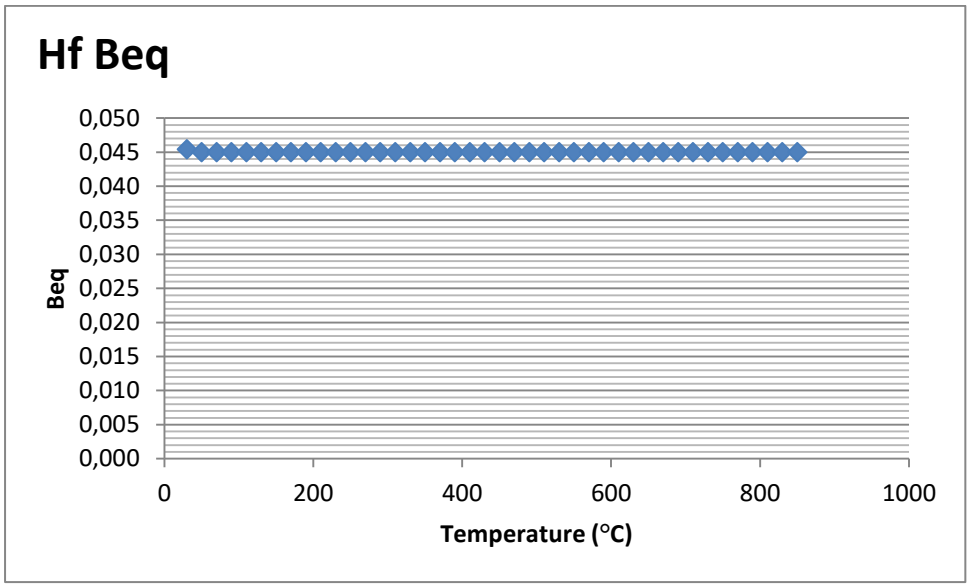


*Figure 4-24: The Hafnium Beq values relative to temperature for the VT-PXRD sequential Rietveld refinement of $Eu_2Hf_2O_7$ diffraction data.*

The thermal parameter for the oxygen atom on position 48f (*F* d-3mZ), plotted against temperature in figure 4.25. Again we see the values increase to the refinement limits.

Figure 4.26 illustrates the thermal parameters of the 8b (*F* d-3mZ) oxygen atom relative to temperature. Again, the refinement has taken these values to the imposed limits.

Figure 4.27 illustrates the change in the position of the 48f oxygen parameter relative to temperature. The values fluctuate over the entire temperature range between x = 0.468 at 310 °C and x= 0.474 at 710°C. The difference between the minimum and maximum values for the X position was 0.006, a value of questionable accuracy. As seen in figure 4.27, although there is fluctuation, the X position values do adhere to an increasing trend line.

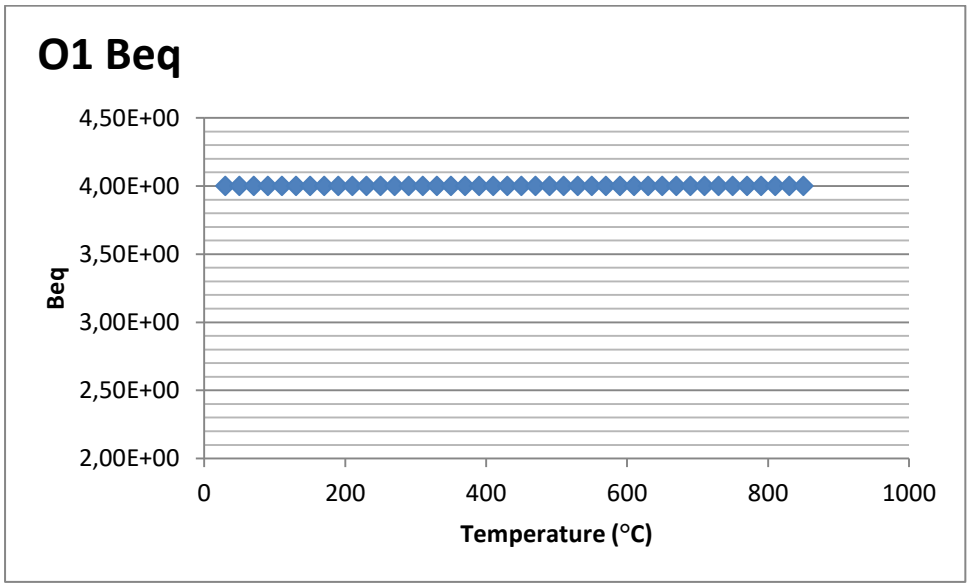


*Figure 4-25: The oxygen Beq values relative to temperature for the VT-PXRD sequential Rietveld refinement of $Eu_2Hf_2O_7$ diffraction data.*

Figure 4.28 is the plot of the coefficient of thermal expansion against temperature for the defect fluorite phase of europium hafnate. The data follows the linear trend given as $\alpha = 3.03 \times 10^{-11}T + 6.58 \times 10^{-6}$. The average of the data taken across the experimental temperature range was 6.60ppm.°C$^{-1}$ which is similar the CTE determined if a linear function was used to fit the lattice parameter data.

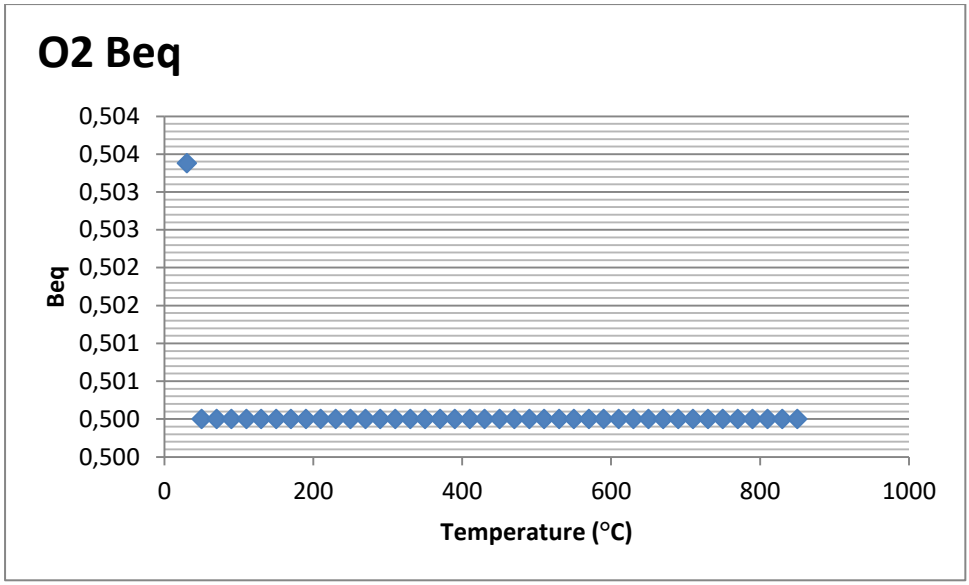


*Figure 4-26: The thermal parameter of the 8f oxygen of europium hafnate pyrochlore relative to temperature.*

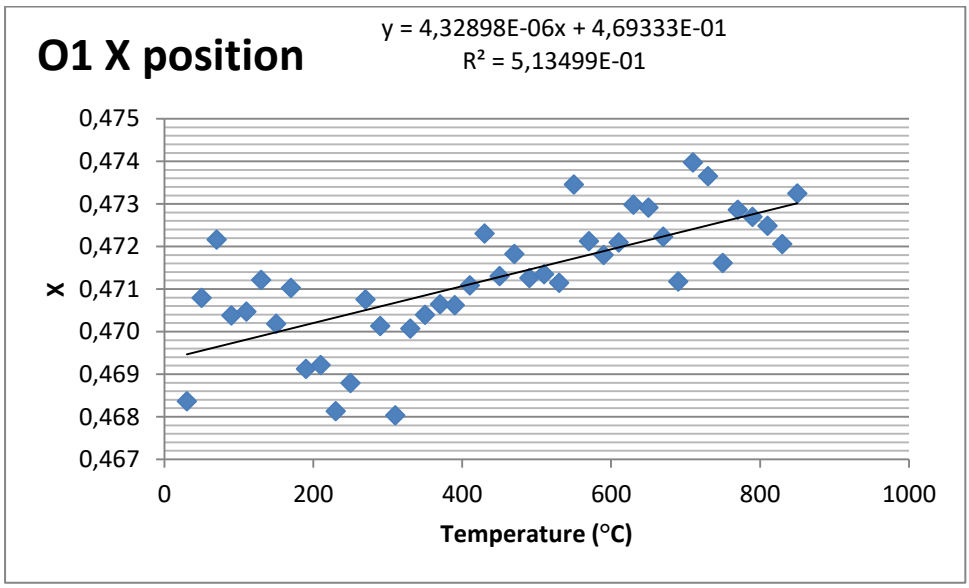


*Figure 4-27: the X position of the 48f oxygen atom of europium hafnate pyrochlore relative to temperature. Note that low resolution from the nanoparticulate nature of the material has caused in accurate modelling of the exact position.*

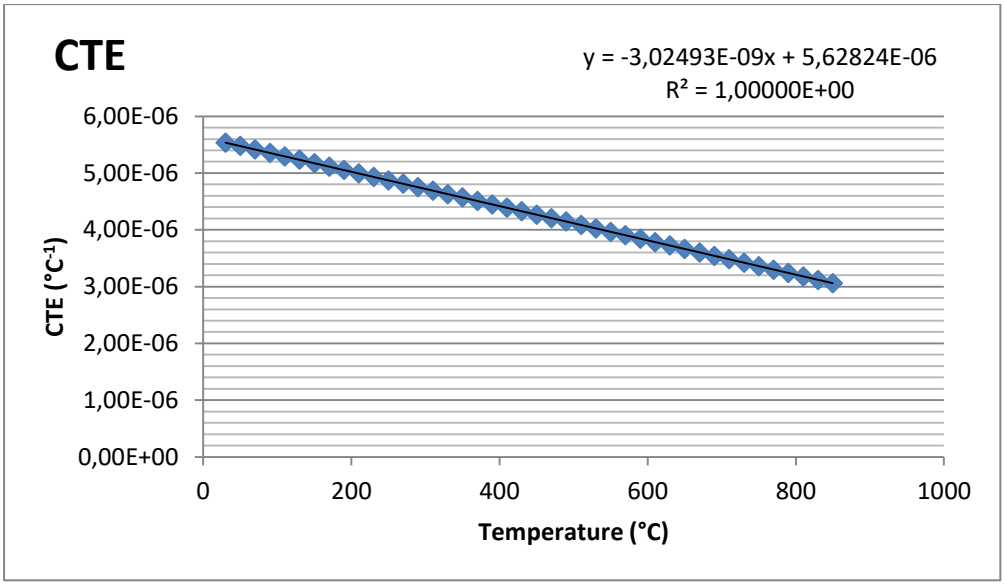


*Figure 4-28: The Coefficient of thermal expansion values relative to temperature for the VT-PXRD sequential Rietveld refinement of $Eu_2Hf_2O_7$ diffraction data.*

### 4.1.3. Gadolinium Hafnate defect fluorite refinement results

#### Phase analysis

In a peak matching analysis of a $CoK_{\alpha 2}$ pattern of $Gd_2Hf_2O_7$, the resulting pure phase was determined to be pyrochlore in nature. The missing pyrochlore superstructure peaks were obscured by the high background observed in the diffraction pattern. The presence of the pyrochlore phase was determined in a separate study by Miller *et al*[*]. The amorphous scattering indicated in figure 4.29 appears near the (111) reflection associated with the pyrochlore phase, although the peak is not resolved enough to provide refinement information.

[*] Miller and Billing, unpublished results

Supporting information may be obtained from Dr Stuart F. Miller; stuart.miller@wits.ac.za

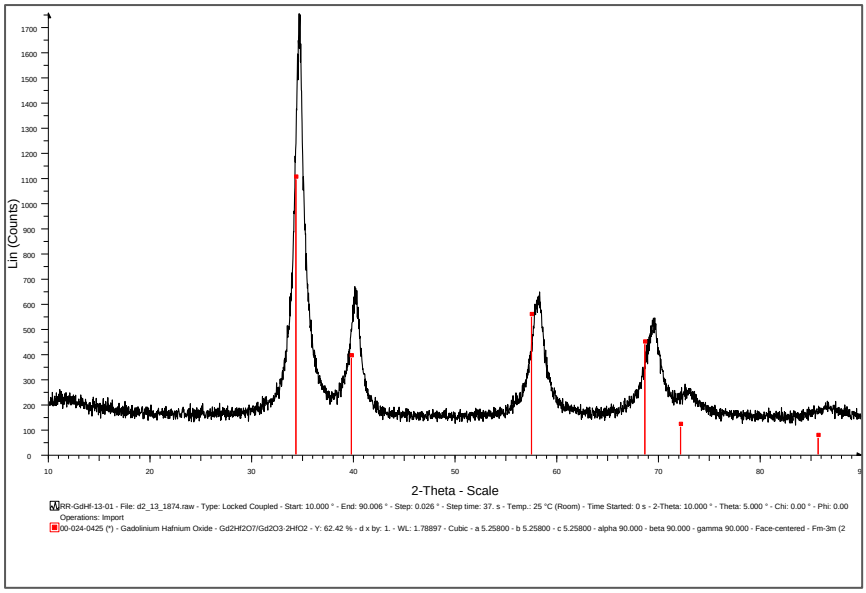


*Figure 4-29: A CoKα2 Pattern for $Gd_2Hf_2O_7$.*

Carefully observing each pattern of the variable temperature measurement the material indicated that no phase transitions had noticeably taken place, and that the material remained as a pyrochlore throughout the whole temperature range. There was a slight shift in the peaks towards lower angles as temperature increased, implying a positive thermal expansion. Observing the patterns taken at 30°C before and after heating indicates that there was no significant change to the substance upon heating. This can be seen in figure 4.30, where the two 30°C patterns are the first black pattern and the last grey pattern respectively. The additional peak observed just before 45 °2θ was due to contamination from corrosion of the XRK 900's furnace chamber.

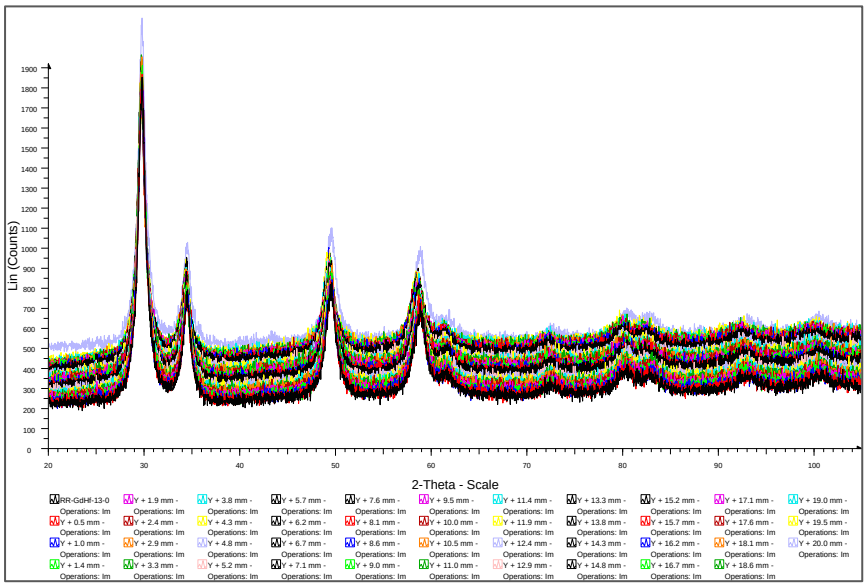


*Figure 4-30: The cascading plot obtained from a VT-PXRD experiment performed on $Gd_2Hf_2O_7$.*

The difference plot obtained from the Rietveld refinement of the $CoK_{\alpha 2}$ pattern (Bruker D2 phaser, ambient temperature) indicated a match between the model and observed data as indicated in figure 4.31. There is a slight mismatch in the heights of each peak arising from a scaling error.

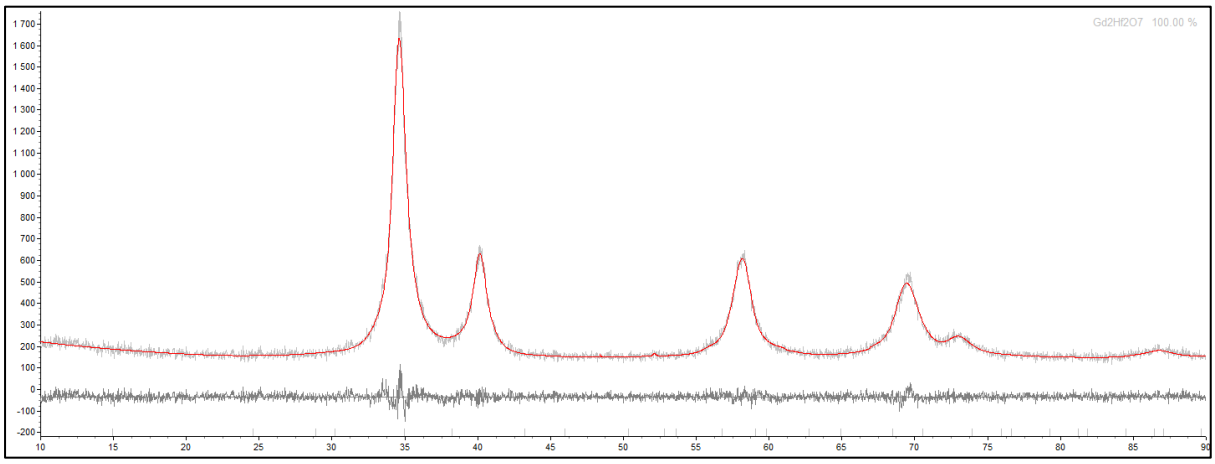


*Figure 4-31: The $CoK_{\alpha 2}$ difference plot of $Gd_2Hf_2O_7$ obtained after completion of the Rietveld refinement procedure discussed in section 2.4.5.*

The difference plot obtained from the Rietveld refinement of the 30°C $CuK_{\alpha 2}$ pattern (Bruker D8) obtained from the VT-PXRD experiment for gadolinium hafnate has some errors, as illustrated in figure 4.32. A calculated peak at approximately 24 °2θ is not present in the observed pattern, and the remaining issues relate to the height of the calculated peaks. However, the peak positions are still adequately described to determine the lattice parameter

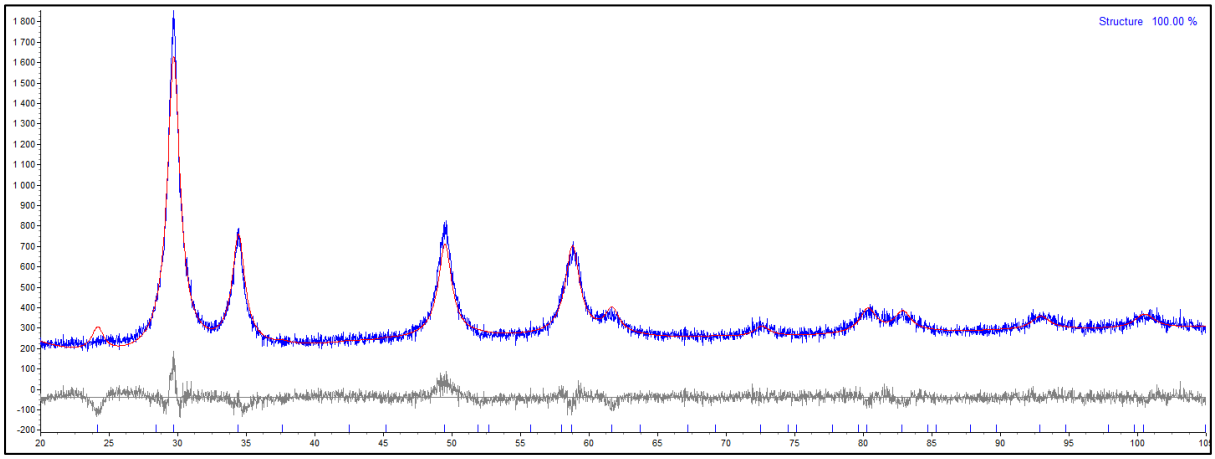


*Figure 4-32: The $CoK_{\alpha 2}$ difference plot of $Gd_2Hf_2O_7$ obtained after completion of the Rietveld refinement procedure discussed in section 2.4.5.*

The lattice parameter followed a slightly varying polynomial fit relative to temperature. The slight discrepancies of the data arose from the poor resolution of the pattern, where the wide diffraction peaks caused by the small domain sizes of the material limited the precision of the peak positions

between refinements. The lattice parameter and volume follow a curving trend line as can be seen in figures 4.33 and 4.34 respectively. This curved trend is best described using a second order polynomial to fit the data. Both plots have very similar $R^2$ values of 0.99, implying an accurate fit of the data. Both plots indicate an increase of dimensional lengths relative to temperature. The lattice parameter data was fitted with the following polynomial function: $a = -9.157 \times 10^{-9}T^2 + 5.5619 \times 10^{-5} + 10.417$.

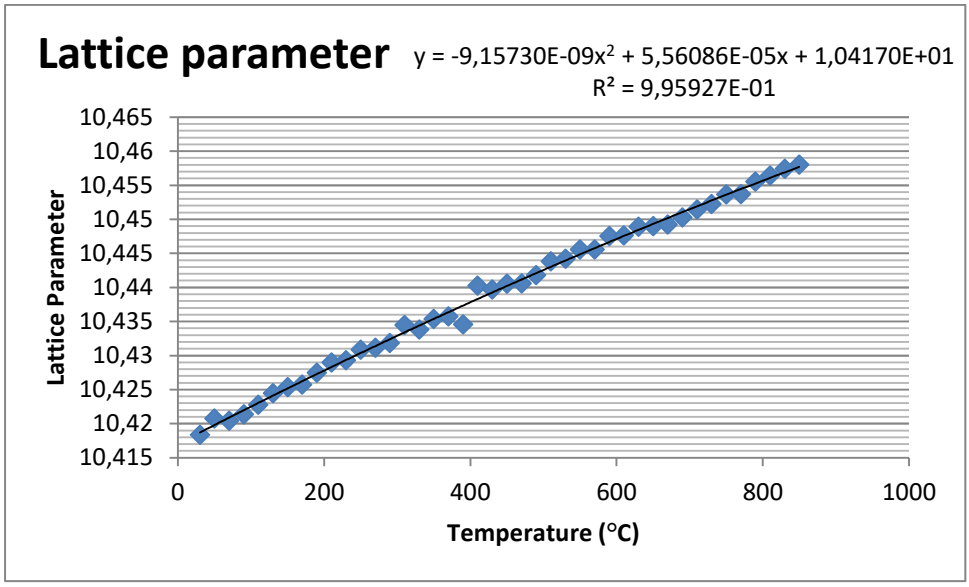


*Figure 4-33: The lattice parameter change relative to temperature for the VT-PXRD sequential Rietveld refinement of $Gd_2Hf_2O_7$ diffraction data.*

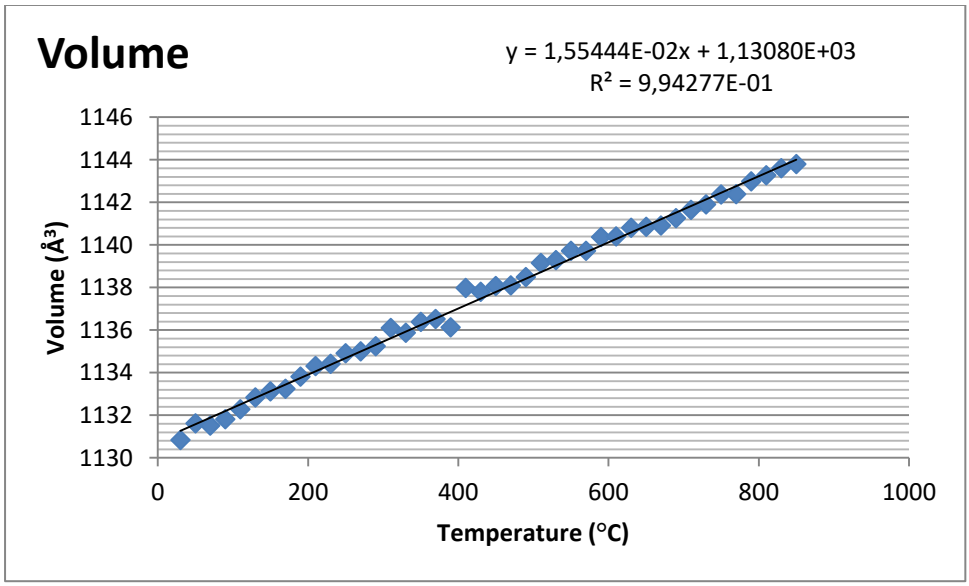


*Figure 4-34: The volume change relative to temperature for the VT-PXRD sequential Rietveld refinement of $Gd_2Hf_2O_7$ diffraction data.*

The goodness of fit plot, given in figure 4.35, indicates the low values of the goodness of fit across the entire temperature range. These values range from 1.22 at 590 °C to 1.34 at 250 °C, with the data entries fluctuating to various degrees across the entire temperature range.

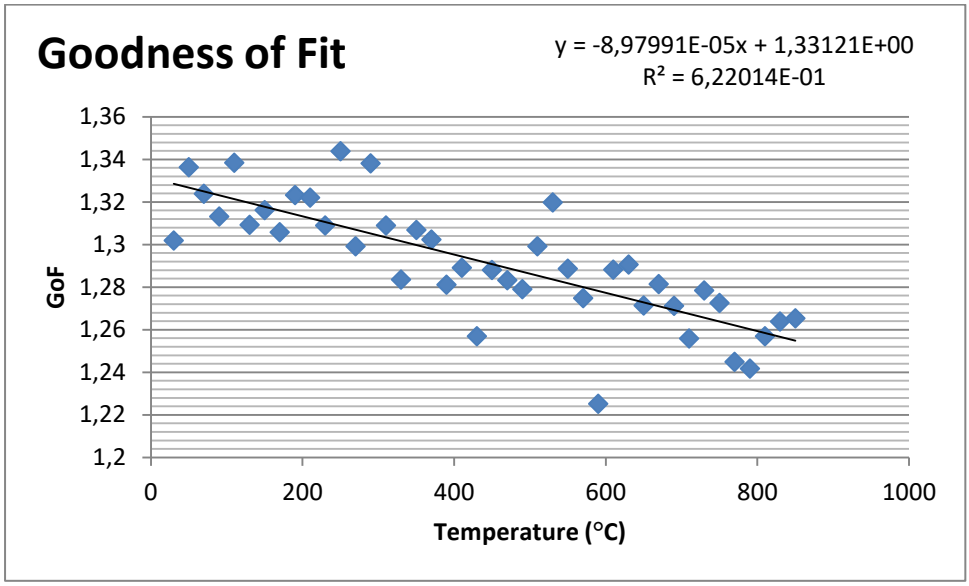


*Figure 4-35: The goodness of fit relative to temperature for the VT-PXRD sequential Rietveld refinement of $Gd_2Hf_2O_7$ diffraction data.*

The thermal parameters of Gd, Hf, O1 (48f) and O2 (8b) are illustrated in figures 4.36 to 4.39. Figures 4.36 and 4.37 indicate an increase in the Beq values relative to temperature for the two metals respectively, although there is a significant amount of scattering of the data points about the trend line in each case. The trend for hafnium follows a polynomial fit over the entire range, whereas the gadolinium Beq values only follow this trend from 290°C. The gadolinium Beq values range from 0.48 at 290°C to 1.715 at 850°C. The hafnium Beq values range from 1.38 at 30°C to 2.44 at 650°C. Figures 4.38 and 4.39, the thermal parameters of the 48f and 8b oxygen atoms relative to temperature respectively, indicate that their refinement values returned immediately to the limits set for refinement stability, although the first refinement at 30°C remained close to the initial starting value obtained from Shlykhtina *et al* (Shlyakhtina, et al., 2007). Similarly, the X position of the 48f oxygen was reduced to the limit imposed for refinement stability.

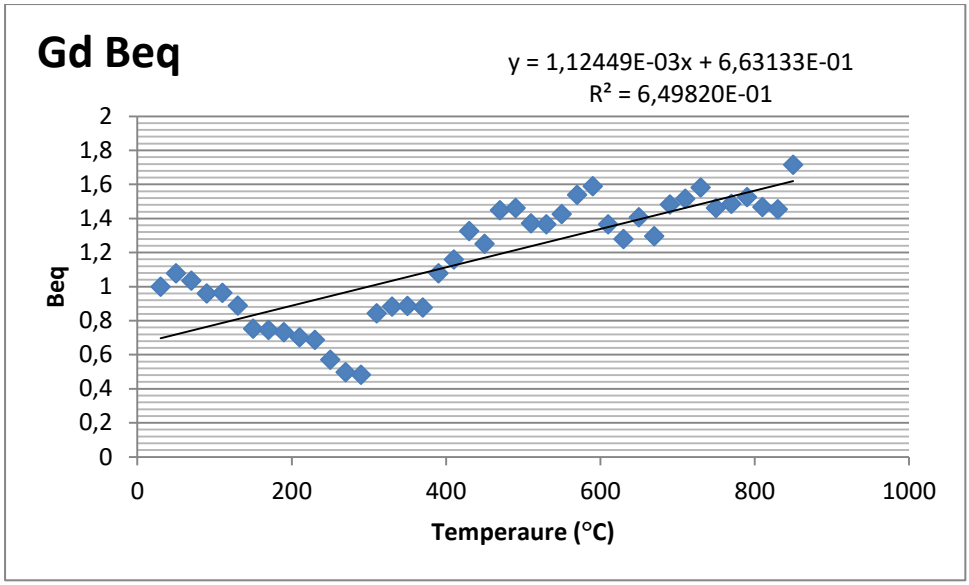


*Figure 4-36: The gadolinium Beq Value relative to temperature for the VT-PXRD sequential Rietveld refinement of $Gd_2Hf_2O_7$ diffraction data.*

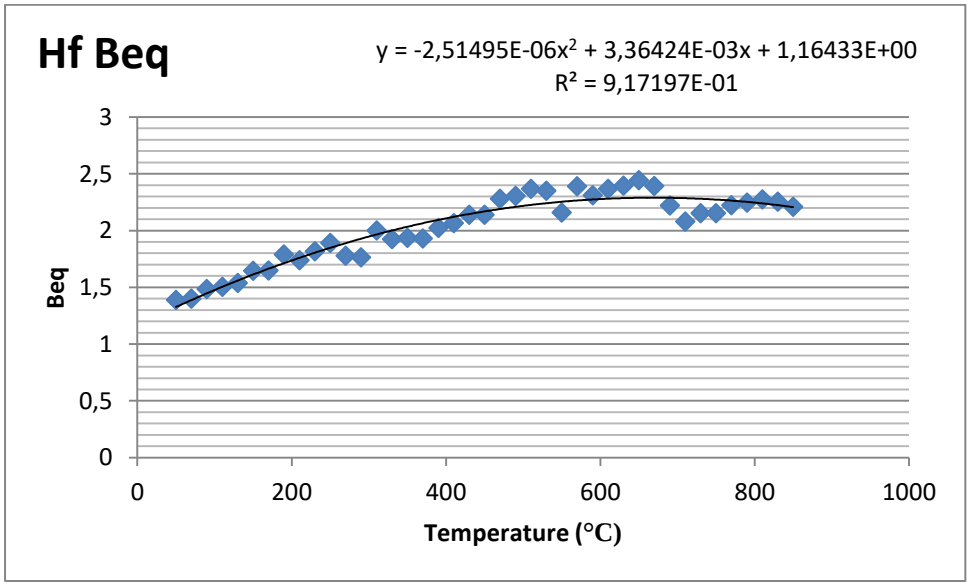


*Figure 4-37: The hafnium Beq value relative to temperature for the VT-PXRD sequential Rietveld refinement of $Gd_2Hf_2O_7$ diffraction data.*

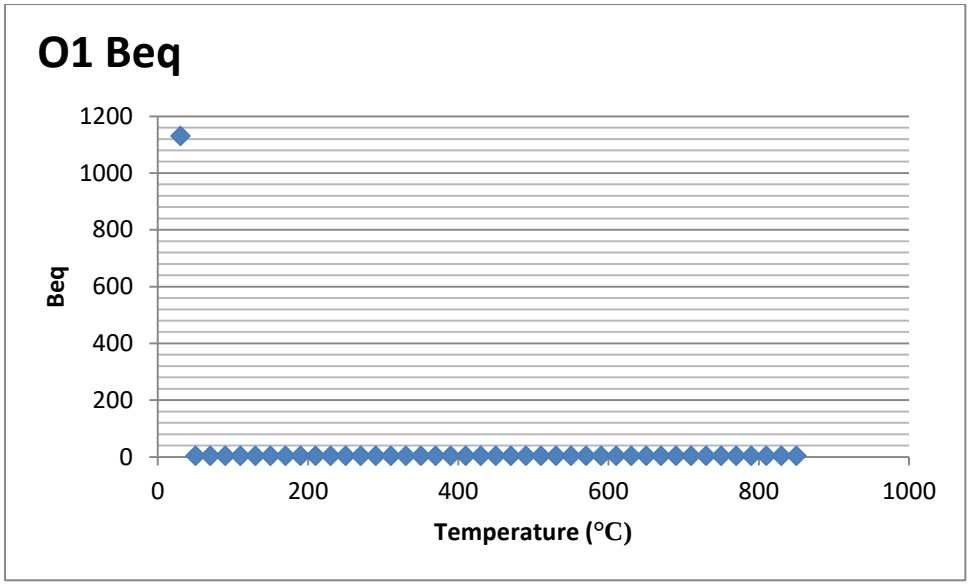


*Figure 4-38: The oxygen Beq value relative to temperature for the VT-PXRD sequential Rietveld refinement of $Gd_2Hf_2O_7$ diffraction data.*

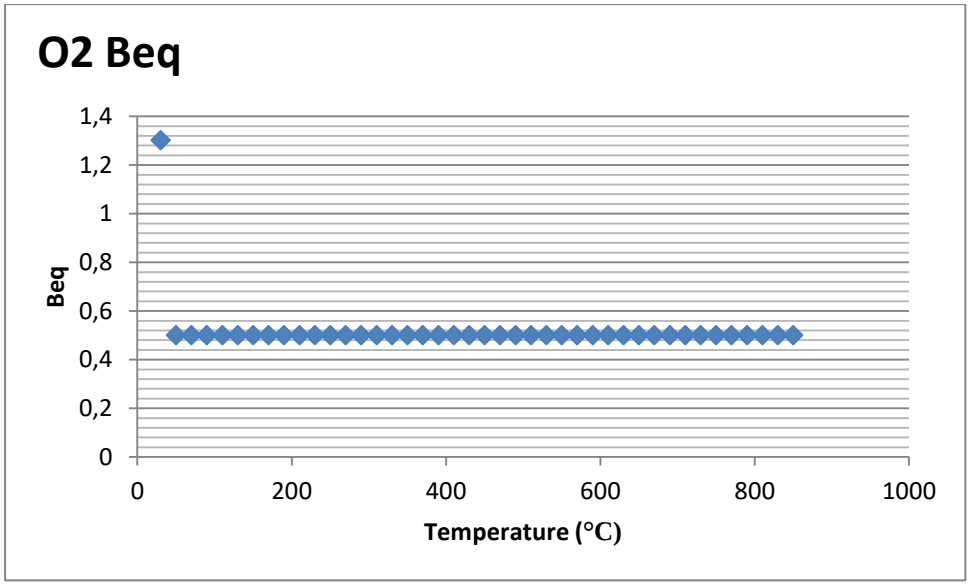


*Figure 4-39: The thermal parameters of the 8f oxygen relative to temperature for gadolinium hafnate pyrochlore.*

The X position for the 48f oxygen atom behaved in a similar fashion to the oxygen Beq values in that it reduced to the imposed limits set in Topas.

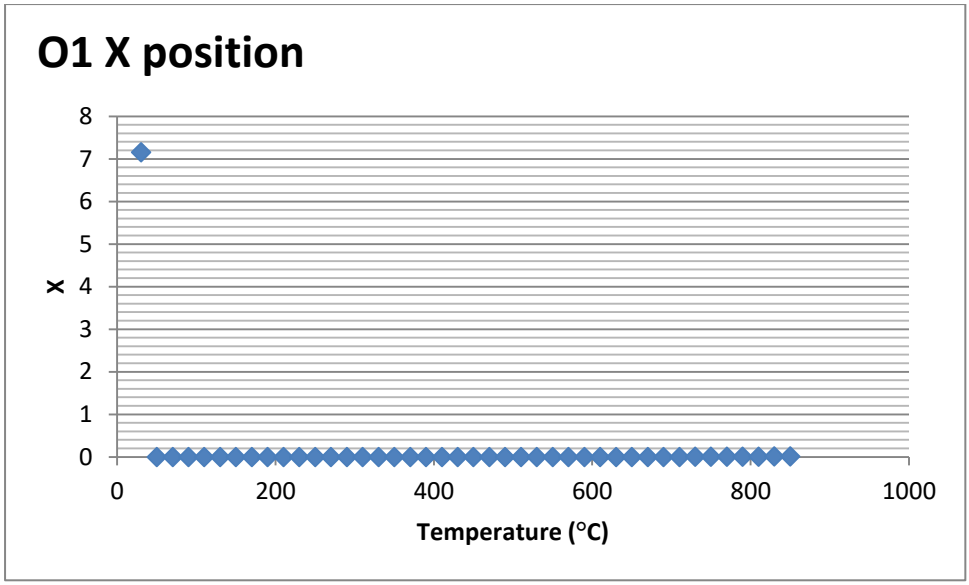


*Figure 4-40: the x positon of the 48f oxygen atom of gadolinium hafnate pyrochlore.*

Figure 4.41 gives the plot of the coefficient of thermal expansion for the gadolinium hafnate pyrochlore. The trend shows a linear decrease in the value of the coefficient with increasing temperature, with a minimum of 3.92 ppm. $°C^{-1}$ at 850 °C and a maximum of 5.39 ppm. $°C^{-1}$ at 30 °C. The average thermal expansion coefficient over the whole range was 4.66 ppm.$°C^{-1}$.

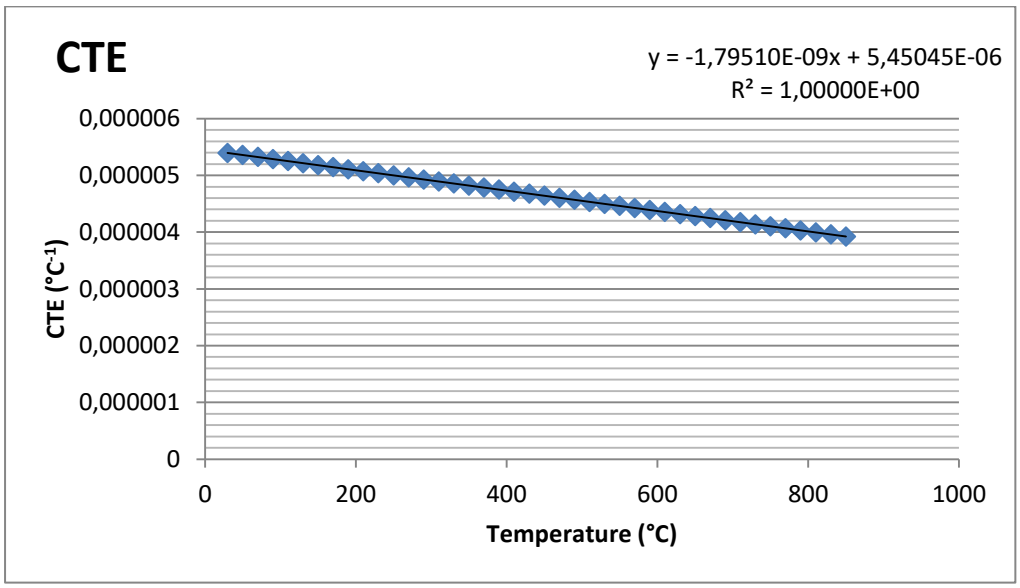


*Figure 4-41: The coefficient of thermal expansion relative to temperature for the VT-PXRD sequential Rietveld refinement of $Gd_2Hf_2O_7$ diffraction data.*

### 4.1.4. Yttrium hafnate

#### Phase analysis

A comparison between patterns taken using $CoK_{\alpha 2}$ radiation *ex situ* from before and after a variable temperature measurement (figure 4.42) indicate that $Y_2Hf_2O_7$ does not undergo permanent phase change from exposure to a heating regime between 30 and 850°C. Similarly, by observing each pattern from the variable temperature measurement of the material, and comparing each pattern to the pattern of the previous temperature, one can confirm that no new phase occurred during the heating regime.

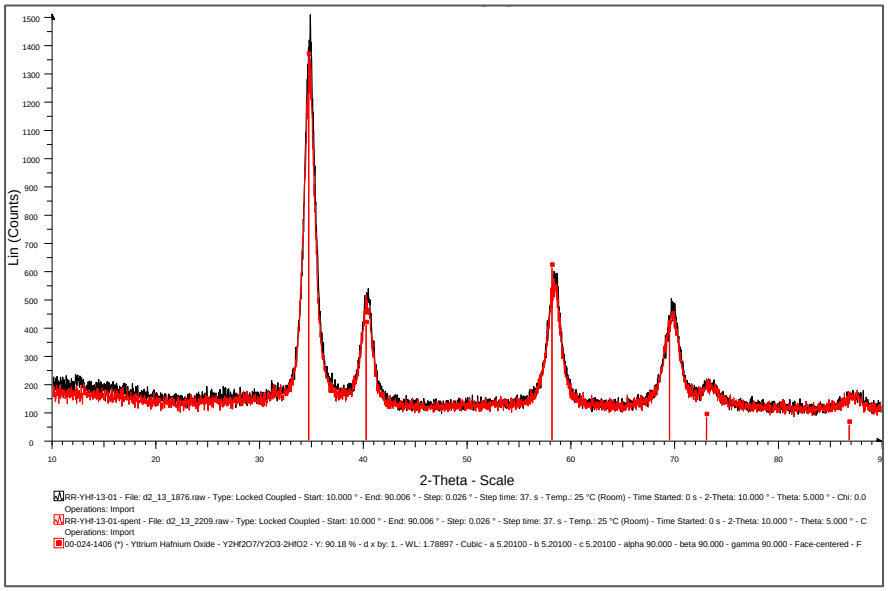


*Figure 4-42: The $CoK_{\alpha 2}$ diffraction patterns of $Y_2hf_2O_7$ taken before and after the VT-PXRD experiment, where the black pattern was taken before and the red pattern was taken after the experiment.*

It is important to note that there was a slight shift in the peaks of the VT patterns towards lower angles, implying a positive thermal expansion. A similar trend can be observed in the cascading plot of the patterns in figure 4.43.

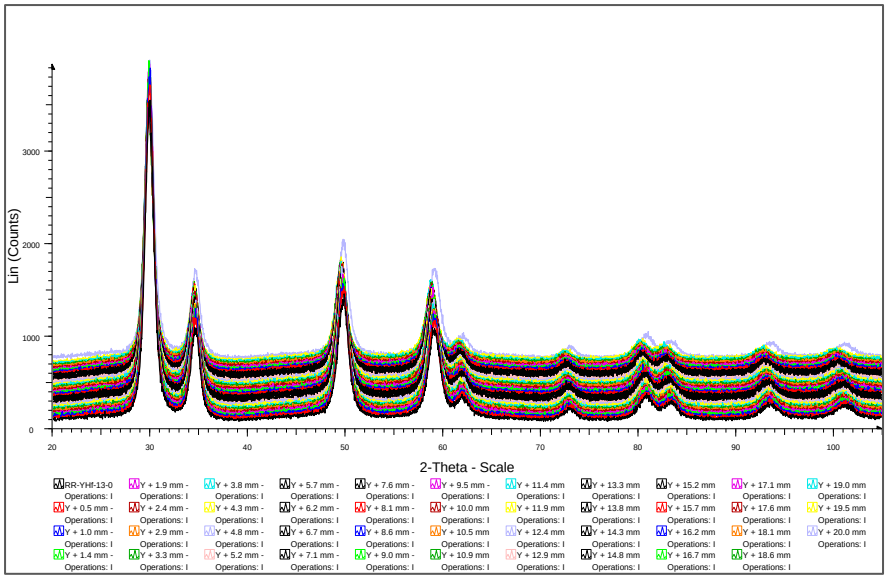


*Figure 4-43: The cascading diffraction patterns of $Y_2Hf_2O_7$ taken during a VT-PXRD experiment.*

A peak searching analysis to determine what phase was present indicated that a defect fluorite phase of $Y_2Hf_2O_7$ was present. However, in the $CoK_{\alpha 2}$ pattern (figure 4.44) taken before the variable temperature measurement, two small diffuse peaks can be observed. These may relate to a pyrochlore phase, although they are difficult to distinguish from the background. From the Raman data from a separate study*, the material was confirmed have a defect-fluorite structure.

* Miller and Billing, unpublished results

Supporting information may be obtained from Dr Stuart F. Miller; stuart.miller@wits.ac.za

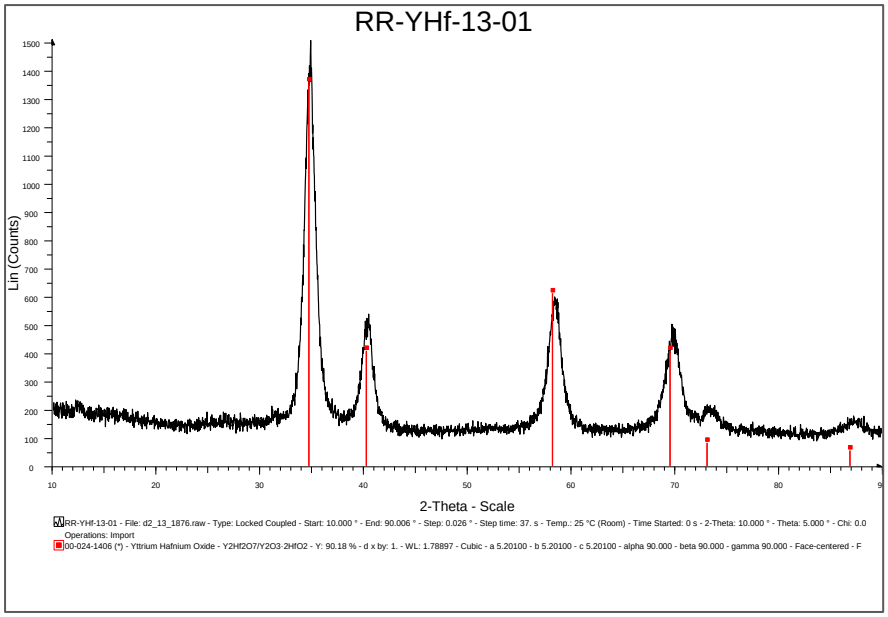


*Figure 4-44: A CoK$_{\alpha 2}$ diffraction pattern of $Y_2Hf_2O_7$ with a peak matched phase indicated by the red lines, coinciding with the experimental pattern. The peak match implies that the material is indeed of a defect-fluorite phase.*

## Structural observations

The Difference plot obtained from the Rietveld refinement of CoK$_{\alpha 2}$ data of yttrium hafnate shows little mismatch, indicating a good model was calculated. There is a slight amount of additional noise at the principle peak, as can be seen in figure 4.45.

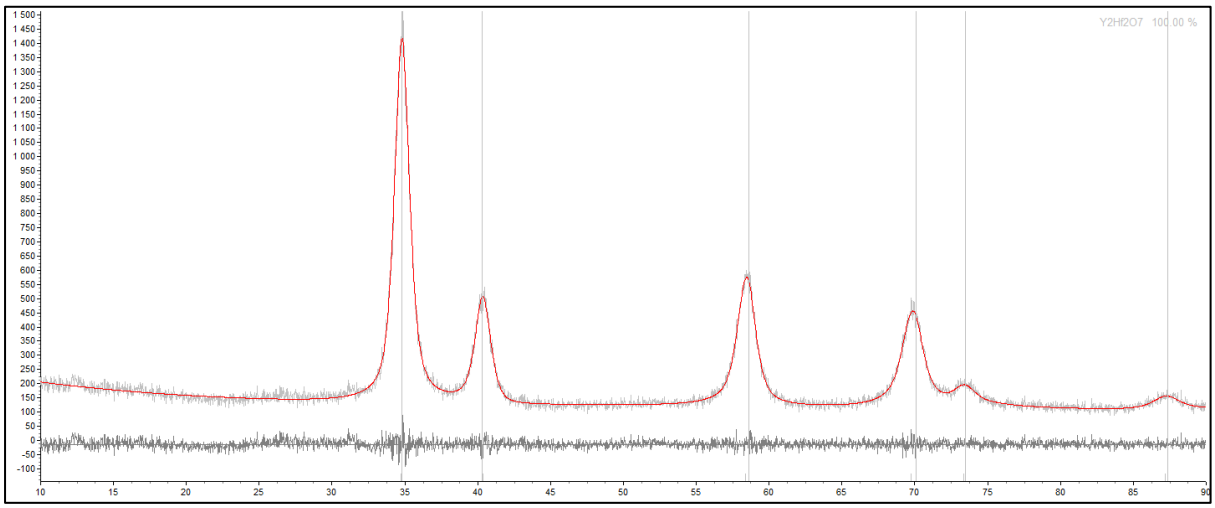


*Figure 4-45: The CoK$_{\alpha 2}$ difference plot of $Y_2Hf_2O_7$ obtained after completion of the Rietveld refinement procedure discussed in section 2.4.4.*

Similarly, the difference plot (figure 4.46) obtained from the 30°C plot from the VT-PXRD experiment for yttrium hafnate yielded a good match, indicating the model of the structure was calculated to a good precision. There are small amounts of noise associated with the larger peaks.

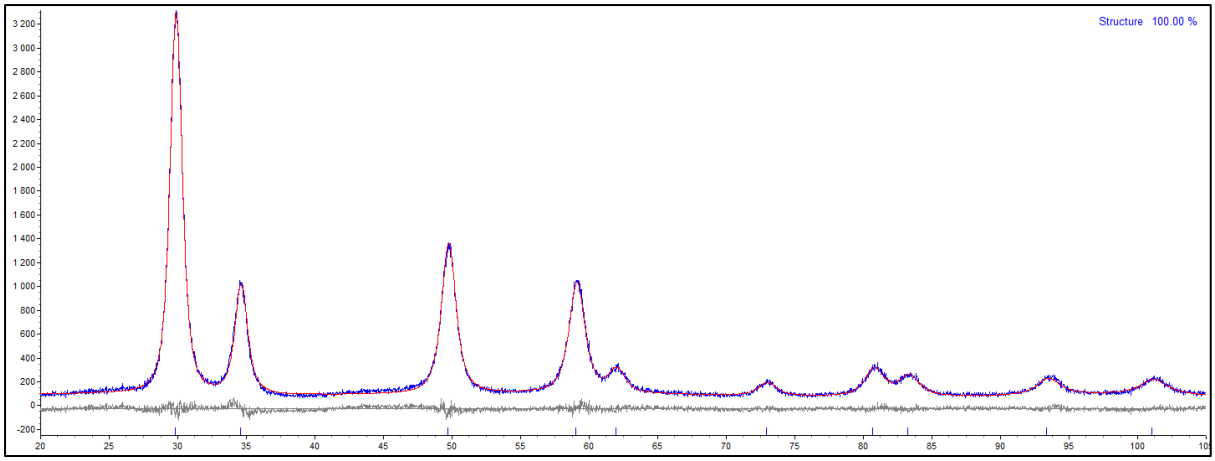


*Figure 4-46: The $CuK_{\alpha 2}$ difference plot of $Y_2Hf_2O_7$ obtained after completion of the Rietveld refinement procedure discussed in section 2.4.4.*

Figure 4.47 is the plot of the lattice parameter of defect fluorite phase of yttrium hafnate against measurement temperature. The data was fitted with a second order polynomial, given by: $a = -5.00 \times 10^{-9}T^2 + 3.11 \times 10^{-5}T + 5.19$. A second order polynomial was chosen as it gave the lowest $R^2$ value (that of 0.99) and it provided more information about the thermal expansion coefficient relative to temperature, which is discussed later in this passage.

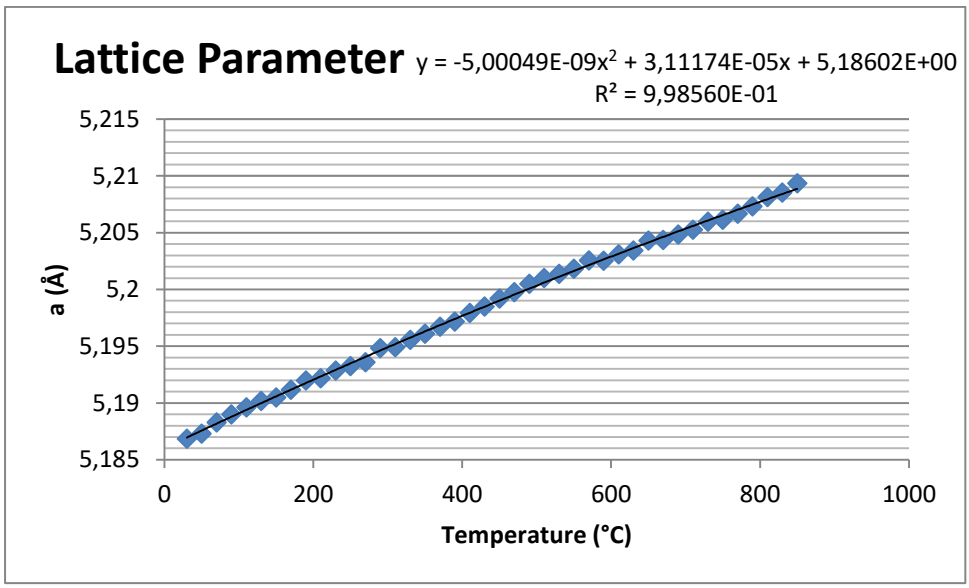


*Figure 4-47: The lattice parameter change relative to temperature for the VT-PXRD sequential Rietveld refinement of $Y_2Hf_2O_7$ diffraction data.*

The figures of merit, the Rwp and the goodness of fit, were plotted against temperature and illustrated in figures 4.48 and 4.49 respectively. Rwp values range from 7.85 at 90°C to a maximum

of 9.73 at 850°C, following a near polynomial trend. The goodness of fit values, however, do not follow the same trend and have a wide range from 1.25 at 290°C to 1.41 at 850°C.

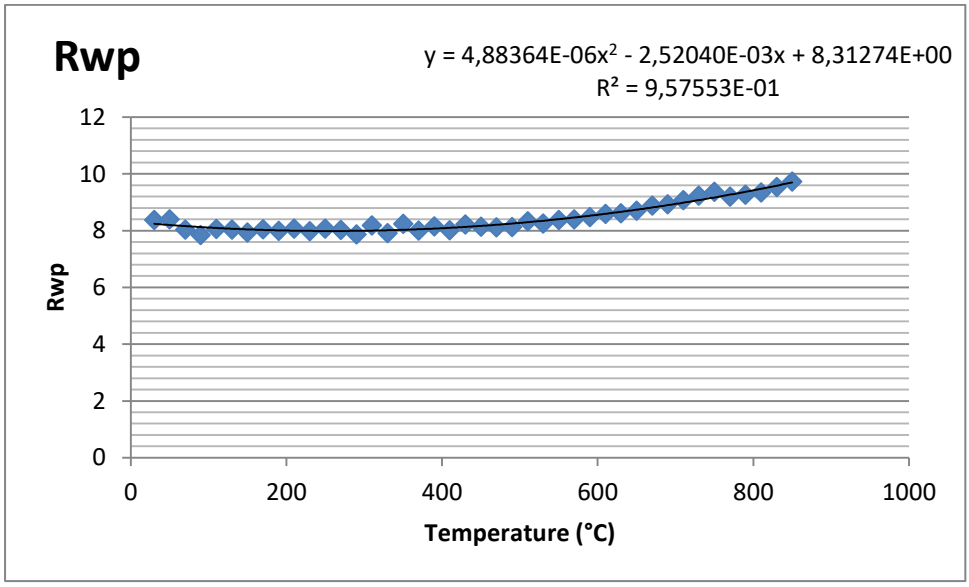


*Figure 4-48: The Rwp values relative to temperature for the VT-PXRD sequential Rietveld refinement of $Y_2Hf_2O_7$ diffraction data.*

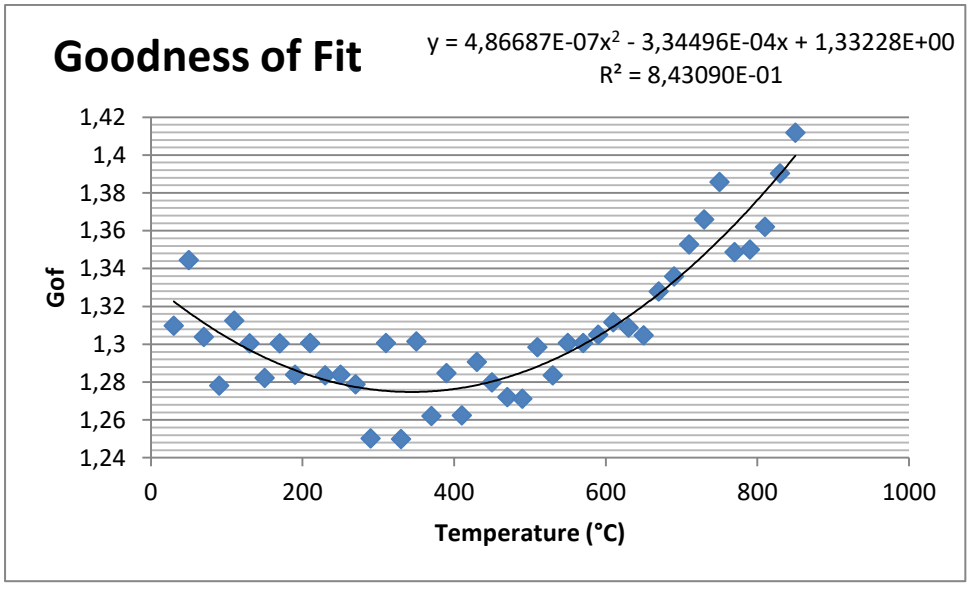


*Figure 4-49: The goodness of fit values relative to temperature for the VT-PXRD sequential Rietveld refinement of $Y_2Hf_2O_7$ diffraction data.*

The thermal parameters (Beq values) of Y, Hf, and O were plotted against temperature in figures 4.50 to 4.52. In each case, there are three peaks and valleys in the plot, which become almost linear after 600°C. This trend was less visible for the case of oxygen as can be seen in figure 4.52.

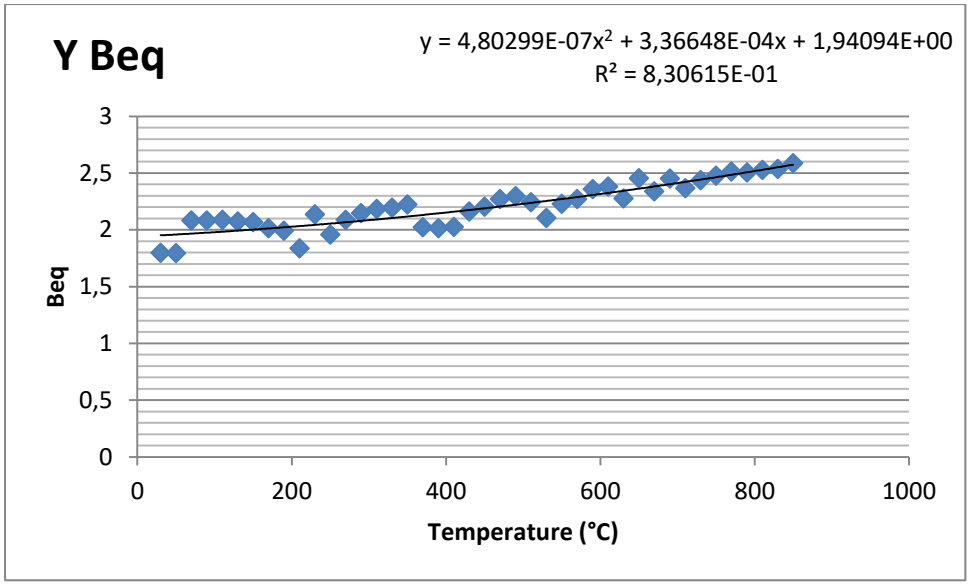


*Figure 4-50: The yttrium Beq values relative to temperature for the VT-PXRD sequential Rietveld refinement of $Y_2Hf_2O_7$ diffraction data.*

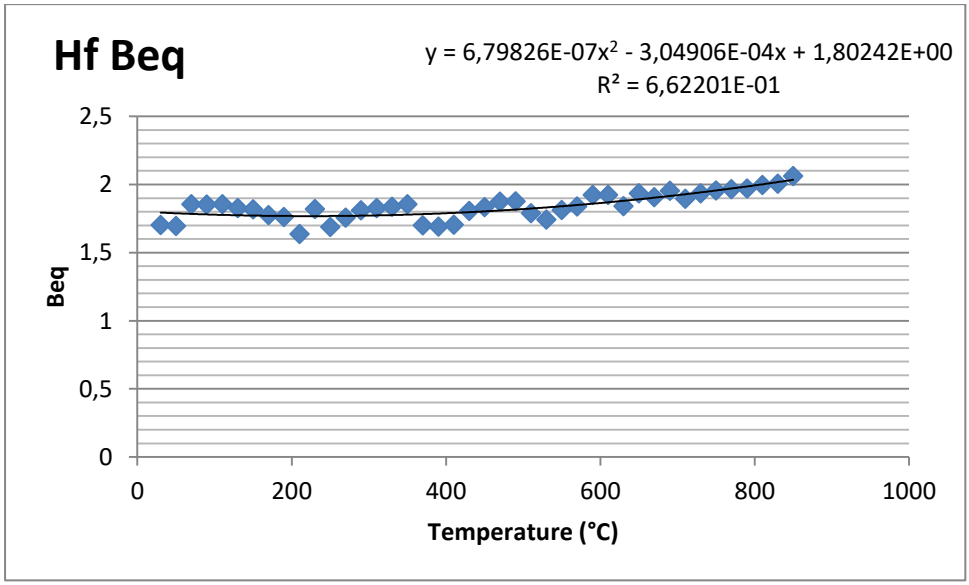


*Figure 4-51: The hafnium Beq values relative to temperature for the VT-PXRD sequential Rietveld refinement of $Y_2Hf_2O_7$ diffraction data.*

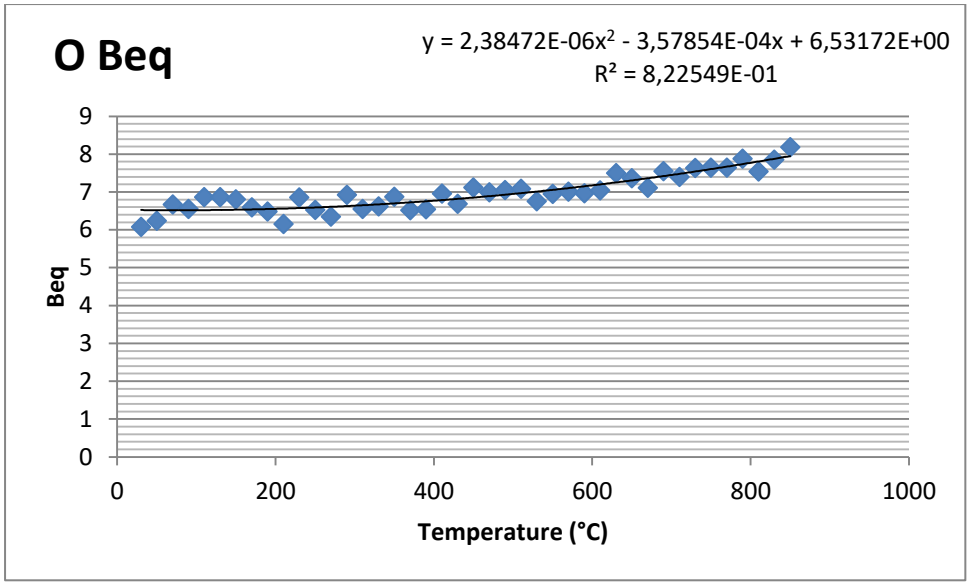


*Figure 4-52: The oxygen Beq values relative to temperature for the VT-PXRD sequential Rietveld refinement of $Y_2Hf_2O_7$ diffraction data.*

The coefficient of thermal expansion, illustrated in figure 4.53, was found to follow the following linear trend: $\alpha = -1.93 \times 10^{-9}T + 6.00 \times 10^{-6}$. The average value of the coefficient of thermal expansion across the entire temperature range was found to be 5.15ppm.°C$^{-1}$, which matches to the CTE determined for a linear fit as opposed to the polynomial fit used here. Within the temperature range of the experiment, the CTE ranges from 4.36ppm.°C$^{-1}$ at 850 °C to 5.94ppm.°C$^{-1}$ at 30°C.

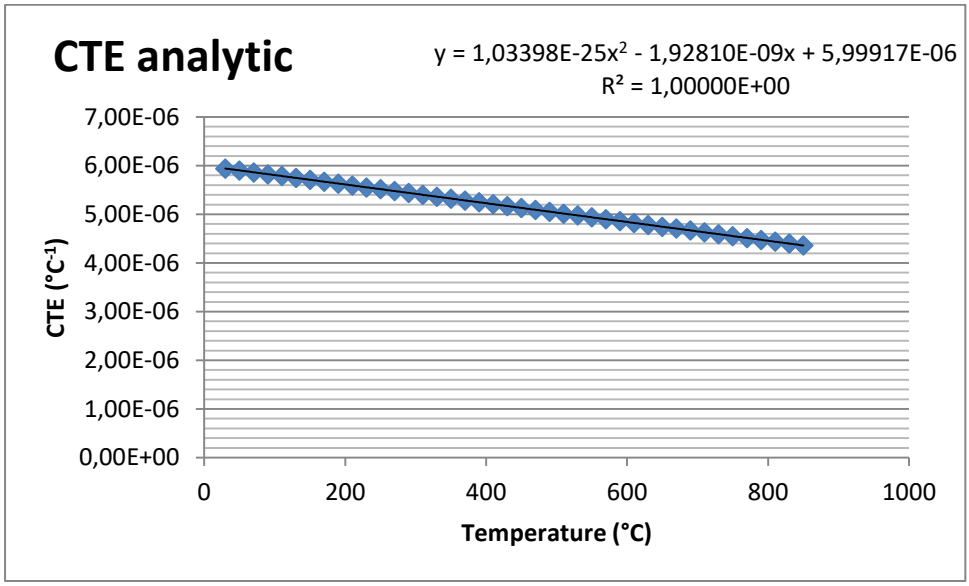


*Figure 4-53: The coefficient of thermal expansion relative to temperature for the VT-PXRD sequential Rietveld refinement of $Y_2Hf_2O_7$ diffraction data.*

## 4.2. Lanthanide zirconates

### 4.2.1. Gadolinium Zirconate

#### Phase analysis

A peak matching analysis on a $CoK_{\alpha 2}$ radiation pattern of $Gd_2Zr_2O_7$, illustrated in figure 4.54, did not directly indicate the presence of the pyrochlore phase, only indicating the peaks shared with the defect fluorite phase. The materials was determine to be a pyrochlore in a separate study*. The lack of the lower intensity peaks throughout the pattern was caused by the low signal to noise ratio. This is immediately observable by the height of the background relative to the most intense peak. The low signal to noise ratio was caused by the poor crystallinity of the sample, evident from the width of the peaks.

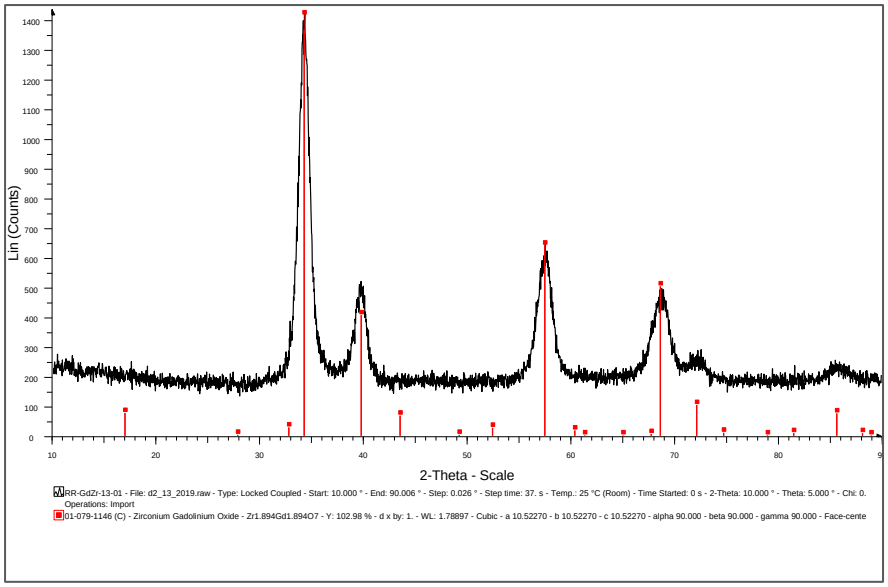


*Figure 4-54: A $CoK_{\alpha 2}$ diffraction pattern of $Gd_2Zr_2O_7$ taken before the VT-PXRD experiment.*

Carefully observing each of the patterns from the variable temperature measurement of the material did not indicate the formation of any new phases over the entire temperature range. This implies temperature stability across the entire experimental temperature range.

* Miller and Billing, unpublished results

Supporting information may be obtained from Dr Stuart F. Miller; stuart.miller@wits.ac.za

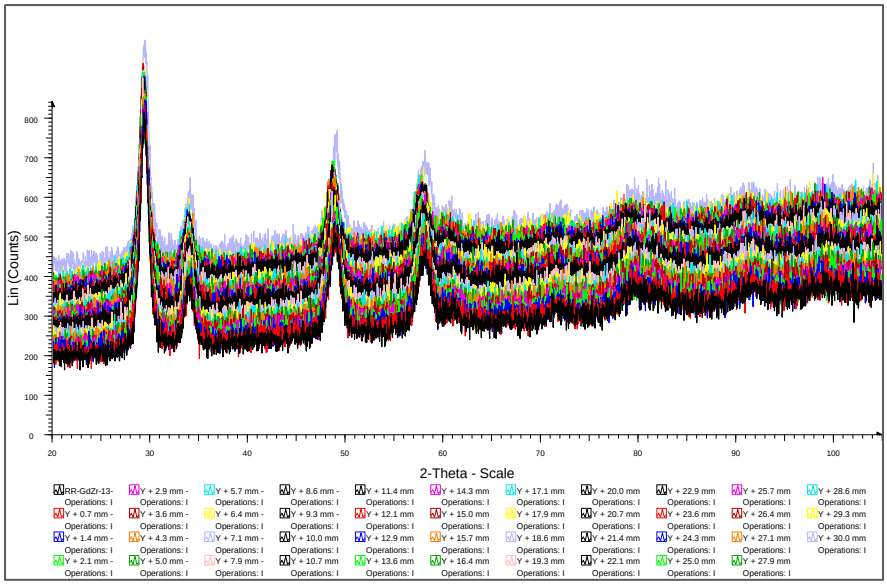


*Figure 4-55: The Cascading diffraction patterns of the VT-PXRD experiment performed on $Gd_2Zr_2O_7$.*

Another notable phenomenon was that of the shift of the peaks of the variable temperature measurement towards lower angles, implying that a positive thermal expansion did take place. This can be clearly seen in figure 4.55. Also an important phenomena was the fact that the peak widths did not change significantly, as can be seen in figure 4.55 and accounted for by the crystallite size in figure 4.56. This implies little sintering occurred over the temperature range.

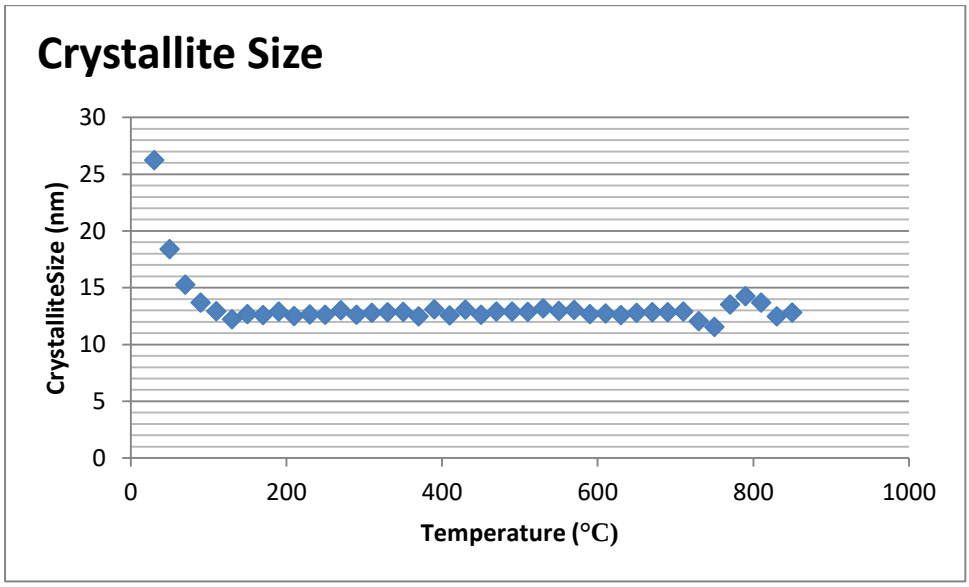


*Figure 4-56: The calculated crystallite size of gadolinium zirconate pyrochlore*

The difference plot obtained from the Rietveld refinement of the ambient $CoK_{\alpha 2}$ (Bruker D2 phaser) data for gadolinium zirconate indicates that the match between the model and the observable data is of high precision. As illustrated in figure 4.57, there is a slight amount of additional noise beneath the major peaks.

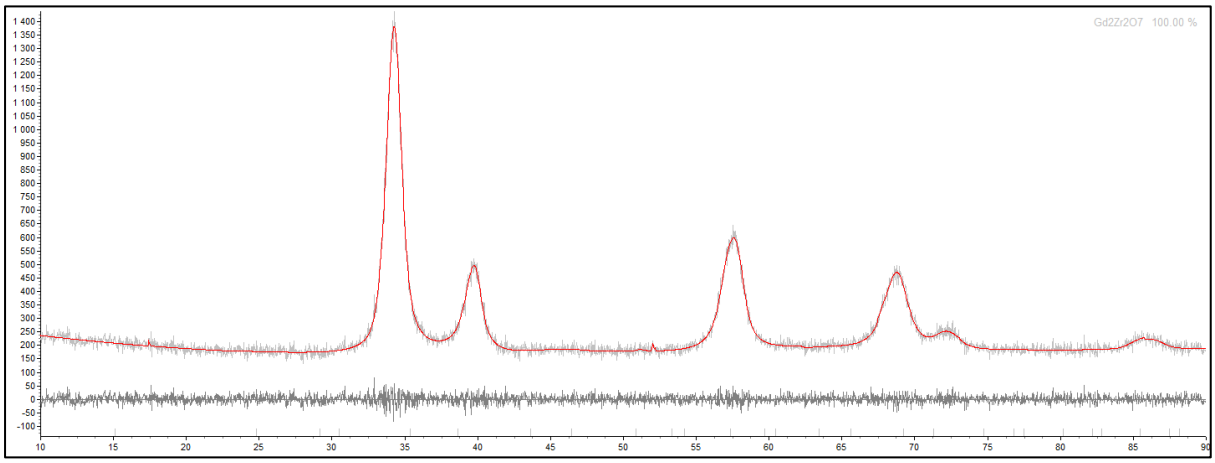


*Figure 4-57: The $CoK_{\alpha 2}$ difference plot of $Gd_2Zr_2O_7$ obtained after completion of the Rietveld refinement procedure discussed in section 2.4.8.*

The difference plot obtained from the Rietveld refinement of the 30°C VT-PXRD pattern of gadolinium zirconate ($CuK_{\alpha 2}$, Bruker D8 advance) indicates a good match between the observed and calculated patterns. Due to the low intensity of the pattern and the high background, a visually large amount of noise is apparent in the difference plot, illustrated in figure 4.58.

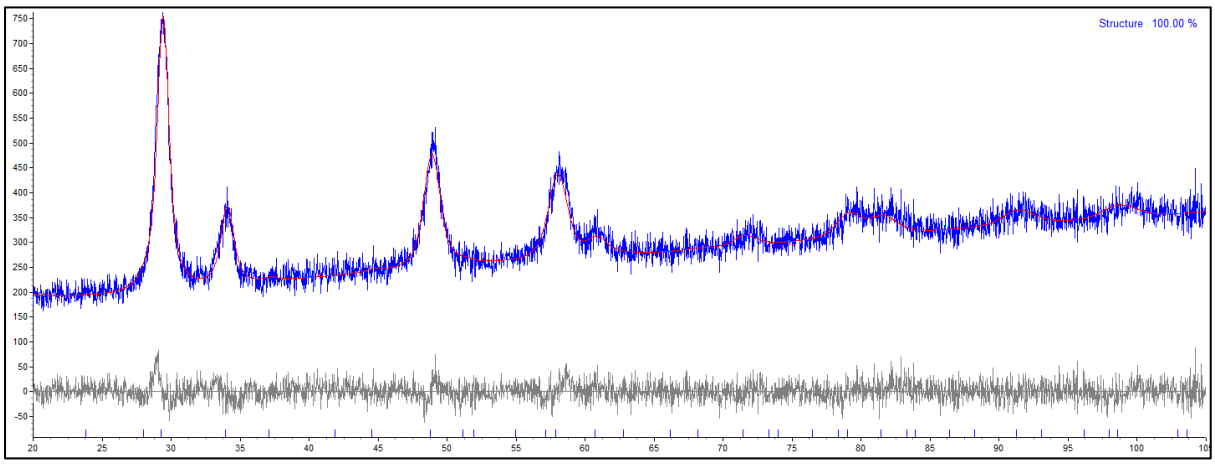


*Figure 4-58: The $CuK_{\alpha 2}$ difference plot of $Gd_2Zr_2O_7$ obtained after completion of the Rietveld refinement procedure discussed in section 2.4.8.*

The plot of lattice parameter against temperature for the defect fluorite phase of gadolinium zirconate is illustrated in figure 4.59, which is, by the fitted second order polynomial, given by $a =$

$-7.549 \times 10^{-9}T^2 + 6.482 \times 10^{-5}T + 10.561$ with $R^2 = 0.991$. The range of the lattice parameter of over the temperature extends from 10.565(3)Å at 30°C to 10.611(3)Å at 850°C.

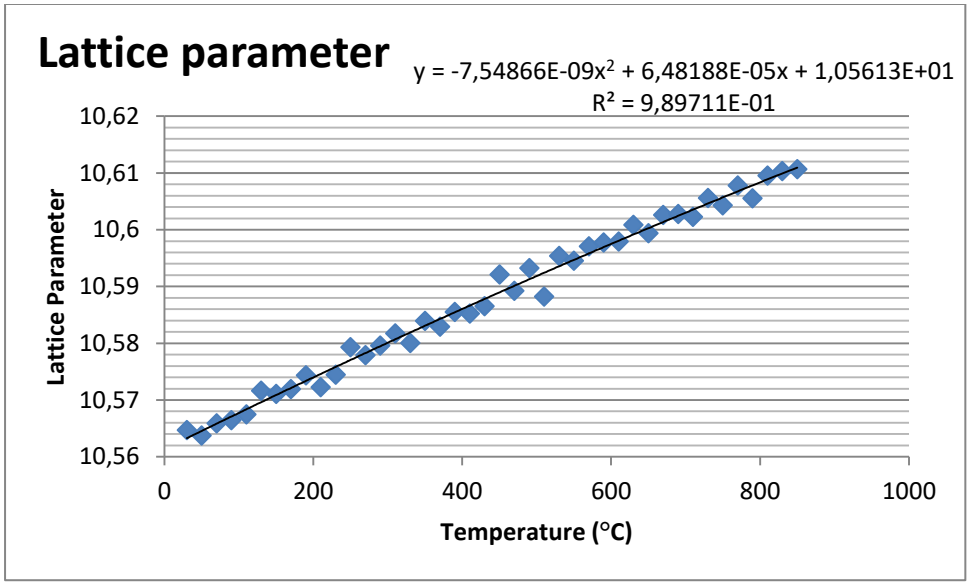


*Figure 4-59: The lattice parameter change relative to temperature for the VT-PXRD sequential Rietveld refinement of $Gd_2Zr_2O_7$ diffraction data.*

Figures 4.60 and 4.61 illustrate the plots of goodness of fit and Rwp against temperature respectively. Both figures fluctuate about a fitted second order polynomial added solely as a rough guide of the trend. Both plots indicate low values for the respective figures of merit.

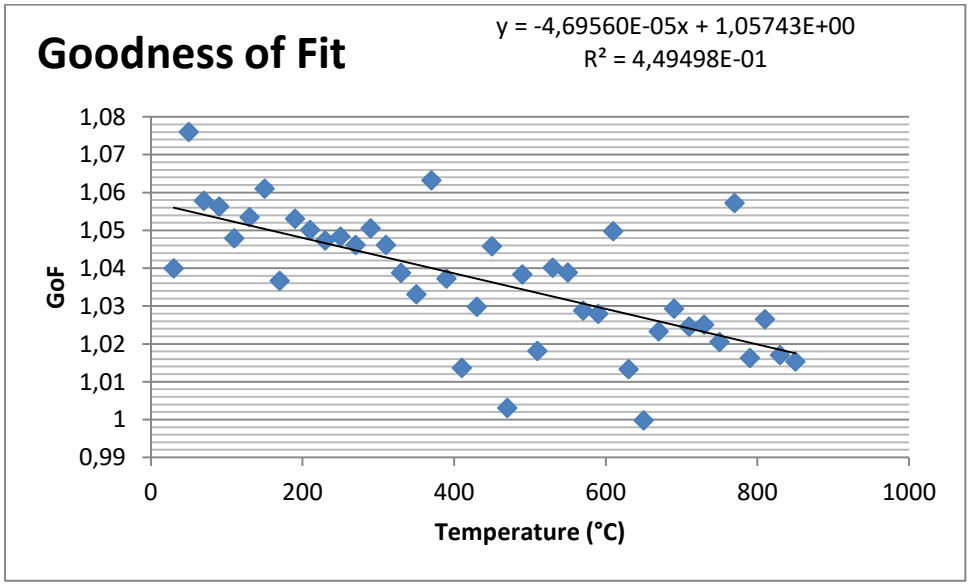


*Figure 4-60: The goodness of fit relative to temperature for the VT-PXRD sequential Rietveld refinement of $Gd_2Zr_2O_7$ diffraction data.*

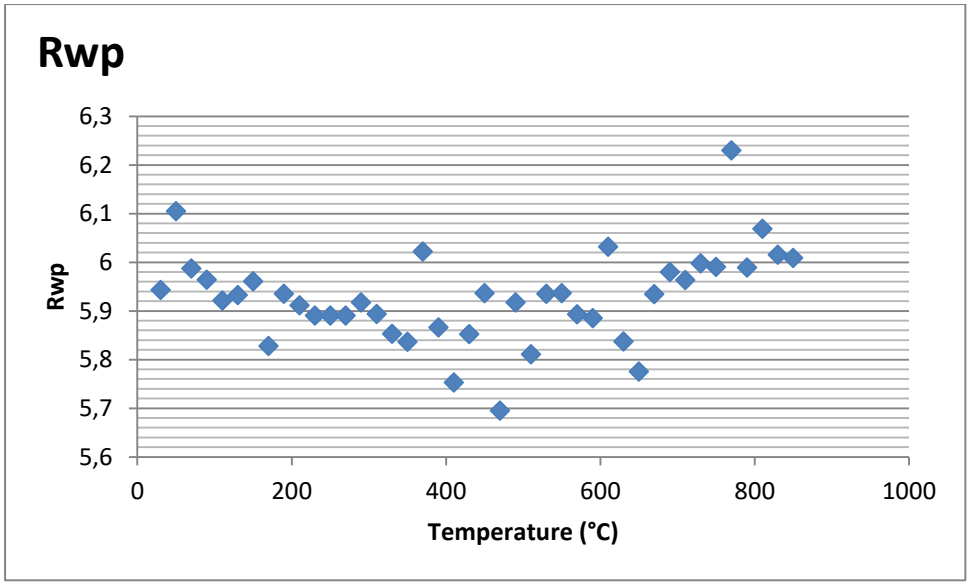


*Figure 4-61: The Rwp values relative to temperature for the VT-PXRD sequential Rietveld refinement of $Gd_2Zr_2O_7$ diffraction data.*

The thermal parameter plots against temperature of both the gadolinium and zirconium ions both can be seen in figures 4.62 and 4.63 respectively. The gadolinium thermal parameters follow an erratic trend whilst the zirconium thermal parameters reduced to the limits set in Topas for refinement stability. Figure 4.64 illustrates the plot of the 48f oxygen thermal parameter against temperature, which also follows an erratic trend. The thermal parameters for the 8b oxygen atom, illustrated in figure 4.65 indicate the value for the thermal parameter extending to the upper limits set in Topas.

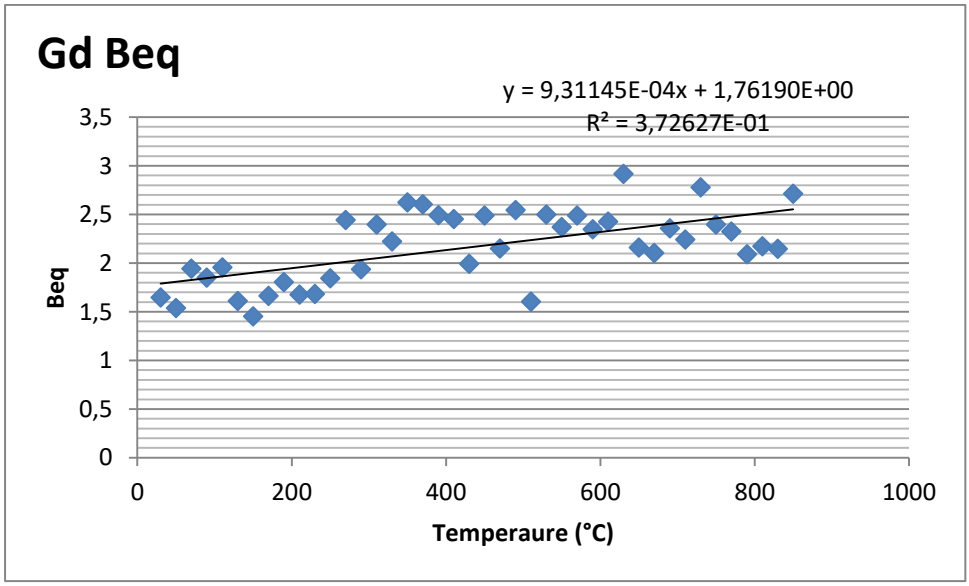


*Figure 4-62: The gadolinium Beq values relative to temperature for the VT-PXRD sequential Rietveld refinement of $Gd_2Zr_2O_7$ diffraction data.*

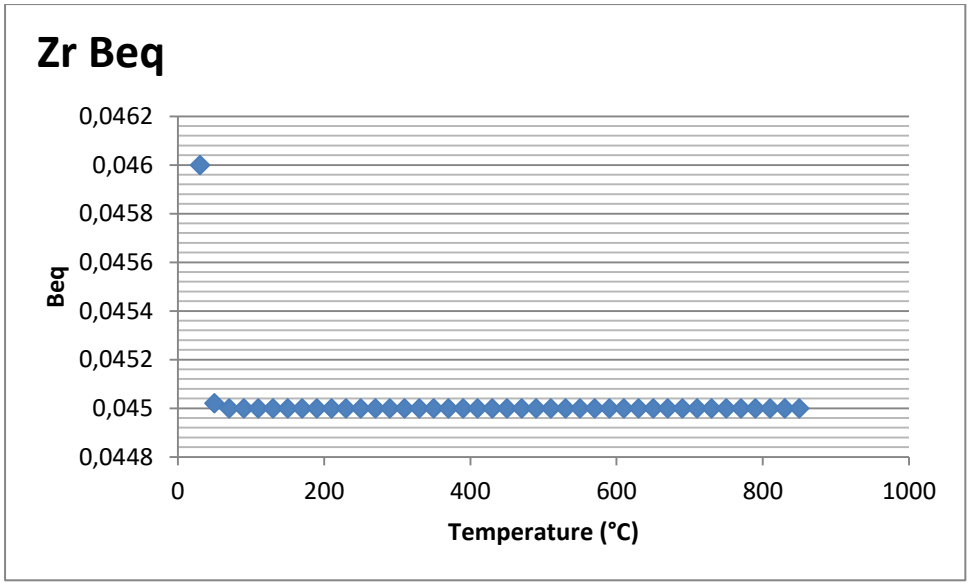


*Figure 4-63: The zirconium Beq values relative to temperature for the VT-PXRD sequential Rietveld refinement of $Gd_2Zr_2O_7$ diffraction data.*

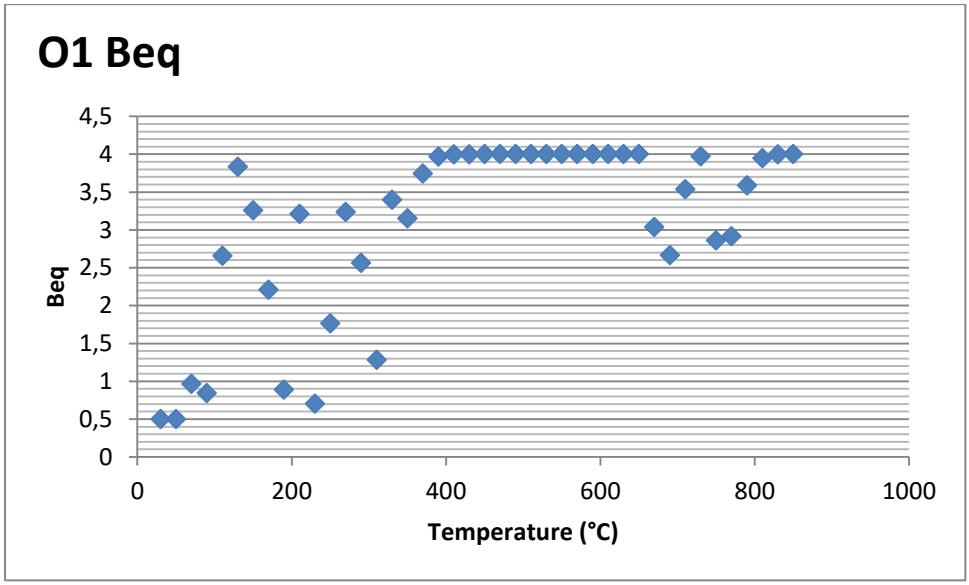


*Figure 4-64: The 48f oxygen Beq values relative to temperature for the VT-PXRD sequential Rietveld refinement of $Gd_2Zr_2O_7$ diffraction data.*

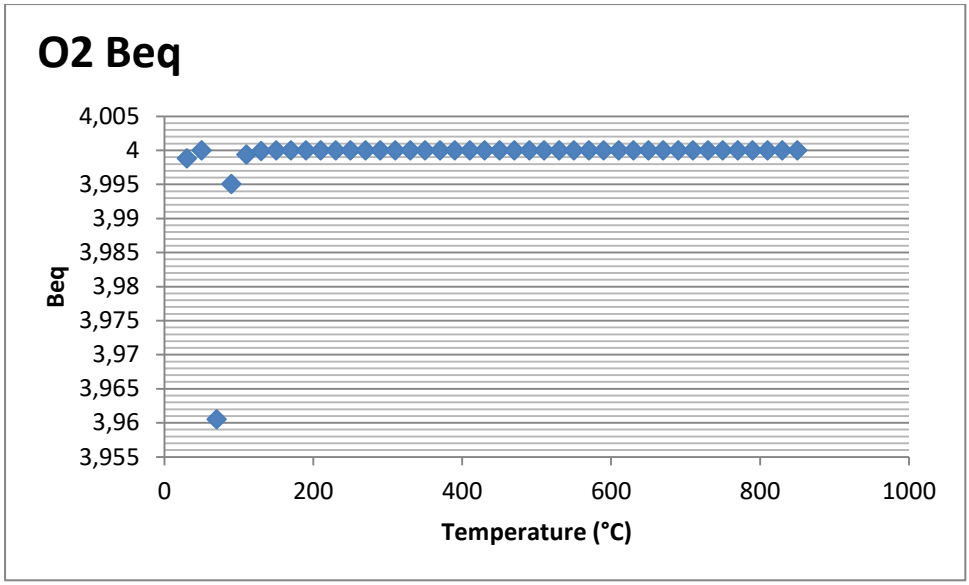


*Figure 4-65: the thermal parameters of the 8f oxygen atom of gadolinium zirconate pyrochlore relative to temperature*

The plot of the position of the 48f oxygen's x position was illustrated in figure 4.66. The trend is erratic and occurs over the range between 0.38 at 650°C and 0.41 at 70 °C. The erratic behaviour was most likely caused by the lack of super-cell peaks for refinement (i.e. peaks unique to the *F* d-3m space group), hence limiting the resolution of the refinement.

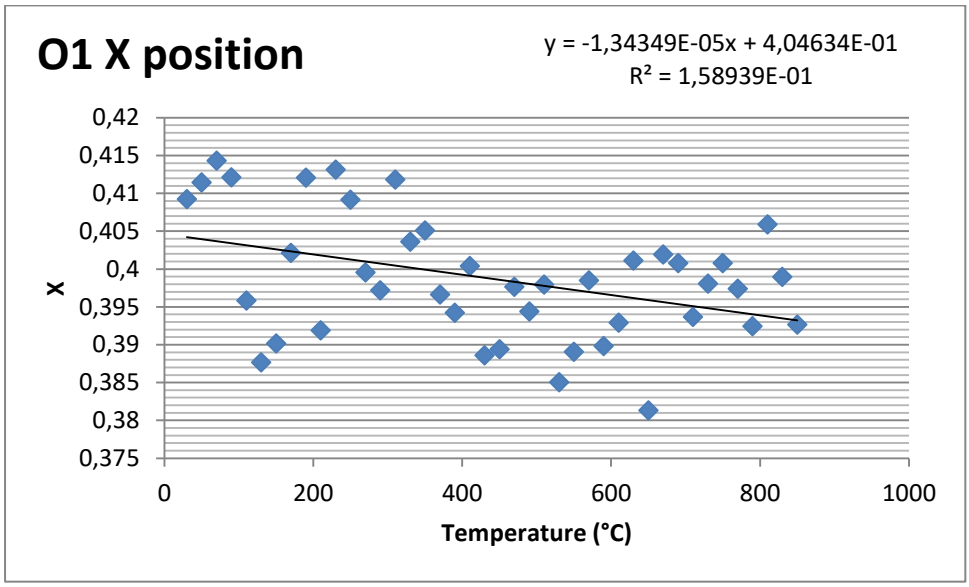


*Figure 4-66: the x position of the 48f oxygen of gadolinium zirconate pyrochlore relative to temperature.*

The coefficient of thermal expansion for the pyrochlore phase of gadolinium zirconate, illustrated in figure 4.67 was determined to be a linear function given by $\alpha = -1.479 \times 10^{-9}T + 6.353 \times 10^{-6}$, implying that the thermal expansion coefficient decreases with temperature. The minimum of 5.09 ppm. $°C^{-1}$ was obtained at 850°C and the maximum of 6.31 ppm. $°C^{-1}$ was obtained at 30°C. The average thermal expansion coefficient over the entire temperature range was found to be 5.70 ppm. $°C^{-1}$.

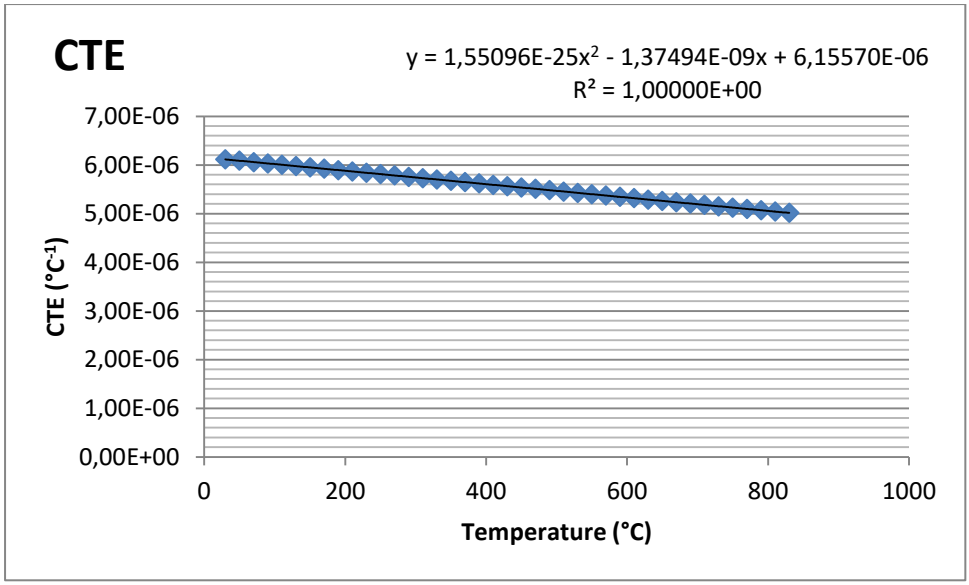


*Figure 4-67: The coefficient of thermal expansion relative to temperature for the VT-PXRD sequential Rietveld refinement of $Gd_2Zr_2O_7$ diffraction data.*

### 4.2.2. Yttrium Zirconate

#### Phase Analysis

A peak matching analysis for phase identification on the $CoK_{\alpha 2}$ pattern of $Y_2Zr_2O_7$ did not yield any results. The closest match to the observed pattern was that of a non-stoichiometric phase of similar composition to the desired composition, namely $Y_{0.15}Zr_{0.85}O_{0.193}$, although the peaks did not match exactly, there were no additional peaks.

A search of the ICSD did not yield any fluorite or pyrochlore phases of the correct stoichiometry, and only yielded four results of non-stoichiometric defect fluorite phases, whilst only regarding high quality data. Comments from the authors as listed in the ICSD indicate that two of the four structures were oxygen deficient. Figure 4.68 illustrates the diffraction pattern of the material in question taken before the thermal cycle of the XRK 900. As stated previously, there were no patterns matching that of the correct stoichiometry. In figure 4.68 the peaks displayed are of gadolinium zirconate, solely placed in the figure to indicate that the material is in fact a pyrochlore phase. The evidence of the pyrochlore phase comes from the peaks at approximately 15 °2θ and 21 °2θ, however, the peaks are not resolved enough to confirm this. The pyrochlore phase was confirmed in a separate study through Raman spectroscopy as a complimentary technique.

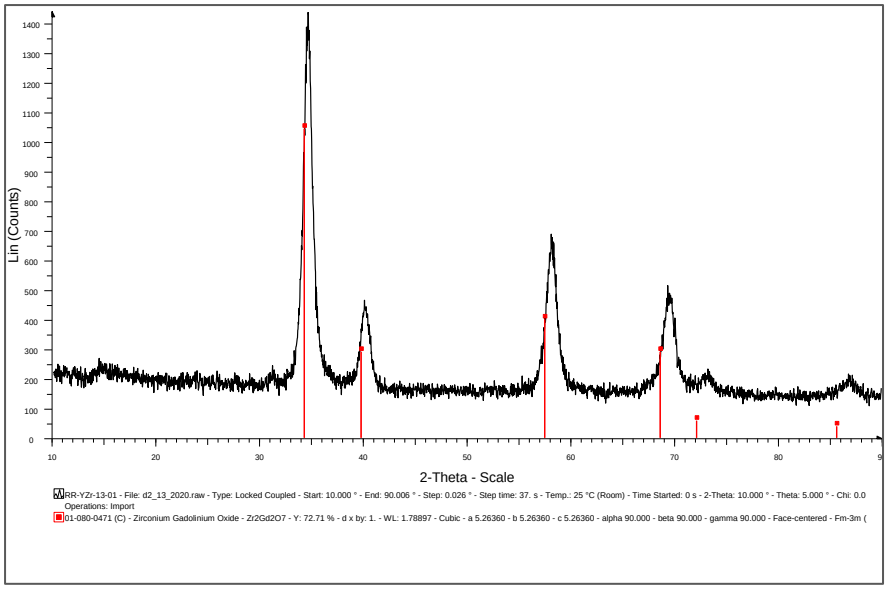


*Figure 4-68: A CoK$_{\alpha 2}$ pattern of $Y_2Zr_2O_7$.*

Figure 4.69 is the sequential overlaying of patterns, offset on the y axis for clarity. From the figure, it can be seen that no observable phase changes occurred over the temperature range. However, there is a slight shifting of the peaks towards lower angles. This is indicative of positive thermal expansion.

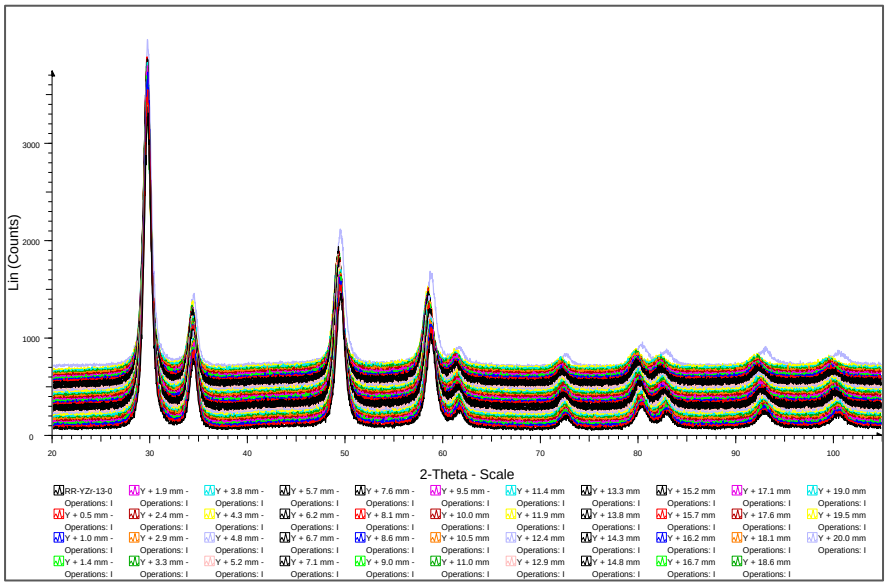


*Figure 4-69: The cascading diffraction patterns of $Y_2Zr_2O_7$ taken from a VT-PXRD experiment.*

## Structural observations

The difference plot obtained from the Rietveld refinement of the ambient CoK$_{\alpha 2}$ data of yttrium zirconate indicates a good match between the calculated and observed patterns, as illustrated in figure 4.70. the is a slight amount of diffuse scattering at approximately 15 °2θ which was not accounted for in the model.

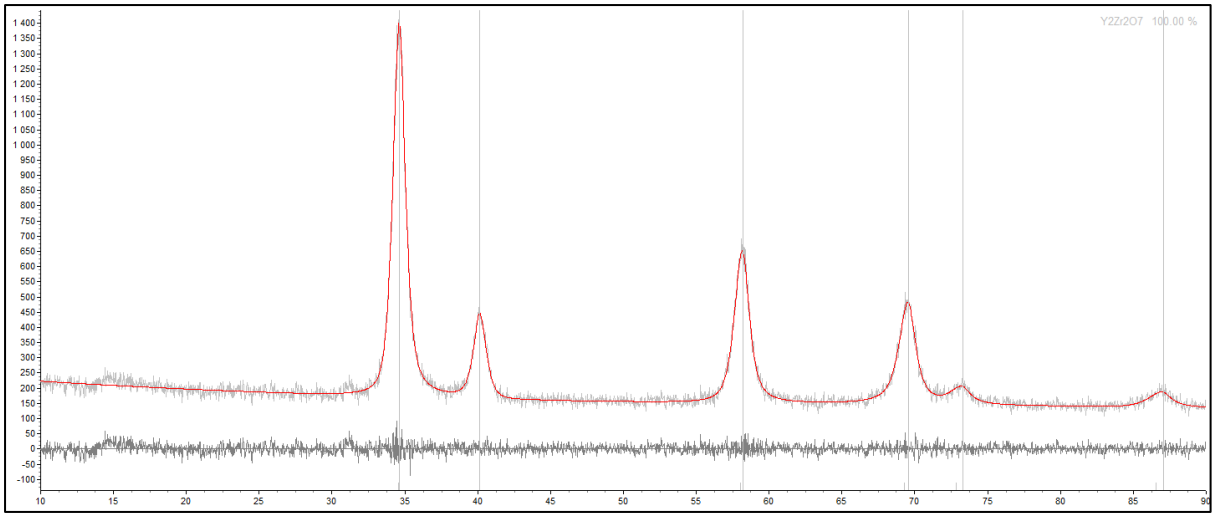


*Figure 4-70: The CoK$_{\alpha 2}$ difference plot of $Y_2Zr_2O_7$ obtained after completion of the Rietveld refinement procedure discussed in section 2.4.7.*

The difference plot for the 30°C CuK$_{\alpha 2}$ pattern's Rietveld refinement was not as accurate as the ambient variant in figure 4.70. As can be seen in figure 4.71, the larger peaks has a calculated height lower than what was observed. The peak positions still remain precise, allowing for the calculation of the lattice parameter.

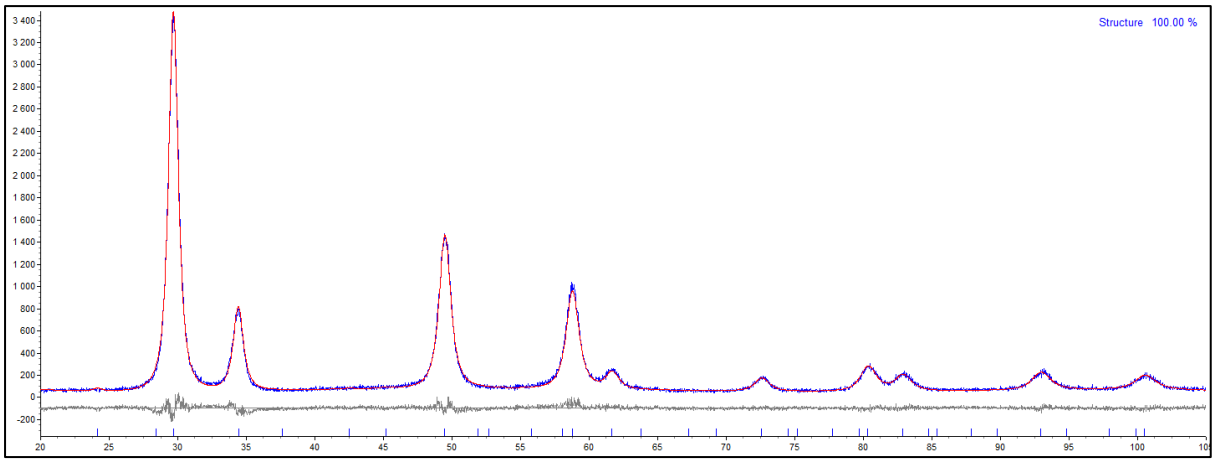


*Figure 4-71: The CuK$_{\alpha 2}$ difference plot of $Y_2Zr_2O_7$ obtained after completion of the Rietveld refinement procedure discussed in section 2.4.7.*

The plot of the lattice parameter against temperature is illustrated in figure 4.72, and was fitted with a second order polynomial given by $a = 1.960 \times 10^{-8}T^2 + 8.701 \times 10^{-5}T + 10.405$ with $R^2 = 0.998$. The minimum size of the lattice parameter was 10.408(1)Å at 30°C and the maximum was 10.491(1)Å at 850°C. Interestingly, of the 27 structures containing only Yttrium, zirconium and oxygen, limited to only the defect fluorite and pyrochlore phases, only one entry in the ICSD was of the pyrochlore phase. This structure reported a unit cell parameter of $a = 10.335$Å and did not supply an

R value. The R value was not supplied for the literature structure as it was determined by first principles (Pruneda & Artacho, 2005).

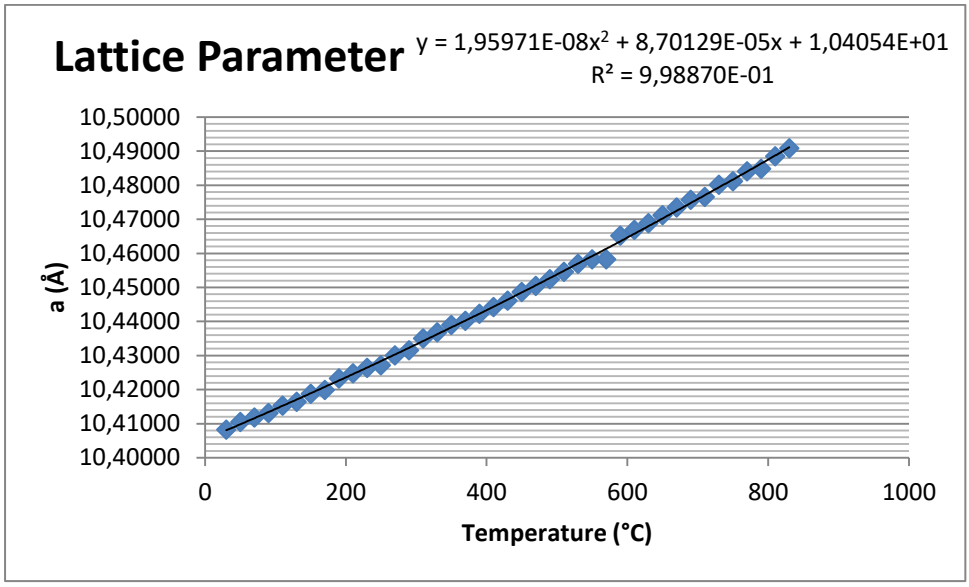


*Figure 4-72: The lattice parameter change relative to temperature for the VT-PXRD sequential Rietveld refinement of $Y_2Zr_2O_7$ diffraction data.*

Figures 4.73 and 4.74 illustrate the goodness of fit and the Rwp against temperature respectively. Both plots appear quite erratic, yet all the values lie within acceptable ranges, for example, the minimum for the goodness of fit was 1.203 at 50 °C and the maximum was 1.252 at 470 °C.

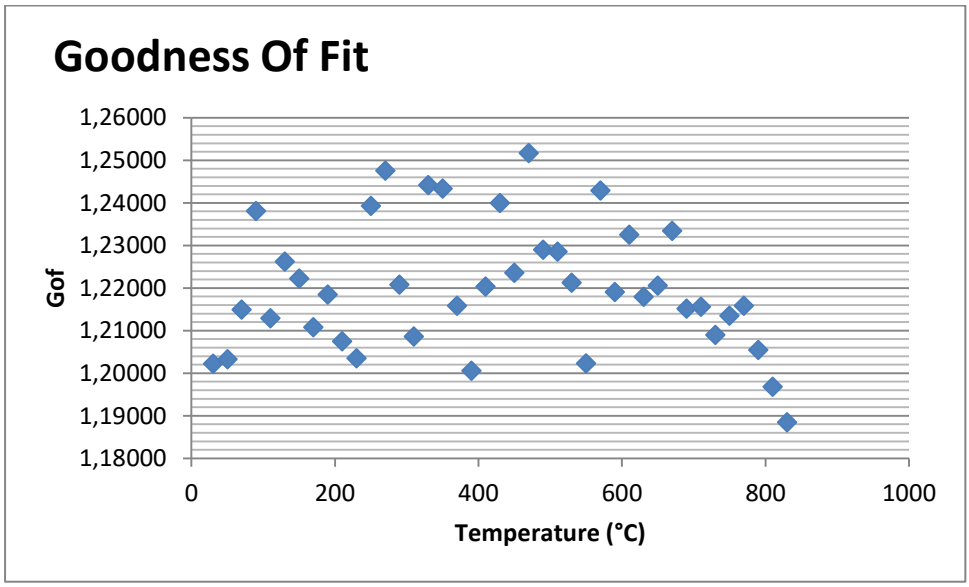


*Figure 4-73: The goodness of fit relative to temperature for the VT-PXRD sequential Rietveld refinement of $Y_2Zr_2O_7$ diffraction data.*

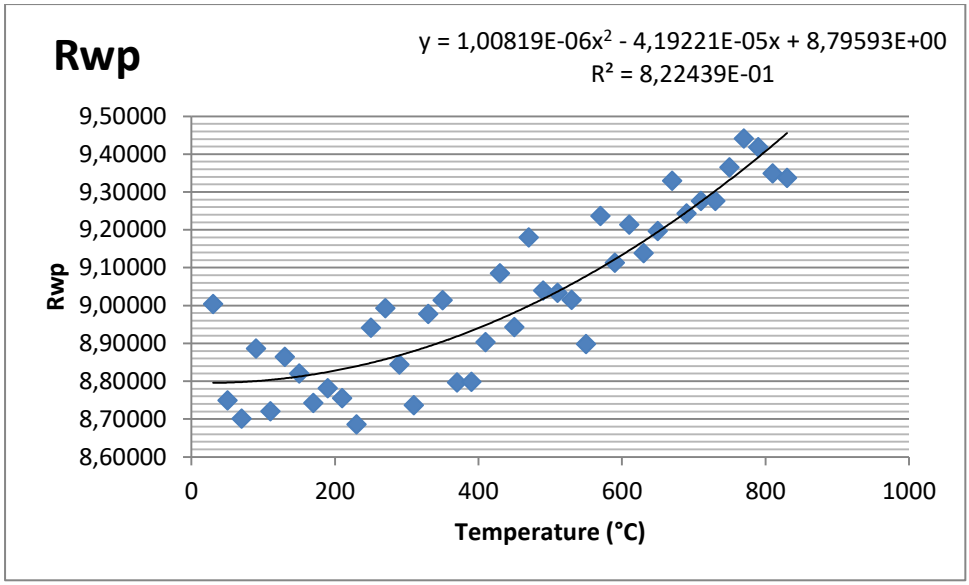


*Figure 4-74: The Rwp values relative to temperature for the VT-PXRD sequential Rietveld refinement of $Y_2Zr_2O_7$ diffraction data.*

The thermal parameters for yttrium, zirconium and the 48f oxygen all follow similar trends when plotted against temperature, as can be seen in figures 4.75, 4.76, and 4.77. The 8a oxygen displayed a similar trend, but had more significant fluctuations around the fitted trend line in figure 4.78.

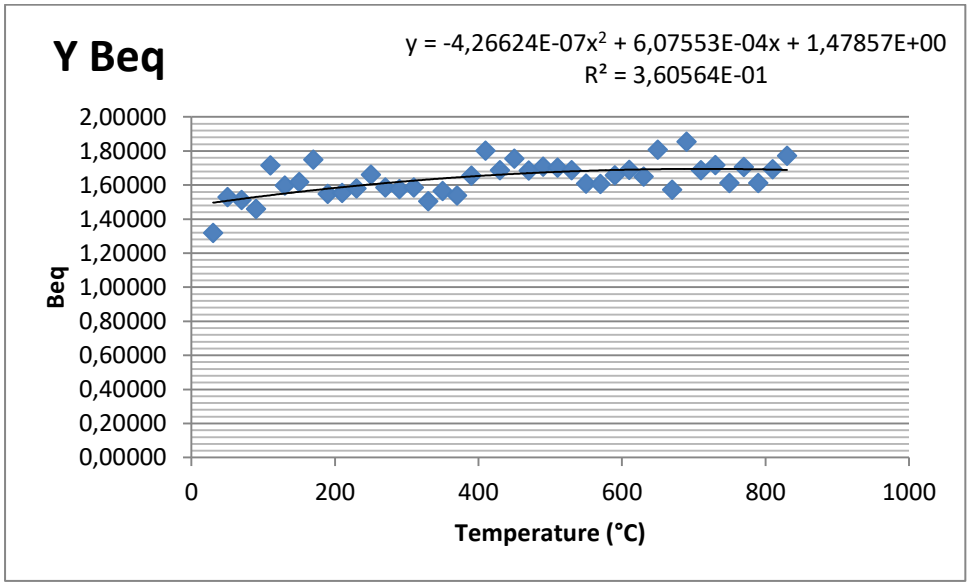


*Figure 4-75: The yttrium Beq values relative to temperature for the VT-PXRD sequential Rietveld refinement of $Y_2Zr_2O_7$ diffraction data.*

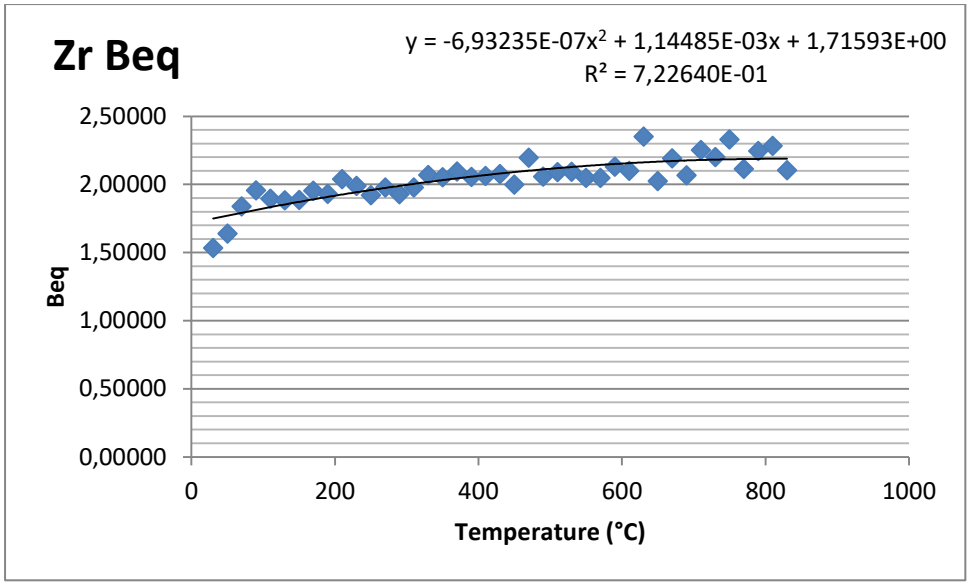


*Figure 4-76: The zirconium Beq values relative to temperature for the VT-PXRD sequential Rietveld refinement of $Y_2Zr_2O_7$ diffraction data.*

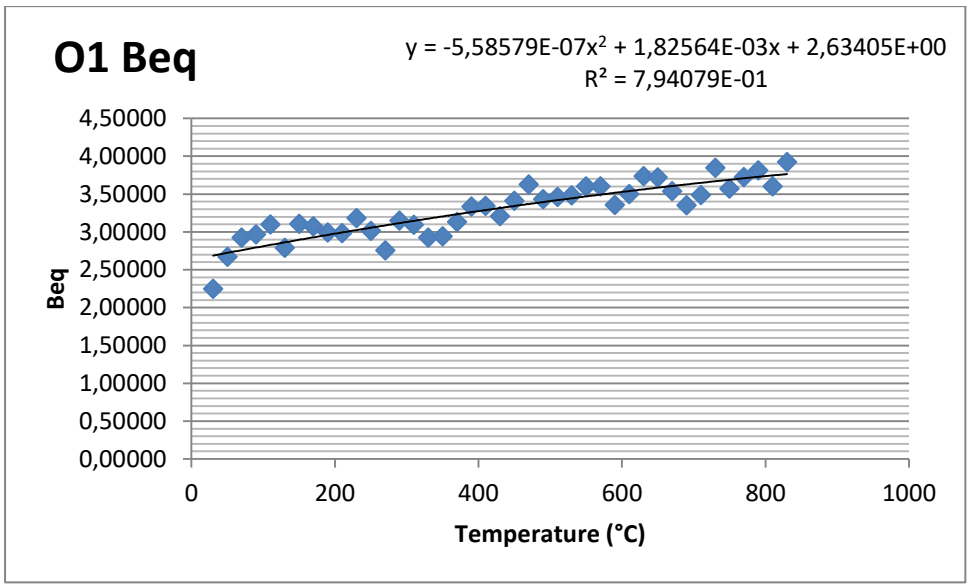


*Figure 4-77: The 48f oxygen Beq values relative to temperature for the VT-PXRD sequential Rietveld refinement of $Y_2Zr_2O_7$ diffraction data.*

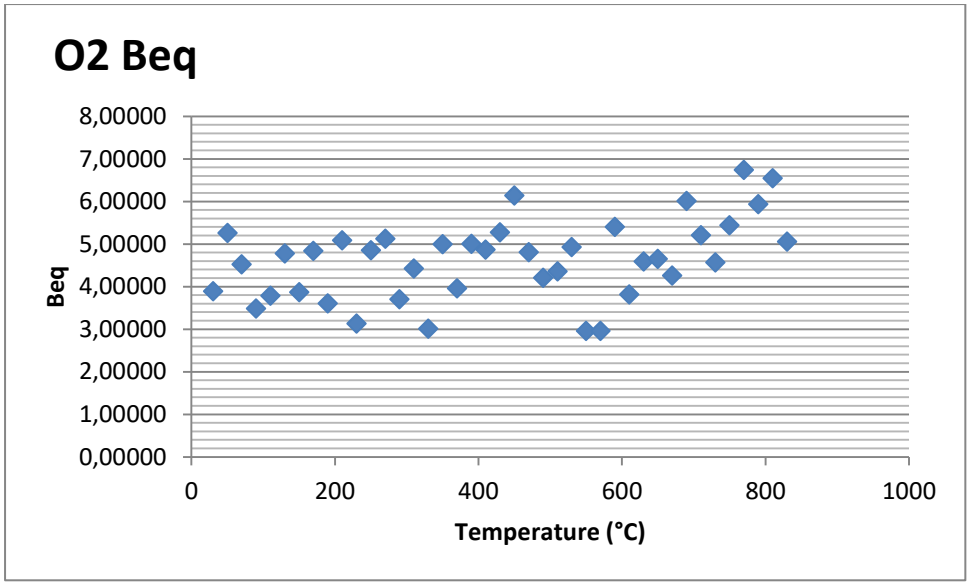


*Figure 4-78: The 8a oxygen values relative to temperature for the VT-PXRD sequential Rietveld refinement of $Y_2Zr_2O_7$ diffraction data.*

The X position of the 48f oxygen ion displayed erratic movement about the trend line as can be seen in figure 4.79, hence an accurate position of the atom relative to temperature is not possible to elucidate from this data.

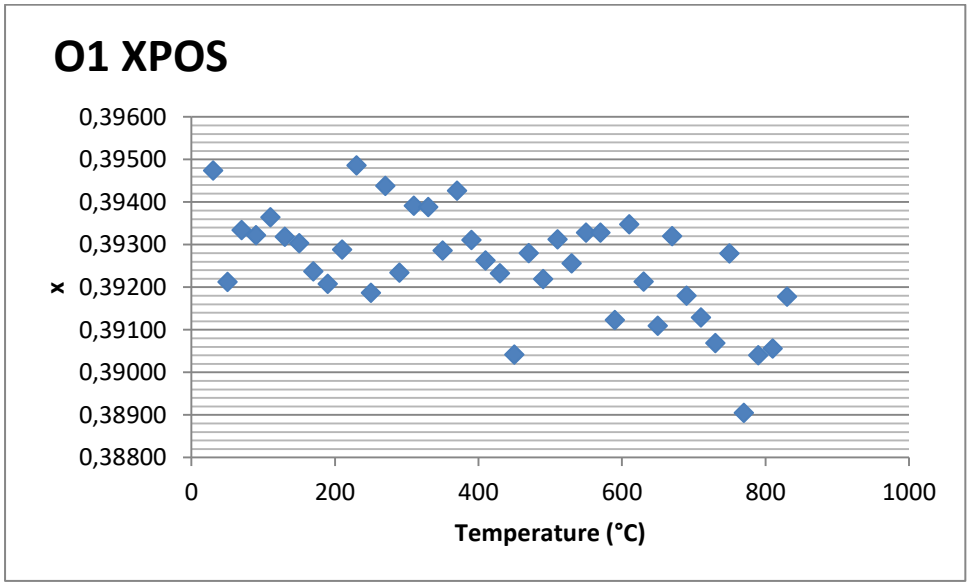


*Figure 4-79: The 48f x-position relative to temperature for the VT-PXRD sequential Rietveld refinement of $Y_2Zr_2O_7$ diffraction data.*

The thermal expansion coefficient of the pyrochlore phase of yttrium zirconate, illustrated in figure 4.80, was shown to follow a linearly increasing trend following the function $\alpha = 3.77 \times 10^{-9}T + 8.36 \times 10^{-6}$ with a minimum of 8.47 ppm. $°C^{-1}$ at 30 °C and a maximum of 11.48 ppm. $°C^{-1}$ at 830°C.

The average thermal expansion coefficient over the entire temperature range was found to be 9.98 ppm. $°C^{-1}$.

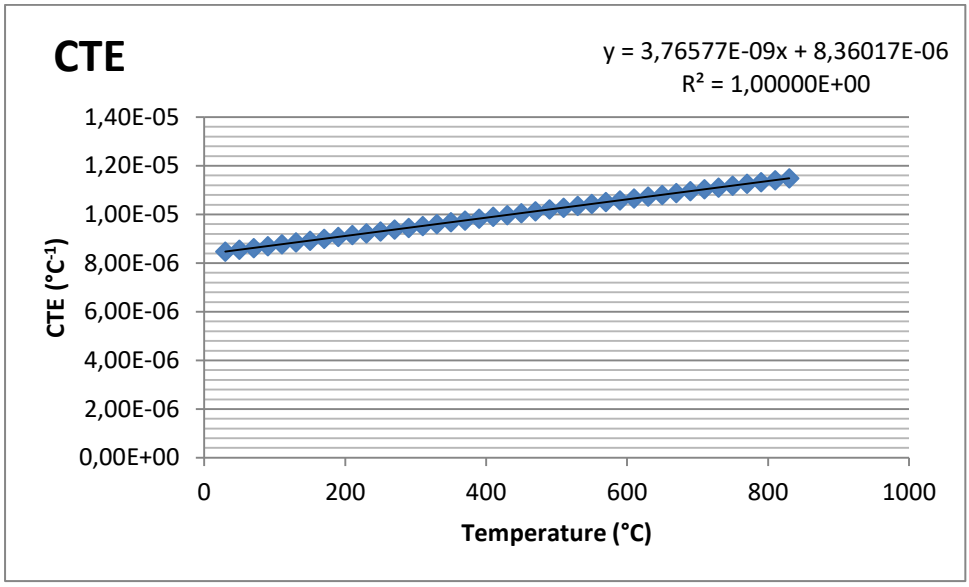


*Figure 4-80: The coefficient of thermal expansion relative to temperature for the VT-PXRD sequential Rietveld refinement of $Y_2Zr_2O_7$ diffraction data.*

## 4.3. Lanthanide Titanates

### 4.3.1. Europium Titanate

#### Phase analysis

With all the plots overlaid, one can clearly see that there is a thermal expansion taking place in that the patterns are not perfectly aligned. The cascading plot (figure 4.81) of the patterns reveals that the peaks shift toward lower angles, implying a positive thermal expansion. This change, upon inspection, is very subtle.

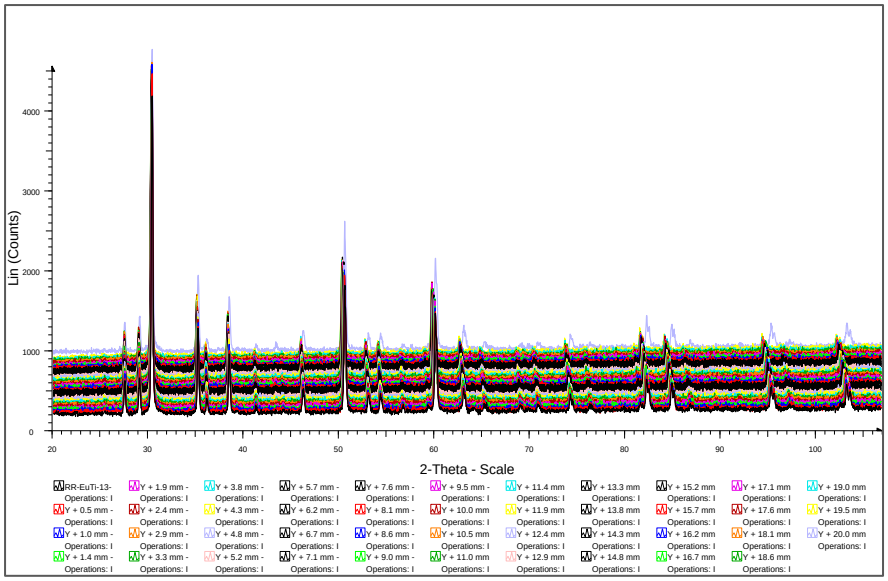


*Figure 4-81: Cascading diffraction patterns of $Eu_2Ti_2O_7$ taken during a VT-PXRD experiment.*

Looking through each scan individually, and comparing it to the scan of the previous temperature, it can be noted that there are no significant changes other than a slight shifting of the peaks towards lower angles, again indicating that the material is of positive thermal expansion, and a gradual reduction in intensity of each peak. The change appears to be minimal. This change shall be better described by a sequential Rietveld refinement.

Comparing the patterns, at 30°C, before (figure 4.82) and after (figure 4.83) exposure to the programmed temperature regime, one can see very little difference between the patterns.

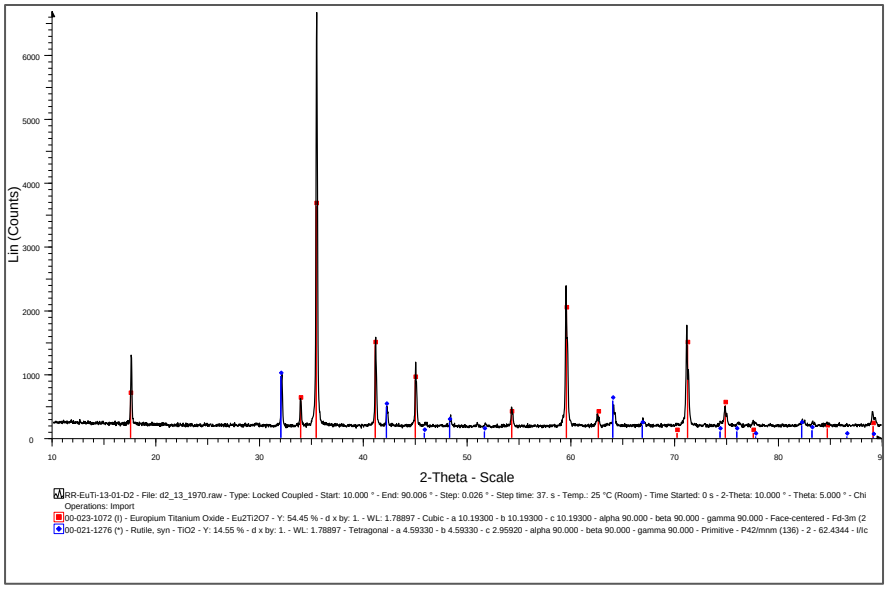


*Figure 4-82: A $CoK_{\alpha 2}$ diffraction pattern of$Eu_2Ti_2O_7$ taken before the VT-PXRD experiment. The red sticks indicate the search matched phase of $Eu_2Ti_2O_7$ and the blue stick are of the rutile impurity.*

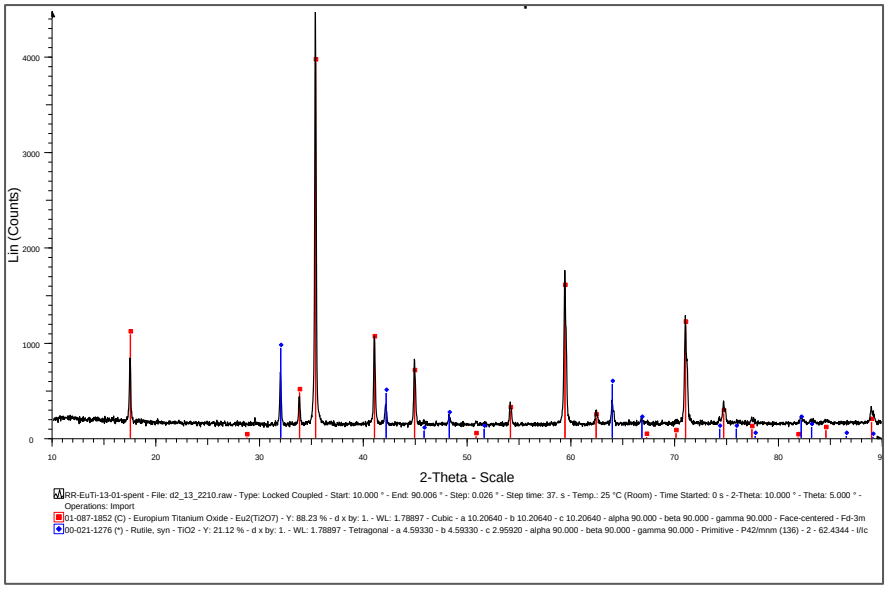


*Figure 4-83: A CoK$_{\alpha 2}$ diffraction pattern of$Eu_2Ti_2O_7$ taken after the VT-PXRD experiment. The red sticks indicate the search matched phase of $Eu_2Ti_2O_7$ and the blue stick are of the rutile impurity.*

In the phase matching of the substance, it was shown that the pyrochlore phase of $Eu_2Ti_2O_7$ was the principle phase, with a significant Rutile impurity phase present (figure 4.82 & 4.83), possibly due to excess titanium isopropoxide present in the initial gel or a side reaction forming rutile. The rutile phase was confirmed by a peak matching procedure using the DiffracEva software package.

## Structural observations

The difference plot of the CoK$_{\alpha 2}$ (ambient) pattern of europium titanate indicates little mismatch between the calculated and observed patterns. The calculated height of the principle peak is lower than what was indicated in the observed pattern, as illustrated in figure 4.84.

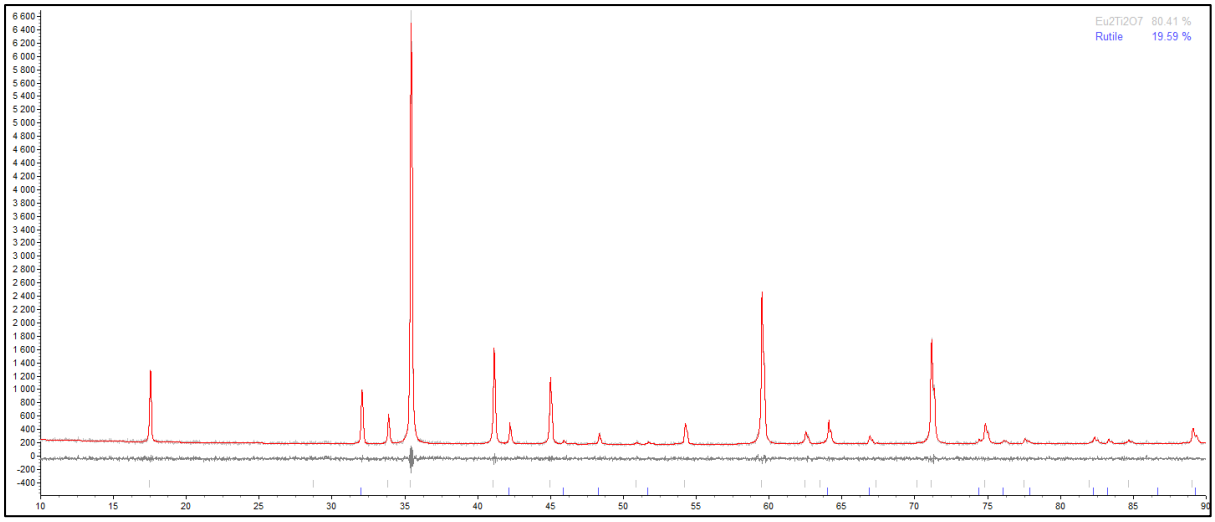


*Figure 4-84: The CoK$_{\alpha 2}$ difference plot of $Eu_2Ti_2O_7$ obtained after completion of the Rietveld refinement procedure discussed in section 2.4.9.*

The 30°C difference plot obtained from the CuK$_{\alpha 2}$ VT-PXRD experiment for europium titanate yielded a greater mismatch of peaks. This may have occurred from an incorrect sample height refinement as the same error occurred for all peaks. This was illustrated in figure 4.85

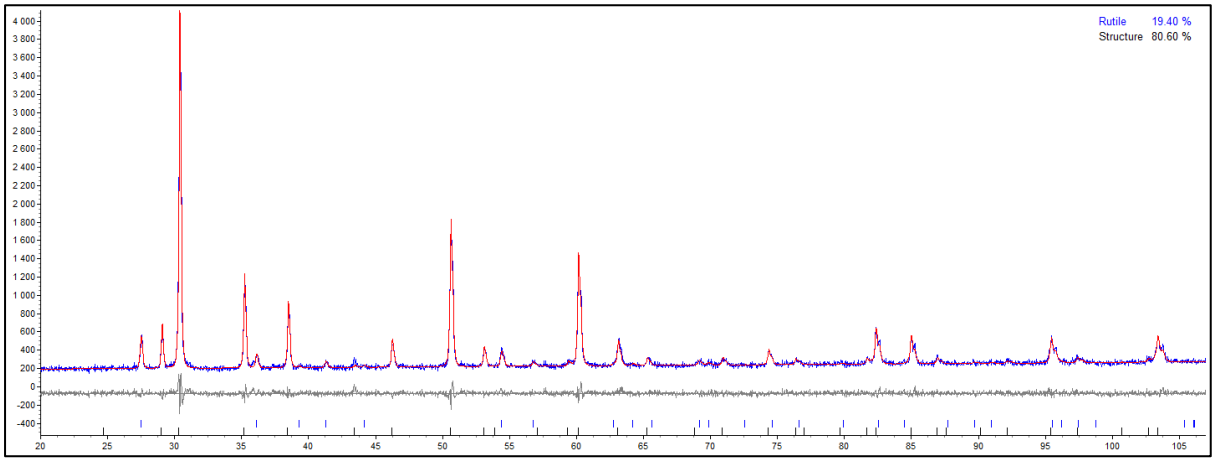


*Figure 4-85: The CoK$_{\alpha 2}$ difference plot of $Eu_2Ti_2O_7$ obtained after completion of the Rietveld refinement procedure discussed in section 2.4.9.*

Figure 4.86 is a plot of the lattice parameter of europium titanate against temperature, and upon visual inspection appears linear. A polynomial function was chosen to fit the data as it gives further detail to the change in the coefficient of thermal expansion, to be discussed later in this passage. The function fitting the data was found to be: $a = 6.35 \times 10^{-9}T^2 + 9.86 \times 10^{-5}T + 1.02 \times 10^{1}$. The minimum and maximum lattice parameter lengths were found at the edges of the observable data, with magnitudes of 10.2027(2)Å and 10.2879(2)Å respectively.

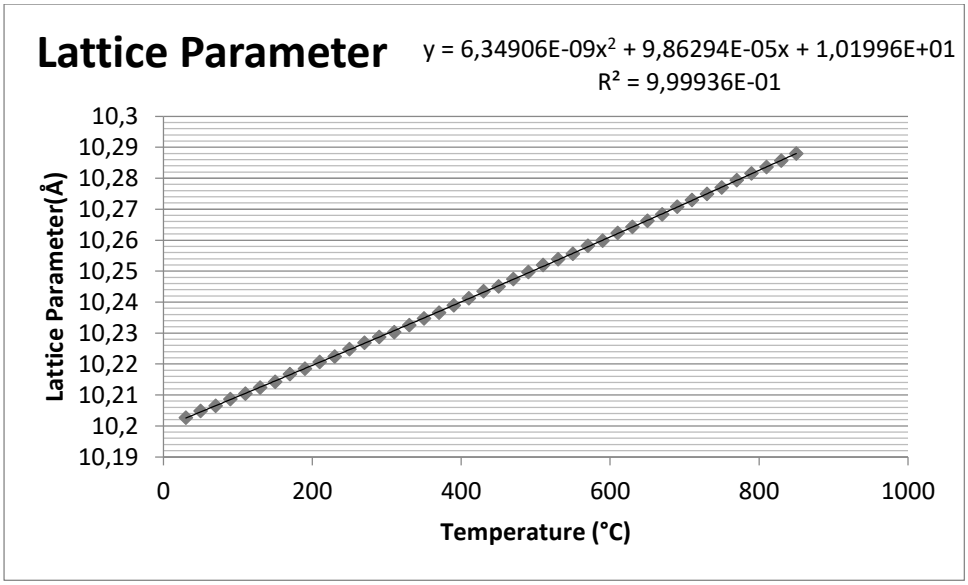


*Figure 4-86: The lattice parameter expansion relative to temperature for the VT-PXRD sequential Rietveld refinement of $Eu_2Ti_2O_7$ diffraction data.*

The Rwp and goodness of fit values do not follow any particular trend respectively (figures 4.87 and 4.88). However, their values lie within ranges that imply that the refinement that took place was correct. The range for Rwp is from 6.27 at 210°C to 7.17 at 770°C. The range for the goodness of fit data (figure 4.88) matches what was observed for the Rwp data in that the range extends from 1.06 at 210°C to 1.14 at 770°C.

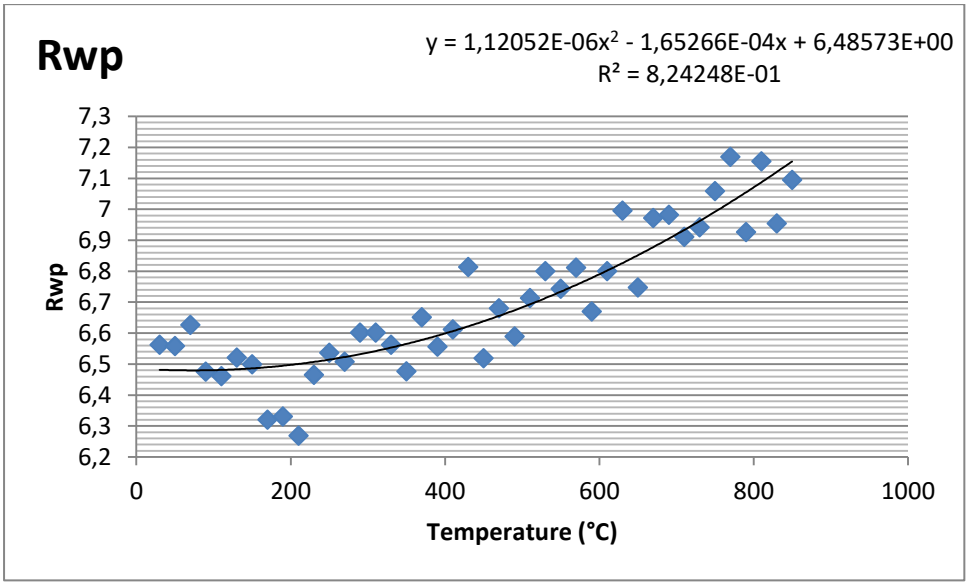


*Figure 4-87: The Rwp values relative to temperature for the VT-PXRD sequential Rietveld refinement of $Eu_2Ti_2O_7$ diffraction data.*

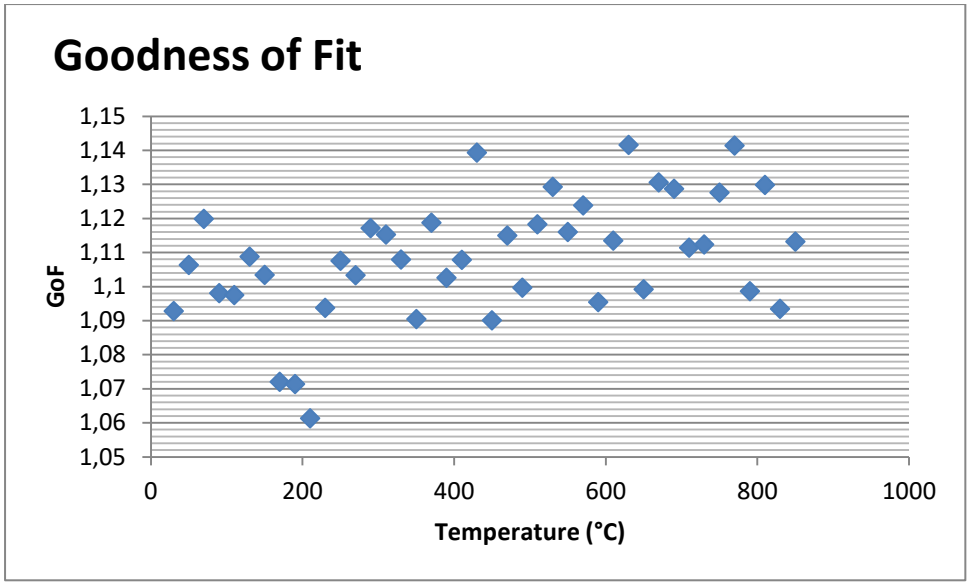


*Figure 4-88: The goodness of fit relative to temperature for the VT-PXRD sequential Rietveld refinement of $Eu_2Ti_2O_7$ diffraction data.*

The Beq values for each element can be seen plotted against temperature in figures 4.89 to 4.92. The only notable trend that can be seen is that for Eu, which increases in magnitude as temperature increases. There is however a large spread around the trend line yielding a poor fit. The Ti Beq values stay consistent up to 230°C, after which the values spread out to a maximum of 0.68 at 770°C. This coincides with the highest Rwp and goodness of fit values.

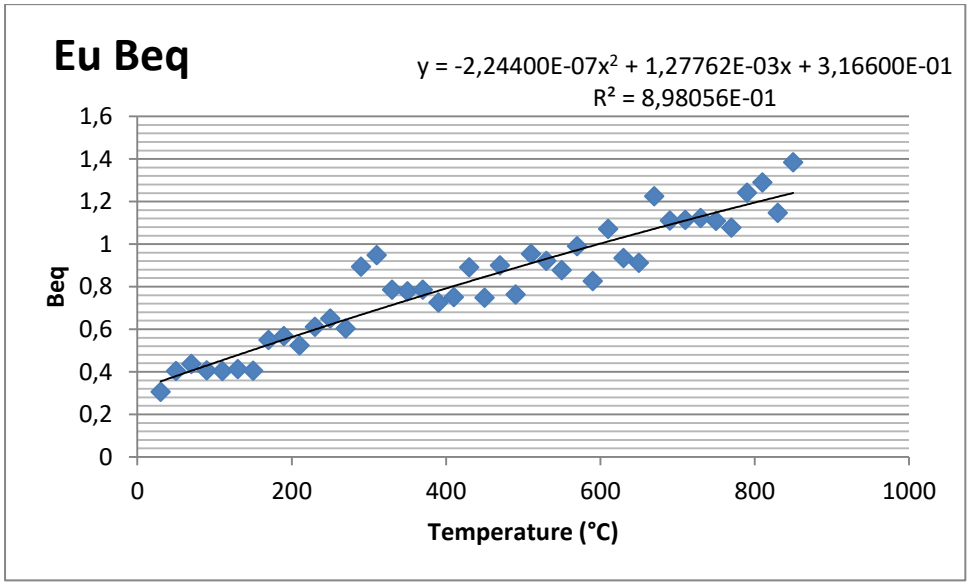


*Figure 4-89: The europium Beq values relative to temperature for the VT-PXRD sequential Rietveld refinement of $Eu_2Ti_2O_7$ diffraction data.*

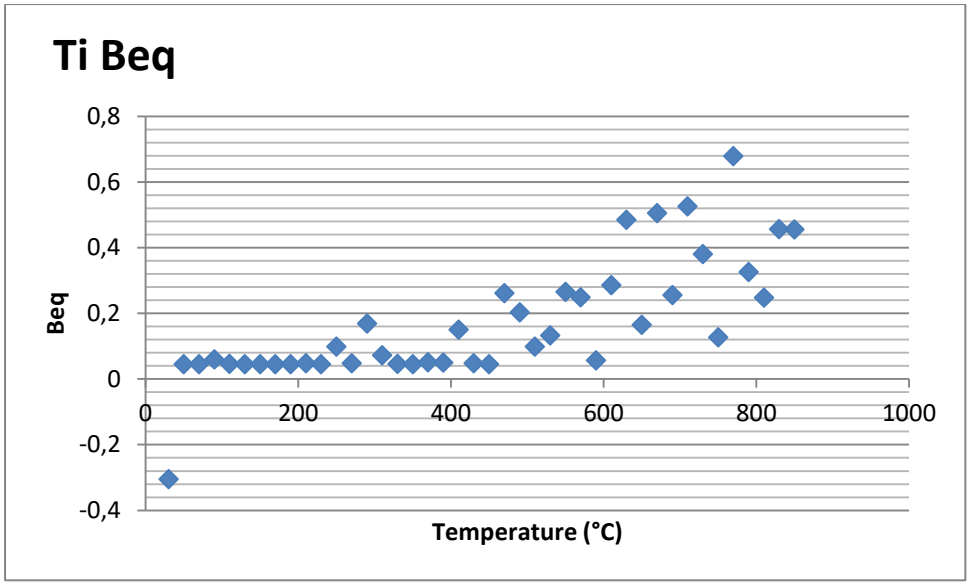


*Figure 4-90: The titanium Beq values relative to temperature for the VT-PXRD sequential Rietveld refinement of $Eu_2Ti_2O_7$ diffraction data.*

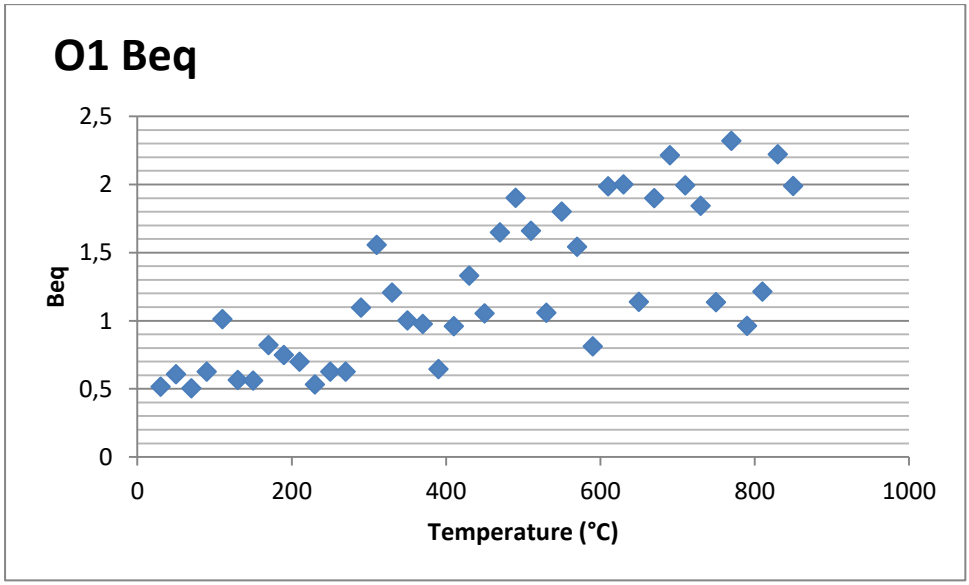


*Figure 4-91: The 48f oxygen Beq values relative to temperature for the VT-PXRD sequential Rietveld refinement of $Eu_2Ti_2O_7$ diffraction data.*

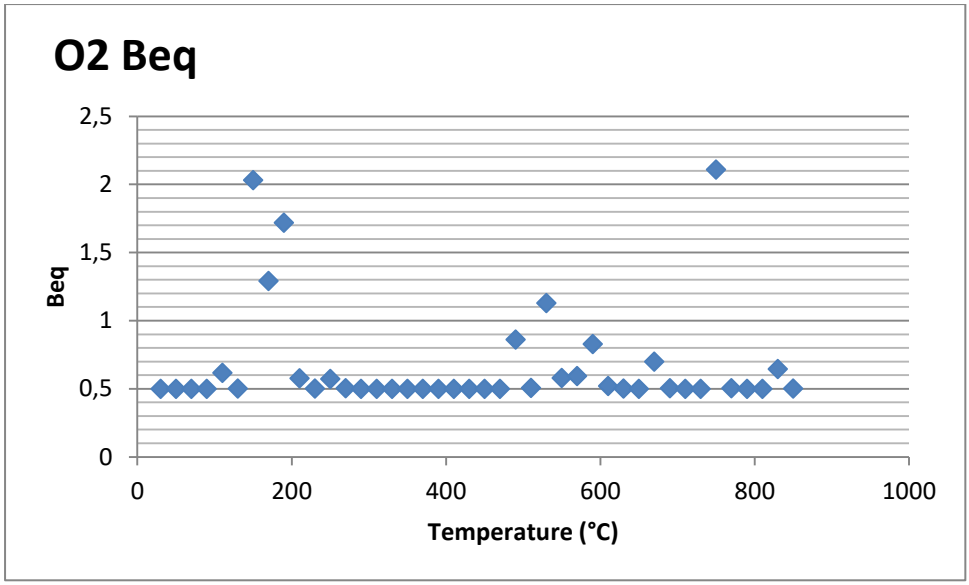


*Figure 4-92: The 8a oxygen Beq values relative to temperature for the VT-PXRD sequential Rietveld refinement of $Eu_2Ti_2O_7$ diffraction data.*

The X position of the 48f oxygen (O1) follows no observable trend (figure 4.93). The range of values extends from 0.327 at 790°C to 0.332 at 490°C.

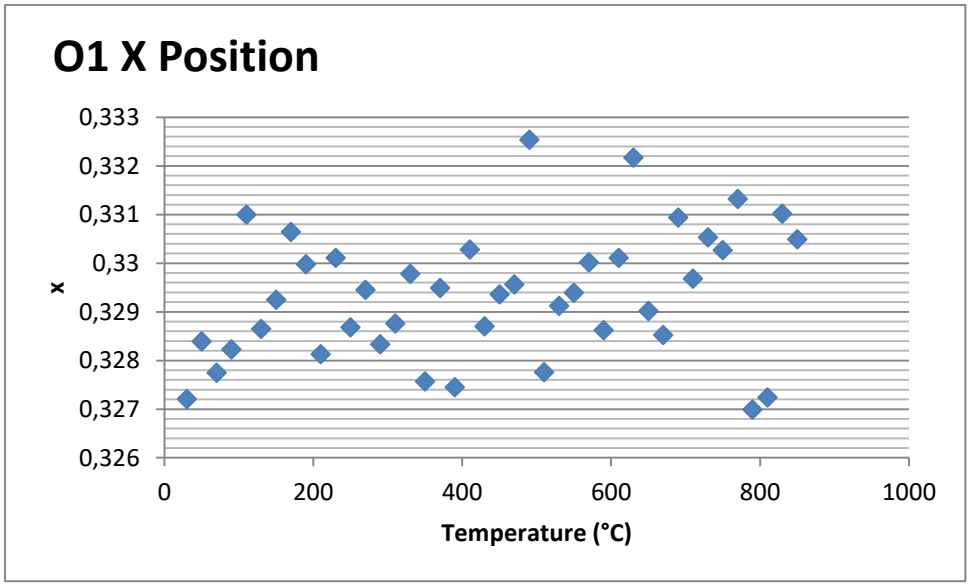


*Figure 4-93: The 48 x-position relative to temperature for the VT-PXRD sequential Rietveld refinement of $Eu_2Ti_2O_7$ diffraction data.*

The coefficient of thermal expansion for europium titanate pyrochlore, as illustrated in figure 4.94, was found to follow the linear trend $\alpha = 1.24 \times 10^{-9}T + 9.67 \times 10^{-6}$. This trend implies that the coefficient of thermal expansion extends from 9.71ppm.°C$^{-1}$ to 10.725ppm.°C$^{-1}$ across the temperature range of the experiment. The average thermal expansion coefficient was found to be 10.21 ppm. °C$^{-1}$.

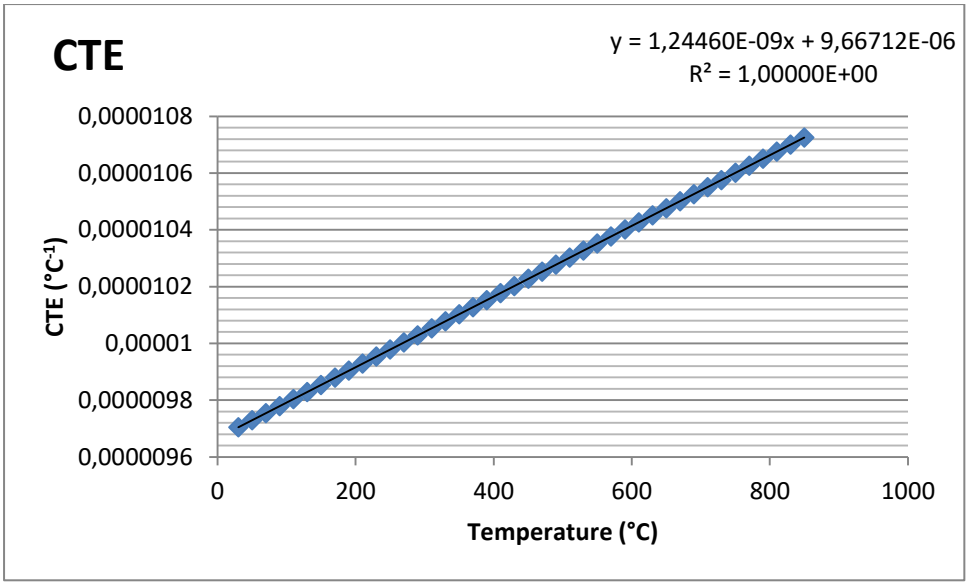


*Figure 4-94: The coefficient of thermal expansion relative to temperature for the VT-PXRD sequential Rietveld refinement of $Eu_2Ti_2O_7$ diffraction data.*

### 4.3.2. Gadolinium Titanate

#### Phase analysis

Visual inspection of the overlaid plots of the variable temperature PXRD experiment indicates that $Gd_2Ti_2O_7$ has a significant thermal expansion as the peaks are clearly not overlaid at each temperature. The shift of the peaks towards lower angles, as stated before, implies a positive thermal expansion (see figure 4.95).

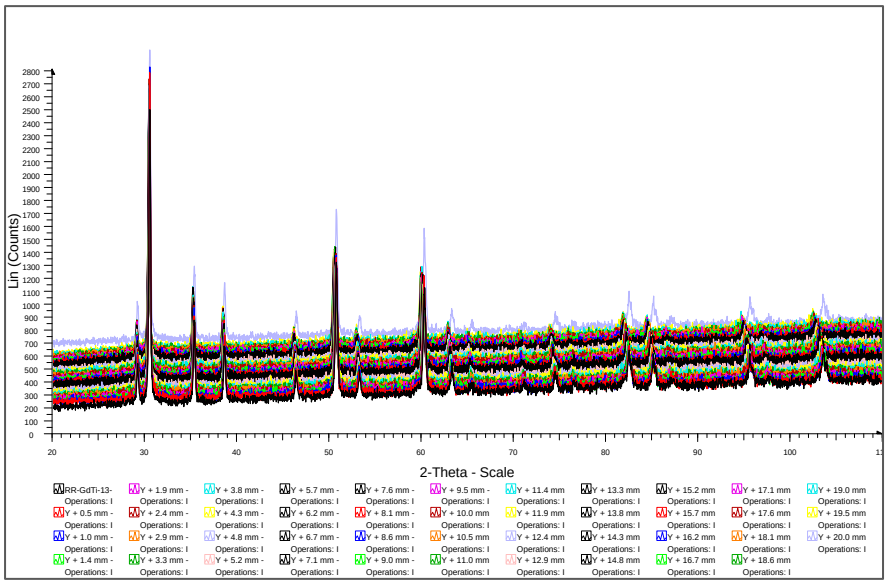


*Figure 4-95: Cascading diffraction patterns of $Gd_2Ti_2O_7$, obtained from a VT-PXRD experiment.*

Observing a Cascading plot of the patterns corroborates the previous assertion of a positive thermal expansion. Also, no other phases have formed across the entire temperature range, thus implying that the material is stable across the entire temperature range. It is important to note that the higher angled peaks of the patterns are not visible in the cascading plot due to their low intensity.

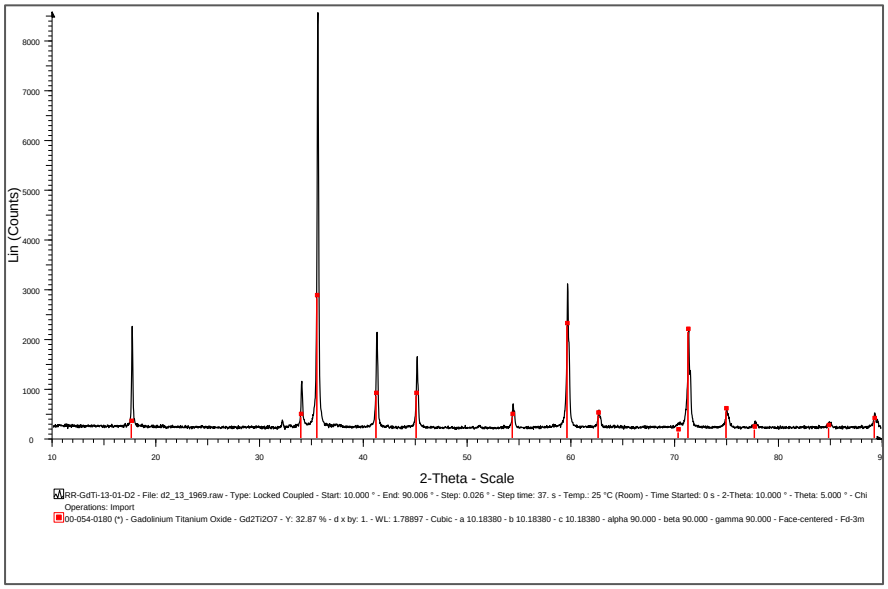


*Figure 4-96 : A CoK$_{\alpha 2}$ diffraction pattern taken of $Gd_2Ti_2O_7$ taken before the VT-PXRD experiment.*

Observing each pattern individually, and comparing it to the pattern of the previous temperature, no observable difference can be seen other than a gradual loss of intensity and a shift of the peaks towards lower angles.

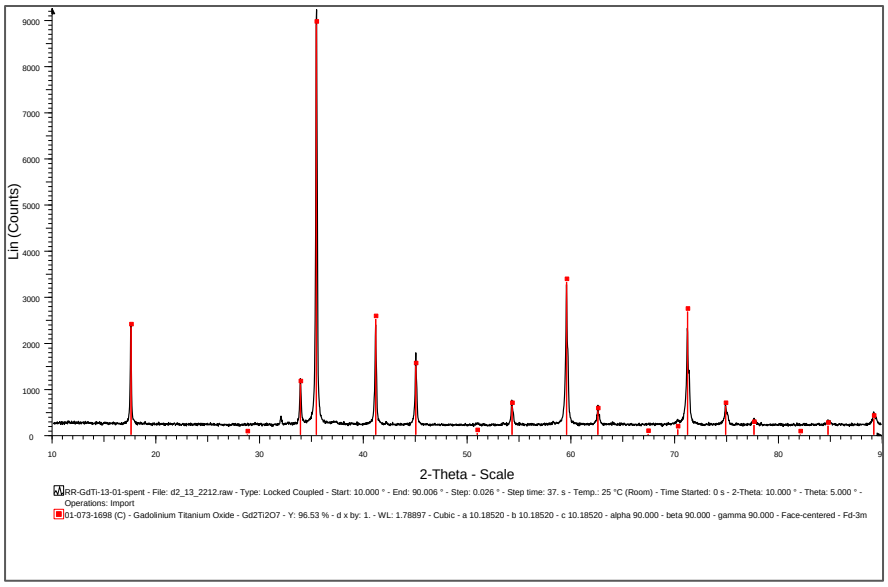


*Figure 4-97: A CoK$_{\alpha 2}$ diffraction pattern taken of $Gd_2Ti_2O_7$ taken after the VT-PXRD experiment.*

A comparison of the patterns taken at 30°C, before (figure 4.96) and after (figure 4.97) heating, shows no difference, implying that no new permanent phases were formed upon cooling

A search match on the final pattern indicates that the pyrochlore $Gd_2Ti_2O_7$ is the sole phase, with no observable impurities due to excess starting reagents.

### Structural observations

The difference plot for the ambient $CoK_{\alpha 2}$ data for gadolinium titanate indicates a match between the observed and calculated patterns from the Rietveld refinement. The principle peak has slight mismatch due to a height difference between the calculated and observed peak, as illustrated in figure 4.98.

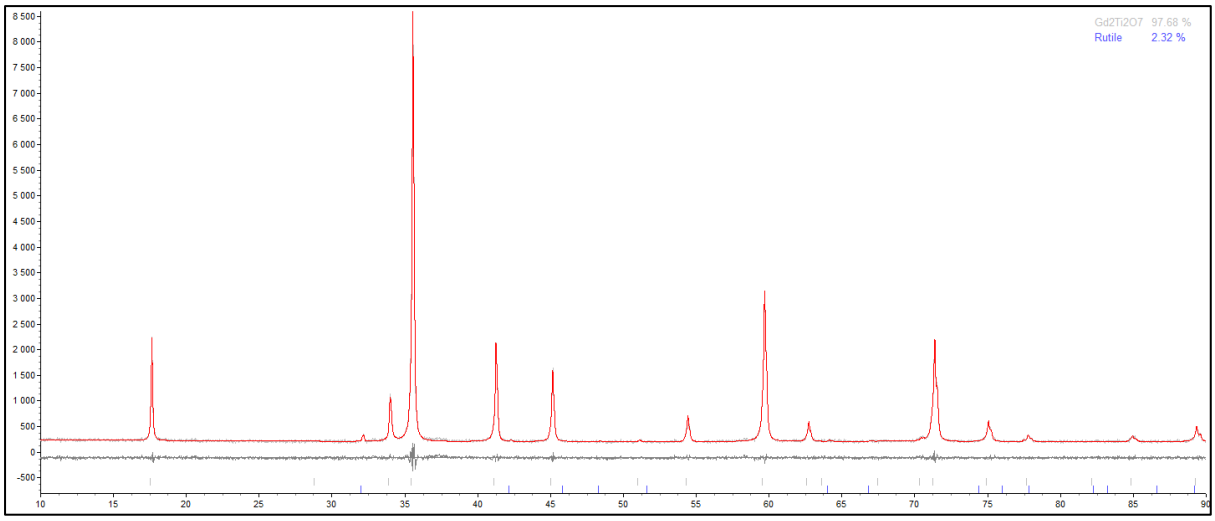


*Figure 4-98: The $CoK_{\alpha 2}$ difference plot of $Gd_2Ti_2O_7$ obtained after completion of the Rietveld refinement procedure discussed in section 2.4.11.*

The difference plot for the $CuK_{\alpha 2}$ data at 30°C did not achieve as accurate a match as illustrated in figure 4.99 the mismatch may have arose from an the refinement of the sample displacement, which would have led to a shift in all peaks.

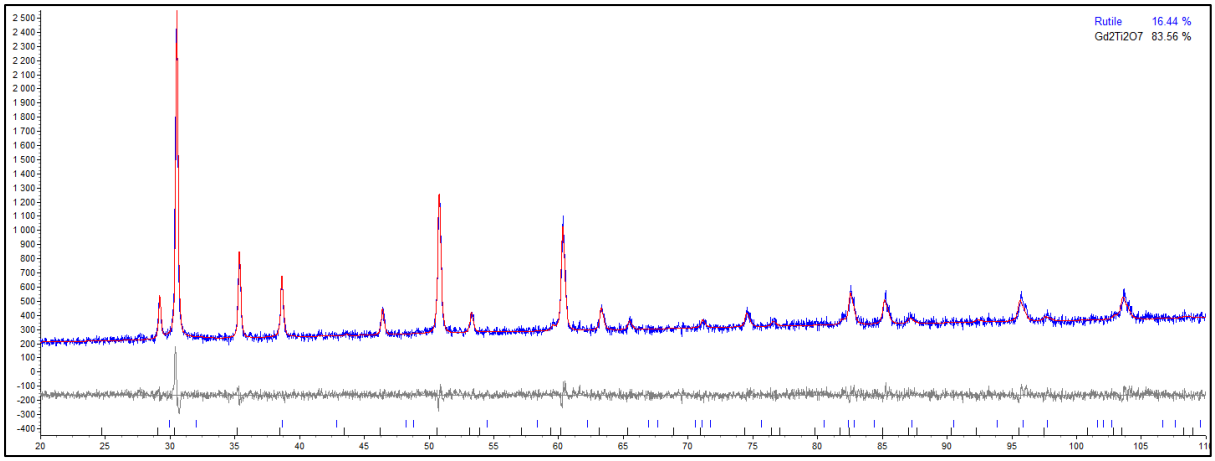


*Figure 4-99: The $CuK_{\alpha 2}$ difference plot of $Gd_2Ti_2O_7$ obtained after completion of the Rietveld refinement procedure discussed in section 2.4.11.*

The observed lattice parameter changes in the gadolinium titanate sample ranged from 10.1940(3) Å at a temperature of 30 °C to 10.2481(3) at 850 °C, hence implying positive thermal expansion across the entire temperature range. Observing figure 4.100, the change in lattice parameter was not linear, but followed a second order polynomial, tapering off towards higher temperatures. The function describing this change is $a = -3.05 \times 10^{-8}T^2 + 9.33 \times 10^{-5}T + 1.02 \times 10^{-1}$. The function fits the observed data well as indicated by $R^2 = 0.99911$.

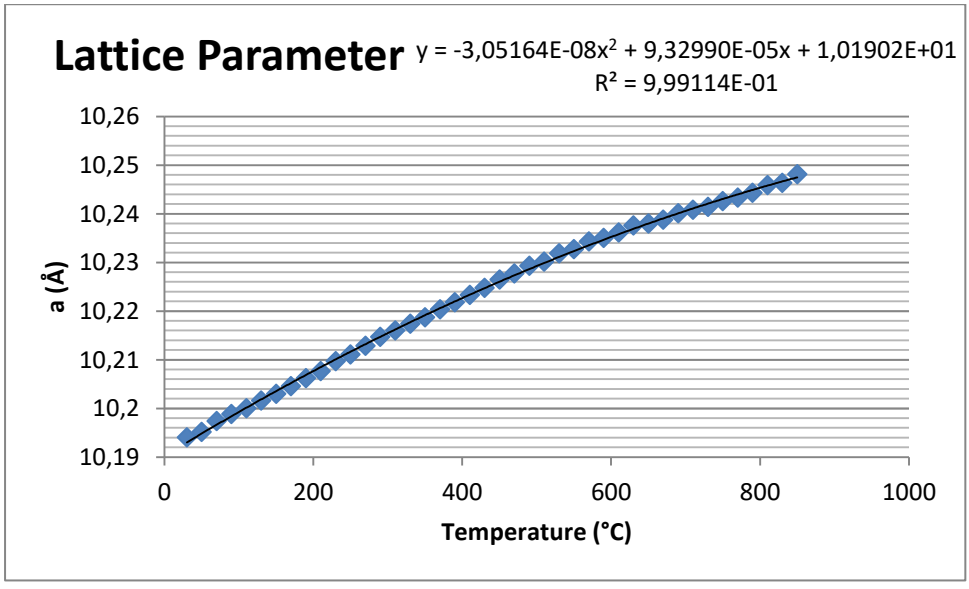


*Figure 4-100: The lattice expansion relative to temperature for the VT-PXRD sequential Rietveld refinement of $Gd_2Ti_2O_7$ diffraction data.*

The goodness of fit for the refinement relative to temperature is illustrated in figure 4.101 and has a range from $GoF = 1.05$ at 230 °C to $Gof = 1.27$ at 850 °C. In observing figure 4.101, it is clear that the goodness of fit improves in the mid-range of the temperature scale for the experiment. The data was fitted with a third order polynomial, which only corresponded approximately, as can be seen in the lower $R^2$ value of 0.9473.

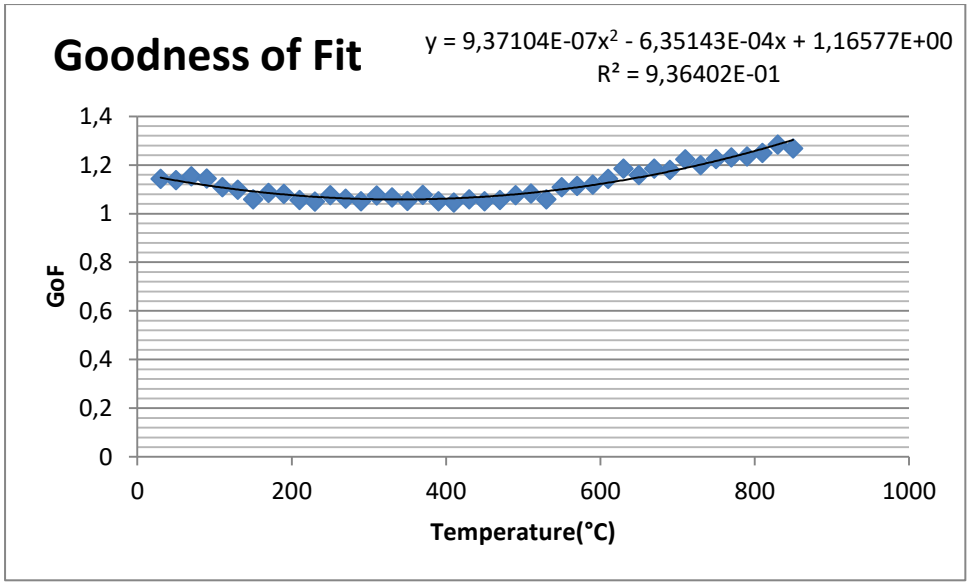


*Figure 4-101: The goodness of fit relative to temperature for the VT-PXRD sequential Rietveld refinement of $Gd_2Ti_2O_7$ diffraction data.*

Similarly, the Rwp values against temperature indicated a minimum at 5.66 at 230 °C and a maximum of 7.42 at 850 °C (figure 4.102). The Rwp values indicate an improvement of the refinement as temperature increased to 230 °C, after which the refinement deteriorated until the highest temperature was reached.

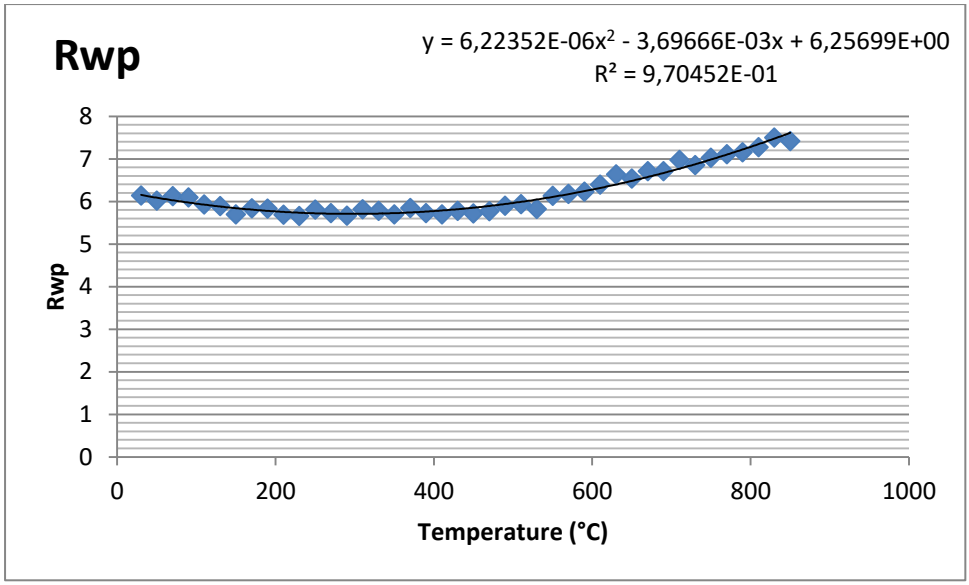


*Figure 4-102: The Rwp values relative to temperature for the VT-PXRD sequential Rietveld refinement of $Gd_2Ti_2O_7$ diffraction data.*

Although the goodness of fit and Rwp plots indicate satisfactory refinements, the Beq values obtained for the two oxygen atoms do not follow any trend (figures 4.103 and 4.104). The Beq values for the Gd and Ti atoms do however follow an increasing trend. As can be seen in figures 4.105 and 4.106, both Gd and Ti Beq's hit the lower limits set for the refinement up until 230 and 470°C respectively.

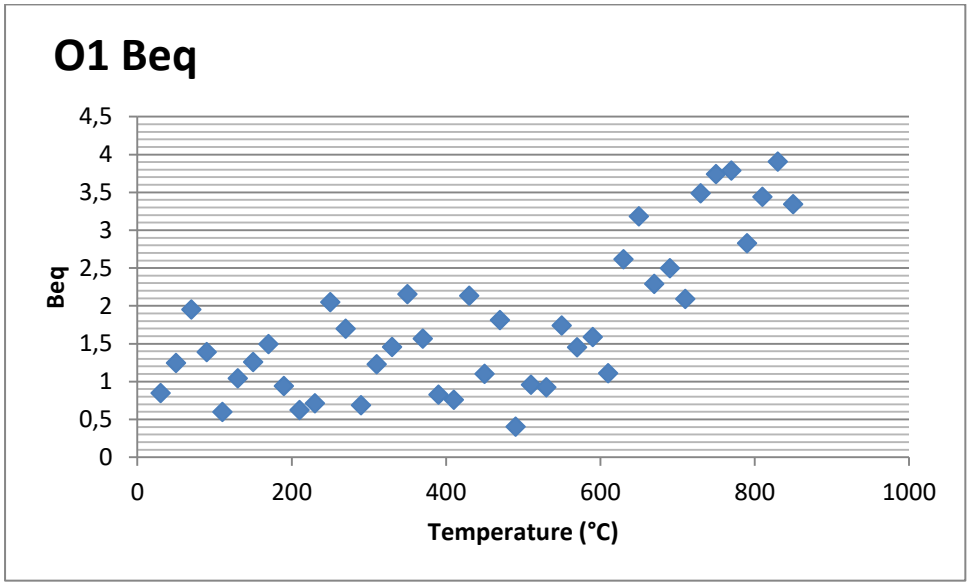


*Figure 4-103: The 48 oxygen Beq values relative to temperature for the VT-PXRD sequential Rietveld refinement of $Gd_2Ti_2O_7$ diffraction data.*

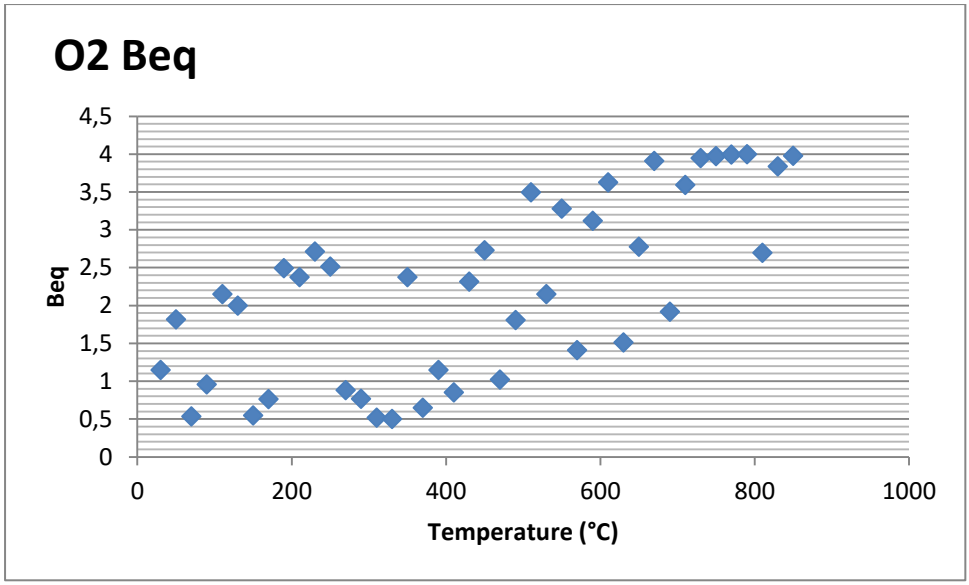


*Figure 4-104: The 8 oxygen Beq values relative to temperature for the VT-PXRD sequential Rietveld refinement of $Gd_2Ti_2O_7$ diffraction data.*

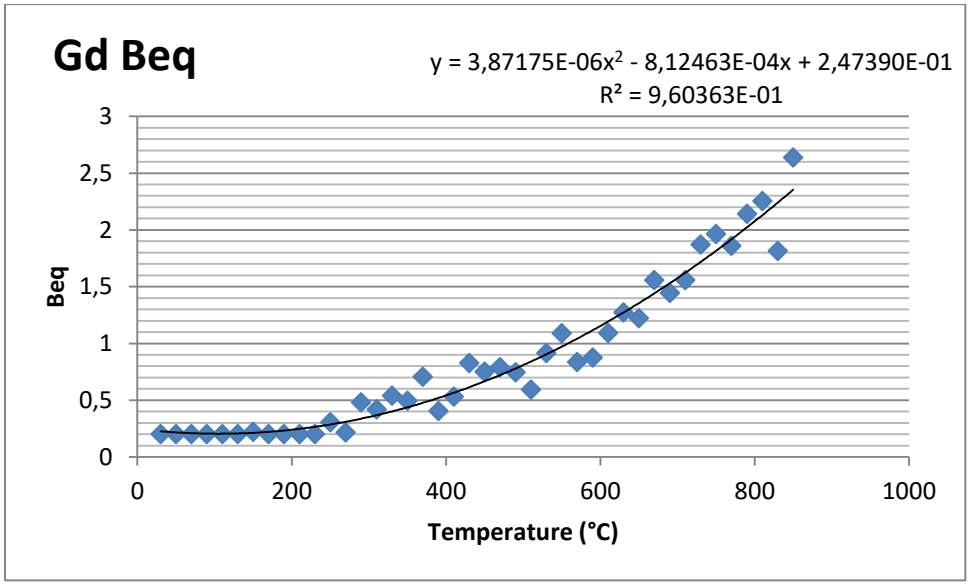


*Figure 4-105: The gadolinium Beq values relative to temperature for the VT-PXRD sequential Rietveld refinement of $Gd_2Ti_2O_7$ diffraction data.*

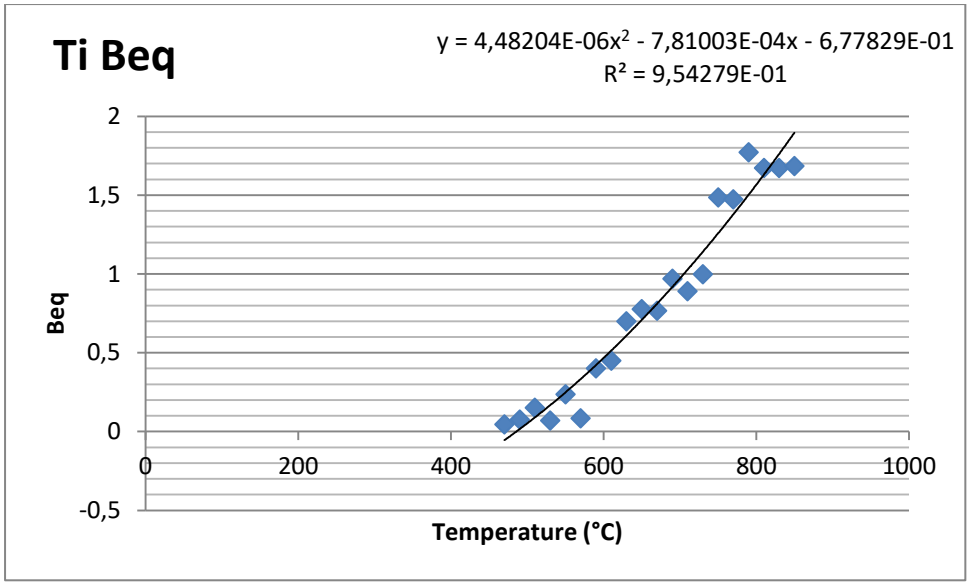


*Figure 4-106: The titanium Beq values relative to temperature for the VT-PXRD sequential Rietveld refinement of $Gd_2Ti_2O_7$ diffraction data.*

The x position of the 48f oxygen atom does not display any realistic trend as can be seen from figure 4.107. The position oscillates around a trend line and increases in amplitude as temperature increases. The range of positions extend from $x = 0.3288$ at 450°C to $x = 0.3401$ at 830°C.

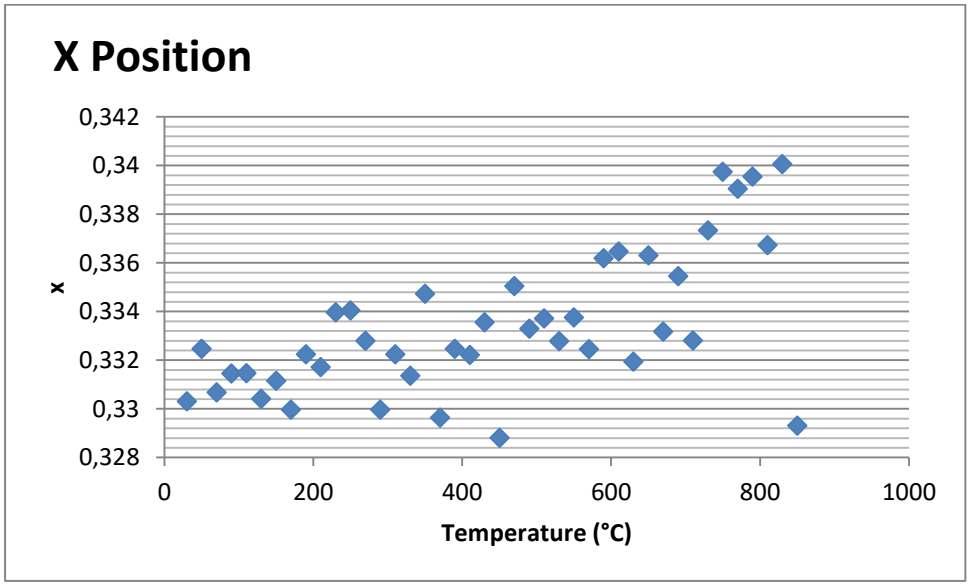


*Figure 4-107: The 48f x-position relative to temperature for the VT-PXRD sequential Rietveld refinement of $Gd_2Ti_2O_7$ diffraction data.*

From the function fitted to the lattice parameter data relative to temperature, as well as knowing the formula for the coefficient of thermal expansion, one can easily predict that the α will be a linear function, and not a single value. This function is $\alpha = -5.99 \times 10^{9}T + 9.15 \times 10^{-6}$ and is illustrated in figure 4.108. due to the linear nature of the function, the highest α value occurs at 25°C with a

magnitude of 8.97 ppm.°C$^{-1}$ and a minimum at 850 °C with a value of 4.06 ppm.°C$^{-1}$. The average thermal expansion coefficient was found to be 6.52 ppm. °C$^{-1}$.

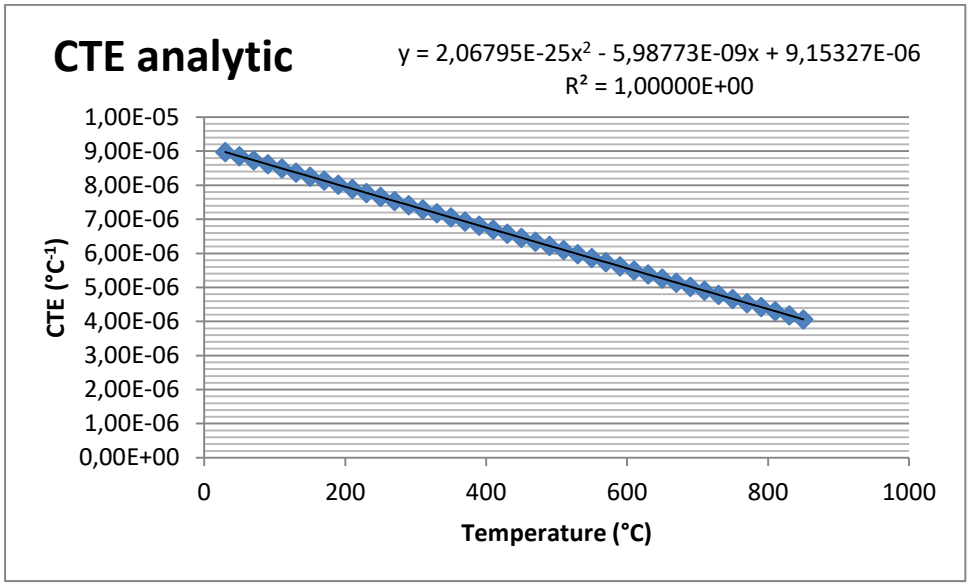


*Figure 4-108: The coefficient of thermal expansion relative to temperature for the VT-PXRD sequential Rietveld refinement of $Gd_2Ti_2O_7$ diffraction data.*

### 4.3.3. Yttrium Titanate

#### Phase analysis

In a comparison between the patterns of $Y_2Ti_2O_7$ taken using $CoK_{\alpha 2}$ radiation before and after the variable temperature experiment as seen in figures 4.109 and 4.110 respectively, it is clear that no permanent change to the sample occurred during the heating process up to 850°C during the variable temperature measurement.

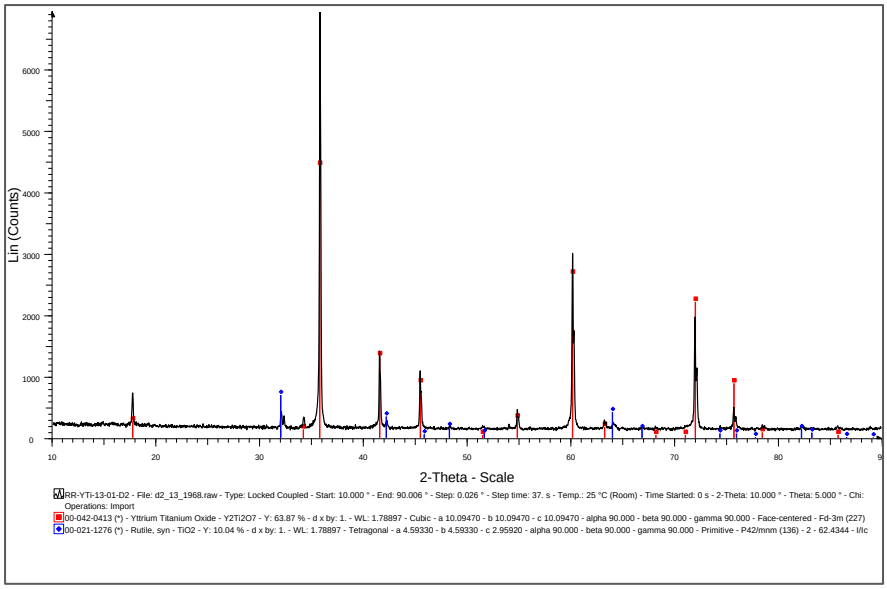


*Figure 4-109: A CoK$_{\alpha 2}$ diffraction pattern taken of $Y_2Ti_2O_7$ taken before the VT-PXRD experiment.*

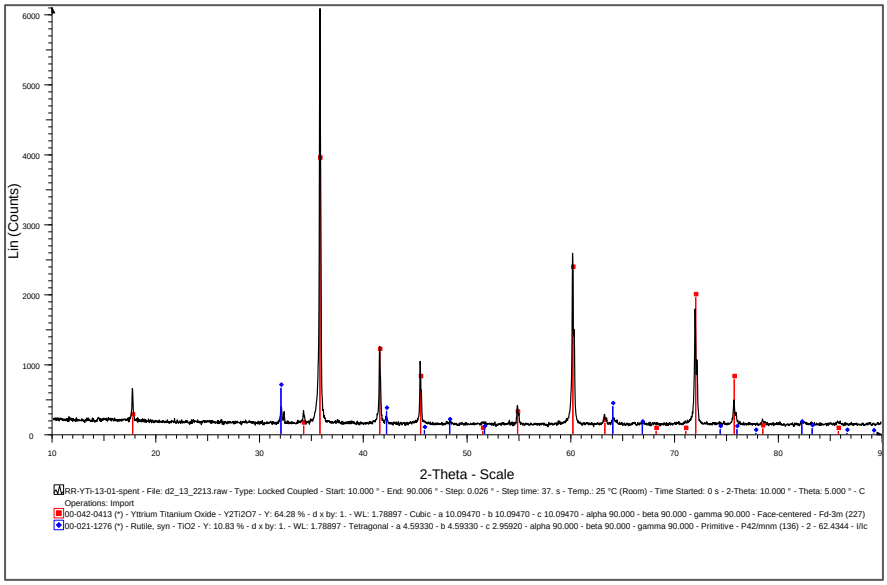


*Figure 4-110: A CoK$_{\alpha 2}$ diffraction pattern taken of $Y_2Ti_2O_7$ taken after the VT-PXRD experiment.*

A peak matching analysis indicates that the material formed was indeed a pyrochlore structure. An impurity phase was also identified within the sample, which was determined to be the rutile phase of titanium oxide, thus serving as an indication of excess titanium isopropoxide in the initial sol-gel synthesis or a possible side reaction occurred during synthesis.

The variable temperature measurements indicate no phase change occurred during the heating process as can be seen in the cascading plot of figure 4.111. This was confirmed by observing each pattern and comparing it to the pattern of the previous temperature. This confirms that the material was thermally and structurally stable over the entire temperature range.

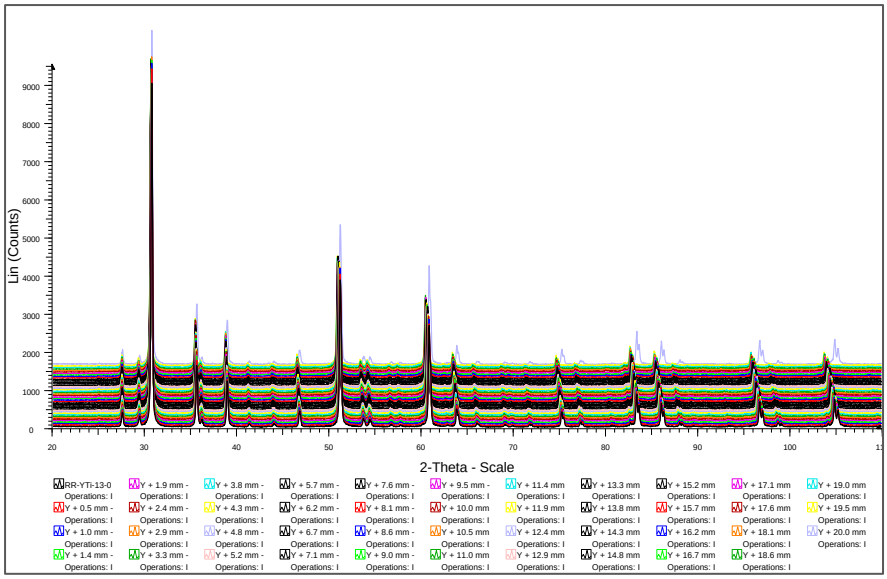


*Figure 4-111: Cascading diffraction patterns of $Y_2Ti_2O_7$ obtained from a VT-PXRD experiment.*

The shift of the peaks in the variable temperature measurement to lower angles implies the presence of positive thermal expansion.

## Structural observations

The difference plot for the Rietveld refinement of the $CoK_{\alpha 2}$ (ambient) data of yttrium titanate indicates a minor mismatch between the calculated and observed pattern. This error arose from the model underestimating the width of the peaks, as illustrated in figure 4.112.

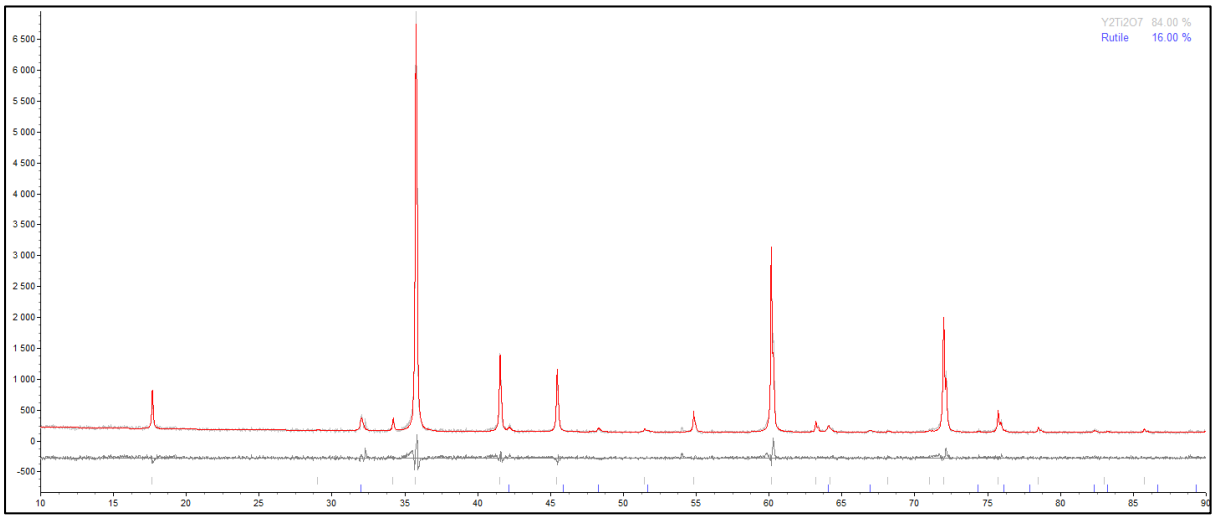


*Figure 4-112: The $CoK_{\alpha 2}$ difference plot of $Y_2Ti_2O_7$ obtained after completion of the Rietveld refinement procedure discussed in section 2.4.10.*

A similar result was obtained for the difference plot obtained from the Rietveld refinement of the 30°C $CuK_{\alpha 2}$ pattern (Bruker D8) of yttrium titanate. The calculated peak width is slightly less than that of the observed peak, leading to the distortions of the difference plot observable in figure 4.113

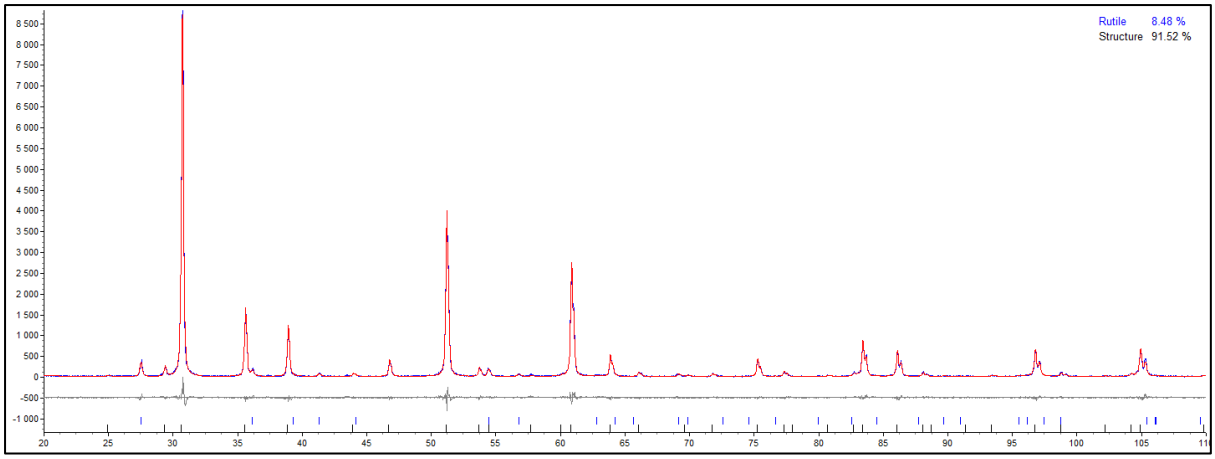


*Figure 4-113: The $CoK_{\alpha 2}$ difference plot of $Gd_2Ti_2O_7$ obtained after completion of the Rietveld refinement procedure discussed in section 2.4.11.*

The plot of lattice parameter against temperature is given in figure 4.114. The plot appears linear by inspection, but a second order polynomial was chosen to fit the data as it better describes the change in the coefficient of thermal expansion, to be discussed later in this passage. The function describing the lattice parameter magnitude with respect to temperature is $a = 3.45 \times 10^{-9}T^2 + 1.01 \times 10^{-4}T + 1.01 \times 10^{1}$. Only considering observable data, the minimum lattice parameter was determined to be 10.0974(1)Å at 30°C and the maximum lattice parameter magnitude was 10.1825(1)Å at 850°C.

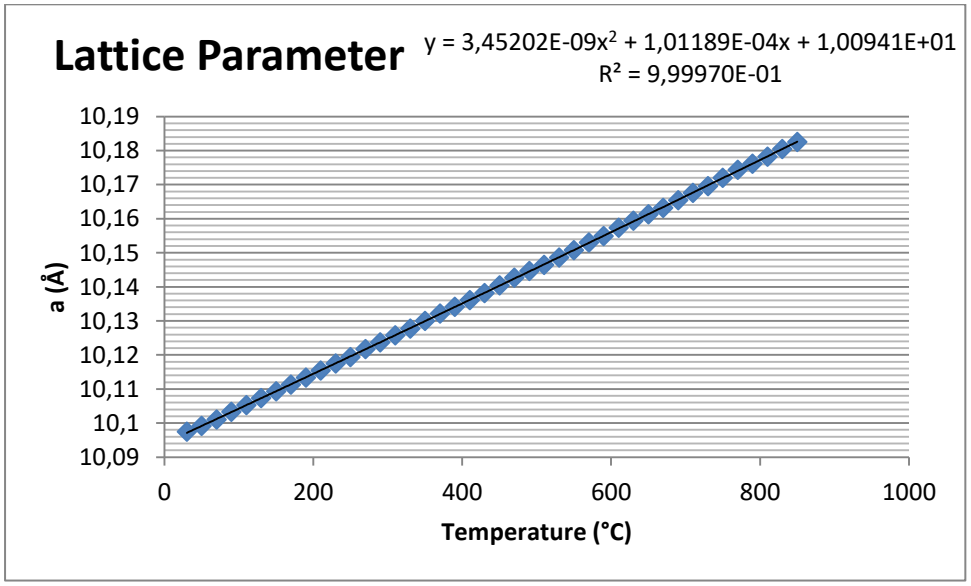


*Figure 4-114: The lattice expansion relative to temperature for the VT-PXRD sequential Rietveld refinement of $Y_2Ti_2O_7$ diffraction data.*

The Rwp value relative to temperature did display some oscillations about its trend line, as can be seen in figure 4.115, resulting in the poor $R^2$ value of 0.94. The lowest Rwp value occurred at 70°C with a value of 12.03, and the maximum occurred at 830°C with a value of 14.42.

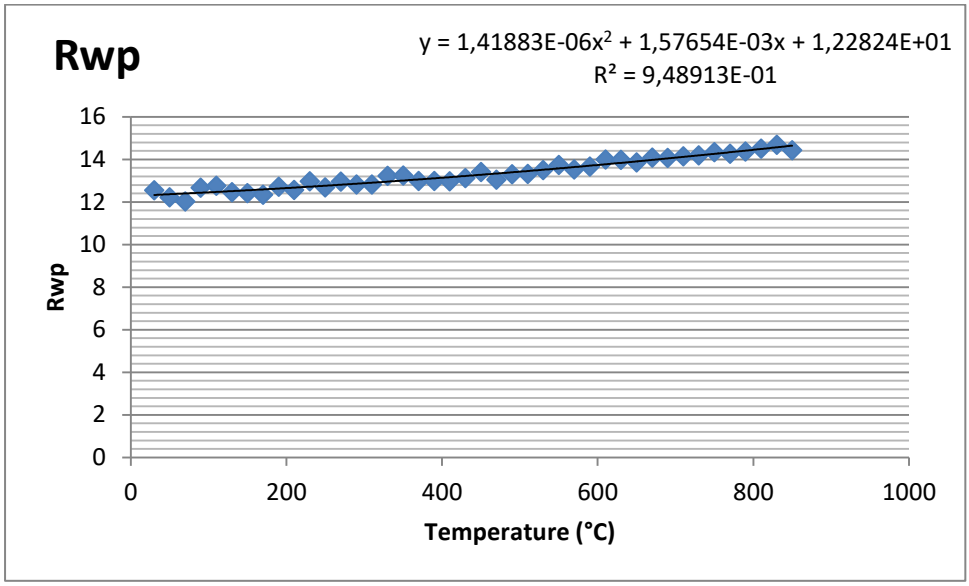


*Figure 4-115: The Rwp values relative to temperature for the VT-PXRD sequential Rietveld refinement of $Y_2Ti_2O_7$ diffraction data.*

The high Rwp values in turn have produced high goodness of fit values, as can be seen in figure 4.98. What is immediately evident from figure 4.116 is that the oscillations about the trend line have increased in comparison to the Rwp values. This is due to how the goodness of fit is calculated, which causes changes to appear inflated in comparison to it Rwp analogue. Like the Rwp value, the minimum for the goodness of fit occurred at 70 °C with a value of 1.29 and a maximum occurring at 830 °C with a value of 1.42. These values are high and indicate that the fit is not entirely satisfactory, however, the positions of the peaks can be considered accurate, hence providing accuracy for the lattice parameter and other values derived from it.

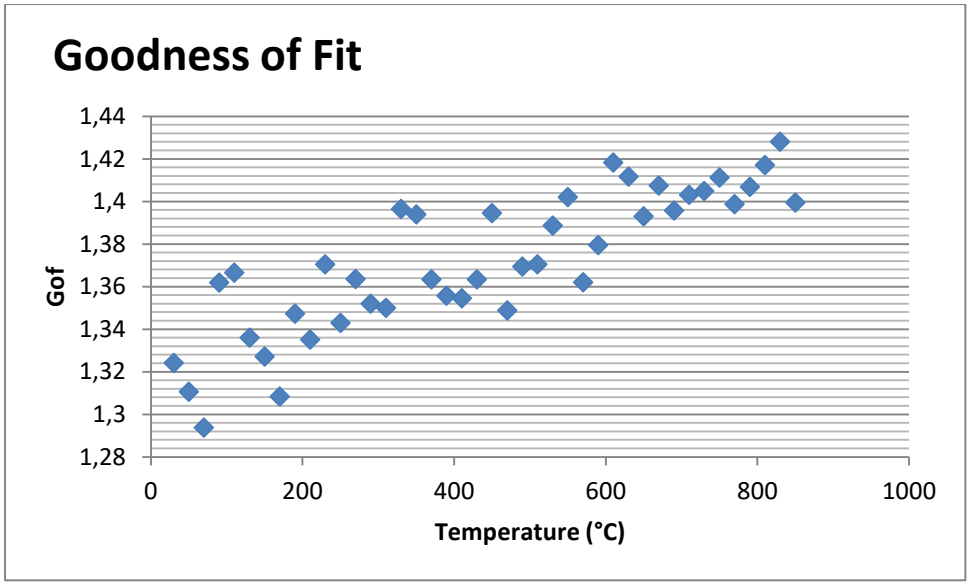


*Figure 4-116: The goodness of fit relative to temperature for the VT-PXRD sequential Rietveld refinement of $Y_2Ti_2O_7$ diffraction data.*

The X position of the 48f oxygen atom (O1) displayed a decreasing trend with significant oscillation about the trend line, yielding a poor $R^2$ value of 0.60, as can be seen in figure 4.117. The maximum for this value occurred at 230°C with a magnitude of 0.4198.

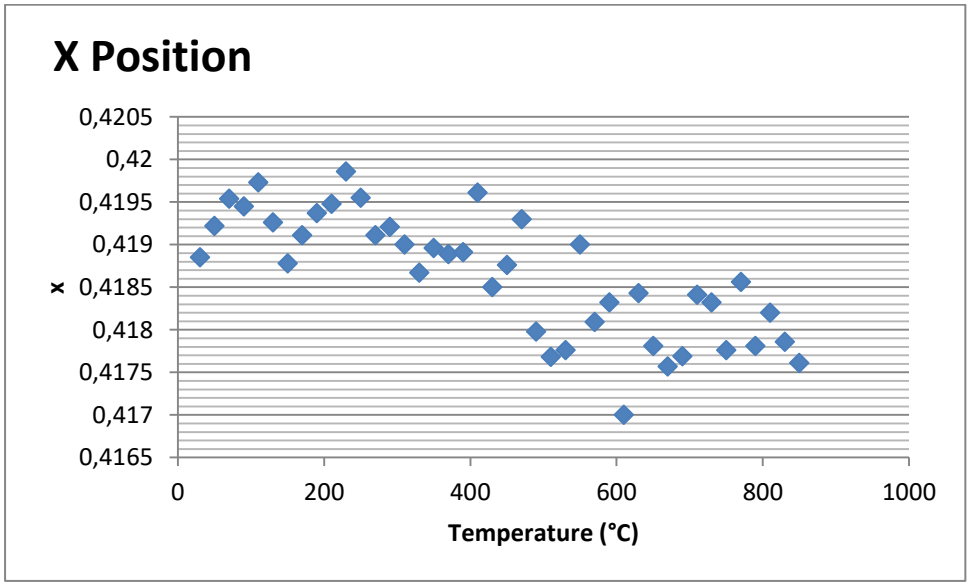


*Figure 4-117: The 48 x-position relative to temperature for the VT-PXRD sequential Rietveld refinement of $Y_2Ti_2O_7$ diffraction data.*

The thermal parameters for Y, Ti, and O1 all displayed reasonable trends, increasing in magnitude with temperature. O2 did have two Beq values of zero occurring at 290°C and 310°C respectively. All of the thermal parameters oscillated about each of their trend lines respectively, which can be seen in figures 4.118 to 4.121.

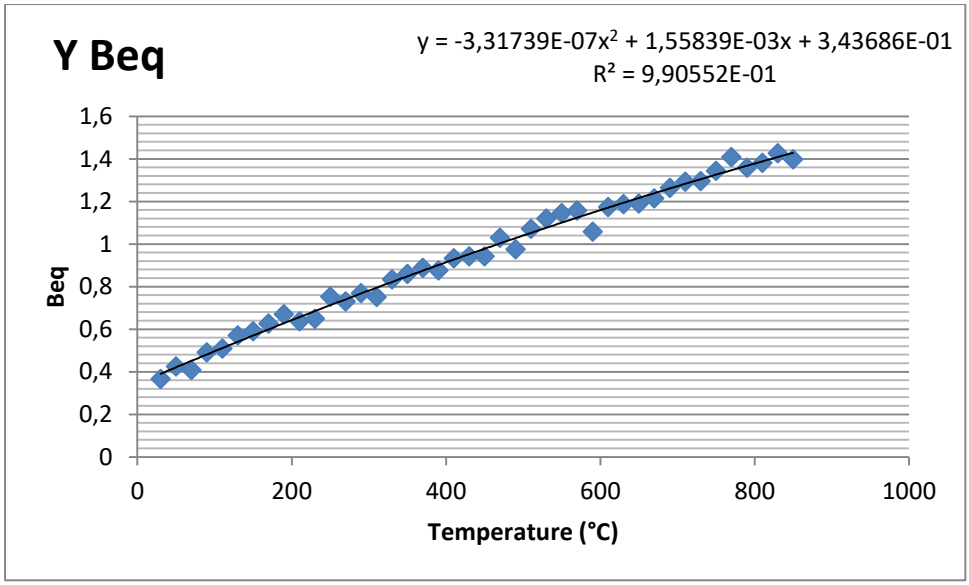


*Figure 4-118: The yttrium Beq values relative to temperature for the VT-PXRD sequential Rietveld refinement of $Y_2Ti_2O_7$ diffraction data.*

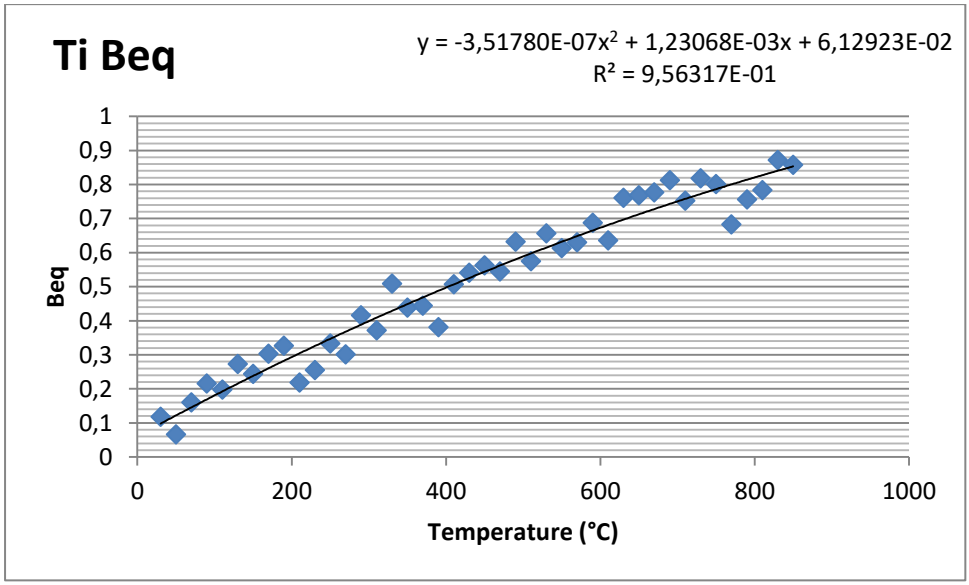


*Figure 4-119: The titanium Beq values relative to temperature for the VT-PXRD sequential Rietveld refinement of $Y_2Ti_2O_7$ diffraction data.*

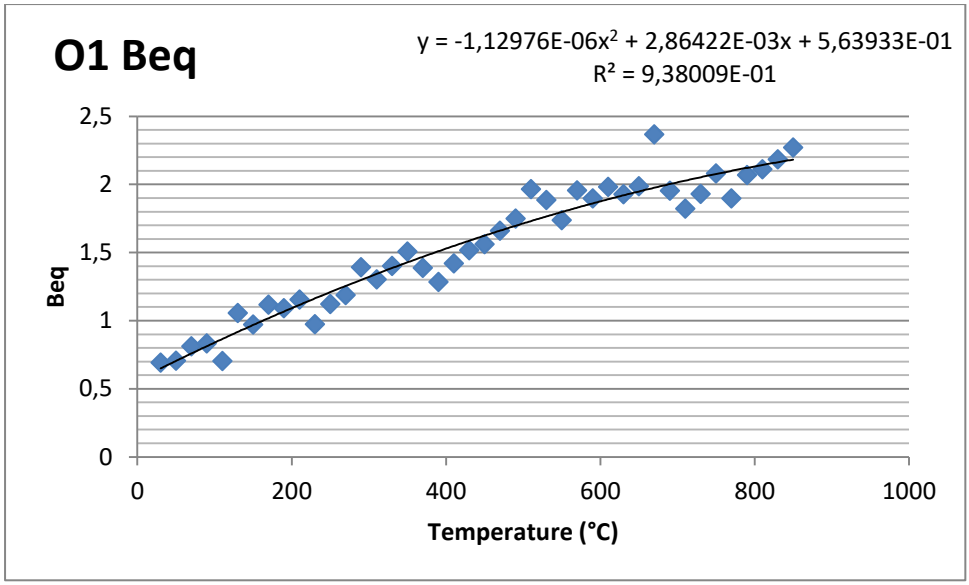


*Figure 4-120: The 48f oxygen Beq values relative to temperature for the VT-PXRD sequential Rietveld refinement of $Y_2Ti_2O_7$ diffraction data.*

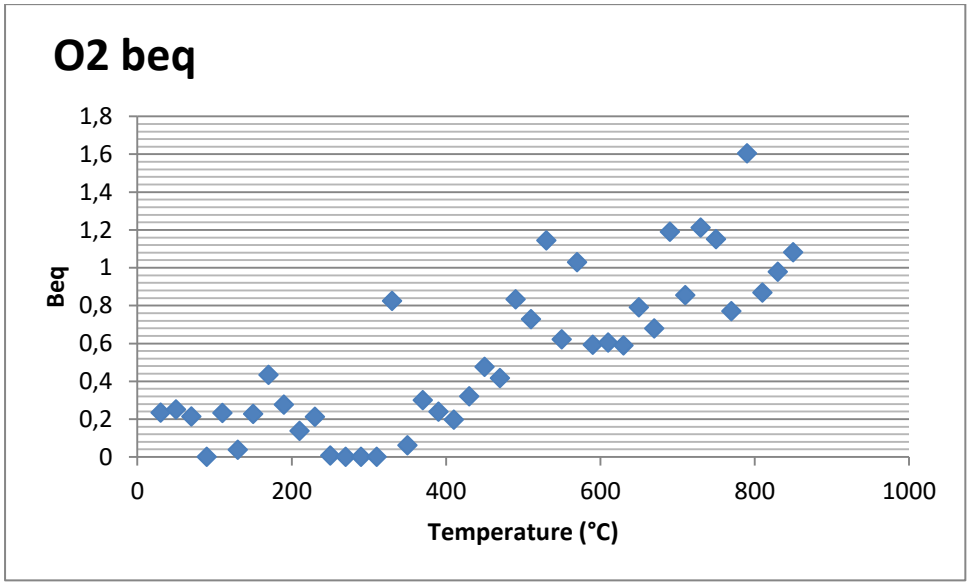


*Figure 4-121: The 8a oxygen Beq values relative to temperature for the VT-PXRD sequential Rietveld refinement of $Y_2Ti_2O_7$ diffraction data.*

The yttrium titanate pyrochlore displayed an increasing thermal expansion coefficient, illustrated in figure 4.122, following the linear function $\alpha = 6.84 \times 10^{-10}T + 1.00 \times 10^{-5}$. The lowest α value within the experimental temperature range was found to be 10.05ppm.°C$^{-1}$ at 30°C, and the maximum of 10.59ppm.°C$^{-1}$ at 850°C. The average of all the plotted α values corresponded with the α of the data had the lattice parameter been described using a linear function, which was a value of 10.33 and 10.32ppm.°C$^{-1}$ for the linear and polynomial variants respectively. This indicates that the choice of a

polynomial over a linear function did yield more information. The average thermal expansion coefficient was found to be 10.32 ppm. $°C^{-1}$.

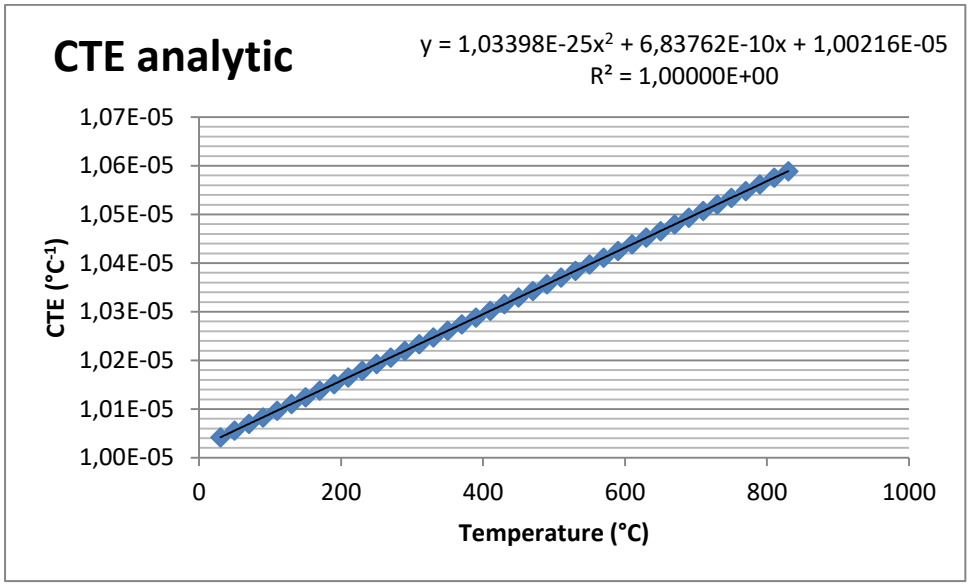


*Figure 4-122: The coefficient of thermal expansion relative to temperature for the VT-PXRD sequential Rietveld refinement of $Y_2Ti_2O_7$ diffraction data.*

# 5. Discussion

## 5.1. Phase analysis

The pyrochlore stability plot found in figure 3.1 gives the previously defined region of stable pyrochlores at ambient pressures, as discussed by Ewing *et al* (Ewing, Weber, & Lian, 2004). Table 5.1 below lists the materials of this work, comparing their phases to that of the defined stable structure according to the stability range as proposed by Ewing *et al*, as well as what has been observed in literature for stoichiometric oxides.

*Table 5.1: Pyrochlore/defect-fluorite populations*

| Species | Experimental Phase | Pyrochlore stability (Ewing *et al*) | No. of pyrochlores in the ICSD | No. of defect fluorites in the ICSD |
|---|---|---|---|---|
| $La_2Hf_2O_7$ | Pyrochlore | Stable | 2 | 0 |
| $Eu_2Hf_2O_7$ | Pyrochlore | Stable | 2 | 0 |
| $Gd_2Hf_2O_7$ | Pyrochlore | Stable | 1 | 0 |
| $Y_2Hf_2O_7$ | Defect-Fluorite | Unstable | 0 | 0 |
| $Gd_2Zr_2O_7$ | Pyrochlore | Stable | 12 | 8 |
| $Y_2Zr_2O_7$ | Pyrochlore | Unstable | 1 | 26 |
| $Eu_2Ti_2O_7$ | Pyrochlore | Unstable | 3 | 0 |
| $Gd_2Ti_2O_7$ | Pyrochlore | Stable | 9 | 0 |
| $Y_2Ti_2O_7$ | Pyrochlore | Stable | 8 | 0 |

Of the eleven materials listed in table 7.1, only $La_2Hf_2O_7$, $Gd_2Zr_2O_7$, $Gd_2Ti_2O_7$, $Gd_2Hf_2O_7$ and $Y_2Ti_2O_7$ correctly followed literature and formed the pyrochlore phase.

It should be noted that $La_2Hf_2O_7$ was an exception due to its odd peak profile, leading to its poor figures of merit in the Rietveld refinement. Also, observing figure 4.1, the diffraction peaks unique to the pyrochlore lattice are of low intensity when compared to the most intense peak. In figure 4.1, the peaks are not visible, this is due to the use of a zero background holder, which reduced peak intensity due to less available diffracting material. In all diffraction patterns obtained for lanthanum hafnate pyrochlore, the peak shapes are broad. This may be a result of the synthetic procedure producing nanoscale-crystalline material. However, the size of the crystallites was not obtained due to the poor peak shape observed. The particle size of a material is related to the width of the peaks, with smaller

nanoparticles causing wider diffraction peaks. An accurate means of determining the width of these particular peaks is not available. Figure 4.2 illustrates a calculated pattern graphed from the use of a structure obtained from the ICSD (reference code 173790 (Whittle, Cranswick, Redfern, Swainson, & Lumpkin, 2009)) overlaid on an experimental pattern obtained from a Bruker D2 Phaser fitted with a CoKα X-Ray tube (see section 2 for details). In this illustration, the extent to which the peaks have a very poor profile can be seen, particularly at high 2θ angles. The calculated pattern coincides with the first inflection of the peak. The peaks continue to tail on after this co-incision point. One speculation is that there are two similar, non-stoichiometric phases which have been formed from the initial stoichiometric reagents. Confirmation of this possibility lies outside the scope of the project and has been suggested for future endeavours. It is important to note that this unusual peak shape is stable over the entire temperature range of the VT-PXRD experiment.

The diffraction patterns for $Gd_2Ti_2O_7$ display only the pyrochlore phase of the material with no other impurities. The peaks, as for all the titanate pyrochlore phases in this study, are sharper than what was observed for the other materials. The peak shape was ideal as the goodness of fit obtained for the Rietveld refinement of the VT-PXRD sequential refinement was low, as discussed in section 4.3.2., and illustrated in figure 4.85. Comparing the CoKα2 diffraction patterns of the material before and after the VT-PXRD experiment, one can clearly see that there are no phase changes observed for this material. This notion was further proven from the lack of phase changes observed in the cascading plot illustrated in figure 4.81. The plot indicates no high temperature phase changes, with the only changing observable being the peak positions gradually moving to lower angles, which reveals a positive thermal expansion of this material. The quality of the peak fit also indicates consistency in the peak shape.

$Y_2Ti_2O_7$ also crystallized in the pyrochlore system, yet displayed evidence of either excess titanium isopropoxide in the synthetic procedure, or the possibility of side reactions. In either case, the material may not be a stoichiometric oxide. The material was shown to crystallise solely in the pyrochlore phase, although the high goodness of fit values indicate that the peak shape is not ideal for the model. The cascading plot of the VT-PXRD experiment had no evidence of phase change, implying the material is stable over the entire temperature range. The experimental value of the lattice parameter compared matched the lattice parameters of the stoichiometric oxides in literature closer than the non-stoichiometric oxides. The closest match was to the structure determined by Chtoun *et al* (with ICSD reference number 83593). The lattice parameters of each material will be discussed in section 5.2.

Gadolinium hafnate crystallised in the pyrochlore phase as determined in a separate Raman spectroscopic study*. The CoKα2 diffraction pattern (illustrated in figure 4.25) provides little evidence of the pyrochlore phase, except for very slight elevations from the background signal close to suspected pyrochlore supercell peaks. These peaks are too unresolved to add any useful information to the refinement. Also, the peak width and height were indicative of a nano-crystalline material. The material contains only the pyrochlore phase as no impurity phases have been detected. The cascading diffraction patterns obtained from the variable temperature experiment indicate no phase changes of the entire temperature range of the experiment. Also, there is little observable change in the width of the peaks before and after the VT-PXRD experiment, implying little annealing took place, and that the nano-crystalline nature of the product is stable over the temperature range. There was only one entry of stoichiometric gadolinium hafnate in the ICSD. The other non-stoichiometric entry was also a pyrochlore phase

Gadolinium zirconate was shown to crystallise in the pyrochlore phase in a separate Raman spectroscopic study*. This was not evident in the diffraction pattern illustrated in figure 4.46, where none of the super-cell peaks characteristic of the pyrochlore phase were visible. This is due to the intensity of the broad peaks. The material was shown in a VT-PXRD experiment to be stable over the entire temperature range although drastically lower intensity counts were obtained in this experiment as can be seen in the cascading diffraction patterns in figure 4.47. The lower counting statistics may have occurred due to the presence of gadolinium, known for X-ray absorption. Using information from the ICSD, it was noted that 12 of the 20 entries for gadolinium zirconate crystallised in the pyrochlore phase whilst 8 did so in the defect-fluorite phase. This was the most evenly spread distribution of the two phases out of all the presented materials. Observing figure 3.1, (the pyrochlore stability chart) it is clear that the ratio of $r_a/r_b$ lies on the lower limits of stability, indicating that the material is likely to exist stably in both phases. It is important to state that the alkoxide condensation sol-gel methodology produced nano-crystalline gadolinium hafnate in the pyrochlore phase, which remained stable over the temperature range of 30-850°C.

At this point it is important to note that none of the materials followed the theory described by Ewing *et al* without corresponding to literature. However, there were several species that show promise to crystallise according to the stability region plot, but there are not enough structures available in the literature to confirm this. These materials include $Eu_2Hf_2O_7$, and $Y_2Hf_2O_7$.

* Miller and Billing, unpublished results

Supporting information may be obtained from Dr. Stuart Miller; stuart.miller@wits.ac.za

$Eu_2Hf_2O_7$ crystallised in the pyrochlore phase, and remained stable over the entire temperature range of the VT-PXRD experiment. Contemplating the diffraction patterns obtained for the material using CoKα2 radiation, there are unassigned peaks occurring at approximately 12 °2θ and at 31 °2θ (see figure 4.13). The lower angle peak, on inspection, appears as if they belong to the pyrochlore (111) reflection, but the peak was too diffuse and too low in intensity to adequately contribute to the refinement. The remaining anomalous peak is most likely associated with the pyrochlore super-structure, however, the peak is not resolved enough to adequately place its location. The model did not allow for the peak to be refined as the (111) reflection indicating the low resolution of the reflection. (Note: The (111) peak was too diffuse for Topas to minimise the position of the peak's centre) Also, a calculated powder pattern of the material (figure 5.1) indicates that this peak should occur near 17 °2θ. The diffraction pattern of the material was obtained after the VT-PXRD experiment using CoKα2 radiation as a comparison to the initial CoKα2 pattern. The anomalous peaks were no longer observable in this pattern, as can be seen in figure 4.15. A possible reason for this change could be that the peaks were hidden below the background. The pattern was measured using a zero-background holder for the sample. This was due to less material being available for the measurement. As a result, there was less material to diffract the incident radiation, and hence less intensity. As can be seen by the cascading plots, additional peaks occurred upon cooling down back to 30 °C, which were attributed contamination by corrosion products of the XRK 900 sample chamber. This corrosion was not removed from the sample, and did not appear in the CoKα2 diffraction pattern. This was attributed again, to the low concentration of the material.

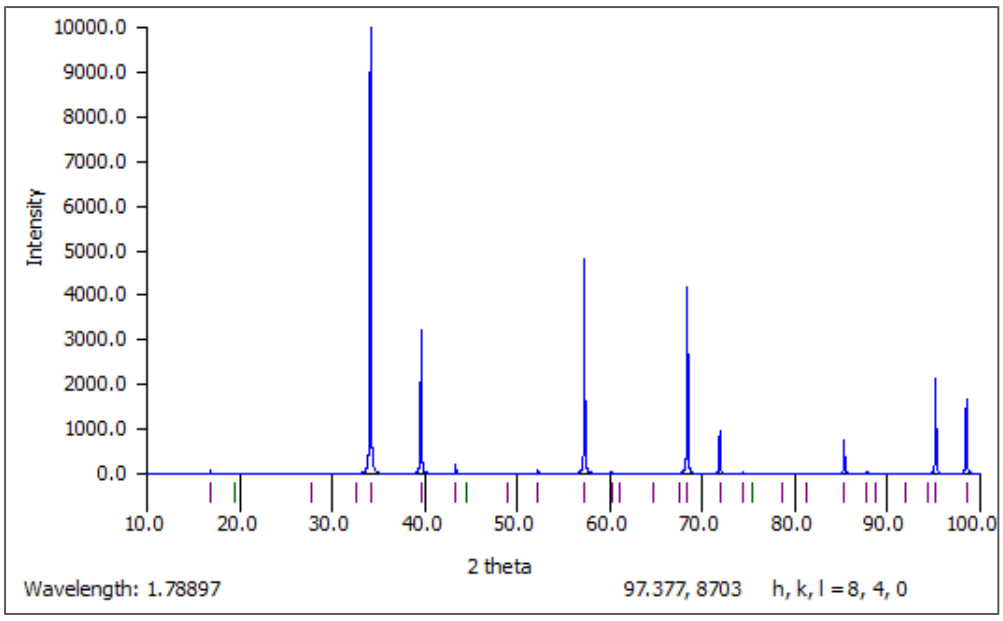


*Figure 5-1: A calculated pattern of $Eu_2Hf_2O_7$. (Chien, 1978).*

The figures of merit from the Rietveld refinement are low enough to consider that the model chosen for the material adequately describes the material, and hence the peak shape is correct for a single phase material. Table 7.3.1, shows a list of all available structures on the ICSD of materials related to this study and indicates that only three structures were submitted for materials containing europium hafnium and oxygen in the pyrochlore phase. Two were non stoichiometric, and the stoichiometric variant did not have an R factor associated with it. The stoichiometric entry was obtained from A Mossbauer study by Chien *et al,* and the paper does not describe the means by which the structure was elucidated (Chien, 1978).

$Gd_2Hf_2O_7$, behaved in a similar manner to its europium containing equivalent discussed previously, in that it matched the pyrochlore stability range plot illustrated in figure 3.1 but there was not enough evidence to suggest that it will necessarily obey that rule. The material did however crystallise in the pyrochlore phase. The cascading plot implies that the material was stable in this phase over the entire temperature range; this can be seen in figure 4.26. As with europium hafnate, the last diffraction pattern in the cascading plot displays anomalous peaks, the most intense occurring at approximately 43 °2θ. This was attributed to corrosion falling on the sample during the cooling cycle of the XRK 900. The peak shape and intensity of this material is broader and lower than what was observed for europium hafnate.

The figures of merit obtained from the Rietveld refinement of the VT-PXRD experiment for gadolinium hafnate were sufficiently low to establish that the diffraction peaks were suitably modelled, and that the material was single phase. This applied throughout the entire experiment, and hence implies that the phase was stable up to 850 °C. The crystallographic information table in section 7.3.1 only lists two entries for gadolinium hafnate, both of which are pyrochlore. However, upon inspection of the cif files of each material, both cif files appear identical, with the exception of details such as the ICSD database code numbers, the chemical name, the structural formulae, and the name of the publications from whence came each structure including different journals. It is for this reason that the number of structures listed in table 5.1 for gadolinium hafnate has been reduced to one. It is suspected that the defect fluorite phase for Gadolinium hafnate may be possible to synthesise as it has a $r_a/r_b$ ratio on the lower limits of the pyrochlore stability region (see figure 3.1).

$Y_2Zr_2O_7$ crystallised in the pyrochlore phase, which according to Ewing *et al*, is unlikely, as the $r_a/r_b$ ratio for the oxide lies below of the recommended region, as can be seen in figure 3.1. The crystallographic information table in section 7.3.1. indicates that only one entry in the ICSD of $Y_2Zr_2O_7$ crystallises in the pyrochlore phase. This phase was determined by first principles methods by Pruneda *et al*, hence describing the lack of an R factor for the measurement (Pruneda & Artacho, 2005). The

calculated pattern of this structure by Pruneda *et al* does not display the low angle peak seen in figure 5.2, the pattern taken before the VT-PXRD experiment was performed. It is important to note that no match for the pyrochlore or defect fluorite phase could be found for yttrium zirconate in Diffrac Eva, so the defect fluorite phase for gadolinium zirconate was used to indicate the cubic nature of the material in figure 5.2. Also, the peak that lies between 15 and 17°2θ is quite wide and poorly formed. The choice of refinement with using the pyrochlore phase was based on the fit of this peak, which was adequate for the refinement. This can be seen in figures 4.61 and 4.62 as both the goodness of fit and the Rwp remain low across the entire temperature range of the VT-PXRD experiment. The cascading patterns (figure 4.59) show no signs of phase change across the entire temperature range, and hence the material is stable as a pyrochlore in the temperature range. A further study could be conducted to determine the phase change point of the material.

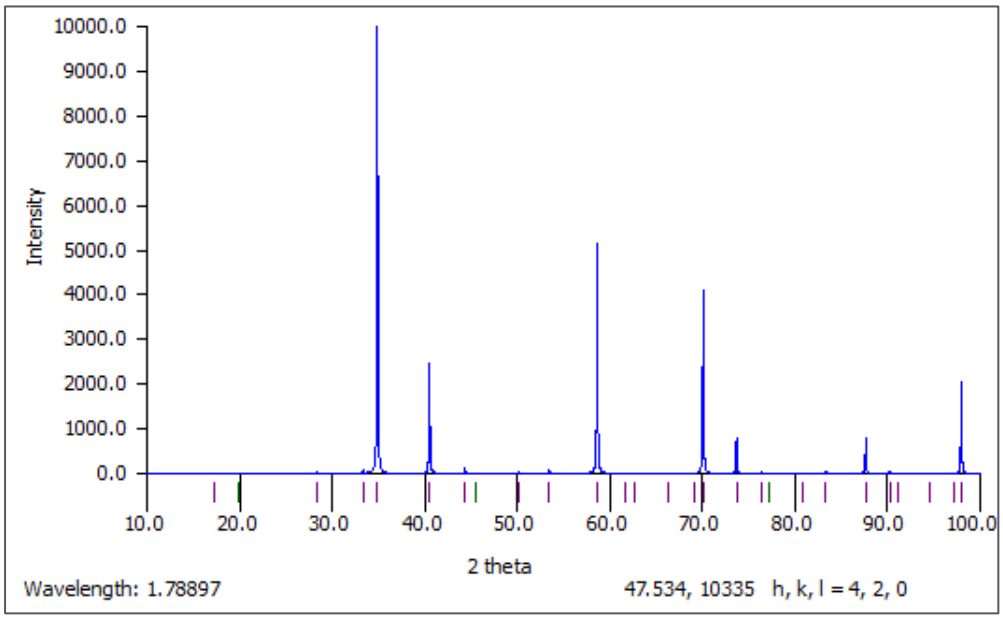


*Figure 5-2: A calculated pattern of $Y_2Zr_2O_7$ (Pruneda & Artacho, 2005).*

$Eu_2Ti_2O_7$ was the only material that crystallised in the pyrochlore phase that according to the stability region plot (figure 3.1), should not be stable as a pyrochlore. It also shows no evidence in the literature and the ICSD to possible phase changes. The crystallographic information table in section 7.3.1. indicates only three structures reported for this mixed metal oxide, all of which are of the pyrochlore crystal structure. Two of the structures are non-stoichiometric, whilst the third is. The stoichiometric structure was obtained from the work by Chien *et al*, which was a Mossbauer study on europium pyrochlores. This explains why there is no R factors associated with the structure submitted into the ICSD. Figure 4.70 is the diffraction pattern of the material taken under CoKα2 radiation. It clearly labels the presence of two phases, namely the europium hafnate pyrochlore as the main phase (indicated in red), and the rutile phase of titanium dioxide (indicated in blue). There are two possible ways by which

the rutile phase occurred. The first being an excess of titanium isopropoxide being present in the initial sol gel experiment. The other two situations involve either a side reaction in which the pyrochlore decomposes slightly to form rutile, or titanium dioxide is removed from the mixed metal oxide (forming a non-stoichiometric mixed metal oxide). As there are no europium oxides present in the diffraction pattern, it would imply that the material formed was non-stoichiometric, as the pyrochlore phase has remained intact (or the concentration of the alkoxide reactant had changed with time). There is a complication with this in that for every titanium ion used in the decomposition reaction, two europium ions would be used, halving the amount of $Eu_2O_3$ available for diffraction. This is not an issue in this case as the peak height for the rutile phase is significantly higher than the background noise. The exact means by which the rutile phase occurred in the diffraction pattern shall be fully discussed in section 5.2, where the Rietveld refinement of the material was discussed in greater detail. Comparing the CoKα2 patterns taken before and after the VT-PXRD experiment for europium titanate, it becomes clear that there is little change, apart from the intensities of the peaks. The differing intensities, as discussed for other materials in this study, occurred due to less available material for the second measurement. This observation was also observed in the cascading plot of figure 4.69. The plot indicates no phase change throughout the temperature range, and upon inspection, little change to peak width (although this was better described by the sequential Rietveld refinements). This acts as evidence of the stability of the material over the given temperature.

Using the specific outcomes discussed above, some trends can be noted. All the titanate systems in this study formed pyrochlore phases, with little evidence of having a stable defect-fluorite phase. Both zirconate systems formed the pyrochlore phase despite the yttrium zirconate system being unstable according to the stability region proposed by Ewing *et al*. Of the hafnate systems, only yttrium hafnate formed the defect fluorite phase, which was not obvious from the diffraction results, and required external Raman analysis.

## 5.2. Refinement output

As previously discussed in section 4, the refinement output of the VT-PXRD experiments include the lattice parameter and volume of the unit cell, the goodness of fit and the Rwp of the refinement, the calculated crystallite size, the thermal parameters of each symmetrically unique atom in the unit cell and the x-position of the 48f oxygen when applicable. To discuss the particulars of the refinement process, each of the parameter outputs shall be discussed in turn, focussing on trends in and across each oxide system, while comparing these trends to the literature.

The lattice parameter, and its associated change with temperature are of the most importance to this study as this data answered the hypothesis questions given in section 3.2.2. and 3.2.3., i.e. does the

synthesis method in this study produce materials of significantly similar lattice parameter, or does the material exhibit a different value, and secondly, does the thermal expansion of the material match a single constant value, such as what was reported by Zhang *et al* (Zhang, Xiao, Zu, Fei, & Weber, 2009) or does it follow the change in value as observed by Kutty *et al*. These questions, along with the actual coefficients of thermal expansion, which shall be discussed in section 5.3.

The lattice parameter of a material is determined based on the positions of the peaks in the diffraction pattern, implying that other factors do not influence this property. This however is not the case, as the peak shape of the material may mask the true position of the peak. This was the most likely problem experienced with the lanthanum hafnate system, due to its peculiar peak shape. This however did have a significant effect on the lattice parameter when compared to the two sole entries in the ICSD. Entry 153815 (as can be seen in the crystallographic information table in section 7.3.1.) was obtained from a first principles calculation of the structure in the pyrochlore phase and hence has no associated R factor (Pruneda & Artacho, 2005). The lattice parameter as reported for this structure is 10.673 Å, which is smaller than what was seen for the 30 °C pattern in this study. It was determined to be 10.717(1) Å with a weighted R factor of 10.977. The other entry, ICSD number 173790, was determined experimentally using both neutron diffraction and electron microscopy, which generated an R factor. Given that the structure determined by Whittle *et al* was solved from neutron diffraction data, it can be expected that the quality of the refinement was higher than what was seen in this study. The reason for this can be attributed to the ability of neutron sources to resolve the positions of light elements in contrast to heavy elements, as the neutron does not interact with the electron cloud (as is seen with PXRD) but rather with the nucleus. This can be seen quite clearly in that Whittle *et al* plotted the x position of the 48f oxygen atom against changing stoichiometry generating an observable and rational trend. The refinement of the 48f x-position from this study for the lanthanum hafnate oxide system appeared very noisy and did not follow any particular trend. Also the plot did not coincide with the fluctuations in the figures of merit. The super cell peaks of unique to the pyrochlore phase could not be refined, reducing the amount of information available to determine the lattice parameter.

This changing position of the x position of the 48f oxygen can be seen in all pyrochlore structures involved in this study. As can be seen in figure 4.67, the 48f x position for the yttrium zirconate system, the variation of the 48f x parameter fluctuates over the fractional coordinate range of 0.00581. Similarly, Lanthanum hafnate and europium, gadolinium and yttrium titanates have their 48 f coordinates fluctuate over the fractional coordinate ranges of 0.00687, 0.00555, 0.01125, and 0.00286 respectively. Although the range of fractional coordinates in this case is in fact small, the trend of the change in the 48f x-parameter is not adequately observable which is evidenced by the poor R-

factors of the fitted plots. In a Mossbauer study of the axial field effect gradient of the Eu site in various europium pyrochlores by Chien *et al*, the structure of the materials was determined by refinement of PXRD data, including the refinement of the x position of the 48f oxygen atom. Both structures relevant to this study, namely the europium hafnate and titanate structures were available in the ICSD, both of which were missing R factors in the cif files (see table 7.3.1.). Figure 2 in the paper by Chien *et al* (not illustrated in this document) indicates that the error in the 48f x position is approximately 0.01 fractional units, where the variation for the 48f x parameter over the entire temperature range in the VT-PXRD experiment in this study was 0.00555. This implies very little change actually occurred in the position of the 48f oxygen over the entire temperature range when compared to the error limits of literature (Chien, 1978). However, the study by Chien *et al* was performed in 1978, and the diffractometer used was not mentioned in the paper. This would definitely have an influence on the accuracy of the results in that detection limits of diffractometers have improved vastly over the last three decades. However, the fluctuating nature of the output results of the 48f oxygen's x position still beg the question if X-ray diffraction can be adequately used to determine this position accurately. The room temperature value for the 48f oxygen parameter of europium hafnate as determined by Chien *et al* was 0.342. The titanate system reported in the Chien *et al* paper was 0.327, where the value determined by this study at 30 °C was 0.3272, implying a very close correspondence to literature. Comparing this value to the other entries in the ICSD we see very similar values of 0.328(1) for both entries (Chtoun, Hanebali, Garnie, & Kiat, 1997), (Chtoun, Hanebali, & Garnier, Analyse par diffraction des rayons X, methode de Rietveld, de la structure des, 2001).

Gadolinium titanate was found to have a 48f x-position of 0.3303 according to this study. The values for stoichiometric gadolinium titanate compounds from the ICSD include 0.4319(2), 0.327, 0.3292, 0.4263(34) for the work by Heredia *et al,* Tabira *et al*, Zhang *et al*, and Knop *et al* (Heredia, Quintana Garcia, Perez Mazariego, & Escamilla, 2010), (Tabira, Withers, Minervini, & Grimes, 2000), (Zhang, Xiao, Zu, Fei, & Weber, 2009), (Knop, Brisse, & Castelliz, 1969). The x-position from this study lies closer to the ICSD structures that were determined by computer simulations, namely the structures submitted by Tabira *et al* and Zhang *et al* (ISCD codes 150210 and 164024 respectively). The x-positions determined by Heredia *et al* and Knop *et al* however do not correlate with the observed value from this study, and lie outside of what was defined as a pyrochlore structure. This discrepancy was attributed to different choices in origin, where the structures submitted by Heredia *et al* and Knop *et al* placed the lanthanide on the origin, and the structures submitted by Tabira *et al* and Zhang *et al* placed the titanium ion on the origin. Both Origin choices are listed in the Bilbao crystallographic server (Aroyo, Kirov, Capillas, Perez-Mato, & Wondratshek, 2006) (Aroyo, et al., 2006) (Aroyo, et al., 2011). The choice of origin used for gadolinium titanate places the 16c position on the origin, holding

a site symmetry of -3m. To convert the position of the 48f x-position from the origin choice from the lanthanide to the transition metal, one simply needs to subtract 0.125 from the initial position of the 48f oxygen, as a shift in the unit cell by that fractional distance along the x direction is all that is required to convert the origin. Doing this we find that the 48f positions of the structures submitted by Heredia *et al* and Knop *et al* become 0.3060 and 0.3013.

The refinement for the Yttrium titanate system in this study used the alternate origin choice, where the origin lies on lanthanide element, hence placing the x-position of the 48f oxygen at 0.4189 fractional units at 30 °C. Only two stoichiometric structures of yttrium titanate were reported in the ICSD having values of 0.3253(4) and 0.42082 for entries 83593 and 66874 respectively. Correcting the position of for entry 83593 we find its new position to be 0.4503, a significantly larger value than what was seen in entry 66874.

For the sake of a comparison between yttrium titanate and gadolinium zirconate, a Powder Neutron Diffraction study of the pyrochlore phase of gadolinium zirconate by Kennedy *et al* may give some insight into how the position of the 48f oxygen changes in the pyrochlore phase. In this study, the position also fluctuated over a similar range to what was seen for the materials in this study. The x-position fluctuated over a range of 0.003 fractional units, which is of the same decimal placement as what was seen in this study. Another important note to make is that the errors determined in the study by Kennedy *et al* were over 0.001 fractional units. This is an improvement on the error found in the study by Chien *et al* by a factor of ten, hence implying that the neutron diffraction technique is more suited to accurate determination of the 48f x-position, yet the X-Ray diffraction technique does still hold merit for such measurements.

The discussion of the lattice parameters in this text shall be divided into two sections, namely that for the pyrochlore phases and the defect fluorite phases respectively. Table 5.2 lists all of the lattice parameters obtained at 30 °C from this study.

*Table 5.2: Lattice parameters refined from diffraction data taken at 30°C*

| System | Lattice Parameter |
|---|---|
| $Gd_2Zr_2O_7$ | 10.565(3)Å |
| $Eu_2Hf_2O_7$ | 10.477(1)Å |
| $Gd_2Hf_2O_7$ | 10.418(2)Å |
| $Y_2Hf_2O_7$ | 5.1868(3)Å |
| $La_2Hf_2O_7$ | 10.717(1)Å |
| $Y_2Zr_2O_7$ | 10.408(1)Å |

| | |
|---|---|
| $Eu_2Ti_2O_7$ | 10.2027(2)Å |
| $Gd_2Ti_2O_7$ | 10.1940(3)Å |
| $Y_2Ti_2O_7$ | 10.0974(3)Å |

The only system which crystallized in the defect fluorite phase in this study was yttrium hafnate, which yielded a lattice parameter of 5.1868(3)Å. The ICSD did not contain any data for $Y_2Hf_2O_7$, regardless of the phase. This further limits comparison to defect fluorite phases of different compositions. The closest comparison is that of $Y_2Zr_2O_7$, of which only one entry from the ICSD was a stoichiometric defect-fluorite. The rest were non-stoichiometric, thus eliminating them from comparison. The literature lattice parameter for yttrium zirconate was 5.212(1) Å, obtained from Mandel *et al* (Mandal B.P., 2007). This is a larger value than what was observed for yttrium hafnate. The reason for this discrepancy is that the $Zr^{4+}$ ionic radius is larger than that of $Hf^{4+}$, with lengths of 0.84 Å and 0.83 Å respectively. An important note to make is that the yttrium zirconate samples in the study by Mandel *et al* were synthesised by solid state method, producing a more crystalline sample than what was achieved with the alkoxide condensation sol gel method employed in this study. This is evident in the Rwp of both materials refinements. The yttrium zirconate refinement achieved an Rwp of 1.19%, whereas the yttrium hafnate measurement achieved 8.23% due to its poor peak shape possibly caused by its nano-crystalline sizes.

A further comparison can be made between yttrium hafnate and gadolinium zirconate, which yielded eight defect-fluorite phases out of 20 available structures. The lowest Rwp was for entry 68265 with a lattice parameter of 5.2636(1) Å as determined by Moriga *et al* and an Rwp of 1.9% (Moriga, Yoshiasa, Kanamaru, & Koto, 1989). This lattice parameter is larger, again due to the larger ions present.

Yttrium hafnate was one of the few materials in this study to have very stable thermal parameters over the temperature range of 30 - 850°C. These can be seen in figures 4.42 to 4.44 for yttrium, hafnium and oxygen respectively. Each trend line can be seen to increase with temperature, despite some fluctuations about their polynomial trend lines. The $R^2$ values of these trend lines indicate that the fit is not exact. The structure determined by Mandal *et al* for yttrium zirconate did not refine the thermal parameters of the material and chose arbitrary set values, hence removing the possibility for comparison. The increase in the thermal parameters is a justifiable result in that higher thermal energy causes greater atomic vibrations, and is one of the mechanisms of thermal expansion. The erratic nature of the trend lines is indicative of the poor peak shape data, with the fit not being reproduced

exactly with the refinement of each temperature change in the heating regime. Longer counting statistics would improve the peak shape and hence the quality of the refined thermal parameters.

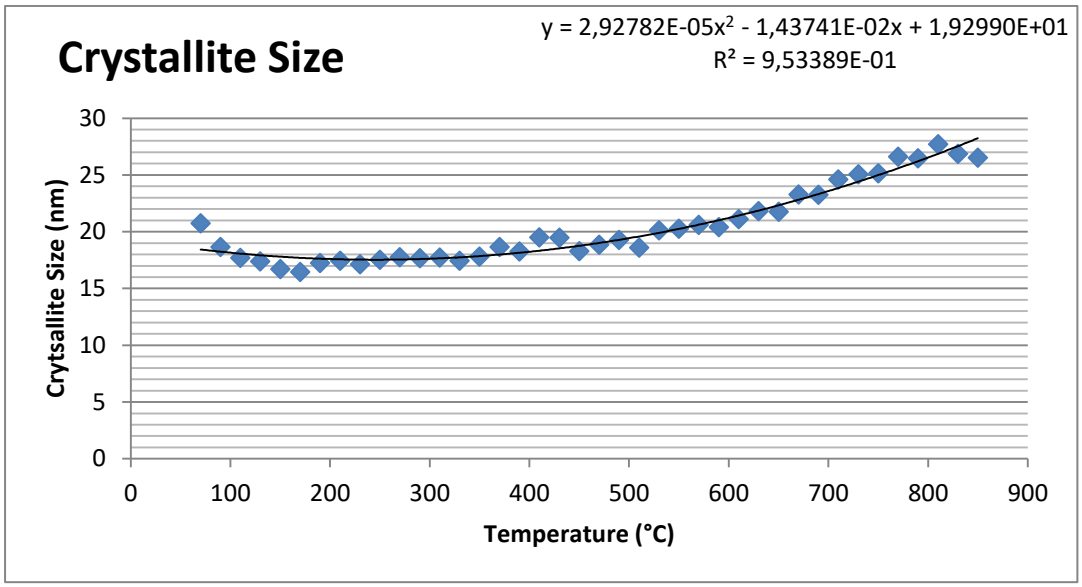


*Figure 5-3: A plot of the crystallite size of $Y_2Hf_2O_7$. It must be noted that this was a guideline to the crystallite size and should not be understood as an exact value. For exact values, an internal standard would be required for the measurement.*

The pyrochlore phases, listed in decreasing lattice parameter size, sequentially refined in this study were $La_2Hf_2O_7$, $Gd_2Zr_2O_7$, $Eu_2Hf_2O_7$, $Gd_2Hf_2O_7$, $Y_2Zr_2O_7$, $Eu_2Ti_2O_7$, $Gd_2Ti_2O_7$, and $Y_2Ti_2O_7$. The $R^2$ values for each of these plots were 0.998709, 0.989711, 0.995919, 0.995927, 0.998870, 0.999762, 0.999114, and 0.999970 respectively. Of the eight materials, yttrium titanate yielded the best plot, with an $R^2$ value close to unity. There was very little to no observable variations of data points about the trend line 4.96. Figure 4.95, the cascading plot of the VT-PXRD experiment for this material gives an indication as to why this was the case. The background for the diffraction patterns is very flat, and each peak was sharp and of high intensity (relatively speaking, that is). This allows for very precise determination of the peak positions with each refinement going up in temperature. Although the lattice parameter plot was precise, the Rwp and Goodness of fit plots in figures 4.97 and 4.98, respectively, indicate a poor fit due to their consistently high values. The reason for the poor fit lies in the intensity of the peaks. A significantly intense peak with a minor mismatch (leading to a significant change in the difference plot) will cause a significant difference between the experimental and calculated pattern. This has little effect on the calculated peak positions in this case. The lattice parameter for yttrium titanate pyrochlore was determined to be 10.0974(3) Å at 30 °C. Only two entries in the ICSD for yttrium titanate pyrochlore were stoichiometric. With values of 10.0986(5) (Chtoun *et al*) and 10.0947(1) (Haile *et al*) (Chtoun, Hanebali, Garnie, & Kiat, 1997) (Hail, Wuensch, &

Prince, 1990). The experimental value was accurate relative to literature up to two decimal places after which variations are observed. These discrepancies may be related to vacancies and/or the presence of excess titanium atoms within the unit cell. A means of determining this would be through oxygen conductivity measurements, where a vastly different conductivity may indicate the presence of non-stoichiometry.

The 30 °C pattern of gadolinium titanate pyrochlore attained a lattice parameter of 10.1940(3) Å as determined by a Rietveld refinement. Of the nine structures available on the ICSD of gadolinium titanate pyrochlore, only four entries were stoichiometric oxides, with lattices parameters of 10.1840(1) Å, 10.182(1) Å, 10.206 Å, and 10.1852(9) Å for entries 167918, 150210, 164024, and 24207 respectively (Heredia, Quintana Garcia, Perez Mazariego, & Escamilla, 2010) (Tabira, Withers, Minervini, & Grimes, 2000) (Zhang, Xiao, Zu, Fei, & Weber, 2009) (Knop, Brisse, & Castelliz, 1969)). The entry by Zhang *et al*, the structure with the lattice parameter of 10.206 Å lies outside of the average range formed by the other three compounds. This can be attributed to the means by which the lattice parameter was determined, namely by first principles calculation. The lattice parameter determined by this study was slightly higher than what was seen in literature. The nano-crystalline nature of the material can be seen in figure 5.4., where the approximate crystallite size was plotted against temperature. This may have occurred due to the nano-crystalline nature of the material, as discussed previously with regard to the defect fluorite phase of yttrium hafnate. Importantly, the plot of the lattice parameter for gadolinium titanate in figure 4.84 adheres closely to the trend line, but does not follow a linear trend. The plot flattens towards higher temperatures (above 500 °C) implying a reduction in the coefficient of thermal expansion, which is to be discussed in section 5.3. The plot's consistency lies in the nature of the diffraction patterns obtained in the VT-PXRD experiment for the material. The peaks are sharp, allowing for accurate peak placement. They are of less intensity than what was seen in yttrium titanate. This gives rise to a lower goodness of fit and Rwp across the entire temperature range, since the lower intensity reduces the effect of mismatch between the calculated pattern and experimental pattern.

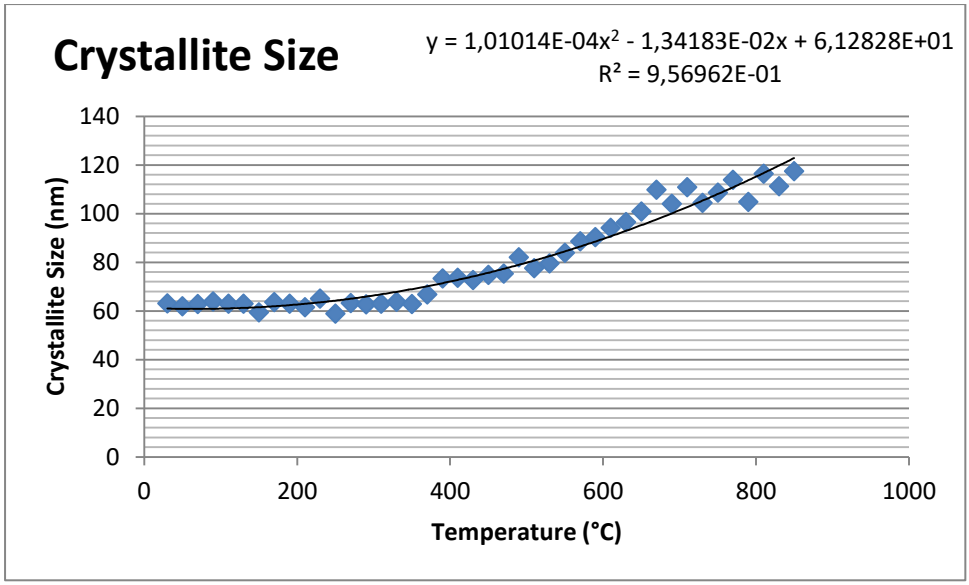


*Figure 5-4: The Crystallite size of gadolinium titanate relative to temperature. It must be noted that this was a guideline to the crystallite size and should not be understood as an exact value. For exact values, an internal standard would be required for the measurement.*

The lattice parameter, as determined by Rietveld refinement within this study, of $Eu_2Ti_2O_7$ was found to be 10.2027(2) Å. The three ICSD entries for the material had lattice parameters of 10.2064(5) Å, 10.2048(6) Å, and 10.197(1) Å for entries 83596, 92767, and 173945 respectively (Chtoun, Hanebali, Garnie, & Kiat, 1997) (Chtoun, Hanebali, & Garnier, Analyse par diffraction des rayons X, methode de Rietveld, de la structure des, 2001) (Chien, 1978). The lattice parameter determined in this study correlates closely to all three ICSD entries. The plot of the lattice parameter relative to temperature, illustrated in figure 4.72, indicates little to no deviation from the trend line, implying that the refinement was stable. This can be attributed to the sharp, intense peaks of the cascading diffraction patterns of the VT-PXRD experiment, illustrated in figure 4.69. Both the Rwp and Goodness of fit plots in figures 4.73 and 4.74, respectively, indicate that there was little mismatch between the observed and calculated patterns, even with the presence of the rutile phase within the diffraction pattern. The thermal parameters for the metals of the material display a trend increasing with temperature, as can be seen in figure 4.75 and 4.76 for europium and titanium respectively. The plot for the titanium thermal parameter (figure 4.76) fluctuated more so than what was seen in europium. This fluctuation may have occurred due to the sizes of the atoms involved. Europium(III) in an eightfold coordination sphere has an ionic radius of 1.066Å, whereas titanium(IV) with a coordination sphere of six has an ionic radius of 0.605Å. This implies that x-rays are less likely to interact with the electron cloud of titanium(IV), hence finding its position less accurate, creating an instability in the reported Beq values for the ion. This effect was amplified in the Beq values of both the 48f and 8b oxygen atoms. The presence of the large europium(III) ion also limits resolution of these ions.

The lattice parameter $Y_2Zr_2O_7$ was found to be 10.408(1) Å at 30 °C with an R value of 9.00. As listed in table 3.3.1 and stated in section 3.3.2, there are 26 submitted structures of yttrium zirconate in either the pyrochlore or defect fluorite structure. Only two of these entries were stoichiometric, with one of each structure type. The defect fluorite entry (reference code: 130000) reported a lattice parameter of 5.212(1) Å (Mandal B.P., 2007). The listed stoichiometric pyrochlore phase (reference code: 153818) reported a lattice parameter of 10.335 Å (Pruneda & Artacho, 2005) (standard deviation not available). However, this phase was determined by first principles, and hence no associated R value was reported. This entry was the only reported pyrochlore phase, implying that it was the sole literature to which the structure reported by this study can be compared. The two structures do not agree as the lattice parameters have a difference of 0.073 Å, which lies outside of the standard deviation. This implies that the phase reported here was the only available structure determined by experimental means. Observing figure 4.58, the Co Kα2 diffraction pattern of the material, one can see that the super cell peaks unique to the pyrochlore phase are of low intensity relative to the peaks shared between the two phases respectively. Figure 4.59, the cascading plot of diffraction patterns obtained from the VT-PXRD experiment for yttrium zirconate indicates no phase changes, but little difference between the two phases. This was due to the 2θ range of the diffraction patterns, chosen from 20 to 120 °2θ, which misses the (111) peak of the pyrochlore phase. However, the defect-fluorite phase was ignored for this refinement due to R values in the refinement. Figure 4.61 and 4.62 illustrate the goodness of fit an Rwp values respectively, which were in an acceptable range, unlike what was obtained for the defect fluorite phase. The plots of the thermal parameters relative to temperature are illustrated for Yttrium, zirconium, and the 48f and 8a oxygens in figures 4.63 to 4.66 respectively. All of these thermal parameters displayed stability with only minor fluctuation about the trend-line in each case. The 8a oxygen ion displayed the largest fluctuation, and also the largest average magnitude of the thermal parameter, with an average magnitude of 4.63.

$Gd_2Hf_2O_7$ had a lattice parameter of 10.419(2) Å at 30 °C with an associated Rwp value of 7.15%. There were only two entries in the ICSD for the material, only one of which was stoichiometric. Both phases had the pyrochlore structure. The stoichiometric pyrochlore had a lattice parameter of 10.5186(3) Å with an R value of 4.77%. Curiously, the non-stoichiometric compound had the exact same results. Both of these structures were reported by the same authors in separate papers (Shlyakhtina, et al., 2007) (Shlykhtina, 2006). The stoichiometric entry shall be considered for comparison. The experimental phase had a lattice parameter 0.1 Å shorter than what was seen in literature. The literature compound was synthesised via solid state methods, implying that the material could sinter more effectively, and hence produce a more crystalline product, unlike the nano-crystalline product obtained in this study through alkoxide condensation sol-gel synthesis. Figures 4.30 to 4.33 illustrate

the plots of the gadolinium, titanium, 48f Oxygen and the 8a oxygen atoms respectively. The Beq values for the 48f and 8a oxygens both immediately refined to self-imposed limits from Topas, where the literature values were not refined. All the literature Beq values were set to zero for their structural submission. The Beq values for gadolinium were erratic across the temperature range, where the 30°C measurement was 1.077. The hafnium Beq values were less erratic than what was obtained for gadolinium, with the Beq value being 1.38 at 30 °C.

$Eu_2Hf_2O_7$ had a lattice parameter of 10.477(1) Å at 30 °C. There were three ICSD structures of europium hafnate, all of which were pyrochlore, but only one was a stoichiometric compound. The lattice parameter for the stoichiometric compound was 10.560 Å with no R value. The reason for the missing R value was due to the structure being reported from Mossbauer effects (Chien, 1978). The non-stoichiometric lattice parameters were identical to each other with a value of 10.4847(3) Å. These structures were submitted by the same authors who submitted the same structures for gadolinium hafnate from the same papers (Shlyakhtina, et al., 2007) (Shlykhtina, 2006). The lattice parameter obtained from this study lies closer to what was reported for the non-stoichiometric oxide. As before, the thermal parameters of the ions in the literature structure were not reported. The lattice parameter plotted against temperature (figure 4.16) illustrates a gently sloping curve, becoming flatter with increasing temperature. The plot fit well with an $R^2$ value of 0.995. However, the Rwp and goodness of fit curves indicate that the refinement was not as accurate as required, this can be seen in figures 4.17 and 4.18. Both trends are erratic and high, with a maximum Rwp of 12.336%. This can be accounted for from the width of the diffraction peaks observable in figure 4.14, the cascading variable temperature plot of the data used in the refinements. Also, the missing pyrochlore peaks, obscured by the high background and low counting stats of the diffraction peaks, adds to the poor figures of merit.

$Gd_2Zr_2O_7$ attained a lattice parameter of 10.564(3) Å at 30 °C. Gadolinium zirconate has 20 entries in the ICSD and 12 of those are of the pyrochlore phase, 9 of which are stoichiometric. Several of these were obtained from a study which determined the defect-fluorite – pyrochlore phase transition for the material *ex situ*. The first of these structures had a lattice parameter of 10.5327(4) Å, which lies reliably close to the value obtained from this study. Similarly, the remaining structures had similar lattice parameters. The Beq values for the literature structures were not refined, but fixed at certain values. The thermal parameters obtained from gadolinium zirconate in this study either fluctuated across the temperature range, as was the case for gadolinium and the 48f oxygen parameter, or they were refined to the self-imposed limits in Topas. This can be seen in figure 4.52 to 4.55. The gadolinium Beq values were the most stable, and followed a rough trend. Similarly, the 48f x position also followed an erratic trend, despite the range over which the values followed was 0.034 fractional units. The

missing pyrochlore peaks reduced the amount of information to reliably determine this trend. The literature value of the 48f x position was 0.3888, which lies close to the lower limit of the values obtained in this study.

$La_2Hf_2O_7$ had a lattice parameter of 10.717(1) Å at 30 °C with an associated Rwp value of 10.977 %. There are two entries in the ICSD of the pyrochlore phase of lanthanum hafnate with lattice parameters of 10.673 Å and 10.772 Å for entries 153815 and 173790 respectively (Pruneda & Artacho, 2005) (Whittle, Cranswick, Redfern, Swainson, & Lumpkin, 2009)(standard deviations not available). The structure reported by Pruneda *et al* (reference code 153815) was determined by first principles and hence has no reported R value. The structure reported by Whittle *et al* had an R factor of 3.87. This structure was determined via neutron diffraction of significantly sintered powders, allowing for sharper peak shapes. The thermal parameters for each element in the structure determined by Whittle *et al* were set to unity, and hence not refined. Pruneda *et al* also did not report the thermal parameters for each ion. There is no exact correlation between the lattice parameter obtained from this study, and those of the ICSD structures. A possible reason for this lies in the asymmetric peak shapes obtained in the diffraction patterns illustrated in figures 4.1 to 4.4. This caused difficulties in matching the calculated patterns and the experimental pattern. This can be seen in figures 4.5 and 4.6, the goodness of fit and Rwp values with respect to temperature, respectively. These values are particularly high implying a poor match between the calculated and experimental pattern. The lattice parameter change due to temperature, illustrated in figure 4.11, depicts a non-linear increase of the lattice parameter with temperature. The data entries do display visible changes from the trend line, giving rise to the lowest $R^2$ value ($R^2$ = 0.9987) out of the pyrochlore materials of this study.

This result leads to a trend involving the lattice parameter versus the $R^2$ values of the trend lines. The smallest lattice parameter yields the $R^2$ value closest to unity (as seen in yttrium titanate), and vice versa (as seen in lanthanum hafnate). An explanation as to why this trend was observed involves the peak shapes observed in each material respectively. In a descending order of $R^2$ values, yttrium titanate has the most well defined peaks, for both the material and for the impurity phase of rutile. Both phases in the diffraction pattern were well resolved, hence allowing for accurate tracking of peak positions, and hence a smoother plot of lattice parameter against temperature. Also, the effect of the background for yttrium titanate was negligible, as the background was flat, as can be seen in figure 4.93. In the case of gadolinium titanate, the peaks were both intense and sharp, allowing for accurate tracking with temperature, but the background of the diffraction patterns increases with increasing 2θ angles, as can be seen in the figure 4.81. This lowers the intensity of high angle peaks relative to the background. Although the peaks in figure 4.76 are well defined, they have lower intensity than those of yttrium titanate, limiting the accuracy of the exact peak position. Figure 4.69 is an illustration

of the diffraction patterns obtained for europium titanate from the VT-PXRD experiment. Although the patterns have a superior background function when compared to that of the gadolinium titanate plots (figure 4.81), it still produced a slightly lower $R^2$ value than what was observed for the previously mentioned titanate pyrochlores. Yttrium zirconate had a lower $R^2$ value than what was observed for the titanate materials as its diffraction peaks were much wider and of lower intensity than what was observed for the titanates, reducing the ability to accurately track the progression of the peak position via Rietveld refinement. The peaks are symmetric, but their width reduces the resolution between the kα1 and kα2 diffraction peaks, again limiting resolution for the refinement. Lanthanum hafnate experienced the same peak width problems as observed in yttrium zirconate, but the errors generated were amplified through the poor peak symmetry, which can be seen in figures 4.2, 4.3, and 4.4. This lowered the resolution of the peak position further. A plot of a calculated pattern overlaid on the experimental pattern of the material indicates the first bulge formed by the peaks corresponds with the pattern from literature. This implies that the Rietveld method employed here did not resolve the shape of the peaks, and tracked the peak position at higher 2θ angles than what was observed in the structure determined by Pruneda *et al* (Pruneda & Artacho, 2005).

As a final note regarding the effect of the 48f X position on the structure of the pyrochlore phase is that an increase in the fractional coordinate leads to a severe distortion of the octahedron of the transition metal and a movement towards a cubic shape for the lanthanide polyhedra. This can be seen in figure 5.5 and figure 5.6. Figure 5.5 illustrates yttrium titanate rendered from the structure submitted by Chtoun *et al* (Chtoun, Hanebali, Garnie, & Kiat, 1997). Here the 48f x parameter is 0.3253, as determined by Chtoun *et al*, and the shape of the blue titanate octahedron seems reasonable, and the green yttrium polyhedron has a slight distortion to it. To exaggerate the effect, figure 5.6 has the 48f x parameter set at 0.4000. What can be seen is that the titanate octahedron has been severely flattened, and the length of the bonds has increased, whereas the yttrium polyhedron has become more square-like. In each case in this study, although the exact measurements were not accurate due to fluctuations, each trend line for the 48f oxygen parameter did increase with temperature, indicating that high temperatures cause a distortion of the octahedron and form a more perfect cube like polyhedra for the lanthanide. Also, an increase in temperature increases the M-O bond lengths and reduces the Ln-O bond lengths.

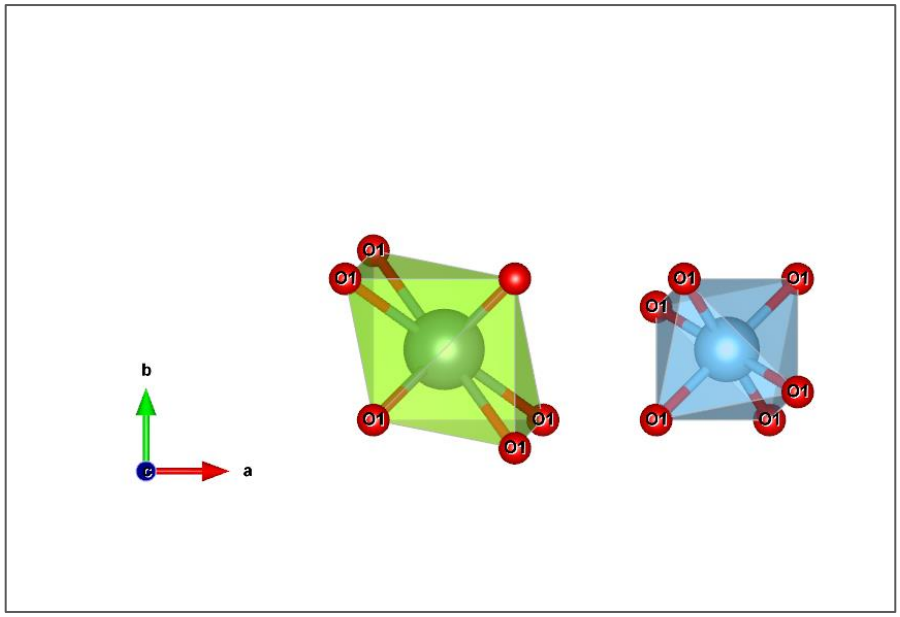


*Figure 5-5: The polyhedra of yttrium titanate with 48f x = 0.325300*

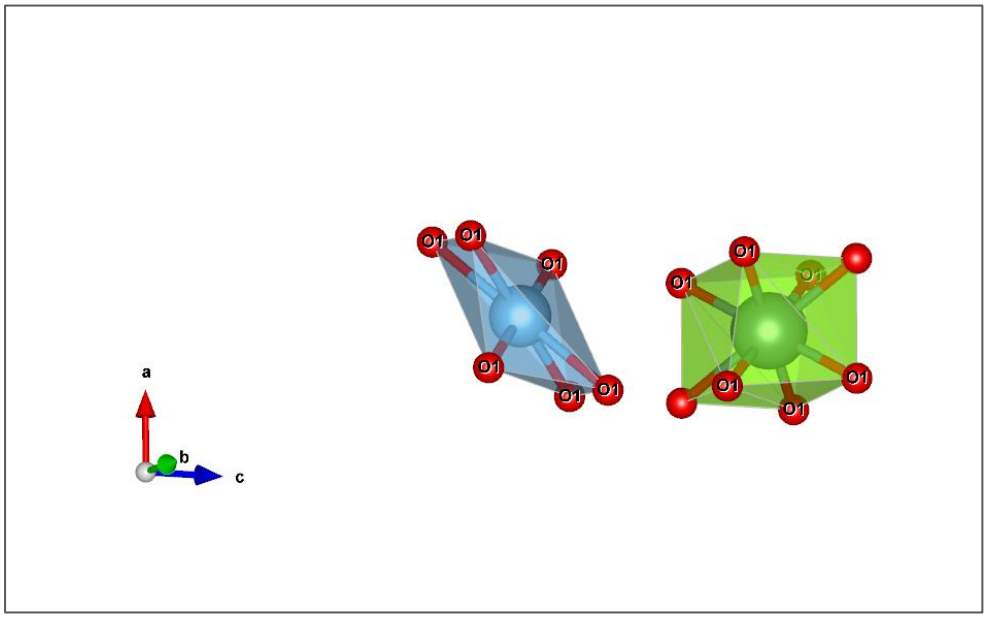


*Figure 5-6: The polyhedra of yttrium titanate with 48f x = 0.40000*

## 5.3. Lattice expansion

Table 5.3 includes a list of the coefficients of thermal expansion (CTE's) for each material included in this study. Listed in the table are the compounds, the room temperature CTE, the average CTE over the entire temperature range (including the standard deviation), the difference between the highest and lowest CTE over the entire temperature range, the trend of the CTE relative to temperature (i.e. does it increase positively or negatively) and the formula for the trend line.

The purpose for this discussion was to answer the question proposed in section 3.1.1., that being an imposed dilemma of whether the materials experience a single constant thermal expansion co-

efficient, or one that varies with temperature, and if so, how does it vary. Table 5.3 appears to answer this question with the description of a trend line formula, and the presence of a positive or negative trend. To truly answer this question, the extent to which the CTE's change with temperature needs to be reviewed.

*Table 5.3: (table references (a: (Kutty, Rajagopalan, & Mathews, 1994) (b: (Mandal, Pandey, & Tyagi, 2010)) (c: (Mori, Tompsett, Sammes, Suda, & Takeda, 2003)) (d: (Farmer, et al., 2014))*

| **Material** | **Room temperature CTE (ppm.°C$^{-1}$)** | **Average CTE (ppm.°C$^{-1}$)** | **Change in CTE (ppm.°C$^{-1}$)** | **Literature CTE (ppm.°C$^{-1}$)** | **Trend line formula** |
|---|---|---|---|---|---|
| Gadolinium Hafnate | 5.397 | 4.661 ± 0.43 | -1.472 | Not found | $\alpha = -1.795 \times 10^{-9}T + 5.545 \times 10^{-6}$ |
| Yttrium Hafnate | 5.941 | 5.151 ± 0.467 | -1.581 | Not found | $\alpha = -1.928 \times 10^{-9}T + 5.999 \times 10^{-6}$ |
| Gadolinium Zirconate | 6.308 | 5.702 ± 0.35 | -1.213 | 10.0 – 11.0 (a), 11.4 (b) | $\alpha = -1.480 \times 10^{-9}T + 6.353 \times 10^{-6}$ |
| Europium Hafnate | 5.537 | 4.297 ± 0.7 | -2.480 | Not found | $\alpha = -3.025 \times 10^{-9}T + 5.628 \times 10^{-6}$ |
| Lanthanum Hafnate | 8.317 | 9.229 ± 0.539 | 1.822 | Not found | $\alpha = 2.222 \times 10^{-9}T + 8.25 \times 10^{-6}$ |
| Yttrium Zirconate | 8.473 | 9.979 ±0.891 | 3.013 | Not found | $\alpha = 3.765 \times 10^{-9}T + 8.360 \times 10^{-6}$ |
| Gadolinium Titanate | 8.974 | 6.519 ± 1.451 | -4.910 | 10.8 (c), 11.1 (d) | $\alpha = -5.988 \times 10^{-9}T + 9.153 \times 10^{-6}$ |
| Europium Titanate | 9.704 | 10.214 ± 0.302 | 1.021 | 11.2 (d) | $\alpha = 1.244 \times 10^{-9}T + 9.67 \times 10^{-6}$ |
| Yttrium Titanate | 10.042 | 10.315 ± 0.164 | 0.547 | 10.6 (d) | $\alpha = 6.838 \times 10^{-10}T + 10.02 \times 10^{-6}$ |

Please note that the Co-efficients of thermal expansion were evaluated over the experimental temperature range only (i.e. 30°C-850°C)

Figure 5.7 illustrates the Room temperature CTE's of each material, along with the associated average CTE for each material. The purpose of this plot is to determine whether reporting a single CTE or reporting a CTE trend against temperature is more appropriate. For the specific cases of europium and yttrium titanate, reporting a single CTE appears suitable as the average and room temperature CTE's lie close to each other in magnitude. This is further confirmed by the standard deviation of the average CTE's for these materials (listed in table 5.3). In each case, the magnitude of the standard deviation is two orders of magnitude away from the CTE implying that little change in the CTE occurs over the entire temperature range.

The materials can be divided into two groups, those being positively changing CTE's and those with negatively changing CTE's. The materials which display significantly positively changing CTE's are the pyrochlore phases of Lanthanum hafnate, yttrium zirconate, europium titanate and yttrium titanate. The material that exhibits the largest positive change in CTE was yttrium zirconate, with a change in CTE of 3.013 ppm.°C$^{-1}$. This large variation gave the average CTE of the material the second largest standard deviation of all the materials in this study. The remaining positively changing CTE materials are arranged in the following order: lanthanum hafnate (0.822 ppm.°C$^{-1}$); europium titanate (1.021 ppm.°C$^{-1}$); and yttrium titanate (0.547 ppm.°C$^{-1}$). The extent to which the CTE changes in the case for the positive changing ones does not correlate to the size of the lattice parameter, as lanthanum hafnate has a larger unit cell than what was seen for yttrium zirconate, yet yttrium zirconate has a significant change in its CTE.

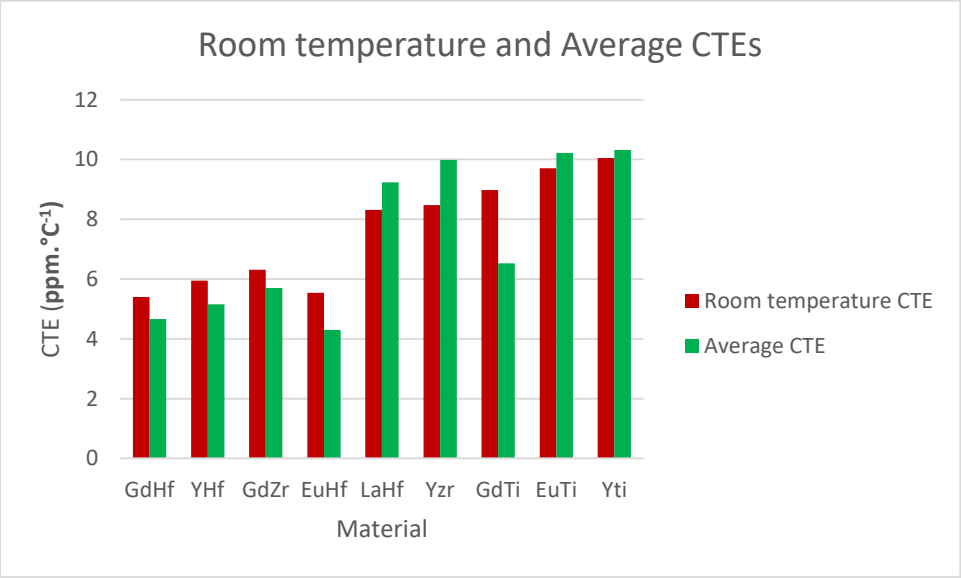


*Figure 5-7: A comparison of the Room CTE values against the average CTE for all materials reported in this study*

The material to exhibit the largest negative change in CTE was gadolinium titanate with a change of 4.910 ppm.°C$^{-1}$. This was the largest change in CTE in this study, which can clearly be seen in figure

5.7, which illustrates the material to have the third largest room temperature CTE, yet its average lies below that of europium hafnate. At 850 °C, as can be seen in figure 4.92, the material exhibits a CTE of 4.063 ppm.°$C^{-1}$. The lowest observed CTE was for europium hafnate with a value of 3.05ppm.°$C^{-1}$. The remaining negatively changing CTE materials are listed in descending order: europium hafnate (-2.480 ppm.°$C^{-1}$); yttrium hafnate (-1.581 ppm.°$C^{-1}$); gadolinium hafnate (-1.422 ppm.°$C^{-1}$) and gadolinium zirconate (-1.213 ppm.°$C^{-1}$).

According to Roy *et al*, thermal expansion materials can be categorised into three groups, namely high thermal expansion ($\alpha$ > 8ppm.°$C^{-1}$), intermediate thermal expansion (2ppm.°$C^{-1}$ < $\alpha$ < 8ppm.°$C^{-1}$), and low thermal expansion (0ppm.°$C^{-1}$ < $\alpha$ < 2ppm.°$C^{-1}$) (Roy, Agrawal, & Mckinstry, Very Low Thermal Expansion Coefficient Materials, 1989). These categories highlight a trend in the CTE values of the materials of this study. The hafnates along with gadolinium zirconate all experience intermediate CTE's with europium hafnate venturing close to low thermal expansion at higher temperatures. The remaining materials, with particular attention being paid to the titanates, are high thermal expansion materials. The only exception from this trend was gadolinium titanate, which has a room temperature CTE in the high expansion region, but an average CTE in the intermediate region. Figure 4.97, the CTE of gadolinium titanate plotted relative to temperature, indicates the change from high to intermediate thermal expansion occurred at approximately 210°C.

The fact that all these materials have CTE's which lie in the intermediate and high thermal expansion zones does limit the use of the materials in industrial applications, but some materials will fare better in thermally dynamic situations than others. The most stable CTE value found in this study was that of yttrium titanate, which only experienced a change of 0.547 ppm.°$C^{-1}$. The largest change in CTE was experienced by gadolinium titanate with a change of 4.910 ppm.°$C^{-1}$, and more importantly this change was in the negative direction, placing the material in the intermediate thermal expansion zone at operating temperatures. In brief, the pyrochlore materials, with the exception of gadolinium titanate would not be useful in situations of high temperature change, given that they are both high thermal expansion materials and that they increase their thermal expansion with temperature more so than what is observed in the defect fluorite phase.

Although these are not ideal candidates for thermal expansion applications, their CTE's, and how they change with temperature, do indicate how the specific heats of the materials change with temperature. This was explained in section 1 with regard to the Grüneisen equations, which relates the thermal expansion to the specific heat of a material. The fact that the pyrochlore materials are high thermal expansion materials, and that these CTE values increase with temperature implies an increase in specific heat with increases in temperature.

Although literature values for CTE's corresponding to all materials in this study were not found, several examples do highlight some important issues. The most prominent being the comparison between the CTE of gadolinium zirconate found in this study versus the CTE found in literature (Mandal, Pandey, & Tyagi, 2010). The literature values place the pyrochlore phase in the high thermal expansion zone with a value of 11.4 ppm.°$C^{-1}$, whereas the defect-fluorite variant obtains a CTE of only 6.308 ppm.°$C^{-1}$. This difference changes the designation of the material from a high thermal expansion to an intermediate thermal expansion material.

As stated in the section 1, the causes of negative thermal expansion often rely in the ability of atoms or polyhedra to move in a transverse fashion (Miller, Smith, Mackenzie, & Evans, 2009). Similarly, as discussed by Roy *et al*, low thermal expansion materials require one of four structural, chemical or physical characteristics to be considered low thermal expansion materials (Roy, Agrawal, & Mckinstry, Very Low Thermal Expansion Coefficient Materials, 1989). These include: a three dimensional nano-porous structure exhibiting strong stable bonds between atoms; Doped silica-based glasses; ferromagnetic alloys; and ferroelectric relaxors. The last two causes of low thermal expansion involve energy being taken up in a phase transition over being used in thermal vibrations. The fact that none of the materials in this study are low thermal expansion materials implies that the four reasons for low thermal expansion and four sub-microscopic reasons for negative thermal expansion either do not exist or are not as prevalent.

The yttrium, europium and gadolinium hafnate, along with gadolinium zirconate all produced broad diffraction peaks, implying the possibility of nano-scaled particles. The surface effects of drawing layers of atoms closer then further apart in pairs would also allow for transverse vibrations and rigid unit modes to occur in those layers. The combination of both the vacancies and the nano-scaled particles would reduce the CTE of the observed material. This may be a cause to their intermediate CTE status. The opposite can be seen for the remaining materials with the exception of lanthanum hafnate. The remaining materials were highly crystalline, and such rigid unit modes were not available.

The nano-scaled particle argument presented previously may explain the deviations in the CTE's of the pyrochlore materials from those of literature. All pyrochlore titanates had lower CTE's than what was reported in literature, with the closest comparison being that of yttrium titanate. Yttrium(III) is a much smaller ion than europium(III) or gadolinium(III) and hence would allow for more efficient sintering, and hence the formation of larger particle sizes at lower temperatures. The materials for the literature CTE values all involved high temperature solid state synthesis, which naturally allows for sintering to occur before diffraction data can be collected.

# 6. Conclusions

## 6.1. Conclusions

As outlined in section two, proposed in section 3, discussed in section four, listed in table 5.3 and illustrated in figure 5.7, the coefficients of thermal expansion and the lattice parameters measured relative to temperature have been determined for $Eu_2Hf_2O_7$, $Gd_2Hf_2O_7$, $Gd_2Zr_2O_7$, and $Y_2Hf_2O_7$, $La_2Hf_2O_7$, $Y_2Zr_2O_7$, $Eu_2Ti_2O_7$, $Gd_2Ti_2O_7$, and $Y_2Ti_2O_7$. It was shown that gadolinium hafnate, yttrium hafnate, gadolinium zirconate, and europium hafnate exhibited intermediate thermal expansion as described by Roy *et al* (Roy, Agrawal, & H.A., Very Low Thermal Expansion Coefficient Materials, 1989). The remaining materials all exhibited high thermal expansion  The CTE's also varied with temperature, with the larges change in CTE occurring for $Gd_2Ti_2O_7$, where the CTE reduced by 4.910 ppm.°$C^{-1}$. This change placed the material in the intermediate thermal expansion region at temperatures above 200 °C, even though it was a high thermal expansion material at room temperature. It was the only pyrochlore phase to exhibit this change from high to intermediate thermal expansion.

The synthetic procedure improved the product by allowing for nano-scaled particles to be formed without significant sintering. Also the CTE values for the materials of this study were lower than the available literature values. A proposed reason for this was due to the nano-scaled particles, increasing the prevalence of surface effects on the CTE, which was discussed in detail towards the end of section 5.3.

There were no structural changes observed for all materials. This increases the usefulness of these materials for use in practical applications such as electrolyte materials for solid oxide fuel cells in that a dimension changing phase change will not occur over the entire operating range.

The eight pyrochlore phases all had erratic trend lines in their plots of the 48f x parameter against temperature. However, all of these trends did increase with temperature i.e. the lower limits of the fluctuation increased with temperature. An increase of the 48f x parameter lead to a further distortion of the transition metal octahedral, and the lanthanide polyhedra to have a more square-like appearance. The result of this was that the M-O bonds increased in length, whilst the Ln-O bonds decreased in length

In short, the alkoxide condensation sol-gel synthesis produced nano-particulate materials from the zirconate and hafnate samples, where the smaller titanium ions allowed for more effective sintering. The nano-particulate samples, with the exception of lanthanum hafnate, had the lower thermal expansion coefficients. All the materials with literature data available for the CTE's, had lower CTE values than what was previously reported. The Increase in temperature causes the 48f oxygen to

change position such that the x coordinate increases, which causes distortions of the transition metal octahedron.

## 6.2. Future Work

As stated in section 2.6.7, lanthanum zirconate yielded phase changes and possible solid state reactions beginning at approximately 350°C. A future endeavour would involve an in depth tracking of the evolution of this phase transformation/solid state reaction via *in situ* variable temperature powder X-ray diffraction.

Lanthanum hafnate exhibited a strange peak profile which appeared as if the phase had split into two separate pyrochlore phases of differing lattice parameter. An interesting venture would be to reproduce this phenomenon and determine the compositions of each non-stoichiometric phase, and elucidate a reason for the split if it is the case.

A study into how oxygen mobility is affected by stoichiometry would possibly provide a quick means by which chemical formulae of non-stoichiometric pyrochlore and defect fluorite phases could quickly be elucidated. However, this would require the development of standards in order to accurately determine stoichiometry from oxygen mobility.

A molecular dynamics study could be performed to determine why these materials do not exhibit phase changes over the experimental temperature range.

# 7. Appendix

## a. Methodologies

### i. Use of an Anton Paar XRK 900

Correct set-up of the Anton Paar XRK 900 is pivotal in obtaining accurate data. The most common procedures shall be discussed here for future reference and as a completion to the methodology section of this text.

#### *1. Installing the sample holder*

The sample holder (figure7.1) is a Macor rod with a sample dish located on top, and screw mounts located at the bottom. The sample holder is placed into the sample mount via a steel attachment piece. The screws ought to be tightened in place in an alternating fashion to avoid stresses building up across the Macor, which may result in cracking during a high temperature experiment. The steel attachment piece is then bolted into the sample mount through the base of the sample mount.

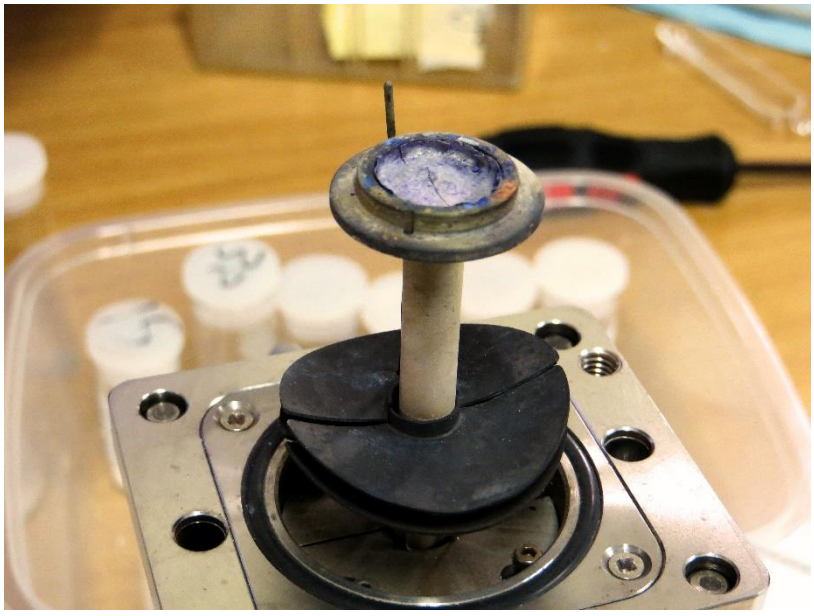

*Figure 7.7-1: An example of Macor sample holder mounted in its steel mount. The wire protruding above the sample dish is the thermocouple for monitoring temperature. A platinum dish has been placed inside the holder to prevent leaching of certain samples into the holder*

The next step is to install the heat shields. These shields prevent heat escaping the furnace to ensure stable high temperatures and help prevent damage to external parts. Care must be taken when installing the heat shield to prevent damage to the thermocouple, which has to be fed through an opening in one half of the heat shields. The shields are secured in place by bolts, again to be tightened in an alternating fashion to prevent stresses that lead to cracking and/or warping.

A platinum plate is fitted into the recess of the sample holder as to prevent sample from falling down the holder, and to prevent leaching of certain samples into the Macor itself.

Sample is loaded into the sample holder by placing a sufficient amount into the recess, and flattening it with a microscope slide. Due to the shape, size, and fragile nature of the sample holder and mount, it is not possible to load the sample via a side mounting procedure.

Installing the sample mount into the furnace involves inserting the mount into the furnace along the built in guide rails, and bolting the assembly in place. Again, this is to be done in an alternating fashion to avoid stresses. The last step is to connect the thermocouple connection from the sample mount to the furnace. This procedure is important as the software will prevent the experiment from proceeding as temperature control is not possible.

### *2. Sample height determination*

Sample height determination for the Anton Paar XRK 900 is a significantly important procedure, and hence is included here. The procedure requires an accurate value for a low angle peak of adequate intensity and slender breadth. These are required as low angles are more susceptible to height errors due to the Bragg-Brentano geometry, and the slender peak ensures the apex of the peak can be determined easily, even when lower counts are observed.

There are three options for finding the exact 2θ position of the peak. If the material to undergo an X-ray experiment is a standardised sample, such as NIST $LaB_6$, then an accurate peak list can be obtained for the particular sample. This is often not the case with as experimental samples by their very nature are not standardised. If the sample has an elucidated structure available in literature, the pattern can be calculated in structural graphics software such as Mercury (Macrae, 2008) or VESTA (Momma, 2011). From this calculated pattern, the desired peak position can be determined. Similarly, in the peak matching software package Evaluation Plus, the database entries can be accessed directly and a peak list can be saved from this. This methodology is not entirely sound as an experimental sample may have deviations. The methodology used in this study was to obtain a pattern of the sample on a different diffractometer with a calibrated sample height. This ensures that sample variations do not affect the reference peak position. This does require careful sample preparation to ensure that a height error does not occur from poor sample packing.

With regard to the later method of determining the reference peak position, conversion from one wavelength of radiation to another may be required, which was the case in this study (involving a conversion for Co Kα1 to Cu Kα1). This can be accomplished by the following procedure.

1. Find the position of the desired reference peak from radiation source A

2. Determine the d-spacing associated with that peak using Bragg's law (see Introduction)
3. Use the d-spacing to determine the 2θ position by using Bragg's law again, but with the wavelength of radiation source B

Once the position of the reference peak is found, the sample height can be determined. Find the desired peak using the GUI for the diffraction software and determine its position. If the position is greater than the reference peak, then the sample height require a higher position. Likewise, if the position is lower than that of the reference peak, then the sample height must be lowered. This is an iterative process and it is suggested that the scan range is limited to the peak in question to lower time of measurement, and to lower equipment degradation on measurements that do not provide useful data.

### ii. Use of A Bruker D2 Phaser

#### *1. Operation*

The Bruker D2 Phaser is a very simple instrument with regards to operation. As can be seen in figure 2.4, the sample holder mount in the centre of the machine has a latch mechanism which draws the sample up to the correct height prior measurement. This feature saves much time as height calibration can take some time and requires a standardised material such as NIST $LaB_6$. Other than operating the latch and the opening mechanism for the instrument door, the on-board software requires inputting an experiment file (which can be written via a graphical user interface in a separate piece of software). The instrument does not require any external cooling as the close geometry of the tube tower, sample mount and detector does not require a high flux of X-rays, implying lower voltages are needed for the X-ray tube. Upon completion of the diffraction experiment, the file is automatically saved in a directory specified initially in the experimental set-up window.

#### *2. Sample preparation*

##### a. Side packing

Side packing a sample holder (figure 2.4) involves loading small amounts of sample into the standard sample holder at a time and tapping on a surface sideways (with a glass slide held tightly against the opening of the holder) such that the sample is packed tightly into the side of the sample holder. This process is repeated several times until the entire sample holder is full.

The advantages to using this technique include a reduction in preferred orientation. The method also allows for a flatter surface to be obtained, hence reducing errors from surface roughness.

### b. Zero-background holder

The zero background holder, as described previously (figure 2.5), is a single crystal of silicon cut such that no Bragg reflections of the silicon can diffract in the path of the detector, hence providing little to no background to the observed pattern. This allows for a pattern to be obtained from very little sample.

Sample preparation for a zero-background sample holder differs from the standard sample holder due to the low amounts of sample used. Often is the case (as is the case with this document) that sample is smeared across the centre of the silicon insert and flattened (gently) with a glass slide.

Other techniques can be employed, such as dusting sample over the surface of the silicon insert by passing through a sieve. This has the effect of lowering particle size dispersion and preventing preferred orientation. A similar technique involves coating the silicon insert with a thin layer of petroleum jelly. The sieved sample sticks to the petroleum jelly, preventing sample movement during sample spinning. This also reduces preferred orientation greatly.

## b. Refinement data output

### Lanthanum Hafnate

| Temperature | Lattice parameter | Volume | Goodness of fit | Rwp | Crystallite Size | La Beq | Hf Beq | O1 Beq | O2 Beq | XPOS |
|---|---|---|---|---|---|---|---|---|---|---|
| 30 | 10,71724 | 1230,974 | 1,3946 | 10,97686 | 9863,28114 | 0,00003 | 0,49831 | 0,00202 | 2,99895 | 0,33487 |
| 50 | 10,71716 | 1230,947 | 1,43483 | 11,18474 | 9982,91014 | 0 | 0,71777 | 0,00025 | 2,86088 | 0,33175 |
| 70 | 10,72014 | 1231,975 | 1,42415 | 11,03755 | 9997,86377 | 0 | 0,7654 | 0,22175 | 3,26922 | 0,33404 |
| 90 | 10,72074 | 1232,179 | 1,41053 | 10,94081 | 9999,86649 | 0 | 0,83287 | 0,28359 | 3,44234 | 0,33319 |
| 110 | 10,72308 | 1232,988 | 1,42668 | 11,04914 | 9999,98331 | 0 | 0,78931 | 0,03545 | 4,80069 | 0,3342 |
| 130 | 10,72448 | 1233,471 | 1,41571 | 10,95453 | 9999,99896 | 0 | 0,81687 | 0,00222 | 2,79885 | 0,33244 |
| 150 | 10,72593 | 1233,972 | 1,41293 | 10,94382 | 9999,99993 | 0 | 0,84145 | 0,00014 | 0,51672 | 0,33116 |
| 170 | 10,72868 | 1234,922 | 1,42856 | 11,04689 | 10000 | 0 | 0,85968 | 0,01648 | 2,09133 | 0,33173 |
| 190 | 10,72953 | 1235,214 | 1,4053 | 10,92957 | 10000 | 0 | 0,84218 | 0,34474 | 0,69228 | 0,33353 |
| 210 | 10,73068 | 1235,611 | 1,42461 | 11,1324 | 10000 | 0 | 0,80833 | 0,03949 | 3,25007 | 0,33296 |
| 230 | 10,73257 | 1236,263 | 1,45095 | 11,28145 | 10000 | 0 | 0,93136 | 0,00247 | 2,94648 | 0,33345 |
| 250 | 10,73594 | 1237,427 | 1,37383 | 10,76266 | 10000 | 0 | 0,83962 | 0,20107 | 2,99669 | 0,33199 |
| 270 | 10,73771 | 1238,042 | 1,40466 | 10,94101 | 10000 | 0 | 0,97206 | 0,01257 | 2,95153 | 0,3318 |
| 290 | 10,73846 | 1238,302 | 1,39972 | 10,89884 | 10000 | 0 | 0,93928 | 0,00079 | 0,37537 | 0,33144 |
| 310 | 10,7412 | 1239,25 | 1,40883 | 10,96551 | 10000 | 0 | 0,99952 | 1,55565 | 0,82381 | 0,33526 |
| 330 | 10,7424 | 1239,664 | 1,40364 | 10,90055 | 10000 | 0 | 1,0314 | 0,31394 | 1,14158 | 0,33199 |
| 350 | 10,74448 | 1240,384 | 1,4306 | 11,16855 | 10000 | 0 | 0,99083 | 0,18079 | 0,8268 | 0,33175 |
| 370 | 10,74729 | 1241,356 | 1,42176 | 11,08704 | 10000 | 0 | 1,01697 | 0,0113 | 0,76367 | 0,32989 |
| 390 | 10,74797 | 1241,592 | 1,4357 | 11,21318 | 10000 | 0 | 0,98974 | 0,32436 | 1,28907 | 0,33168 |
| 410 | 10,75159 | 1242,848 | 1,39274 | 10,95978 | 10000 | 0 | 1,18765 | 0,48833 | 0,51583 | 0,33285 |
| 430 | 10,75264 | 1243,212 | 1,37393 | 10,82672 | 10000 | 0 | 1,07453 | 0,09235 | 0,75192 | 0,33094 |
| 450 | 10,75549 | 1244,202 | 1,39675 | 10,98517 | 10000 | 0 | 1,00973 | 0,72389 | 1,85378 | 0,33244 |
| 470 | 10,75871 | 1245,321 | 1,44164 | 11,36768 | 10000 | 0,00721 | 1,07124 | 0,01131 | 0,38766 | 0,32839 |
| 490 | 10,75789 | 1245,033 | 1,39576 | 10,99822 | 10000 | 0,0039 | 1,12521 | 0,00141 | 0,28343 | 0,32937 |
| 510 | 10,76156 | 1246,31 | 1,40425 | 11,04828 | 10000 | 0,00012 | 1,14905 | 0,00924 | 0,70371 | 0,32879 |
| 530 | 10,76451 | 1247,335 | 1,39026 | 10,9963 | 10000 | 0,01095 | 1,18207 | 0,00057 | 0,15014 | 0,32994 |
| 550 | 10,7658 | 1247,784 | 1,40313 | 11,21155 | 10000 | 0,00269 | 1,24881 | 0,30785 | 0,67508 | 0,33189 |
| 570 | 10,76722 | 1248,278 | 1,38167 | 11,07082 | 10000 | 0,00008 | 1,23674 | 0,43926 | 1,187 | 0,32905 |
| 590 | 10,76863 | 1248,768 | 1,35844 | 10,94516 | 10000 | 0,00001 | 1,14925 | 0,02746 | 1,14488 | 0,33007 |
| 610 | 10,77244 | 1250,091 | 1,40358 | 11,27033 | 10000 | 0,10614 | 1,17582 | 0,02119 | 0,2571 | 0,33019 |
| 630 | 10,77431 | 1250,745 | 1,40453 | 11,34759 | 10000 | 0,00083 | 1,04065 | 0,00109 | 0,00201 | 0,3293 |
| 650 | 10,77599 | 1251,331 | 1,34154 | 10,93125 | 10000 | 0,08311 | 1,10988 | 0,33841 | 0,00013 | 0,32975 |
| 670 | 10,77908 | 1252,405 | 1,37293 | 11,21284 | 9843,75469 | 0,03828 | 0,93252 | 0,00529 | 1,57795 | 0,32991 |
| 690 | 10,78037 | 1252,855 | 1,36899 | 11,22587 | 9990,23467 | 0,04377 | 1,11901 | 0,00033 | 0,60708 | 0,32872 |
| 710 | 10,78109 | 1253,107 | 1,37666 | 11,34952 | 9998,77933 | 0,02488 | 1,06744 | 0,00004 | 0,10836 | 0,32905 |
| 730 | 10,78412 | 1254,164 | 1,34979 | 11,23212 | 9999,96185 | 0,05077 | 1,15506 | 0 | 0,24011 | 0,32842 |
| 750 | 10,78521 | 1254,544 | 1,32513 | 11,10029 | 9999,99523 | 0,00891 | 1,12407 | 0,13086 | 1,66496 | 0,3301 |
| 770 | 10,78655 | 1255,01 | 1,37401 | 11,53767 | 9999,9997 | 0,01538 | 1,04642 | 0,00818 | 0,18429 | 0,32931 |
| 790 | 10,7888 | 1255,796 | 1,35151 | 11,35222 | 9999,99993 | 0,00385 | 1,20704 | 0,49658 | 0,04607 | 0,32953 |
| 810 | 10,79244 | 1257,067 | 1,34691 | 11,41388 | 3250,91494 | 0,00068 | 1,078 | 0,7719 | 0,96689 | 0,32985 |
| 830 | 10,79426 | 1257,704 | 1,33296 | 11,32685 | 6732,97094 | 0,0994 | 0,99696 | 0,14235 | 0,14575 | 0,32972 |
| 850 | 10,79642 | 1258,461 | 1,35694 | 11,55525 | 9591,62137 | 0,13726 | 1,1733 | 1,04597 | 0,01823 | 0,33266 |
| 30 | 10,72019 | 1231,992 | 1,47796 | 11,78041 | 9999,9003 | 0,00003 | 0,51197 | 0,00026 | 3,02069 | 0,33434 |

Europium Hafnate

| Temperature | Lattice Parameter | Volume | Goodness of Fit | Rwp | Crystallite size |
|---|---|---|---|---|---|
| 30 | 10,477 | 1150,029 | 1,790 | 11,481 | 9967,595 |
| 50 | 10,478 | 1150,439 | 1,921 | 11,507 | 10000,000 |
| 70 | 10,480 | 1150,942 | 2,006 | 11,834 | 10000,000 |
| 90 | 10,480 | 1151,012 | 1,987 | 11,661 | 9986,704 |
| 110 | 10,482 | 1151,550 | 1,959 | 11,488 | 1544,983 |
| 130 | 10,482 | 1151,672 | 1,985 | 11,615 | 2803,968 |
| 150 | 10,483 | 1152,102 | 1,941 | 11,400 | 9943,781 |
| 170 | 10,484 | 1152,367 | 1,978 | 11,592 | 9999,973 |
| 190 | 10,485 | 1152,766 | 1,976 | 11,576 | 2166,573 |
| 210 | 10,486 | 1152,968 | 1,972 | 11,550 | 3821,390 |
| 230 | 10,488 | 1153,503 | 1,969 | 11,550 | 1675,356 |
| 250 | 10,488 | 1153,822 | 1,919 | 11,288 | 3808,695 |
| 270 | 10,490 | 1154,322 | 1,932 | 11,350 | 9996,977 |
| 290 | 10,491 | 1154,487 | 1,936 | 11,422 | 9992,648 |
| 310 | 10,491 | 1154,623 | 1,913 | 11,295 | 8009,142 |
| 330 | 10,492 | 1155,061 | 1,950 | 11,508 | 9998,056 |
| 350 | 10,493 | 1155,166 | 1,964 | 11,580 | 9999,970 |
| 370 | 10,494 | 1155,583 | 1,954 | 11,552 | 10000,000 |
| 390 | 10,495 | 1155,994 | 1,933 | 11,429 | 7942,964 |
| 410 | 10,496 | 1156,210 | 1,933 | 11,444 | 9983,929 |
| 430 | 10,497 | 1156,676 | 1,910 | 11,322 | 9999,749 |
| 450 | 10,498 | 1156,933 | 1,941 | 11,502 | 9999,996 |
| 470 | 10,500 | 1157,507 | 1,935 | 11,470 | 10000,000 |
| 490 | 10,501 | 1157,979 | 1,910 | 11,314 | 10000,000 |
| 510 | 10,502 | 1158,199 | 1,911 | 11,363 | 10000,000 |
| 530 | 10,503 | 1158,596 | 1,967 | 11,674 | 10000,000 |
| 550 | 10,504 | 1159,083 | 1,911 | 11,396 | 10000,000 |
| 570 | 10,505 | 1159,233 | 1,913 | 11,415 | 10000,000 |
| 590 | 10,506 | 1159,471 | 1,891 | 11,362 | 10000,000 |
| 610 | 10,506 | 1159,730 | 1,894 | 11,365 | 10000,000 |
| 630 | 10,507 | 1160,073 | 1,927 | 11,583 | 10000,000 |
| 650 | 10,507 | 1160,085 | 1,940 | 11,687 | 10000,000 |
| 670 | 10,508 | 1160,295 | 1,940 | 11,731 | 10000,000 |
| 690 | 10,509 | 1160,445 | 1,913 | 11,634 | 10000,000 |
| 710 | 10,509 | 1160,583 | 1,958 | 11,959 | 10000,000 |
| 730 | 10,509 | 1160,705 | 1,954 | 11,946 | 10000,000 |
| 750 | 10,510 | 1160,837 | 1,967 | 12,081 | 10000,000 |
| 770 | 10,510 | 1161,070 | 1,933 | 11,928 | 10000,000 |
| 790 | 10,511 | 1161,320 | 1,937 | 12,036 | 10000,000 |
| 810 | 10,512 | 1161,634 | 1,966 | 12,228 | 10000,000 |
| 830 | 10,513 | 1162,087 | 1,966 | 12,278 | 10000,000 |
| 850 | 10,515 | 1162,508 | 1,970 | 12,336 | 10000,000 |
| 30 | 10,476 | 1149,708 | 1,894 | 11,398 | 2419,661 |

Gadolinium Hafnate

| Temperature | Lattice Parameter | Volume | Goodness of Fit | Rwp | Crystallite size |
|---|---|---|---|---|---|
| 30 | 10,41836 | 1130,83217 | 1,30194 | 7,15591 | 49,69416 |
| 50 | 10,42076 | 1131,61401 | 1,33633 | 7,31036 | 34,69891 |
| 70 | 10,42044 | 1131,50789 | 1,32394 | 7,23058 | 33,00056 |
| 90 | 10,42137 | 1131,81279 | 1,31319 | 7,15054 | 30,1618 |
| 110 | 10,42277 | 1132,26922 | 1,3384 | 7,2781 | 28,89505 |
| 130 | 10,4245 | 1132,83222 | 1,30929 | 7,11654 | 27,79385 |
| 150 | 10,42539 | 1133,12279 | 1,31618 | 7,13274 | 27,20177 |
| 170 | 10,42576 | 1133,24277 | 1,30579 | 7,07787 | 27,37925 |
| 190 | 10,42748 | 1133,80455 | 1,32331 | 7,18706 | 26,72385 |
| 210 | 10,429 | 1134,30058 | 1,32209 | 7,1788 | 26,66246 |
| 230 | 10,42932 | 1134,40546 | 1,30895 | 7,10794 | 25,97017 |
| 250 | 10,43087 | 1134,91188 | 1,34394 | 7,32069 | 26,02672 |
| 270 | 10,43116 | 1135,0049 | 1,29924 | 7,1112 | 24,35585 |
| 290 | 10,43188 | 1135,24032 | 1,33811 | 7,29733 | 23,91502 |
| 310 | 10,43451 | 1136,09832 | 1,30903 | 7,17839 | 22,07761 |
| 330 | 10,43383 | 1135,87724 | 1,28355 | 7,03617 | 20,52898 |
| 350 | 10,43537 | 1136,38002 | 1,30685 | 7,16165 | 19,89322 |
| 370 | 10,43578 | 1136,51287 | 1,30234 | 7,13128 | 19,09858 |
| 390 | 10,43458 | 1136,12061 | 1,2812 | 7,05548 | 16,98468 |
| 410 | 10,44027 | 1137,9824 | 1,28914 | 7,06874 | 16,52155 |
| 430 | 10,43971 | 1137,79744 | 1,25691 | 6,91453 | 15,2305 |
| 450 | 10,44054 | 1138,06882 | 1,28814 | 7,06795 | 14,35919 |
| 470 | 10,4406 | 1138,08884 | 1,28335 | 7,06287 | 13,70174 |
| 490 | 10,4418 | 1138,48114 | 1,27906 | 7,01998 | 13,35654 |
| 510 | 10,44385 | 1139,15345 | 1,29918 | 7,16698 | 12,48611 |
| 530 | 10,44423 | 1139,27796 | 1,31983 | 7,2721 | 12,33931 |
| 550 | 10,44559 | 1139,72072 | 1,28874 | 7,12412 | 11,63847 |
| 570 | 10,44557 | 1139,71439 | 1,27489 | 7,08133 | 11,38956 |
| 590 | 10,44757 | 1140,36902 | 1,22518 | 6,80336 | 11,50148 |
| 610 | 10,44766 | 1140,39872 | 1,28817 | 7,18564 | 10,95461 |
| 630 | 10,44891 | 1140,81036 | 1,29063 | 7,21297 | 10,83935 |
| 650 | 10,44902 | 1140,84475 | 1,27136 | 7,13587 | 10,92199 |
| 670 | 10,44923 | 1140,9141 | 1,2815 | 7,21861 | 10,68184 |
| 690 | 10,45027 | 1141,25594 | 1,27129 | 7,18481 | 10,41622 |
| 710 | 10,45144 | 1141,63839 | 1,25588 | 7,11663 | 10,57113 |
| 730 | 10,45224 | 1141,89901 | 1,27854 | 7,2815 | 10,56312 |
| 750 | 10,45368 | 1142,37141 | 1,27265 | 7,28735 | 10,93282 |
| 770 | 10,45372 | 1142,38599 | 1,24496 | 7,14242 | 10,76076 |
| 790 | 10,45555 | 1142,98587 | 1,24183 | 7,18508 | 10,8951 |
| 810 | 10,45642 | 1143,2714 | 1,25695 | 7,26569 | 10,94677 |
| 830 | 10,45743 | 1143,60124 | 1,26392 | 7,31848 | 10,98766 |
| 850 | 10,45802 | 1143,79655 | 1,2654 | 7,3364 | 11,19474 |
| 30 | 10,41756 | 1130,57063 | 1,28851 | 7,12124 | 10,28129 |

Yttrium Hafnate

| Temperature | Lattice Parameter | Volume | Goodness of Fit | Rwp | Crystallite size | Y Beq | Hf Beq | O Beq |
|---|---|---|---|---|---|---|---|---|
| 30 | 5,18687 | 139,5458 | 1,30976 | 8,38255 | 122,91948 | 1,79907 | 1,70085 | 6,07918 |
| 50 | 5,18732 | 139,5823 | 1,34446 | 8,40342 | 83,80375 | 1,79515 | 1,69496 | 6,23751 |
| 70 | 5,18831 | 139,6616 | 1,30393 | 8,03924 | 20,73547 | 2,08255 | 1,85357 | 6,67092 |
| 90 | 5,189 | 139,7172 | 1,27812 | 7,84887 | 18,66411 | 2,08243 | 1,85255 | 6,55158 |
| 110 | 5,18963 | 139,7685 | 1,3125 | 8,06591 | 17,69239 | 2,08849 | 1,85361 | 6,86478 |
| 130 | 5,19018 | 139,8128 | 1,3005 | 8,03904 | 17,38342 | 2,07344 | 1,82599 | 6,86413 |
| 150 | 5,1905 | 139,8385 | 1,28217 | 7,93426 | 16,71313 | 2,06921 | 1,81665 | 6,80503 |
| 170 | 5,19118 | 139,8938 | 1,30042 | 8,05179 | 16,4378 | 2,01386 | 1,77421 | 6,59436 |
| 190 | 5,19198 | 139,9583 | 1,28387 | 7,99719 | 17,24403 | 1,99255 | 1,75945 | 6,48616 |
| 210 | 5,19219 | 139,975 | 1,30065 | 8,07555 | 17,43212 | 1,83724 | 1,63541 | 6,15564 |
| 230 | 5,19287 | 140,0305 | 1,28357 | 7,9806 | 17,13842 | 2,13631 | 1,81967 | 6,85376 |
| 250 | 5,19326 | 140,0617 | 1,28394 | 8,07561 | 17,53368 | 1,95876 | 1,68848 | 6,52537 |
| 270 | 5,19361 | 140,0904 | 1,27887 | 8,03394 | 17,74662 | 2,08919 | 1,75621 | 6,34829 |
| 290 | 5,19484 | 140,1896 | 1,25028 | 7,87093 | 17,66228 | 2,14787 | 1,81032 | 6,92322 |
| 310 | 5,19492 | 140,1962 | 1,30062 | 8,18704 | 17,70707 | 2,18338 | 1,82653 | 6,55432 |
| 330 | 5,19556 | 140,2485 | 1,24988 | 7,91389 | 17,44368 | 2,1944 | 1,83467 | 6,62258 |
| 350 | 5,1961 | 140,2919 | 1,30156 | 8,24726 | 17,79407 | 2,22418 | 1,8541 | 6,87475 |
| 370 | 5,19674 | 140,3434 | 1,26202 | 8,01171 | 18,66138 | 2,02344 | 1,69814 | 6,52019 |
| 390 | 5,19718 | 140,3795 | 1,28474 | 8,14924 | 18,25416 | 2,01606 | 1,69039 | 6,54147 |
| 410 | 5,19794 | 140,4413 | 1,2625 | 8,0235 | 19,49775 | 2,02538 | 1,7029 | 6,95751 |
| 430 | 5,1985 | 140,4861 | 1,29064 | 8,22347 | 19,45724 | 2,16069 | 1,80411 | 6,68922 |
| 450 | 5,19922 | 140,5451 | 1,27976 | 8,14315 | 18,28457 | 2,20464 | 1,83256 | 7,11939 |
| 470 | 5,19976 | 140,5885 | 1,27211 | 8,11833 | 18,85902 | 2,27054 | 1,87404 | 6,99087 |
| 490 | 5,20052 | 140,6498 | 1,27121 | 8,12836 | 19,27757 | 2,29596 | 1,87456 | 7,04868 |
| 510 | 5,20102 | 140,6911 | 1,29844 | 8,33757 | 18,58167 | 2,24315 | 1,78811 | 7,0864 |
| 530 | 5,20139 | 140,7208 | 1,2836 | 8,2581 | 20,12736 | 2,10576 | 1,74132 | 6,75535 |
| 550 | 5,20182 | 140,7556 | 1,30068 | 8,38116 | 20,24993 | 2,22882 | 1,8128 | 6,94738 |
| 570 | 5,20257 | 140,8167 | 1,3006 | 8,40315 | 20,59973 | 2,27047 | 1,83844 | 7,00496 |
| 590 | 5,20255 | 140,8146 | 1,30498 | 8,48193 | 20,40828 | 2,35985 | 1,92234 | 6,96654 |
| 610 | 5,2031 | 140,8598 | 1,31168 | 8,59741 | 21,11281 | 2,38229 | 1,92258 | 7,04641 |
| 630 | 5,20344 | 140,8871 | 1,30878 | 8,61884 | 21,81737 | 2,27598 | 1,84062 | 7,49877 |
| 650 | 5,2043 | 140,9574 | 1,30471 | 8,71021 | 21,76493 | 2,45355 | 1,93312 | 7,36376 |
| 670 | 5,20436 | 140,9618 | 1,32781 | 8,88819 | 23,27474 | 2,33938 | 1,90672 | 7,11227 |
| 690 | 5,20484 | 141,0013 | 1,33584 | 8,93042 | 23,23701 | 2,45314 | 1,95331 | 7,54788 |
| 710 | 5,20528 | 141,0371 | 1,35274 | 9,07726 | 24,59597 | 2,36832 | 1,89433 | 7,39987 |
| 730 | 5,20599 | 141,0949 | 1,36598 | 9,23597 | 25,04688 | 2,4383 | 1,93354 | 7,63187 |
| 750 | 5,20615 | 141,1076 | 1,38579 | 9,36916 | 25,14323 | 2,47596 | 1,95439 | 7,64321 |
| 770 | 5,20668 | 141,1509 | 1,34875 | 9,1991 | 26,59089 | 2,51355 | 1,96461 | 7,64062 |
| 790 | 5,20734 | 141,2043 | 1,35013 | 9,27081 | 26,47082 | 2,50548 | 1,97069 | 7,88336 |
| 810 | 5,20815 | 141,2705 | 1,36215 | 9,34449 | 27,68908 | 2,52869 | 1,99579 | 7,54131 |
| 830 | 5,20854 | 141,3016 | 1,39035 | 9,54507 | 26,84791 | 2,53561 | 2,00536 | 7,85878 |
| 850 | 5,20937 | 141,3693 | 1,41174 | 9,72792 | 26,53058 | 2,58845 | 2,06093 | 8,18793 |
| 30 | 5,18611 | 139,4845 | 1,26196 | 8,24369 | 19,9937 | 1,91634 | 1,73267 | 6,5052 |

Gadolinium Zirconate

| Temperature | Lattice Parameter | Volume | Goodness of Fit | Rwp | Crystallite size |
|---|---|---|---|---|---|
| 30 | 10,56472 | 1179,16407 | 1,03996 | 5,94342 | 26,21965 |
| 50 | 10,56372 | 1178,82795 | 1,07595 | 6,10521 | 18,39305 |
| 70 | 10,56586 | 1179,54493 | 1,05775 | 5,98706 | 15,2596 |
| 90 | 10,56642 | 1179,73207 | 1,05624 | 5,96389 | 13,68834 |
| 110 | 10,56744 | 1180,07395 | 1,04789 | 5,9213 | 12,91451 |
| 130 | 10,57163 | 1181,47847 | 1,05342 | 5,93238 | 12,20471 |
| 150 | 10,57109 | 1181,29783 | 1,061 | 5,96105 | 12,66498 |
| 170 | 10,57193 | 1181,58071 | 1,03662 | 5,82788 | 12,57721 |
| 190 | 10,57433 | 1182,38351 | 1,05302 | 5,93546 | 12,88867 |
| 210 | 10,57228 | 1181,69752 | 1,05008 | 5,91139 | 12,50517 |
| 230 | 10,57443 | 1182,41798 | 1,04732 | 5,89034 | 12,64928 |
| 250 | 10,5793 | 1184,05184 | 1,04832 | 5,89064 | 12,61417 |
| 270 | 10,57789 | 1183,57977 | 1,04609 | 5,89038 | 13,01226 |
| 290 | 10,57959 | 1184,15073 | 1,05048 | 5,91779 | 12,60643 |
| 310 | 10,58174 | 1184,87017 | 1,04614 | 5,89386 | 12,77263 |
| 330 | 10,58003 | 1184,29673 | 1,03876 | 5,85276 | 12,83089 |
| 350 | 10,58394 | 1185,61071 | 1,03306 | 5,8365 | 12,86608 |
| 370 | 10,58294 | 1185,27574 | 1,06315 | 6,02204 | 12,46858 |
| 390 | 10,58553 | 1186,14448 | 1,03722 | 5,86588 | 13,08145 |
| 410 | 10,58523 | 1186,04286 | 1,01361 | 5,75279 | 12,5545 |
| 430 | 10,58652 | 1186,47824 | 1,02981 | 5,85227 | 13,07034 |
| 450 | 10,59209 | 1188,35073 | 1,04572 | 5,93637 | 12,6046 |
| 470 | 10,58924 | 1187,39228 | 1,00306 | 5,69482 | 12,87852 |
| 490 | 10,59325 | 1188,74175 | 1,03834 | 5,91752 | 12,89911 |
| 510 | 10,58821 | 1187,04487 | 1,01809 | 5,81082 | 12,86209 |
| 530 | 10,59538 | 1189,46071 | 1,04007 | 5,93537 | 13,18251 |
| 550 | 10,59451 | 1189,166 | 1,03885 | 5,93682 | 12,95657 |
| 570 | 10,59707 | 1190,02781 | 1,02875 | 5,89342 | 13,0345 |
| 590 | 10,59773 | 1190,25264 | 1,02793 | 5,88501 | 12,65509 |
| 610 | 10,59792 | 1190,31438 | 1,04975 | 6,03183 | 12,71956 |
| 630 | 10,60083 | 1191,29436 | 1,01327 | 5,83711 | 12,57376 |
| 650 | 10,59937 | 1190,80502 | 0,99974 | 5,77531 | 12,77968 |
| 670 | 10,60262 | 1191,89778 | 1,02322 | 5,93492 | 12,84786 |
| 690 | 10,60277 | 1191,95083 | 1,0293 | 5,98002 | 12,84827 |
| 710 | 10,60226 | 1191,77825 | 1,02454 | 5,96362 | 12,88493 |
| 730 | 10,60558 | 1192,89715 | 1,02503 | 5,99778 | 12,04718 |
| 750 | 10,6043 | 1192,46464 | 1,02049 | 5,99039 | 11,54465 |
| 770 | 10,60779 | 1193,64537 | 1,05722 | 6,22973 | 13,50155 |
| 790 | 10,60553 | 1192,88174 | 1,0162 | 5,98913 | 14,24856 |
| 810 | 10,60956 | 1194,23979 | 1,02645 | 6,06896 | 13,67115 |
| 830 | 10,61032 | 1194,49723 | 1,017 | 6,01548 | 12,48364 |
| 850 | 10,61066 | 1194,61232 | 1,01534 | 6,00917 | 12,82159 |
| 30 | 10,55832 | 1177,02281 | 1,05509 | 6,03061 | 12,40921 |
| | | | | | |

Yttrium Zirconate

| Temperature | Lattice parameter | Volume | Goodness of fit | Rwp | Crystallite size | Y Beq | Zr Beq | O1 XPOS | O1 Beq | O2 Beq |
|---|---|---|---|---|---|---|---|---|---|---|
| 30 | 10,40829 | 1127,55522 | 1,20227 | 9,00422 | 261,52739 | 1,31806 | 1,53389 | 0,39474 | 2,24461 | 3,88823 |
| 50 | 10,41051 | 1128,27614 | 1,20328 | 8,74960 | 244,54711 | 1,52933 | 1,64015 | 0,39212 | 2,66847 | 5,26291 |
| 70 | 10,41186 | 1128,71605 | 1,21492 | 8,70103 | 261,96599 | 1,51159 | 1,83947 | 0,39334 | 2,92527 | 4,52032 |
| 90 | 10,41315 | 1129,13587 | 1,23814 | 8,88642 | 253,13849 | 1,46002 | 1,95581 | 0,39322 | 2,96597 | 3,48932 |
| 110 | 10,41532 | 1129,84224 | 1,21288 | 8,72042 | 244,27652 | 1,71477 | 1,89443 | 0,39364 | 3,09546 | 3,78980 |
| 130 | 10,41640 | 1130,19409 | 1,22625 | 8,86439 | 272,52836 | 1,59710 | 1,88258 | 0,39318 | 2,78940 | 4,77641 |
| 150 | 10,41883 | 1130,98614 | 1,22226 | 8,82014 | 230,32919 | 1,61698 | 1,88600 | 0,39303 | 3,10515 | 3,87264 |
| 170 | 10,41995 | 1131,35113 | 1,21078 | 8,74232 | 216,46021 | 1,74867 | 1,95499 | 0,39237 | 3,07090 | 4,83824 |
| 190 | 10,42331 | 1132,44599 | 1,21849 | 8,78110 | 235,96632 | 1,54793 | 1,93022 | 0,39208 | 2,99131 | 3,60349 |
| 210 | 10,42477 | 1132,92107 | 1,20752 | 8,75501 | 250,69070 | 1,55410 | 2,03911 | 0,39288 | 2,98086 | 5,08816 |
| 230 | 10,42641 | 1133,45640 | 1,20350 | 8,68609 | 284,71711 | 1,57917 | 1,98993 | 0,39486 | 3,17996 | 3,13106 |
| 250 | 10,42717 | 1133,70247 | 1,23930 | 8,94143 | 243,00836 | 1,66080 | 1,92079 | 0,39187 | 3,01371 | 4,85281 |
| 270 | 10,43005 | 1134,64123 | 1,24758 | 8,99317 | 265,48182 | 1,58614 | 1,97848 | 0,39438 | 2,75531 | 5,12498 |
| 290 | 10,43158 | 1135,14278 | 1,22078 | 8,84397 | 245,62102 | 1,57551 | 1,92728 | 0,39234 | 3,14779 | 3,70074 |
| 310 | 10,43507 | 1136,28340 | 1,20860 | 8,73697 | 249,97650 | 1,58553 | 1,97843 | 0,39391 | 3,09269 | 4,42367 |
| 330 | 10,43684 | 1136,86043 | 1,24417 | 8,97756 | 251,16277 | 1,50492 | 2,06921 | 0,39388 | 2,92546 | 3,01322 |
| 350 | 10,43904 | 1137,57984 | 1,24340 | 9,01446 | 215,80659 | 1,56564 | 2,05337 | 0,39286 | 2,94214 | 4,99990 |
| 370 | 10,44022 | 1137,96458 | 1,21587 | 8,79704 | 234,56163 | 1,53901 | 2,09567 | 0,39427 | 3,12892 | 3,95754 |
| 390 | 10,44230 | 1138,64633 | 1,20058 | 8,79878 | 269,08578 | 1,65419 | 2,05529 | 0,39311 | 3,33301 | 5,00213 |
| 410 | 10,44425 | 1139,28211 | 1,22038 | 8,90359 | 236,46477 | 1,80202 | 2,06225 | 0,39263 | 3,34233 | 4,86549 |
| 430 | 10,44615 | 1139,90404 | 1,23999 | 9,08518 | 265,93019 | 1,68655 | 2,07642 | 0,39233 | 3,20610 | 5,27836 |
| 450 | 10,44869 | 1140,73583 | 1,22360 | 8,94315 | 254,36814 | 1,75444 | 1,99828 | 0,39042 | 3,41161 | 6,14273 |
| 470 | 10,45045 | 1141,31205 | 1,25175 | 9,18032 | 235,08842 | 1,68431 | 2,19571 | 0,39280 | 3,62612 | 4,81110 |
| 490 | 10,45243 | 1141,96309 | 1,22900 | 9,03990 | 228,36864 | 1,70838 | 2,05822 | 0,39219 | 3,42912 | 4,20643 |
| 510 | 10,45458 | 1142,66854 | 1,22853 | 9,03371 | 256,71670 | 1,70287 | 2,08958 | 0,39312 | 3,46001 | 4,36117 |
| 530 | 10,45694 | 1143,44039 | 1,22126 | 9,01501 | 235,01968 | 1,68779 | 2,09324 | 0,39256 | 3,48238 | 4,93216 |
| 550 | 10,45829 | 1143,88511 | 1,20230 | 8,89846 | 235,04230 | 1,60704 | 2,04887 | 0,39328 | 3,60065 | 2,95738 |
| 570 | 10,45829 | 1143,88415 | 1,24288 | 9,23664 | 235,04230 | 1,60700 | 2,04890 | 0,39328 | 3,60070 | 2,95740 |
| 590 | 10,46522 | 1146,15939 | 1,21909 | 9,11279 | 286,26007 | 1,65666 | 2,12956 | 0,39123 | 3,35433 | 5,40557 |
| 610 | 10,46695 | 1146,72705 | 1,23251 | 9,21416 | 225,80918 | 1,68962 | 2,10083 | 0,39348 | 3,49915 | 3,81490 |
| 630 | 10,46890 | 1147,36879 | 1,21793 | 9,13846 | 255,49205 | 1,64988 | 2,35040 | 0,39213 | 3,73475 | 4,58726 |
| 650 | 10,47125 | 1148,14192 | 1,22055 | 9,19711 | 230,29110 | 1,80639 | 2,02560 | 0,39109 | 3,71675 | 4,65303 |
| 670 | 10,47350 | 1148,88349 | 1,23343 | 9,32952 | 246,31314 | 1,57287 | 2,19116 | 0,39320 | 3,53722 | 4,25822 |
| 690 | 10,47578 | 1149,63317 | 1,21518 | 9,24361 | 261,90067 | 1,85500 | 2,06655 | 0,39180 | 3,35133 | 6,01182 |
| 710 | 10,47662 | 1149,90956 | 1,21559 | 9,27664 | 226,53052 | 1,68740 | 2,25134 | 0,39129 | 3,48565 | 5,21128 |
| 730 | 10,48017 | 1151,07821 | 1,20898 | 9,27667 | 243,76181 | 1,71668 | 2,20110 | 0,39069 | 3,84397 | 4,57213 |
| 750 | 10,48117 | 1151,40877 | 1,21355 | 9,36536 | 259,29536 | 1,61152 | 2,32969 | 0,39279 | 3,56913 | 5,44247 |
| 770 | 10,48412 | 1152,38095 | 1,21587 | 9,44152 | 275,33736 | 1,70577 | 2,11401 | 0,38905 | 3,72432 | 6,73809 |
| 790 | 10,48486 | 1152,62399 | 1,20544 | 9,41886 | 240,28591 | 1,61168 | 2,24553 | 0,39040 | 3,81246 | 5,93780 |
| 810 | 10,48850 | 1153,82449 | 1,19681 | 9,34937 | 242,23929 | 1,69312 | 2,28377 | 0,39056 | 3,60094 | 6,54327 |
| 830 | 10,49091 | 1154,62151 | 1,18845 | 9,33758 | 235,43669 | 1,77243 | 2,10352 | 0,39178 | 3,91973 | 5,05432 |
| 30 | 10,41207 | 1128,78578 | 1,21225 | 8,96744 | 212,47172 | 1,46958 | 1,80158 | 0,39208 | 2,90098 | 4,55514 |

Europium Titanate

| Temperature | Lattice Parameter | Volume | Goodness of Fit | Rwp | Crystallite size | Eu Beq | Ti Beq | O1 Beq | O2 Beq |
|---|---|---|---|---|---|---|---|---|---|
| 30 | 10,20272 | 1062,057 | 1,09281 | 6,56216 | 122,14965 | 0,30575 | -0,30517 | 0,51505 | 0,50026 |
| 50 | 10,20481 | 1062,71 | 1,10633 | 6,55738 | 130,84881 | 0,4029 | 0,045 | 0,60765 | 0,50002 |
| 70 | 10,20649 | 1063,235 | 1,11986 | 6,62632 | 130,56645 | 0,43613 | 0,045 | 0,50336 | 0,5 |
| 90 | 10,20869 | 1063,924 | 1,09806 | 6,47545 | 121,97058 | 0,40624 | 0,06018 | 0,62573 | 0,5 |
| 110 | 10,21045 | 1064,473 | 1,09754 | 6,46049 | 128,58528 | 0,40311 | 0,04595 | 1,01091 | 0,6175 |
| 130 | 10,21243 | 1065,094 | 1,10876 | 6,52062 | 117,86366 | 0,41269 | 0,04501 | 0,56521 | 0,50092 |
| 150 | 10,2142 | 1065,647 | 1,10347 | 6,49861 | 120,06734 | 0,40412 | 0,045 | 0,5602 | 2,03181 |
| 170 | 10,21668 | 1066,423 | 1,07208 | 6,31998 | 125,63289 | 0,5483 | 0,045 | 0,82004 | 1,29031 |
| 190 | 10,21845 | 1066,978 | 1,07142 | 6,33045 | 124,12713 | 0,56731 | 0,045 | 0,74697 | 1,71976 |
| 210 | 10,22064 | 1067,664 | 1,06137 | 6,26873 | 124,37398 | 0,52268 | 0,04802 | 0,69867 | 0,57624 |
| 230 | 10,22244 | 1068,228 | 1,09372 | 6,46507 | 123,33511 | 0,61014 | 0,04505 | 0,53175 | 0,50119 |
| 250 | 10,2248 | 1068,966 | 1,1076 | 6,53592 | 114,65023 | 0,65024 | 0,09854 | 0,62515 | 0,57293 |
| 270 | 10,22689 | 1069,622 | 1,10334 | 6,50736 | 127,0876 | 0,60245 | 0,04834 | 0,62584 | 0,50456 |
| 290 | 10,22869 | 1070,187 | 1,11715 | 6,60148 | 122,48349 | 0,89356 | 0,16889 | 1,09605 | 0,50029 |
| 310 | 10,23024 | 1070,675 | 1,11525 | 6,60151 | 132,05669 | 0,94795 | 0,07265 | 1,55609 | 0,50002 |
| 330 | 10,23255 | 1071,401 | 1,10792 | 6,56157 | 119,31035 | 0,78541 | 0,04586 | 1,20617 | 0,5 |
| 350 | 10,23472 | 1072,082 | 1,0905 | 6,4764 | 127,36902 | 0,77754 | 0,04503 | 1,001 | 0,5 |
| 370 | 10,23659 | 1072,67 | 1,11875 | 6,65076 | 119,17305 | 0,78436 | 0,05075 | 0,97626 | 0,5 |
| 390 | 10,23892 | 1073,403 | 1,10255 | 6,55587 | 122,7054 | 0,72464 | 0,05004 | 0,64462 | 0,5 |
| 410 | 10,24127 | 1074,141 | 1,10783 | 6,6113 | 130,75514 | 0,7511 | 0,15021 | 0,95974 | 0,5 |
| 430 | 10,24352 | 1074,85 | 1,13938 | 6,81269 | 116,92302 | 0,89108 | 0,04829 | 1,33037 | 0,5 |
| 450 | 10,24511 | 1075,35 | 1,09005 | 6,51811 | 126,41551 | 0,74737 | 0,04521 | 1,05366 | 0,5 |
| 470 | 10,24741 | 1076,076 | 1,11497 | 6,67949 | 122,30621 | 0,8988 | 0,26113 | 1,64826 | 0,5 |
| 490 | 10,24969 | 1076,793 | 1,0997 | 6,58919 | 114,39994 | 0,76184 | 0,20291 | 1,90035 | 0,86091 |
| 510 | 10,25196 | 1077,51 | 1,11833 | 6,71255 | 119,97296 | 0,95376 | 0,09883 | 1,65936 | 0,50564 |
| 530 | 10,25381 | 1078,093 | 1,12928 | 6,79958 | 126,11279 | 0,91991 | 0,13283 | 1,05833 | 1,12934 |
| 550 | 10,25558 | 1078,651 | 1,11605 | 6,74315 | 123,62889 | 0,87697 | 0,26526 | 1,80061 | 0,57866 |
| 570 | 10,25819 | 1079,473 | 1,12384 | 6,81122 | 122,21019 | 0,98955 | 0,2493 | 1,54255 | 0,59335 |
| 590 | 10,25987 | 1080,006 | 1,09542 | 6,66901 | 115,79499 | 0,82502 | 0,05662 | 0,8101 | 0,82892 |
| 610 | 10,26233 | 1080,782 | 1,11349 | 6,79964 | 128,0496 | 1,07021 | 0,28578 | 1,98628 | 0,52056 |
| 630 | 10,26434 | 1081,416 | 1,14159 | 6,99487 | 119,91524 | 0,93426 | 0,48489 | 2,00047 | 0,50129 |
| 650 | 10,26629 | 1082,033 | 1,09922 | 6,74664 | 126,14071 | 0,911 | 0,16517 | 1,13726 | 0,50004 |
| 670 | 10,26834 | 1082,682 | 1,13065 | 6,97138 | 125,01665 | 1,22469 | 0,50549 | 1,89964 | 0,69885 |
| 690 | 10,2708 | 1083,458 | 1,12869 | 6,98211 | 112,1628 | 1,11011 | 0,25527 | 2,21357 | 0,50311 |
| 710 | 10,27294 | 1084,136 | 1,11141 | 6,91029 | 123,38461 | 1,11236 | 0,52604 | 1,99235 | 0,50039 |
| 730 | 10,27492 | 1084,764 | 1,11234 | 6,94111 | 118,79177 | 1,12231 | 0,38074 | 1,84223 | 0,50002 |
| 750 | 10,27696 | 1085,409 | 1,12763 | 7,05792 | 118,95322 | 1,10825 | 0,12723 | 1,1343 | 2,10918 |
| 770 | 10,27938 | 1086,178 | 1,14143 | 7,16837 | 126,30408 | 1,07626 | 0,67882 | 2,31961 | 0,50314 |
| 790 | 10,28153 | 1086,858 | 1,09864 | 6,92576 | 127,28327 | 1,24012 | 0,32591 | 0,96244 | 0,50019 |
| 810 | 10,28358 | 1087,51 | 1,12986 | 7,15451 | 122,42749 | 1,28891 | 0,24802 | 1,21397 | 0,50002 |
| 830 | 10,2857 | 1088,182 | 1,09345 | 6,95394 | 124,37253 | 1,14644 | 0,45677 | 2,22064 | 0,64552 |
| 850 | 10,28792 | 1088,886 | 1,11322 | 7,09442 | 124,67048 | 1,38322 | 0,45507 | 1,98775 | 0,50114 |
| 30 | 10,20263 | 1062,028 | 1,14428 | 6,87232 | 1129,78394 | 0,40307 | 0,0452 | 0,85473 | 1,8316 |

Gadolinium Titanate

| Temperature | Lattice parameter | Volume | Goodness of Fit | Rwp | Crystallite size | Gd Beq | Ti Beq | O1 Beq | O2 Beq | X position |
|---|---|---|---|---|---|---|---|---|---|---|
| 30 | 10,19402 | 1059,34325 | 1,14272 | 6,13937 | 63,04538 | 0,2 | 0,04629 | 0,84539 | 1,1465 | 0,33031 |
| 50 | 10,19514 | 1059,69332 | 1,13774 | 6,01703 | 61,8769 | 0,2 | 0,045 | 1,24294 | 1,81607 | 0,33246 |
| 70 | 10,19742 | 1060,40203 | 1,15368 | 6,12233 | 62,83003 | 0,2 | 0,045 | 1,95088 | 0,53544 | 0,33067 |
| 90 | 10,19886 | 1060,85111 | 1,14388 | 6,09222 | 63,93059 | 0,2 | 0,045 | 1,3874 | 0,95651 | 0,33145 |
| 110 | 10,20002 | 1061,21325 | 1,10844 | 5,92616 | 63,00857 | 0,2 | 0,045 | 0,59785 | 2,15201 | 0,33147 |
| 130 | 10,20163 | 1061,71716 | 1,09815 | 5,89074 | 62,92506 | 0,2 | 0,045 | 1,04025 | 2,00012 | 0,33041 |
| 150 | 10,20297 | 1062,1366 | 1,05891 | 5,69964 | 59,37237 | 0,22125 | 0,045 | 1,25688 | 0,54688 | 0,33115 |
| 170 | 10,2046 | 1062,64532 | 1,08465 | 5,84022 | 63,65287 | 0,20067 | 0,045 | 1,49559 | 0,76361 | 0,32996 |
| 190 | 10,20623 | 1063,15482 | 1,08075 | 5,83313 | 62,9327 | 0,20001 | 0,045 | 0,93896 | 2,49375 | 0,33224 |
| 210 | 10,20765 | 1063,59826 | 1,05659 | 5,68895 | 61,45929 | 0,2 | 0,045 | 0,6244 | 2,37497 | 0,33171 |
| 230 | 10,20974 | 1064,25024 | 1,04882 | 5,65842 | 65,04043 | 0,2 | 0,045 | 0,71302 | 2,7148 | 0,33396 |
| 250 | 10,2111 | 1064,67777 | 1,07527 | 5,8108 | 58,89136 | 0,30599 | 0,045 | 2,04909 | 2,51374 | 0,33404 |
| 270 | 10,21287 | 1065,23015 | 1,06174 | 5,7274 | 63,27013 | 0,21447 | 0,045 | 1,69829 | 0,88263 | 0,3328 |
| 290 | 10,21469 | 1065,80034 | 1,05026 | 5,6684 | 62,67684 | 0,47953 | 0,045 | 0,68773 | 0,7697 | 0,32997 |
| 310 | 10,21605 | 1066,22697 | 1,07486 | 5,81323 | 62,96342 | 0,41816 | 0,045 | 1,22687 | 0,51686 | 0,33224 |
| 330 | 10,21741 | 1066,65143 | 1,0664 | 5,7754 | 63,77633 | 0,5385 | 0,045 | 1,45465 | 0,50136 | 0,33136 |
| 350 | 10,21869 | 1067,05199 | 1,05244 | 5,69514 | 62,86148 | 0,49482 | 0,045 | 2,15581 | 2,375 | 0,33473 |
| 370 | 10,22038 | 1067,58217 | 1,07746 | 5,84655 | 66,85187 | 0,7067 | 0,045 | 1,56652 | 0,65049 | 0,32963 |
| 390 | 10,22183 | 1068,035 | 1,05113 | 5,72478 | 73,38129 | 0,40378 | 0,045 | 0,82682 | 1,14887 | 0,33246 |
| 410 | 10,22331 | 1068,50101 | 1,04567 | 5,69689 | 73,64342 | 0,5319 | 0,045 | 0,75663 | 0,85212 | 0,33221 |
| 430 | 10,22477 | 1068,95895 | 1,05909 | 5,77933 | 72,72708 | 0,82764 | 0,045 | 2,13353 | 2,31715 | 0,33356 |
| 450 | 10,22647 | 1069,49015 | 1,05007 | 5,72185 | 74,83324 | 0,74922 | 0,045 | 1,10164 | 2,73133 | 0,32881 |
| 470 | 10,22775 | 1069,89311 | 1,05593 | 5,77453 | 75,29695 | 0,79008 | 0,045 | 1,80909 | 1,02279 | 0,33504 |
| 490 | 10,22933 | 1070,39011 | 1,07534 | 5,90223 | 82,07148 | 0,7462 | 0,07632 | 0,40114 | 1,80648 | 0,33329 |
| 510 | 10,23016 | 1070,64952 | 1,0822 | 5,93778 | 77,60908 | 0,5925 | 0,15148 | 0,95551 | 3,49777 | 0,33372 |
| 530 | 10,23185 | 1071,18039 | 1,05868 | 5,82365 | 79,61648 | 0,91308 | 0,07032 | 0,92412 | 2,15174 | 0,33278 |
| 550 | 10,23273 | 1071,45699 | 1,10848 | 6,12897 | 83,87113 | 1,08978 | 0,23605 | 1,74013 | 3,28242 | 0,33376 |
| 570 | 10,2343 | 1071,94847 | 1,11368 | 6,1776 | 88,67891 | 0,83492 | 0,08455 | 1,45332 | 1,40895 | 0,33245 |
| 590 | 10,23506 | 1072,18867 | 1,11916 | 6,22937 | 90,34699 | 0,87589 | 0,40163 | 1,58894 | 3,12077 | 0,33619 |
| 610 | 10,23614 | 1072,52679 | 1,14214 | 6,39246 | 94,10058 | 1,09295 | 0,44872 | 1,10783 | 3,62573 | 0,33647 |
| 630 | 10,23758 | 1072,98208 | 1,18503 | 6,63867 | 96,46874 | 1,27101 | 0,69993 | 2,61306 | 1,51418 | 0,33194 |
| 650 | 10,23802 | 1073,11895 | 1,15826 | 6,53644 | 100,87373 | 1,22082 | 0,77642 | 3,1815 | 2,779 | 0,33631 |
| 670 | 10,23882 | 1073,37066 | 1,18463 | 6,71108 | 109,81908 | 1,55629 | 0,76565 | 2,28733 | 3,90912 | 0,33317 |
| 690 | 10,2401 | 1073,77297 | 1,18013 | 6,70803 | 104,08522 | 1,44382 | 0,96988 | 2,49668 | 1,92012 | 0,33545 |
| 710 | 10,24085 | 1074,00821 | 1,22333 | 6,97832 | 110,86244 | 1,55617 | 0,89078 | 2,09029 | 3,59309 | 0,33281 |
| 730 | 10,24139 | 1074,17819 | 1,19978 | 6,85241 | 104,39076 | 1,86972 | 0,99843 | 3,48407 | 3,94914 | 0,33733 |
| 750 | 10,24262 | 1074,56743 | 1,22481 | 7,02655 | 108,61755 | 1,9628 | 1,48556 | 3,74205 | 3,97455 | 0,33974 |
| 770 | 10,24336 | 1074,79871 | 1,2311 | 7,10895 | 113,93015 | 1,85939 | 1,47366 | 3,78624 | 3,99681 | 0,33904 |
| 790 | 10,24431 | 1075,09953 | 1,23553 | 7,15384 | 104,84034 | 2,14011 | 1,77185 | 2,82472 | 3,9998 | 0,33955 |
| 810 | 10,24588 | 1075,59173 | 1,24903 | 7,27408 | 116,45049 | 2,25373 | 1,672 | 3,43759 | 2,69708 | 0,33673 |
| 830 | 10,24637 | 1075,74586 | 1,28381 | 7,5009 | 111,20875 | 1,81473 | 1,67219 | 3,9047 | 3,83714 | 0,34006 |
| 850 | 10,2481 | 1076,29212 | 1,26772 | 7,42109 | 117,50993 | 2,63764 | 1,68349 | 3,34118 | 3,97964 | 0,32931 |
| 30 | 10,19324 | 1059,09939 | 1,1448 | 6,27623 | 509,06775 | 0,42941 | 0,05046 | 1,48794 | 0,8157 | 0,33256 |

Yttrium Titanate

| Temperature | Lattice Parameter | Volume | Goodness of Fit | Rwp | Crystallite Size | Y Beq | Ti Beq | O1 Beq | O2 Beq | O1 X position |
|---|---|---|---|---|---|---|---|---|---|---|
| 30 | 10,09748 | 1029,53 | 1,32408 | 12,54727 | 92,36133 | 0,36569 | 0,11723 | 0,69171 | 0,23292 | 0,41885 |
| 50 | 10,09917 | 1030,048 | 1,31062 | 12,22303 | 91,44977 | 0,42519 | 0,0662 | 0,70677 | 0,25039 | 0,41922 |
| 70 | 10,10106 | 1030,627 | 1,29381 | 12,02629 | 91,72638 | 0,40829 | 0,16003 | 0,81113 | 0,2126 | 0,41954 |
| 90 | 10,10328 | 1031,306 | 1,36195 | 12,66787 | 90,03098 | 0,49063 | 0,21524 | 0,83343 | 0,00083 | 0,41945 |
| 110 | 10,10525 | 1031,908 | 1,36654 | 12,76539 | 91,56293 | 0,50862 | 0,19728 | 0,70437 | 0,2328 | 0,41973 |
| 130 | 10,10731 | 1032,539 | 1,336 | 12,46309 | 92,13707 | 0,57024 | 0,27277 | 1,05737 | 0,03678 | 0,41926 |
| 150 | 10,1093 | 1033,149 | 1,32709 | 12,41616 | 90,84535 | 0,59078 | 0,24333 | 0,97246 | 0,22742 | 0,41878 |
| 170 | 10,11132 | 1033,769 | 1,30832 | 12,33742 | 93,03938 | 0,62634 | 0,30237 | 1,1184 | 0,43282 | 0,41911 |
| 190 | 10,11339 | 1034,404 | 1,34723 | 12,71258 | 89,88314 | 0,67076 | 0,3265 | 1,09225 | 0,27519 | 0,41937 |
| 210 | 10,1154 | 1035,02 | 1,33518 | 12,56768 | 91,1662 | 0,63689 | 0,21863 | 1,15477 | 0,13696 | 0,41948 |
| 230 | 10,11754 | 1035,677 | 1,37047 | 12,97002 | 91,49914 | 0,6492 | 0,25513 | 0,97384 | 0,2115 | 0,41986 |
| 250 | 10,11938 | 1036,244 | 1,3429 | 12,68225 | 91,60213 | 0,7531 | 0,33267 | 1,12234 | 0,0073 | 0,41955 |
| 270 | 10,1217 | 1036,956 | 1,36355 | 12,95722 | 91,03407 | 0,73045 | 0,30093 | 1,18778 | 0,00001 | 0,41911 |
| 290 | 10,12375 | 1037,586 | 1,35193 | 12,82143 | 90,72672 | 0,77003 | 0,41542 | 1,39284 | 0 | 0,41921 |
| 310 | 10,12581 | 1038,22 | 1,35008 | 12,82163 | 90,51308 | 0,75181 | 0,37163 | 1,30227 | 0 | 0,419 |
| 330 | 10,12776 | 1038,818 | 1,39644 | 13,23407 | 92,64375 | 0,83467 | 0,50909 | 1,40123 | 0,82405 | 0,41867 |
| 350 | 10,12997 | 1039,5 | 1,394 | 13,25257 | 90,01618 | 0,85925 | 0,43816 | 1,50646 | 0,06039 | 0,41896 |
| 370 | 10,13218 | 1040,182 | 1,36334 | 12,99158 | 90,20702 | 0,88836 | 0,44364 | 1,38743 | 0,30039 | 0,41889 |
| 390 | 10,13412 | 1040,777 | 1,3557 | 12,98614 | 90,40332 | 0,87622 | 0,38069 | 1,28476 | 0,23921 | 0,41891 |
| 410 | 10,13615 | 1041,404 | 1,35458 | 12,98093 | 91,61891 | 0,93268 | 0,50703 | 1,42067 | 0,19585 | 0,41961 |
| 430 | 10,13822 | 1042,043 | 1,36334 | 13,12757 | 91,27111 | 0,94235 | 0,54058 | 1,51585 | 0,32049 | 0,4185 |
| 450 | 10,14045 | 1042,729 | 1,39446 | 13,40401 | 89,32595 | 0,94255 | 0,56194 | 1,56147 | 0,4762 | 0,41876 |
| 470 | 10,14266 | 1043,413 | 1,34874 | 13,04968 | 88,82623 | 1,02953 | 0,54446 | 1,66042 | 0,41718 | 0,4193 |
| 490 | 10,14463 | 1044,02 | 1,36935 | 13,30593 | 91,29515 | 0,97516 | 0,63131 | 1,74951 | 0,83296 | 0,41798 |
| 510 | 10,14641 | 1044,568 | 1,37051 | 13,32043 | 91,77717 | 1,07157 | 0,57467 | 1,96683 | 0,72735 | 0,41768 |
| 530 | 10,1486 | 1045,246 | 1,38867 | 13,50647 | 91,11656 | 1,12019 | 0,65664 | 1,88639 | 1,14448 | 0,41776 |
| 550 | 10,15076 | 1045,914 | 1,40211 | 13,74112 | 90,62867 | 1,14567 | 0,61328 | 1,73761 | 0,6208 | 0,419 |
| 570 | 10,153 | 1046,606 | 1,36211 | 13,53812 | 90,36707 | 1,15766 | 0,63026 | 1,9559 | 1,02879 | 0,41809 |
| 590 | 10,15492 | 1047,2 | 1,37951 | 13,67168 | 89,80745 | 1,05856 | 0,68729 | 1,89679 | 0,59307 | 0,41832 |
| 610 | 10,15737 | 1047,957 | 1,41836 | 13,99325 | 89,88597 | 1,17405 | 0,63572 | 1,98279 | 0,60416 | 0,417 |
| 630 | 10,15946 | 1048,605 | 1,41173 | 13,98226 | 89,87098 | 1,18728 | 0,76029 | 1,92789 | 0,58829 | 0,41843 |
| 650 | 10,16133 | 1049,185 | 1,39304 | 13,85598 | 89,68935 | 1,19072 | 0,76784 | 1,98645 | 0,79017 | 0,41781 |
| 670 | 10,16318 | 1049,757 | 1,40741 | 14,09426 | 90,58274 | 1,21416 | 0,77611 | 2,36805 | 0,67841 | 0,41757 |
| 690 | 10,16547 | 1050,468 | 1,39575 | 14,07254 | 89,99031 | 1,26348 | 0,81232 | 1,95286 | 1,18923 | 0,41769 |
| 710 | 10,16763 | 1051,138 | 1,40314 | 14,14619 | 89,50651 | 1,2921 | 0,75214 | 1,8224 | 0,85522 | 0,41841 |
| 730 | 10,16958 | 1051,742 | 1,40489 | 14,18853 | 90,2138 | 1,29589 | 0,81805 | 1,93094 | 1,21222 | 0,41832 |
| 750 | 10,17204 | 1052,504 | 1,41116 | 14,33943 | 89,56065 | 1,34414 | 0,8007 | 2,08165 | 1,15092 | 0,41776 |
| 770 | 10,17439 | 1053,234 | 1,3988 | 14,27383 | 89,2424 | 1,40789 | 0,68239 | 1,89805 | 0,77013 | 0,41856 |
| 790 | 10,1762 | 1053,795 | 1,40688 | 14,37792 | 89,56743 | 1,35907 | 0,75594 | 2,06862 | 1,60435 | 0,41781 |
| 810 | 10,1782 | 1054,418 | 1,41716 | 14,50265 | 88,02331 | 1,38113 | 0,78343 | 2,11159 | 0,86863 | 0,4182 |
| 830 | 10,18045 | 1055,117 | 1,42803 | 14,68826 | 89,32409 | 1,42661 | 0,87142 | 2,18509 | 0,97769 | 0,41786 |
| 850 | 10,18256 | 1055,775 | 1,39948 | 14,42899 | 88,25 | 1,39866 | 0,85777 | 2,27182 | 1,08076 | 0,41761 |
| 30 | 10,0972 | 1029,443 | 1,29106 | 12,30216 | 91,25693 | 0,42929 | 0,13068 | 0,69874 | 0,00464 | 0,4195 |

## c. Crystallographic information table

### i. Crystallographic information table

| System | Exact formula | Structure Type | a (Å) | Measurement Temperature (K) | O 48f Position | R factor | Cif reference code |
|---|---|---|---|---|---|---|---|
| $Eu_2Hf_2O_7$ | Eu2.1 Hf1.9 O6.952 | Pyrochlore | 10.4847(3) | Not Given | 0.228(3) | 0.0529 | 158839 |
| | Eu2.096 Hf1.904 O6.952 | Pyrochlore | 10.4847(3) | Not Given | 0.228(3) | 0.0529 | 156142 |
| | Eu2 Hf2 O7 | Pyrochlore | 10.560(1) | Not Given | 0.342(2) | Not available | 173953 |
| $Gd_2Hf_2O_7$ | (Gd1.84 Hf0.16) (Hf1.84 Gd0.16) O7 | Pyrochlore | 10.5186(3) | Not Given | 0.224(3) | 0.0477 | 158840 |
| | (Gd2 Hf2) O7 | Pyrochlore | 10.5186(3) | Not Given | 0.224(3) | 0.0477 | 156143 |
| $La_2Hf_2O_7$ | Hf2 La2 O7 | Pyrochlore | 10.673 | Not Given | 0.3298 | Not available | 153815 |
| | Hf2 La2 O7 | Pyrochlore | 10.7728 | 298 | 0.4202(2) | 0.0387 | 173790 |
| $Y_2Hf_2O_7$ | | | | | | | |
| | | | | | | | |
| $Gd_2Zr_2O_7$ | Gd2 O7 Zr2 | Pyrochlore | 10.5169(3) | Not Given | 0.225(2) | 0.041 | 156140 |
| | Gd2 O7 Zr2 | Fluorite | 5.2593(2) | Not Given | Not Applicable | 0.0234 | 165807 |
| | Gd2 O7 Zr2 | Fluorite | 5.2601(2) | Not Given | Not Applicable | 0.0235 | 165808 |
| | Gd2 O7 Zr2 | Fluorite | 5.2603(2) | Not Given | Not Applicable | 0.0209 | 165809 |
| | Gd2 O7 Zr2 | Fluorite | 5.2605(2) | Not Given | Not Applicable | 0.0255 | 165810 |
| | Gd2 O7 Zr2 | Fluorite | 5.2618(2) | Not Given | Not Applicable | 0.0276 | 165811 |
| | Gd2 O7 Zr2 | Fluorite | 5.2639(2) | Not Given | Not Applicable | 0.0311 | 165812 |
| | Gd2 O7 Zr2 | Pyrochlore | 10.5327(4) | Not Given | 0.3888(9) | 0.0416 | 165813 |
| | Gd2 O7 Zr2 | Pyrochlore | 10.5369(4) | Not Given | 0.389(1) | 0.0366 | 165814 |
| | Gd2 O7 Zr2 | Pyrochlore | 10.5366(4) | Not Given | 0.390(1) | 0.0349 | 165815 |
| | Gd2 O7 Zr2 | Pyrochlore | 10.5428(4) | Not Given | 0.3949(7) | 0.0411 | 165816 |
| | Gd2 O7 Zr2 | Pyrochlore | 10.5106(8) | Not Given | 0.344(1) | 0.0628 | 160158 |
| | Gd2 O7 Zr2 | Fluorite | 5.26 | Not Given | Not applicable | Not Available | 184203 |
| | Gd2 O7 Zr2 | Pyrochlore | 10.520(5) | 298 | 0.346 | Not Available | 185395 |
| | Gd2 O7 Zr2 | Pyrochlore | 10.5249(2) | 4 | 0.3456(3) | 0.04 | 261758 |

| | | | | | | | |
|---|---|---|---|---|---|---|---|
| | Gd2 Zr2 O7 | Pyrochlore | 10.54010(4) | 295 | 0.3456(3) | 0.0957 | 261759 |
| Something is a bit odd with this | Gd1.49 O5.21 Zr1.49 | Pyrochlore | 10.5295(4) | Not Given | 0.0158 | 0.018 | 68264 |
| | Gd1.894 O6.629 Zr1.894 | Pyrochlore | 10.5227(4) | Not Given | 0.346 | 0.025 | 68263 |
| | Gd1.894 O7 Zr1.894 | Pyrochlore | 10.5227(4) | Not Given | 0.01013(77) | 0.019 | 66124 |
| | Gd2 O7 Zr2 | Fluorite | 5.2636(1) | Not Given | Not Applicable | 0.019 | 68265 |
| $La_2Zr_2O_7$ | La0.1 O1.95 Zr0.9 | Fluorite | 5.1149(20) | Not Given | Not applicable | 0.047 | 75064 |
| | La0.1 O1.95 Zr0.9 | Fluorite | 5.1635(3) | Not Given | Not Applicable | 0.047 | 81035 |
| | La0.5 O1.75 Zr0.5 | Fluorite | 5.407 | Not Given | Not Applicable | Not Given | 28991 |
| | La2 O7 Zr2 | Pyrochlore | 10.786 | Not Given | 0.295 | 0.076 | 15165 |
| | La2 O7 Zr2 | Pyrochlore | 10.7997(3) | Not Given | 0.3307(2) | 0.015 | 51573 |
| | La2 O7 Zr2 | Pyrochlore | 10.802(1) | Not Given | 0.333 | Not given | 150206 |
| | La2 O7 Zr2 | Pyrochlore | 10.80470(6) | Not Given | 0.331(3) | 0.0202 | 153222 |
| | La2 O7 Zr2 | Pyrochlore | 10.724 | Not Given | 0.3314 | Not given | 153814 |
| | La2 O7 Zr2 | Pyrochlore | 10.793 | Not Given | 0.33002 | Not given | 154752 |
| | La2 O7 Zr2 | Pyrochlore | 10.882 | Not Given | 0.333 | Not given | 159321 |
| | La2 O7 Zr2 | Pyrochlore | 10.8076(5) | 298 | 0.4189(2) | 0.044 | 173795 |
| | La2 O7 Zr2 | Pyrochlore | 10.808(1) | Not Given | 0.296(1) | 0.0292 | 180491 |
| | La2 O7 Zr2 | Pyrochlore | 10.811(4) | 298 | 0.419 | Not Given | 184089 |
| | La2 O7 Zr2 | Pyrochlore | 10.828(4) | 473 | 0.419 | Not Given | 184090 |
| | La2 O7 Zr2 | Pyrochlore | 10.848(4) | 673 | 0.419 | Not Given | 184091 |
| | La2 O7 Zr2 | Pyrochlore | 10.869(4) | 873 | 0.419 | Not Given | 184092 |
| | La2 O7 Zr2 | Pyrochlore | 10.892(3) | 1073 | 0.419 | Not Given | 184093 |
| | La2 O7 Zr2 | Pyrochlore | 10.810(4) | 1273 | 0.419 | Not Given | 184094 |
| | La2 O7 Zr2 | Pyrochlore | 10.915(4) | 1323 | 0.419 | Not Given | 184095 |
| | La2 O7 Zr2 | Pyrochlore | 10.921(4) | 1373 | 0.419 | Not Given | 184096 |
| | La2 O7 Zr2 | Pyrochlore | 10.927(4) | 1423 | 0.419 | Not Given | 184097 |
| | La2 O7 Zr2 | Pyrochlore | 10.933(4) | 1473 | 0.419 | Not Given | 184098 |
| | La2 O7 Zr2 | Pyrochlore | 10.939(3) | 1523 | 0.419 | Not Given | 184099 |
| | La2 O7 Zr2 | Pyrochlore | 10.945(4) | 1573 | 0.419 | Not Given | 184100 |
| | La2 O7 Zr2 | Pyrochlore | 10.951(4) | 1623 | 0.419 | Not Given | 184101 |
| | La2 O7 Zr2 | Pyrochlroe | 10.957(4) | 1673 | 0.419 | Not Given | 184102 |
| $Y_2Zr_2O_7$ | O1.89316 Y0.21432 Zr0.78584 | Fluorite | 5.1378(14) | Not Given | Not Applicable | 0.045 | 90894 |
| | O1.7 Y0.6 Zr0.4 | Fluorite | 5.227(2) | Not Given | Not Applicable | Not Given | 181238 |

| | | | | | | | |
|---|---|---|---|---|---|---|---|
| | O1.8 Y0.4 Zr0.6 | Fluorite | 5.180(2) | Not Given | Not Applicable | Not Given | 181237 |
| | O1.862 Y0.28 Zr0.72 | Fluorite | 5.16(2) | 298 | Not Applicable | 0.073 | 60396 |
| | O1.875 Y0.25 Zr0.75 | Fluorite | 5.165 | Not Given | Not Applicable | Not Given | 164864 |
| | O1.875 Y0.25 Zr0.75 | Fluorite | 5.108 | Not Given | Not Applicable | Not Given | 185129 |
| | O1.91 Y0.18 Zr0.82 | Fluorite | 5.145(2) | Not Given | Not Applicable | Not Given | 181236 |
| | O2 Y0.18 Zr0.82 | Fluorite | 5.145 | Not Given | Not Applicable | Not Given | 173694 |
| | O1.893 Y0.214 Zr0.786 | Fluorite | 5.14729(7) | Not Given | Not Applicable | 0.0127 | 165036 |
| | O1.906 Y0.188 Zr0.812 | Fluorite | 5.13 | Not Given | Not Applicable | Not Given | 164863 |
| | O1.938 Y0.125 Zr0.875 | Fluorite | 5.077 | Not Given | Not Applicable | Not Given | 185127 |
| | O1.906 Y0.1875 Zr0.8125 | Fluorite | 5.092 | Not Given | Not Applicable | Not Given | 185128 |
| | O1.969 Y0.0625 Zr0.9375 | Fluorite | 5.064 | Not Given | Not Applicable | Not Given | 185126 |
| | O7 Y2 Zr2 | Fluorite | 5.212(1) | Not Given | Not Applicable | 0.0119 | 130000 |
| | O7 Y2 Zr2 | Pyrochlore | 10.335 | Not Given | 0.3417 | Not Given | 153818 |
| | O1.862 Y0.28 Zr0.72 | Fluorite | 5.16(2) | 298 | Not Applicable | 0.073 | 60393 |
| | O1.862 Y0.28 Zr0.72 | Fluorite | 5.21(2) | 1040 | Not Applicable | 0.096 | 60394 |
| | O1.862 Y0.28 Zr0.72 | Fluorite | 5.21(2) | 1040 | Not Applicable | 0.088 | 60395 |
| | O1.862 Y0.28 Zr0.72 | Fluorite | 5.21(2) | 1040 | Not Applicable | 0.091 | 60397 |
| | O1.862 Y0.28 Zr0.72 | Fluorite | 5.21(2) | 1040 | Not Applicable | 0.079 | 60398 |
| | O1.862 Y0.28 Zr0.72 | Fluorite | 5.21(2) | 1040 | Not Applicable | 0.079 | 60399 |
| | O1.862 Y0.28 Zr0.72 | Fluorite | 5.21(2) | 1040 | Not Applicable | 0.072 | 60400 |

| | | | | | | | |
|---|---|---|---|---|---|---|---|
| | O1.9 Y0.2 Zr0.8 | Fluorite | 5.14728(9) | Not Given | Not Applicable | 0.0239 | 75316 |
| * | O1.879 Y0.242 Zr0.758 | Fluorite | 5.15463(5) | Not Given | Not Applicable | 0.005 | 280134 |
| | O1.879 Y0.242 Zr0.758 | Fluorite | 5.15463(5) | Not Given | Not Applicable | 0.009 | 280135 |
| | O1.7 Y0.214 Zr0.786 | Fluorite | 5.1482 | Not Given | Not Applicable | 0.0349 | 60605 |
| | O1.866 Y0.214 Zr0.786 | Fluorite | 5.1482 | Not Given | Not Applicable | 0.0351 | 60610 |
| $Eu_2Ti_2O_7$ | Eu2 O7 Ti2 | Pyrochlore | 10.2064(5) | Not Given | 0.328(1) | 0.048 | 83596 |
| | Eu2 O7 Ti2 | Pyrochlore | 10.2048(6) | Not Given | 0.328(1) | 0.048 | 92767 |
| | Eu2 O7 Ti2 | Pyrochlore | 10.197(1) | Not Given | 0.327(2) | Not Given | 173945 |
| $Gd_2Ti_2O_7$ | (Gd1.84 Ti0.16) (Ti1.84 Gd0.16) O7 | Pyrochlore | 10.212(1) | Not Given | 0.426000 | 0.039 | 154163 |
| | (Gd1.87 Ti0.13) (Ti1.87 Gd0.13) O7 | Pyrochlore | 10.2038(8) | Not Given | 0.428000 | 0.046 | 154162 |
| | (Gd1.881 Ti0.119) (Ti1.881 Gd0.119) O7 | Pyrochlore | 10.2002(1) | Not Given | 0.425(1) | 0.05 | 154160 |
| | (Gd1.893 Ti0.107) (Ti1.893 Gd0.107) O7 | Pyrochlore | 10.2025(2) | Not Given | 0.426(1) | 0.05 | 154161 |
| | Gd1.8 Ti2 O6.46 | Pyrochlore | 10.189(3) | Not Given | 0.418(1) | 0.0383 | 157397 |
| | Gd2 (Ti2 O7) | Pyrochlore | 10.1840(1) | 295 | 0.4319(2) | 0.151 | 167918 |
| | Gd2 O7 Ti2 | Pyrochlore | 10.182(1) | Not Given | 0.327 | Not Given | 150210 |
| | Gd2 O7 Ti2 | Pyrochlore | 10.206 | Not Given | 0.3292 | Not Given | 164024 |
| | Gd2 O7 Ti2 | Pyrochlore | 10.1852(9) | Not Given | 0.4263(34) | 0.0182 | 24207 |
| $La_2Ti_2O_7$ | La2 O7 Ti2 | Pyrochlore | 10.366 | Not Given | 0.3227 | Not Given | 153816 |

| | | | | | | | |
|---|---|---|---|---|---|---|---|
| | La2 O7 Ti2 | Pyrochlore | 10.486 | Not Given | 0.3231 | Not Given | 164027 |
| $Y_2Ti_2O_7$ | (Y0.72 Ti1.28) (Ti0.72 Y1.28) O7 | Pyrochlore | 10.161(1) | | 0.430(1) | 0.052 | 154155 |
| | (Y1.1 Ti0.9) (Ti1.1 Y0.9) O7 | Pyrochlore | 10.1281(5) | | 0.4291(8) | 0.05 | 154154 |
| | (Y1.75 Ti0.25) (Ti1.75 Y0.25) O7 | Pyrochlore | 10.1095(2) | | 0.4204(4) | 0.028 | 154153 |
| | (Y1.93 Ti0.07) (Ti1.93 Y0.07) O7 | Pyrochlore | 10.1004(1) | | 0.4218(3) | 0.09 | 154152 |
| | Y Ti O2.085 | Pyrochlore | 10.1811(6) | | Not applicable | 0.049 | 400624 |
| | Y1.98 Ti1.99 O7 | Pyrochlore | 10.093972(26) | | 0.329133(24) | Not given | 173048 |
| | Y2 (Ti2 O7) | Pyrochlore | 10.0986(5) | | 0.3253(4) | 0.049 | 83593 |
| | Y2 Ti2 O7 | Pyrochlore | 10.0947(1) | | 0.420820 | 0.0996 | 66874 |

### ii. Discussion on the crystallographic information table

#### Europium Hafnate

There are three literature structures, two of which are non-stoichiometric and the third being a stoichiometric variant. All three entries are of the pyrochlore structure type. No measurement temperatures were given in the cif files. Entry 173953 did not have an R factor given

#### Gadolinium hafnate

There are two available structures, one with a non-stoichiometric chemical formula, and the other with stoichiometry. Both structures are pyrochlores. No measurement temperatures were given in the cif files. Both entries had the same R factors of 0.0477

#### Lanthanum Hafnate

There are two available structures, both display chemical stoichiometry. Entry 173790 was measured at 298 K and has an R factor of 0.0387. Entry 153815 has its measurement temperature and its R factor missing.

### Yttrium Hafnate

No Cif files available for this system.

### Gadolinium Zirconate

20 entries were available, 12 of which are of the pyrochlore structure type, and the other eight are of the defect-fluorite structure type. 17 of the structural entries had stoichiometric chemical formulae whilst three exhibited non-stoichiometry. Entries 184203 and 185395 did not have R values recorded. Only three structures had specific measurement temperatures recorded. The measurement temperatures were 298, 4, and 295 K for entries 185395, 261758, and 261759 respectively.

### Lanthanum Zirconate

Of the 26 available structures, 23 were of the pyrochlore structure type, and three of the defect fluorite structure type. All the pyrochlore structures had stoichiometric chemical formulae. All the defect-fluorite structures had non-stoichiometric chemical formulae. Eleven of the structures were missing their R values. Eight structures were listed with their measurement temperatures.

### Yttrium Zirconate

27 structures were available of which one was of the pyrochlore structure type and 26 were of the defect fluorite structure type. Only two of the structures were chemically stoichiometric. This included the pyrochlore structure. Eleven of the structures were missing their R-factors. Only eight of the structures had specified measurement temperatures.

### Europium Titanate

All three available structures crystallize in the pyrochlore structure type. No measurement temperatures were recorded. Entry 175945 was missing an R factor. Entries 83596 and 92767 both had R factors of 0.048. All structures exhibited chemical stoichiometry.

### Gadolinium Titanate

All nine of the available structures are of the pyrochlore structure type. Entry 167918 was measured at 295 K whilst the rest of the entries did not have their measurement temperatures listed. Entries 150210 and 164024 did not have R factors recorded.

### Lanthanum Titanate

Both available structures are of the pyrochlore structure type. Both entries had no measurement temperatures and R factors available Note: a pyrochlore phase was not obtained for this system.

All eight entries are of the pyrochlore structure type. Two of the structures had chemical stoichiometry, whilst the other six were non-stoichiometric. Entry 173048 was missing its R factor.